2019-08-01

Preparation, Functionalization, and/or Characterization by X-ray Photoelectron Spectroscopy of Carbon Surfaces for Biosensors and Other Materials

Varun Jain
Brigham Young University

Preparation, Functionalization, and/or Characterization by X-ray Photoelectron Spectroscopy of Carbon Surfaces for Biosensors and Other Materials

Varun Jain

A dissertation submitted to the faculty of
Brigham Young University
in partial fulfillment for the requirements for the degree of

Doctor of Philosophy

Matthew Richard Linford, Chair
Daniel E. Austin
David V. Dearden
Jaron C. Hansen
Barry M. Lunt

Department of Chemistry and Biochemistry

Brigham Young University

ABSTRACT

Preparation, Functionalization, and/or Characterization by X-ray Photoelectron Spectroscopy of Carbon Surfaces for Biosensors and Other Materials

Varun Jain
Department of Chemistry and Biochemistry, BYU
Doctor of Philosophy

My dissertation is primarily divided into two parts. The first deals with the preparation, functionalization, and characterization of carbon surfaces prepared by direct current magnetron sputtering (DCMS) and high power impulse magnetron sputtering (HiPIMS) as substrates for bioarrays. Part two discusses applications of XPS peak fitting in surface chemical analysis. Chapter 1, the introduction, includes (i) a discussion of the construction of bioarrays and the preparation of sputtered surfaces, e.g., by DCMS and HiPIMS, and also functionalization (bioconjugate) chemistry with special emphasis on the importance of covalent functionalization of surfaces, and (ii) a discussion of the surface characterization techniques and accompanying analysis methods I have primarily used, which include X-ray photoelectron spectroscopy (XPS), near-ambient pressure XPS (NAP-XPS), XPS peak fitting, and contact angle goniometry (wetting). Chapter 2 discusses the preparation, characterization, and functionalization of DCMS and HiPIMS carbon surfaces for bioarrays. Here, two functionalization chemistries are explored, where the activity of DCMS and HiPIMS carbon towards amidation and amination is compared. Chapter 3 focuses on the use of Gaussian-Lorentzian sum (GLS) and Gaussian-Lorentzian product (GLP) line shapes in the context of peak fitting XPS narrow scans. This discussion includes a comparison of the GLS and GLP line shapes with the Voigt function. Chapters 4 and 5 discuss the applications of XPS peak fitting in materials characterization. Chapter 4 talks about XPS data analysis in the context of the chemical vapor deposition of various aminosilanes and their effect on peptide stability and purity. Chapters 5 describes the surface chemical analysis of various materials by NAP-XPS, including accompanying data analysis and/or peak fitting. The materials probed here cannot be analyzed at ultra-high vacuum by conventional XPS, hence, they are analyzed by NAP-XPS. Chapter 5 is divided into 5 sections. Section 5.1.1 discusses the characterization and analysis of a solution of bovine serum albumin (BSA) by peak fitting the C 1s and O 1s peak envelopes. Section 5.1.2 discusses the analysis of polytetrafluoroethylene (PTFE) at different pressures. Here, the effect of increasing background pressure and X-ray illumination time on the equivalent widths of the F 1s narrows scans is shown. Environmental charge compensation is also discussed here. Section 5.1.3 includes the analysis of poly(γ-benzyl L-glutamate) (PBLG), where the C 1s and O 1s peak envelopes were peak fitted to determine/confirm the structure and composition of this polymer. Section 5.1.4 contains an analysis and comparison of three different human hair samples: (i) untreated, (ii) colored, and (iii) bleached. Here, a comparison of the Si 2p, S 2p, and C 1s peaks illustrates the effects of the different treatments. Section 5.1.5 shows the characterization and analysis of liquid and solid phosphate buffered saline (PBS). Chapter 6 presents conclusion of my work and discusses future work.

Keywords: X-ray photoelectron spectroscopy, XPS, near ambient pressure – XPS, NAP-XPS, peak fitting, DCMS, HiPIMS, sputtering, GLP, GLS, Bioarrays, PTFE, PBLG, BSA, PBS

ACKNOWLEDGEMENTS

Graduate school has been a long walk, and my journey through graduate life has not been alone. I certainly got significant help from many good people and they have contributed to my success. I am very grateful to my PhD supervisor Dr. Matthew Linford, a very humble person, for his continuous guidance and support, and for giving me many opportunities to learn and grow as a researcher and as an individual as well. I would like to thank my committee members Drs. Daniel E. Austin, David V. Dearden, Jaron C. Hansen, and Barry M. Lunt for giving me invaluable suggestions and encouraging me to rectify my mistakes. I would also like to thank Dr. Bhupinder Singh for mentoring me during my first years of graduate school.

A good part of the work presented here was completed in collaboration and supported by InSilixa Inc. I would like to give my sincere gratitude to them for funding me for 2 years. I would also like to thank the Department of Chemistry and Biochemistry for providing me a platform to do my research.

During my graduate life, I got the opportunity to meet new people. I would like to acknowledge my lab mates: Dr. Anubhav Diwan, Dr. Cody Cushman, Brain Johnson, Tuhin Roychowdhury, Dr. Shiladitya Chatterjee, Dhananjay Patel, Dhruv Shah, George Major, Tahereh Gholian Avval, Nitish Bhardwaj, Berg Dodson, and Karen Membreno for their help and support.

At BYU, I met many helpful and generous people. I would like to thank the administrative staff of the Department of Chemistry and Biochemistry for their kind support. I would like to give my special thanks to Janet Fonoimoana for being very helpful and caring, and giving me moral support when I was feeling low. I would also like to acknowledge the help of Anna Kennington and Sue Mortensen.

During my stay at BYU, I really missed some of my old friends and I would like to acknowledge them. I am really thankful to two of my old friends and lab mates Manesh Nautiyal and Mradul Shrivastav for always helping me and motivating me to do a good work. I am also very thankful to my friend Ankit Gupta and Ashok Sharma for their support and motivation during my pursuit of getting admission in PhD program in the USA. After coming to the USA, I also got the opportunity at BYU to make other new friends. I would like to thank CJ Madsen and Samm Madsen for always being there for us and for having given me and my family great moral support when we really needed it. I want to thank Jared and Lisa Thomas for giving me great input to improve my writing and speaking skills.

Living away from home has not been easy for me. However, I received continuous encouragement from my family that kept me going. I would like to thank my parents, Mr. Nemkumar Jain and Mrs. Asha Jain, and Mr. Virendra Pradhan and Mrs. Meena Pradhan. I am also thankful to brothers-in-law and sisters-in-law, and my brothers and sisters. The one person who has had the greatest impact on my graduate life since I came here is my wife who has always been very supportive in the truest sense. After getting married in my second year of graduate school, I received moral, financial, and emotional support from my wife irrespective of whether I could fulfill her expectations or not. "Thank you" is really a small way to show my gratitude for the sacrifices she has made for me. I would also like to thank to my darling daughter Varunika Jain for filling my graduate life with happiness and making it smoother.

Last, but not least, I am very grateful to The Almighty God for giving me this opportunity to do good work and for supporting me throughout my life and graduate education.

TABLE OF CONTENTS

LIST OF TABLES

LIST OF FIGURES

LIST OF ABBREVIATIONS

AFM	Atomic force microscopy
APDEMS	3-aminopropyldiethoxymethylsilane
APDIPES	3-aminopropyldiisopropylethoxysilane
APTES	3-aminopropyltriethoxysilane
BA	Benzylamine
BSA	Bovine Serum Albumin
CVD	Chemical vapor deposition
DCMS	Direct current magnetron sputtering
DETA	Diethylenetriamine
DLC	Diamond-like carbon
EDC	1-Ethyl-3-(3-dimethylaminopropyl)carbodiimide
EA	Ethanolamine
GLP	Gaussian-Lorentzian product
GLS	Gaussian-Lorentzian sum
HiPIMS	High-power impulse magnetron sputtering
HFA	2,2,3,3,4,4,4-Heptafluorobutylamine
NAP-XPS	Near-ambient pressure X-ray photoelectron spectroscopy
NHS	N-Hydroxusulfosuccinamide

MBA	4-Methoxybenzylamine
ODA	Octadecylamine
PAM	Polyallylamine
PAC	Poly(diallyldimethylammonium chloride)
PBLG	Poly-(γ-benzyl-L-glutamate)
PBS	Phosphate Buffer Saline
PEI	Polyethylenimine
PTFE	Polytetrafluroethylene
SE	Spectroscopic ellipsometry
SEM	Scanning electron microscopy
ToF-SIMS	Time-of-flight secondary ion mass spectrometry
WCA	Water contact angle
XPS	X-ray photoelectron spectroscopy

CHAPTER 1: Introduction

1.1 Aims and Overview of My Work

Thin film carbon deposition represents an important area of study and has many applications including in protective coatings for optical windows, data storage, micro-electrochemical devices (MEMs), and electrochemical biosensors.[1, 2] Some of the physical vapor deposition processes that can be used to deposit carbon thin films include cathodic arc deposition, pulsed laser deposition, e-beam deposition, ion assisted sputtering, and magnetron sputtering.[3-13] Chemical vapor deposition methods have also been explored for this purpose.[1, 14-16] Of these methods, sputtering is the most commonly used process for depositing amorphous carbon as a thin film, and it is the method of choice for most industrial applications.[8-9, 17-21]

After deposition, thin films should be thoroughly characterized to determine their physical and chemical structures/states. Some of the more important techniques for chemically analyzing surfaces include X-ray photoelectron spectroscopy (XPS), spectroscopic ellipsometry (SE), atomic force microscopy (AFM), scanning electron microscopy (SEM), time-of-flight secondary ion mass spectrometry (ToF-SIMS), low energy ion scattering, and water contact angle goniometry.[22] In many cases, surface characterization involves the top ca. 10 nm (or less) of a material. Informatics (chemometrics) methods for analyzing the data from surface analysis techniques also play an important role in understanding materials. The past few decades have seen consistent improvements and advances in the speed, efficiency, automation, and resolution of the various surface analysis methods, as well as in the accompanying data analysis.[23-25]

The first part of my thesis describes the preparation of carbon films by direct current magnetron sputtering (DCMS) and high power impulse magnetron sputtering (HiPIMS) followed by their characterization and functionalization for their application in biosensors and bioarrays. The

chemical functionalization of these carbon surfaces was approached in two ways. The first route consisted of amidation using 1-Ethyl-3-(3-dimethylaminopropyl)carbodiimide (EDC) and *N*-hydroxusulfosuccinamide (NHS) as activation/coupling agents, and the second route involves halogenation followed by amination. The second part of my work describes the importance of line shapes/functions in XPS peak fitting of narrow scans. These functions include Gaussian Lorentzian sum (GLS), Gaussian Lorentzian product (GLP), and Voigt functions. This part of my work also deals with applications of XPS peak fitting in material characterization and data analysis thorough commercial peak fitting/analysis software. It also includes the characterization of various materials including silanes deposited onto a silicon surface for bioarrays and a series of materials that cannot be analyzed by conventional XPS including proteins, polymers, biological liquids, and some other unconventional materials. Hence, these materials are analyzed by near ambient pressure – X-ray photoelectron spectroscopy (NAP-XPS). In the coming sections, I will describe the following things: the construction of bioarrays, sputtering as a thin film deposition technique, and the importance of material characterization in surface science

1.2 Background of Bioarrays/Biochips and Their Importance

Biosensing is based on the specificity of various biological events for quantitative and/or qualitative detection of analytes like deoxyribonucleic acid (DNA), proteins, toxins, and hormones.[26] Biosensing is of great importance in many biological, clinical, and medicinal applications. [27-34] However, converting biological events into easily detectable electronic signals requires integration of a chemical interface with a biological environment.[32, 34] Some of the important applications of integrating biomolecules onto surfaces include micro and optoelectronic devices, electrochemical biosensors, and carbon- and silicon-based bioarrays.[27, 31, 35-38]

Biochips or biomolecular arrays are defined as collections of multiple miniaturized test sites or biosensors arranged on a solid substrate in order to achieve high throughput and speed.[2] By attachment of multiple biomolecules, bioarrays allow detection of multiple analytes in a massively parallel fashion.[33] Bioarrays show significant promise for effective and early diagnostics of various diseases.[33, 39] Therefore, there is a need for platforms that are selective, sensitive, cost-effective, easy to miniaturize and fabricate, and that provide high throughput and speed.[32-33, 39] Biosensor based research has seen significant advances over the past few decades.[34] Through this process, microarray and bioarray technology has emerged as a versatile platform for the detection of biomolecules. The first high-density peptide arrays were developed in the early 1990s,[40] and this technology has subsequently been extended to arrays of oligonucleotides,[41] RNA, carbohydrates, proteins such as lectins or antibodies, other small molecules, and complete lab-on-a-chip devices.[2, 39, 42] The Southern blot is one of the oldest examples of an array that allows quantitative determination of DNA.[2, 43] Other traditional array methods such as the enzyme-linked immunosorbent assay (ELISA), the radioimmunoassay,[44] electrophoretic immunoassay,[45] mass spectrometric immunoassay,[46] and immunofluorimetric immune-polymerase chain reaction (PCR) assay[47] have the disadvantages of being more time consuming, expensive, and requiring trained operators and/or sophisticated instrumentation.[33]

A lab-on-a-chip is a device where all the laboratory function can be performed on a single platform in a fairly short time yielding high throughput and speed. These include electrochemical[33, 48-49] and optical biochips[33, 50-51] or fully integrated complementary metal-oxide based semiconductor (CMOS) fluorescence biochips for DNA and RNA testing.[42] “The unique features of such CMOS based biochips is the diverse functionality of their biosensor “pixel”, which are basically the elements within the densely packed arrays.” These biochips are constructed with the

intent to perform all the laboratory functions necessary to analyze various biomolecules on a single platform. For example, each pixel may behave as a complete, independent unit and contains molecular detection elements, a transducer to detect biological events (an active electrode or photo diode), electronic sensor interface circuitry, and a temperature control system to adjust the temperature from room temperature to 100 °C. Such biochips can have thousands of biosensors or pixels on their surfaces to detect multiple analytes like DNA, RNA, proteins, peptides, and/or other metabolites. They can be very useful in forensic analysis, disease diagnosis, and in toxicological, environmental, biochemical, and genetics research.[52] An important advantage of such biochips is that they can be directly applied to complex samples including bodily fluids, foodstuffs, cell cultures, and environmental samples.[34] Such a high-performance biochip is lab-on-a-chip in the truest sense. They are particularly important for providing point-of-care treatment, e.g., in the detection of septicemia where a very quick diagnosis of a bacterial strain causing infection is required. Sepsis is a serious medical issue in the United States, affecting as many as 750,000 hospitalized patients in the U.S. annually. According to the Agency for Healthcare Research and Quality (AHRQ), sepsis is the most expensive cause of hospitalization in the U.S., accounting for more than $24 billion annually.[53] Hence, with a simple, sample-to-answer solution, such a platform provides actionable results in less than an hour and gives, by targeted pathogen identification, increased patient care in a cost effective manner and real time surveillance of infectious diseases like sepsis.[54] Consequently, lab-on-a-chip devices can make a significant contribution to the betterment of the health of an affected community.

1.3 Fabrication of Bioarrays

The construction of bioarrays involves three things: (1) a substrate for attaching biomolecules, i.e. the interface, (2) a functionalization chemistry to immobilize the biomolecules

onto the surface – covalent methods are often preferred here, and (3) the biomolecules themselves.[2, 33] However, there are drawbacks associated with the most commonly used substrates that include gold, glass, and silicon. Accordingly, a material like carbon that allows direct covalent coupling through strong, robust bonds deserves greater attention. Different physical vapor deposition (PVD) methods for depositing carbon as a thin film will now be discussed. In particular, the emphasis will be on deposition of carbon by high power impulse magnetron sputtering (HiPIMS) and direct current magnetron sputtering (DCMS). I will then discuss various functionalization chemistries that are important for covalent attachment of biomolecules onto carbon and/or carbon-based materials. I will discuss in detail here two protocols we have used to functionalize HiPIMS and DCMS carbon. In particular, in chapter 2 of this thesis, I show the preparation/deposition of these two types of carbon films and their characterization and functionalization.

1.3.1 Substrate

Currently, there is interest in developing high throughput systems that utilize appropriate transducer materials to optimize detection sensitivities. There is also a need for highly integrated sensor arrays and bio-interfaces with high chemical stability.[55] Such sensor arrays have the ability to improve diagnoses of diseases like cancer through detection of biomarkers.[55-58] There are a number of established substrate materials that are compatible with microelectronic processes and that might be integrated into bioarrays.[59-61] However, most of them lack some of the necessary characteristics for this application such as flatness, homogeneity, chemical stability, reproducibility, and the ability to undergo biochemical surface modifications.[62-65] For example, the stabilities of traditional glass and gold substrate materials with their respective silane and thiol chemistries are questionable at elevated temperatures, at pH values above 11, and/or sometimes

even upon exposure to the atmosphere or aqueous solvents.[30] In the case of silane chemistry, the siloxane bonds formed with the substrate hydrolyze under acidic or basic conditions.[66-68] Gold-sulfur bonds formed by attachment of alkanethiols to gold surfaces become labile if exposed to the atmosphere (oxygen) for extended periods of time or if exposed to a mild oxidizer or UV light.[30, 69-72] Thus, the need for greater stability and biocompatibility have caused researchers to consider the Group IV semiconductors.[73-74] Silicon has a number of virtues, including the strength and robustness of its Si-C bond. However, the silicon surface oxidizes upon prolonged exposure to atmospheric conditions.[59, 75-76] In general, silicon surfaces also require the use of fluoride-containing solutions in their preparation, which are toxic. Unlike silicon, carbon does not oxidize rapidly in the air or under aqueous conditions. Thus it can potentially be a more stable interface material, and it also enjoys tunable semiconductor properties. [2, 55, 76-79] Most forms of carbon are biocompatible, chemically inert, and stable. Thus, various carbon-based materials, e.g., carbon nanotubes, carbon quantum-dots, graphene (sp^2), and diamond (sp3),[55] have been investigated as substrates for bioarrays.[2, 33, 55, 78]

As expected, diamond shows higher mechanical hardness, durability, and chemical inertness than the other forms of carbon mentioned above. In addition, the robust carbon-carbon (C-C) covalent bonds in diamond provide good biocompatibility, which, along with its above mentioned qualities, arguably make diamond a better candidate for bioarrays than glass, silicon, or gold.[1-2, 80-84] Furthermore, due to its sp^3 nature, diamond shows versatility for the attachment of biomolecules by direct covalent attachment.[2, 55] Diamond also has the ability to be readily patterned with a resolution ranging from millimeters to micrometers. [85-87] Because of diamond's strengths, research has been done in the past to functionalize its surfaces.[88-90] However, both diamond itself and other similar forms of glassy carbon require realtively high temperatures to be

prepared. The deposition of amorphous carbon at moderate temperatures on substrates like silicon is a more facile endeavor.[14, 82, 91-93] This non-crystalline form of carbon with a high fraction of sp^3 carbon is known as diamond-like carbon (DLC).[55]

DLC films have been a subject of research over the last few decades. Amorphous DLC is a particularly attractive material because of its sp^3 bonding, which gives DLC many of diamond's physical and chemical properties, such as its hardness, elastic modulus, chemical and electrochemical inertness, resistance to air oxidation, biocompatibility, and wide band gap.[3, 10, 94-100] Also, it is comparatively less expensive to produce than diamond itself and it can be reproducibly functionalized with biomolecules through stable carbon-carbon covalent bonds.[2, 82-83] Moreover, DLC not only displays characteristics of amorphous carbon but it also has some hydrogenated character.[1] All of these attributes make DLC a good choice as an interface for the construction of biosensors.

1.3.2. Deposition Techniques with Special Emphasis on Sputtering

Different deposition methods have been explored to deposit amorphous carbon as a thin film, including physical vapor deposition (PVD) and chemical vapor depostion (CVD),[1, 3, 16, 85, 101-103] where the method chosen depends on the need and suitability of the method for laboratory scale research or industrial scale production.[15-16, 55, 85, 103-104] (As an aside, a reason behind the evolution of the PVD technique was the inabilty of a diffusion-applied aluminide coating to protect aerofoils. These coatings were important for the development of gas turbines.[105]) PVD is a vacuum coating process for depositing a solid material onto a substrate that is physically removed from the source of the material. This solid material can be almost any inorganic material, including, under appropriate conditions, metals, alloys, compounds, or mixtures of them,[106] and the means of transfering this material may be through evaporation or sputtering. For sputtering, the metal will

initially be in the form of a solid target, while for evaporation it may initially be in the form of large granules, i.e., shot. It is common for very high purity materials to be used in these depositions (at least 99.9% pure). In either case, the material deposits/condenses as a thin film (a non-equilibrium process) onto the surface of the substrate.[106-108] Note that reactive depositions are possible by introducing a reactive gas, e.g., oxygen, nitrogen, or perhaps a hydrocarbon, into the deposition chamber, which can chemically interact with the growing film and/or target material. Most PVD processes are named based on the means by which the physical vapor is produced.

As noted above, the two main categories of PVD techniques include evaporation and sputtering. Under evaporation come resistive, inductive, electron beam, activated reactive evaporation, and cathodic arc evaporation (direct, DC, or alternating current, AC). Possibilities for sputtering include diode, triode, ion beam, or magnetron sputtering (MS), including DC-MS, radio frequency (RF) MS, pulsed cathode MS, dual MS, and high-power pulsed magnetron sputtering (HiPIMS)[109] PVD techniques are effective ways of depositing carbon as a thin film. In fact, DLC was first deposited by a PVD technique.[3-4, 15] PVD techniques that can be used to deposit DLC include cathodic arc deposition, ion deposition, sputtering, plasma deposition, pulsed laser deposition, and ion assisted deposition.[56, 104, 110-111] Of the above mentioned PVD techniques, methods based on plasmas are currently in wide use for thin film deposition.[106] Sputtering is one of these plasma based processes. It is a nonthermal vaporization process in which an energetic bombarding particle, generally a gaseous ion accelerated from a plasma or an "ion gun", gives momentum to atoms in a solid target so that they can be physically dislodged from the target surface. In general, the high energy atoms that leave the surface of the target adhere well to a substrate surface.[112] Sputtering can be performed in vacuum or partial vacuum where the sputtered

material does not undergo gas-phase collisions in the blank space between the target and the substrate.[109]

Cathode sputtering was first used to fabricate coatings in the 1930s. Later, sputtering by ion bombardment was used in the 1950s for commercial applications.[109] Sputtering is now widely used in the semiconductor industry to make deposition barriers, adhesion or seed layers, primary conductors, antireflection coatings, and etch barriers.[113] Sputtered films have also been used in the preparation of optical discs.[114-116] Sputtering is the preferred method for most industrial applications, where it is preferred over thermal and electron beam evaporation because they have lower depostion rates and are influenced very easily by changes in the temperature of the target material because the vapor pressure of a material is strongly influenced by its temperature. Sputtering is also relatively inexpensive, reproducible, and scalable.[117] Also, in sputtering the deposition rate can be rather easily controlled by the plasma power and gas pressure inside the chamber, which are mostly independent of the conditions and geometry of the substrate.[1, 107] All of these advantages make sputtering an ideal fit for industry.

Planar and Magnetron Sputtering

Sputtering can be performed in two modes: (i) planar sputtering and (ii) magnetron sputtering. In planar sputtering, there are no magnets placed behind the target. Therefore this mode has a few disadvantages, including the necessity of a higher working gas pressure, a lower deposition rate, a lower ion-to-neutral species ratio, i.e., lower ionization efficiency of the plasma, and substrate heating.[118] However, some of these issues were successfully addressed with the advent of magnetron sputtering[119-120] in which magnets were placed behind the target. Here, with the help of magnets, a cathode is able to restrict the electrons above it and cause them to move in a spiral fashion, which increases their path length and, in turn, improves the degree of ionization

of the plasma.[107] Consequently, a high-density plasma that is magnetically restricted to be around the target surface is produced, and ions are accelerated away from the plasma to the target surface.[118] The increased probability here of ions bombarding the target creates higher sputtering and deposition rates.[109]

Figure 1 depicts the typical workings of a magnetron sputtering system, including how a glowing plasma is produced above the sputter target inside the deposition chamber. In a typical arrangement, a target is placed on a cathode at high voltage and a low pressure of argon is introduced, which is activated to form a plasma. Argon gas ions then sputter the target, which results in the ejection of ions and neutrals.[109] Here, in magnetron sputtering, both the plasma discharge and deposition take place at a lower gas pressure.[15, 118] With the high deposition rates obtained in magnetron sputtering, it becomes possible to do reactive depositions of complex films by introduction of a reactive gas as long as target poisoning does not occur.

Sputtering and DLC deposition

It is advantageous to prepare carbon thin films in a way that is cost-effective, reproducible, and industrially sustainable. Since diamond or materials with diamond-like properties are some of the best possible interface materials for biosensing applications, it is imperative to use a deposition technique that will impart diamond-like properties to the carbon that is deposited. Out of the various PVD techniques, sputtering is the ideal method for depositing thin film DLC for research and industrial development/production, i.e., sputtering provides films with significant diamond-like character, including higher sp^3 character and also an amorphous nature.[1, 8-9, 15, 17-21, 103, 121-122] The drawback associated with sputtering is its comparatively low ratio of energetic ions to neutral species, resulting in less hard DLC films. However, amorphous carbon films with high sp^3 character can still be deposited at the expense of some decrease in deposition rate.[20, 107, 122]

The morphology and thickness of sputtered thin films is influenced by varying the deposition parameters. For example, without substrate heating, there is limited adatom diffusion[123] as atoms have essentially no mobility after impinging on a surface. Also, the angle at which the flux of atoms strikes the substrate can affect the morphology. In general, the higher the oblique angle, the greater the film porosity[123-125] due to a phenomenon known as shadowing.[126-127] Because of shadowing, absorbed atoms and growing features shield their neighbors from the incoming vapor flux, while features that are not shadowed grow in the direction of the incoming flux. This leads to porous structures. To deposit amorphous thin carbon films with some conductivity, we did not use oblique angle deposition and the substrate was rotated to get the most uniform deposition possible.

Types of Magnetron Sputtering: DCMS and HiPIMS

With the advent of new sputtering technology, the fabrication of new materials, including high aspect-ratio structures, becomes possible. The most common modes of magnetron sputtering used to sputter DLC include direct current magnetron sputtering (DCMS), radio frequency (RF) magnetron sputtering, and the newer high-power impulse magnetron sputtering (HiPIMS). The targets for these depositions are made of graphite or carbon, and argon is the typical sputter gas.[1, 128] Since, an RF power supply is generally used for sputtering insulating materials, and carbon enjoys quite good conductivity, DLC will typically be sputtered by DCMS or HiPIMS. It also becomes possible to sputter materials with complex designs that may be in integrated circuits, which has proven to be difficult because of their smaller dimensions and complex shapes.[106] Recently, the application of DLC in the construction of microelectromechanical systems has been recommended.[80, 100, 129] Many such applications require low deposition temperatures ($T_s < 100$ °C), high deposition rates, and films with multifunctional characteristics.[100] As a result, much attention

is being given to ion-assisted thin film growth methods like DCMS and HiPIMS by which the morphology and other properties of the films can be controlled through ion bombardment.[1, 97]

In DCMS, the film is usually grown through the bombardment of a sputtered neutral target with ions with energies of a few tens of electron volts and reflected neutral plasma gas atoms (usually argon). The sputter gas used here may include a mixture of Ar and H_2.[130] The intensity of bombardment depends on deposition parameters like the gas pressure, discharge current/sputtering power, substrate bias, substrate temperature, and geometry of the deposition system.[100] With the bombardment intensity, the structural properties (composition, chemical bonding, structural order, and density) as well as the mechanical properties (internal stress and hardness) of the amorphous carbon films can be altered.[130] Keeping all other parameters fixed, both the deposition process and the properties of the amorphous carbon films can be precisely and reproducibly prepared by changing the sputtering power. It has been reported that films deposited at lower power (<50 W) are very smooth and featureless and do not show columnar growth. However, when deposition is done at higher power (>100 W), there is comparatively higher roughness, and films deposited at 300 – 500 W show some cauliflower-like structure.[128] The disadvantage associated with DCMS is the limited number of ions out of the sputtered material for the deposition/thin film growth process.[131-132]

One such sputtering technique where the deposition flux consists of more ions out of the sputtered material is known as ionized PVD or IPVD.[133] In processes like IPVD, an electric field can control the flow of ions, and the material can be deposited in deep trenches of high aspect-ratio structures because of beam collimation. On the other hand, the neutral ion flux in DCMS only deposits on the upper portion of walls and gives very little coverage on trench bottoms. Therefore, the ionization of sputtered material has many advantages, including improved adhesion

characteristic,[134] higher densities of sputtered films[135], and better possible directionality of the vapor flux.[133]

HiPIMS is an IPVD technique that was introduced by Kouznetsov and coworkers in 1999.[136] "HiPIMS is an emerging pulsed magnetron sputtering technique, which utilizes pulsed plasma discharge where the peak power exceeds the time-averaged power by typically two orders of magnitude."[107] HiPIMS imparts high power density in the range of a few kW/cm^2 with a very low duty cycle (switch on and off ratio of <10%). However, it maintains the time-averaged power on a DCMS level usually of W/cm^2 to protect the target from any heating damage.[137] The width of the pulse and pulse frequency generally range from 10-500 μs and 10-500 kHz, respectively. A shorter pulse (<50 μs) helps achieve a higher deposition rate. For example, 70% of the DCMS deposition rate is achieved in 5 μs as compared to 20 % of the DCMS rate at 20 μs in the case of Ti.[138] The applied voltage is usually about 500 – 1000 V during the pulse with a maximum peak current density, i.e., discharge current/target area of a few amperes per square centimeter.[139] The main attribute of HiPIMS is to combine sputtering from normal magnetrons with that of a pulsed plasma. This combination helps in the generation of a highly ionized plasma and, consequently, the fraction of ionized, sputtered material.[140]

It is important to recognize in HiPIMS that the degree of ionization changes with the target material being used, and that this degree of ionization may range from 2% to almost 100%.[141] This behavior largely depends on the ionization potential (E_{IP}) of the sputtered material. For example, the E_{IP} for aluminum is 5.99 eV while the E_{IP} for carbon is 11.26 eV, suggesting that Al will be more easily ionized than C. However, regardless of the E_{IP}, the ionization or electron density is always higher for HiPIMS than DCMS. The electron density which is achieved in the ionization zone near the target in HiPIMS is about $10^{18} – 10^{19}$ m^{-3} and it has a mean free path of 1 cm.[142-143]

On the other hand, the normal discharge in DCMS has an electron density of about 10^{17} m^{-3} with a mean free path of 50 cm.[144] Because of the high electron density in HiPIMS, a high amount of sputtered material is ionized,[136, 139, 141, 145] which leads to higher density, smoother, and featureless films.[146] Additionally, HiPIMS produces reactively deposited compound films[147-148] with possible control of phase composition, microstructure, morphology, and mechanical and optical properties.[147, 149-150] Compared to DCMS deposited films, HiPIMS films are harder with lower coefficients of friction and improved corrosion resistance.[151] Due to enhanced directionality, HiPIMS films have improved adhesion characteristics, where it is possible to deposit uniform HiPIMS films on complex shaped surfaces and also perform depositions at lower temperatures.[107, 133, 152-153] In contrast, DCMS films are usually porous with columnar structures due to anisotropic deposition and lower electron density, leading to inhomogeneity and poor coverage on the substrate.[154]

Irrespective of the multiple advantages of HiPIMS over DCMS, for the same average power, HiPIMS has the disadvantage of having a lower deposition rate. Indeed, rates obtained with HiPIMS are usually 30 – 80% of those found with DCMS, where these rates vary with target material.[146] These lower rates are a result of back attraction of multiply charged metal ions to the target, enabling self-sputtering. Consequently, the amount of sputtered material reaching the substrate is limited.[155] This decrease in rate can be compensated for by using a lower strength magnetic field.[156]

Though DCMS and HiPIMS both have drawbacks, by virtue of the advantages they have, both types of sputtered carbon surfaces are excellent candidates for applications in bioarrays. Indeed, both are important because they possess DLC characters and hence, can be functionalized reproducibly with comparative ease. Functionalization is vital for the construction of bioarrays for

the integration of biomolecules with an interface. In the coming section, surface functionalization and its importance will be discussed in detail.

1.3.3 Functionalization

The process of the attachment of biomolecules onto a surface is known as functionalization.[157-158] Functionalization of a surface provides an important way to alter its chemical, physical, and electronic properties. Indeed, surface functionalization is one of the most important steps in the construction of a bioarray and consequently in biosensing. This chemical modification is necessary to achieve the desired orientation and association of biomolecules on a surface so that their biological function can be optimized.[159-160] For successful functionalization, a high-quality surface that can be functionalized reproducibly is very important.[36] A careful examination of a functionalization protocol is essential for developing a consistent and reliable surface functionalization strategy, i.e., a strategy that reduces the variations that might take place when biomolecules attach to the bioarray platform or interface.[157]

The biggest hurdle of incorporating microelectronics and biology is developing an appropriate interface between them, which consists of a substrate and accompanying attachment chemistry. The attachment strategy should be selective and must provide the desired stability to the immobilized biomolecules under the future biological or laboratory environment. There are many surface chemistries available to functionalize surfaces of substrates, which include glass, metals, metal oxides, and carbonaceous materials. For functionalization, a surface with available, reactive chemical moieties is necessary. In the past, silanization of glass substrates or the deposition of an alkanethiol monolayer on a noble metal substrate like gold were very important functionalization routes.[2] As noted in this introduction, stable surfaces with chemical handles, like the Group IV semiconductors [73, 74] and more especially carbon-based substrates, are of great

importance for the functionalization/immobilization of biomolecules. In particular, diamond and diamond-like carbon, i.e., DLC, have shown a great ability to be functionalized covalently.[55, 161-162]

Importance of Carbon-based Substrates in Covalent Functionalization of Surfaces

Carbon-based substrates, and in particular DLC, are a subject of interest because of their ability to be functionalized in a covalent fashion through C-C bond formation that gives the resulting, attached biomolecules great stability.[82, 163-164] This general approach has significant potential for both 'in vivo' and 'in vitro' electronic applications like electrochemical biosensors and bioarrays.[55] The ability to attach biomolecules through covalent bond formation is especially important for applications that need long incubation times and repeated washings, and that will undergo exposure to harsh chemical environments.[2] Indeed, during their fabrication and analysis, bioarrays are often exposed for long periods of time to various aqueous, acidic/basic, and biological solvents. Some of these conditions can be harsh. Therefore, bioarrays often require covalent attachment of biomolecules to reduce the likelihood of detachment or washing away of the molecule of interest. A surface chemistry can be tailored to facilitate bonding (coupling) between the exposed moieties on a surface and those on a biomolecule. Conditions in such reactions can also be arranged to minimize non-specific adsorption of the biomolecule. The presence of non-specifically adsorbed species can result in less than ideal array performance.

Reproducible, stable, specific, and inexpensive functionalization chemistries have been a subject of research for a long time.[66-68] After the very first attachment of oligonucleotides on a diamond substrate,[14] other carbon-based materials like DLC (amorphous carbon), glassy carbon, and nanocrystalline diamond have been tested as alternatives to glass-based materials. Some recent studies have demonstrated that functionalization of thin-film diamond can produce high stability

bioarrays with very good recognition/sensing properties.[30] The advantage of these carbon-based substrates is their inherent stability and the presence of functional moieties on them. These moieties provide the substrates with the ability and versatility to immobilize the biomolecule of interest onto the substrate via stable covalent bond formation that can persist under harsh conditions for a significant time.[2, 55] One study compared the stability of spotted arrays of presynthesized oligonucleotides immobilized on amine-terminated diamond, glass, glassy carbon, gold, and silicon substrates. These results confirmed that carbon-based substrates provide much better stability for the attachment of biomolecules. The carbon-based substrates retained almost all of their surface-bound oligonucleotides even after repeated use. In contrast, the other substrates lost a significant amount of their attached biomolecules.[14] The better stability of functionalized carbon substrates gives them greater versatility for the different types of reactions, applications, and analyses that need to be performed on biomolecule arrays. That is, carbon-based materials are a feasible option for bioelectronics sensors and for the fabrication of biomolecular arrays.

Covalent Attachment Protocols

Covalent attachment of organic molecules onto semiconductor/Group IV surfaces has made great progress in recent years. As discussed previously, covalent attachment is essential for applications involving harsh chemical environments because covalent bond formation decreases the chances of unintentional removal of the biomolecule(s) of interest. By utilizing various well-known reactions in organic chemistry, a large number of covalent functionalization chemistries have been developed for carbon-based materials. For example, diamond-related materials have been modified with a peroxide radical initiator,[165-166] a gas-phase halogenation reaction,[167-169] the electrochemical reduction of diazonium salts,[170-171] via ultraviolet photo-assisted attachment of alkene-containing molecules at different energies,[172-174] and by the attachment of primary and

secondary amines through electrochemical oxidation.[175] Other examples include amination or esterification of single-walled carbon nanotubes by acid chloride intermediates or by carbodiimide-activated coupling.[176] Furthermore, amorphous carbon thin films have been functionalized by attaching alkene and alkene-containing molecules through photochemical and thermal methods.[177-178] Another important method for surface modification includes solution-based chlorination and bromination that halogenates carbon-based substrates without the need for gas-phase or complex ultrahigh vacuum methods.[179-180] By terminating the surface with molecules that have reactive moieties themselves, additional surface modification can be performed, e.g., through immobilization of DNA or a protein for biosensor applications.[83]

It has been shown that the oxidation of a carbon substrate (H- vs. O-terminated) enhances its reactivity toward particular organic molecules.[83, 163, 181] Carbon surfaces have various chemical moieties that may be exposed at their surfaces, including: (i) hydrocarbon type (C-C, C-H), (ii) ether type (C-O-C), (iii) carbonyl type (C=O), and (iv) carboxyl type (O=C-O). Based on whether a surface is H-terminated or O-terminated, these moieties can be targeted for covalent functionalization via different synthetic routes.[83, 163, 181-183]

Chapter 2 of this thesis focuses on the preparation, characterization, and functionalization of DCMS and HiPIMS carbon surfaces for applications in bioarrays. DCMS and HiPIMS carbon surfaces were functionalized by two routes: (i) activation/amidation where amidation of the carboxyl moieties (O=C-O) was done by activating surface carboxyl groups through coupling agents (EDC and sulfo-NHS), which form amide bonds after reacting with amines, and (ii) halogenation/amination, where the surface is halogenated and then reacted with an amine, presumably via nucleophilic substitution. A scheme showing these synthetic routes in greater detail is given in Chapter 2. Functionalization of these carbon surfaces was followed by characterization.

I mainly used XPS and wetting to characterize these materials. In the coming sections, material characterization will be discussed in greater detail.

1.4 Material Characterization

Material characterization refers to the general process by which the structure and properties of materials are investigated and determined. It is a vital part of any surface-related research endeavor because it enables one to determine the important characteristics and changes of a surface after preparation, deposition, and/or reaction. The goal of material characterization is to elucidate surface chemical composition qualitatively and quantitatively. Without material characterization, a scientific understanding of engineered materials, deposited films, or modified films cannot be developed or advanced.[184]

A number of characterization techniques are used extensively for surface characterization. These include time-of-flight secondary ion mass spectrometry (ToF-SIMS), atomic force microscopy (AFM), contact angle goniometry, also referred to as wetting, low energy ion scattering (LEIS)[185] optical microscopy, and X-ray photoelectron spectroscopy (XPS). The depth of analysis of the various material characterization tools ranges from zero in the case of LEIS, which only probes the outermost atomic layer of a material, to centimeters in the case of the optical characterization of a transparent material. Our work mainly involves characterization of the top 5 – 10 nm of a material. In such cases, conventional XPS is one of the most useful techniques for quantitatively characterizing surfaces. Near ambient pressure XPS (NAP-XPS), which is a related form of XPS that allows analyses to be performed at relatively high pressures (10s of Torr), has been used to analyze substances that are usually difficult to analyze by conventional XPS. Peak fitting in XPS is an important tool for quantification and determination of the chemical species present at a surface.

In the following sections, I will be focusing on the principles and applications of conventional XPS and NAP-XPS as well as the basics and importance of XPS peak fitting. I will also explore various statistical tools as aids to surface characterization.

1.4.1 X-ray Photoelectron Spectroscopy

X-ray photoelectron spectroscopy (XPS) is a surface-sensitive, quantitative technique that provides information about the elemental compositions and chemical and electronic states of all the elements present within a film or material except H and He.[186-188] In its earlier days, XPS was also known as ESCA (electron spectroscopy for chemical analysis), an abbreviation introduced by Kai Siegbahn's research group.[189] Since the surface of a material is often as important as the bulk, and sometimes even more important, a surface sensitive technique like XPS can play a vital role in understanding materials.

XPS is the most widely used vacuum technique for chemically analyzing surfaces – it is currently receiving more than 10,000 mentions per year in the literature, and there has been a steady increase in the number of instruments sold per year (the number approaches 150 annually).[190-191] [192-193] With the help of chemical shifts, XPS provides chemical (oxidation) state information about the elements.[183] Spectral analysis in XPS ranges from moderately straightforward for some survey spectra,[194] to quite complex and requiring extensive peak fitting for some narrow scans.[182,] [195-197] XPS is surface sensitive, i.e., while the X-rays used in conventional XPS can penetrate fairly deeply into materials, the photoelectrons they generate can only escape from the upper 5 – 10 nm of a surface.[198-199]

1.4.1.1 XPS Instrumentation of XPS

A typical XPS instrument includes an electron source that generates high-energy electrons that strike a metal anode (Al or Mg in conventional XPS) to generate X-rays. A monochromator,

e.g., a quartz crystal, then allows only a specific wavelength of X-rays to pass to the sample. An XPS contains electron optics, i.e., sets of electrostatic and/or magnetic lenses, that collect a portion of the emitted electrons, transfer them through apertures, and focus them onto the analyzer slit. A concentric hemispheric analyzer with an internal electrostatic field permits the electrons of a given energy, also known as the pass energy (PE), to reach the detector. In general, an XPS will also include a flood gun for charge compensation of insulating samples **(Figure 2)**.

1.4.1.2 Working and Basic Physics of XPS

XPS is based on the photoelectric effect. In it, X-rays of a selected wavelength strike a sample surface, which leads to the ejection of core level photoelectrons from the upper 5 – 10 nm of the surface. These photoelectrons then pass through a (hemispherical) analyzer before reaching the detector. The hemispherical analyzer works in two different modes, one is Fixed Analyzer Transmission (FAT) and the other one is Constant Analyzer Energy (CAE), also known as Fixed Retarded Ratio (FRR) or Constant Retarded Ratio (CRR). Most XPS instruments operate in the FAT mode. In the FAT mode, the pass energy of the analyzer remains fixed at a constant value, and the transfer lens retards the kinetic energy of the electrons to bring them down to a range that can be accepted by the analyzer. The kinetic energies of the photoelectron are then measured by the analyzer and converted to their corresponding binding energies. An XPS spectrum is often a plot of the number of counts obtained per second (CPS) or (electrons detected per second) versus the binding energies of the detected electrons. Since each element has its characteristic electron binding energy/energies, the peaks that show up in a spectrum at a particular binding energy are characteristic of that element on the surface of the material being analyzed. These characteristic peaks represent the configuration of the electrons within the atoms, e.g., in the 1s, 2s, 2p, 3d, and

4f orbitals, etc. The number of detected electrons in each of the characteristic peaks in a spectrum is a measure of amount of the element in the sample.

The fundamental equation of XPS is:

$$h\nu = E_{K.E.} + E_{B.E.} + \phi, \tag{1.0}$$

which can be rewritten as

$$E_{B.E.} = h\nu - E_{K.E.} - \phi \tag{1.1}$$

where hν is the energy of the X-rays, $E_{K.E.}$and $E_{B.E.}$are the kinetic and binding energies of the electrons, respectively, and ϕ is the work function of the spectrophotometer. The most commonly used photon energy in conventional XPS is from an Al source: the Al Kα line at 1486.6 eV.

XPS is most often performed under ultrahigh vacuum (UHV) to limit both surface contamination and attenuation of the X-rays and photoelectrons in the experiment. Accordingly, conventional XPS is generally applicable to a wide range of samples including metals, glasses, and many types of thin films. However, many materials are simply not compatible with the UHV environment of a conventional XPS instrument. These include many biological specimens, liquids and gases, cosmetics, foodstuffs, many polymers, zeolites, etc. In general, these materials outgas such that they require very long pump down times in a conventional instrument, or in some cases they simply cannot be analyzed at all. Of course, special sample preparation and mounting may allow some of these samples to be analyzed by conventional XPS.[200] Nevertheless, there is a need for facile XPS analysis of materials that are not compatible with the environment of a conventional XPS system.

1.4.2 Near Ambient Pressure XPS (NAP-XPS)

The need for XPS analysis of materials with little or no vacuum compatibility, and/or the need to analyze samples in their native state, has led to the development of near-ambient pressure XPS (NAP-XPS).26, 201-204 Typically, NAP-XPS systems work at moderate pressures of ca. 2500 Pa or greater.205 In order to allow electrons to travel to a detector, which is still kept under UHV, various stages of differential pumping are used (Figure 3), where differential pumping successively reduces the pressure in an NAP-XPS system from the sample (10^{-1} Pa), to the detector (~10^{-6} Pa). Obvious advantages of the higher working pressures in NAP-XPS are that there is little or no sample preparation and that pump down times/sample introduction times decrease substantially as there is no need for a load lock (sample introduction chamber) in the system – samples are directly loaded into the analytical chamber. The upshot here is that samples can be loaded and analyzed in minutes, which is not the case with conventional XPS. With NAP-XPS, XPS becomes a legitimate real time, process monitoring tool.

A distinctive and desirable feature of NAP-XPS is its intrinsic ability to provide charge compensation. As incident X-rays irradiate a sample, they ionize the gas molecules around it, creating both electrons and cations. These charged species then provide the necessary charge compensation for an analysis. Thus, it can be said that charge compensation happens automatically in NAP-XPS. This charge composition in NAP-XPS is referred as Environmental Charge Compensation. The degree of charge compensation obtained in this way is governed by the pressure of the gas molecules around a sample. In summary, in NAP-XPS, insulating samples can generally be analyzed directly and without the need for a flood gun or any other form of external charge compensation as is often needed in conventional XPS. **[Figure 4]**

1.4.3 Data Analysis: Peak Fitting as an Important Tool in Surface Chemical Analysis

Data analysis is an essential component of material characterization. After acquiring data, it is important to precisely analyze it in order to achieve accurate chemical and structural information about a material. That is, sometimes the analysis of data from surface and material characterization tools is not straightforward and it requires some form of spectral/peak fitting, statistical analysis, and/or modeling. For example, most spectroscopic ellipsometry (SE) studies involve at least some (and often quite a lot of) data modeling.[206-210] The complexity of many time-of-flight secondary ion mass spectrometry (ToF-SIMS) data sets has driven a community of users to consider chemometrics analyses, including principal component analysis (PCA) and multivariate curve resolution (MCR), to better interpret and glean information from these spectra.[211-215] That is, ToF-SIMS images typically contain thousands of spectra so statistical analysis of the data is often essential to thoroughly analyze it.[214, 216, 217] Similarly, analysis of X-ray photoelectron spectroscopy (XPS) data also regularly requires peak fitting.[218,199] Sherwood[219] noted that the peak widths and chemical shifts in XPS are of comparable size, thus providing an important explanation for why peak fitting is often necessary in XPS.[220] Accordingly, peak fitting is often required to obtain the relative populations of chemical/oxidation states in a sample when an element is present in more than one chemical environment.

There are two kinds of scans/spectra in XPS – survey and narrow. Survey scans are generally acquired at lower resolution and over a wider energy range – often over 1000 eV or more. In contrast, narrow scans are generally taken at higher resolution and over a much narrower energy range – often over about 20 eV. Both types of scans are regularly shown and discussed in the scientific literature. In a survey scan, one can often quickly identify the main elements at the surface of one's material – survey spectra are often fairly uncluttered because most elements only

have a small number of signals that correspond to them. Survey scans usually contain a variety of different types of peaks/features. For example, in survey scans we often see rising baselines on the higher binding energy (BE) sides of peaks, Auger peaks, valence band signals, phonon loss peaks due to excitation of phonons by exiting photoelectrons, other loss signals, and multiple peaks from the same element, which act to confirm its presence (some of these signals may be the result of spin-orbit splitting). For example, if there were Si at our surface, we would expect both the Si 2s and Si 2p signals. It is clear that XPS survey scans are important sources of information about a material.

Fortunately for XPS, narrow scans contain even more information about materials than survey spectra do. In narrow scan analysis, we typically focus on a particular region of the spectrum to determine the oxidation/chemical state(s) of an element.[198] For example, a carbon 1s envelope can often be peak fitted to five peaks with the following oxidation states/regions: (i) C-C (C(0)), (ii) C-O (C(I)), (iii) C=O (C(II)), (iv) O=C-O (C(III)), and (v) shake-up peaks/satellites due to $\pi - \pi^*$ transitions.[221-224] This kind of information can be vital for understanding new materials, e.g., polymers and catalysts.[225] Thus, narrow scan analysis is usually the focus of XPS data work up.[220] However, analyzing narrow scans can be a complex process that requires peak-fitting to get precise information about a material. Important decisions in the laboratory and industry are made based on XPS peak fitting results.[226]

Peak-fitting XPS narrow scans is usually based on a combination of fundamental principles, literature precedent, knowledge about the sample, and experience. There is even an element of art/creativity in it. XPS peak fitting/data analysis must also take into account the design of the instrument, the data acquisition settings, and the condition/nature/state of the sample. Peak fitting generally includes (i) subtracting or fitting the background that is produced by inelastically

scattered electrons and (ii) determining and accounting for the various chemical states that are present in a peak envelope.[227] Some of the important parameters/considerations for a fit include (i) the background approximation, (ii) the peak width/full width at half maximum (FWHM) of the synthetic peaks, (iii) the positions/chemical shifts of the peaks, (iv) the synthetic peak shapes/functions, and (v) the peak areas.

Though peak fitting plays a central role in the analysis and interpretation of XPS data, the use of other statistical tools and mathematical analyses of XPS peaks and data are also important.[228, 229] These include the chi-squared figure of merit, showing the residuals, showing the sum of the fit components, the Abbe criterion,[230-232] uniqueness plots,[182] and peak smoothing/denoising such as by wavelets.[233, 234] Chemometrics tools such as principal component analysis, multivariate curve resolution, pattern recognition entropy, and width functions can be other useful tools.[221, 235, 222] In the coming sections, the process of peak fitting and the importance of peak fitting parameters/inputs such as the line shape will be discussed.

Background approximation

The selection of an appropriate background poses a challenge in XPS peak fitting.[223, 236] Indeed, the choice of a background is often complicated by the rise in the baseline towards higher binding energy (lower kinetic energy) that is observed in many XPS signals because of the inelastic scattering experienced by electrons as they travel through materials. In the relatively simple case where there is no rise in the background, a linear background is generally the suitable choice. However, significant baseline rises are typically seen in the case of materials without band gaps, i.e., mostly metals here. Here, Shirley backgrounds may be employed, which is consistent with the underlying assumptions of this sigmoidal shape.[237] Tougaard backgrounds have an even stronger theoretical basis, and they are regularly used for all types of materials. In general, I used a

Tougaard-type background in my peak fitting of data from polymers. However, it is well recognized that none of the background types provides a perfect solution, and the choice of one type of background over another is really the selection of the least wrong background as opposed to the most right.[238]

Selection of Synthetic Line Shape/Function

Chapter 3 of this thesis explains some of the important line shapes/functions that are often used to fit XPS narrow scans. This chapter covers the more commonly used Gaussian, Lorentzian, Gaussian-Lorentzian sum (GLS), Gaussian-Lorentzian product (GLP), and Voigt functions. The mathematical forms of the GLS and GLP, which include mixing parameters, are shown. The comparison of the GLS and GLP line shapes shows that the GLS function more closely resembles the Voigt function. One of the key observations of this chapter is that the GLS and GLP are not interchangeable. Each has unique properties and their place and application in XPS peak fitting. This work was published in *Applied Surface Science*.[195]

Defining Oxidation States of Overlapping Peaks

After selecting the background and determining the type of line shape in an XPS peak fit, one typically determines the number of peaks that contribute to the total peak envelope. In general, one will then use literature precedent and what one knows about one's sample to constrain the peak positions, heights, widths, asymmetries, and/or line shape. A failure to impose reasonable constraints on a fit often makes it statistically meaningless. Prior knowledge about a sample, which can be very helpful in guiding XPS peak fitting, may come from the vendor of the material or results from other characterization methods. After applying reasonable constraints, peak fitting software is allowed to optimize the fit parameters. It is generally better to have fewer rather than more parameters in a fit. That is, a good rule of thumb is to start simple, i.e., with a smaller number

of parameters, and to gradually increase the complexity of the model if there is both a need to do so and a reasonable justification for it. The fit to the peak envelope provides information about the various chemical/oxidation states of an element in a material. Modern peak fitting software, like CasaXPS, is capable of determining the quality of a fit by comparing the experimental data to a fit envelope. A large difference between the two suggests that the model is not appropriate for the data. Quantitatively, the fit difference may be given by the standard deviation of the residuals to the fit or the chi-squared ($\chi 2$) value. The Abbe criterion indicates that large regions of the fit envelope are consistently missing the raw data.[182] In general, a lower error, e.g., standard deviation of the residuals, indicates a better fit. However, this must not be the only criterion one uses to determine the quality and appropriateness of a fit because, as implied above, a large number of floating parameters in a fit can allow it to closely approximate the data while being at the same time statistically meaningless, i.e., there will be fit parameter correlation.[182] That is, there will be no unique solution to the XPS narrow scan peak fit.[220] In summary, a user's experience, based on sound scientific principles, good precedent from the literature, common sense, and restraint in peak fitting can lead to reasonable results.[182]

1.4.4 Other Techniques for Surface Chemical Analysis

A range of techniques can (and should) be used for surface characterization. These include scanning electron microscopy (SEM), spectroscopic ellipsometry (SE), atomic force microscopy (AFM), time-of-flight secondary ion mass spectrometry, low energy ion scattering, and contact angle goniometry (wetting measurements). Rather than attempt to provide a detailed description of each one, I will mention two of the techniques that, in addition to XPS, have been most influential in my work: wetting and AFM.

1.4.4.1 Wetting

Wetting is an important quantitative technique for measuring the change in surface behavior; it is often an important technique to characterize/follow an altered or modified surface.

Wetting, i.e., the interaction between a liquid, often water, and solid surface, is an important process in many technological and biological systems.[239] The water contact angle, Θ, is a quantitative measure of the wetting of a solid by a liquid. It is geometrically defined as the angle formed by a liquid at the three-phase boundary where a liquid-vapor interface interacts with a solid surface. At a given temperature and pressure, a given system of a solid, a probe liquid, and the vapor of the liquid will have a unique equilibrium contact angle. However, in reality this phenomenon is complicated somewhat by contact angle hysteresis, which gives a range of values for the contact angle from the advancing (maximal) contact angle to the receding (minimal) contact angle.[240] Young's well-known equation describes the balance at the three phases (solid, liquid, and gas) at a contact angle.

$$\gamma_{SV} - \gamma_{SL} - \gamma_{LG}cos\theta_C = 0 \qquad (1.2)$$

Where, Υ_{SV}, Υ_{SL}, and Υ_{LG} denote the energies of the solid-vapor, solid-liquid, and liquid-vapor interfaces, respectively. A low contact angle refers to the tendency of the surface to adhere to water (hydrophilicity), i.e., it represents a high surface energy for the surface/material in question. On the other hand, a high water contact angle refers to the tendency of the surface to repel water (hydrophobicity), i.e., it represents a low surface energy for a surface or material. Hence, wetting is an important technique for probing materials. The relative ease with which wetting can be done, and the rather low cost of the equipment needed to perform it, should also be emphasized here. Changes in surface wetting are a reflection of a change in surface properties, and systematic

changes in contact angles can often be well correlated to observations/data from other characterization methods.[241]

In chapter two of this thesis, I have successfully used wetting measurements to characterize sputtered and functionalized DCMS and HiPIMS carbon surfaces. Wetting served here as an important supporting technique to XPS.

1.4.4.2 Atomic Force Microscopy

Atomic force microscopy (AFM) is an important surface characterization tool used to determine surface morphology, roughness, and thickness.[116, 242] In chapter two of this thesis, I show the use of AFM to determine the roughness of DCMS and HiPIMS carbon films. AFM step height measurements performed in tapping mode were also used to determine film thicknesses of DCMS and HiPIMS films.

1.5 Conclusions

The preparation of an interface is a necessary step in the construction of a bioarray. That is, a stable interface is essential for an efficient and high performance bioarray, and attachment of biomolecules onto a bioarray surface by chemical functionalization is arguably the most important step in the successful preparation of a bioarray. Hence, it is very important to have biocompatible surfaces that can be functionalized with comparative ease. For these reasons, there is a need to better understand the surfaces of bioarrays. Because on their biocompatibility and capability for biomolecule attachment via carbon-carbon covalent bond formation, diamond and diamond-like carbon are excellent candidates for bioarray interfaces.

Since diamond requires high temperatures to produce and is comparatively expensive to make, amorphous DLC, which can be deposited directly as a thin film at room temperature by

physical vapor deposition, is an important alternative to it. In my work, I have prepared DCMS and HiPIMS carbon surfaces and functionalized them covalently for their application in bioarrays.

Chapter 2 of this thesis describes the functionalization of DCMS and HiPIMS carbon surfaces by activation/amidation and halogenation/amination. This chapter includes a detailed characterization of DCMS and HiPIMS carbon surfaces.

Material characterization is a critical part of determining the surface chemical composition. The use of XPS and NAP-XPS techniques allows for detailed analysis of the sample's surface, and analysis of the data must be conducted precisely, hence the use of peak fitting. XPS peak fitting or modelling is an essential part of data analysis and material characterization and some sort of peak fitting is necessary in most of the cases. Hence, throughout my graduate research, I have implemented these material characterization tools to characterize and analyze different materials I encountered with during my graduate research including various conventional and unconventional materials.

Chapter 3 describes some of the important line shapes used in XPS peak fitting, including the GLS, GLP, and Voigt functions. It shows the comparison between the GLP, GLS, and Voigt functions. This work demonstrate that the GLS is a better approximation of the Voigt function. In February, 2014 one of the authors of this work (MRL) wrote an article in a trade/technical magazine, Vacuum Technology & Coating (VT&C), on 'The Gaussian-Lorentzian Sum, Product, and Convolution (Voigt) Functions Used in Peak Fitting XPS Narrow Scans, and an Introduction to the Impulse Function". I took on the task of adapting this original article and my contributions have been significant. Note that the position taken by MRL in the VT&C article was that the GLP should be avoided for mathematical reasons. This article represents his/our latest thinking on this topic. Hence, we have changed the conclusion of the original article and modify it based on various

example reported and recommended in literature. Also, we reported here some of those examples to demonstrate the ability of GLP function to peak fit XPS narrow scans Also, I used this This modification is turned out to be very significant in data analysis by peak fitting XPS narrow scans. In my work itself, I have used GLP function at many places which imply that this modified work now has broader application than from its original idea.

Peak fitting was implemented to determine/understand the surface chemical compositions of various materials including three amino silanes (APTES, APDIPES, APDEMS), which were characterized by conventional XPS, and a series of unconventional materials that had been analyzed by NAP-XPS. Chapters four through nine of this thesis describe this characterization. In particular, Chapter 4 of this thesis focuses on the deposition of different silanes through chemical vapor deposition and their effect on peptide growth, stability, and purity. My contribution to this work includes application XPS peak fitting of the data using the CasaXPS software package. Through XPS peak fitting of different narrow scans, the deposition of the different silanes was confirmed. To improve the quality of this fit, the original spectra were reanalyzed and/or replotted. I received co-authorship for my contribution. This work was published in Langmuir.[243]

Chapter 5 of this thesis describes characterization of a solution of bovine serum albumin (BSA) by NAP-XPS and its analysis by peak-fitting the C 1s, O 1s and N 1s narrow scans.

Chapter 6 discusses the analysis of polytetrafluoroethylene (PTFE) by NAP-XPS and the effects of sample charging at lower residual gas pressures, which causes a dramatic shift in the C 1s and F 1s peak positions. However, acquiring the data at higher pressure, i.e., ca. 1 mbar or more, leads to automatic environmental charge compensation by the background gas. With increasing pressure, the voltage shifts decreases and the C 1s and F 1s peaks tend to their natural (true)

positions. Changes in the equivalent widths of these peaks with different gas pressures and different illumination times at constant pressure are also discussed.

Chapter 7 of this thesis includes the analysis of a new polymer, poly(γ-benzyl L-glutamate) (PBLG), by NAP-XPS and the determination of its surface chemistry through peak fitting the C 1s and O 1s narrow scans. In this work, we utilized Hartee-Fock first principles calculations to confirm the spacings between the peaks corresponding to the different C 1s and O 1s orbitals. This provided a theoretical basis for the peak fitting, especially for understanding the theoretical chemical shifts between the different peaks present in the total peak envelope.

Chapter 8 of this thesis includes the analysis of different human hair samples by NAP-XPS. This work consists of three different hair samples: (i) untreated (blank) hair, (ii) colored hair, and (iii) bleached hair. Here I compare the amounts of silicon, sulfur, and carbon in these materials. The results indicate that, presumably as a result of exposure/treatment with dimethicon (polydimethylsiloxane, PDMS) in the commercial treatments applied to the hair samples, the colored and bleached samples show silicon, which is absent in the case of the blank sample. Also, due to an increase in silicon, the colored and bleached samples do not show any sulfur, and there is a peak at lower binding energy in C 1s narrow scan. In the case of the bleached sample, the presence of the C-Si moiety suggests the presence of the linear siloxane polymer dimethicon/PDMS.

Chapter 9 of this thesis includes the analysis of an important biological buffer solution (phosphate buffer saline, PBS) and also the solid PBS material. The purpose of this study is to demonstrate the kinds of chemical species/peaks possible in solid PBS and the corresponding liquid solution. This study can serve as a reference for NAP-XPS analysis of other buffers with similar composition.

1.6 Figures

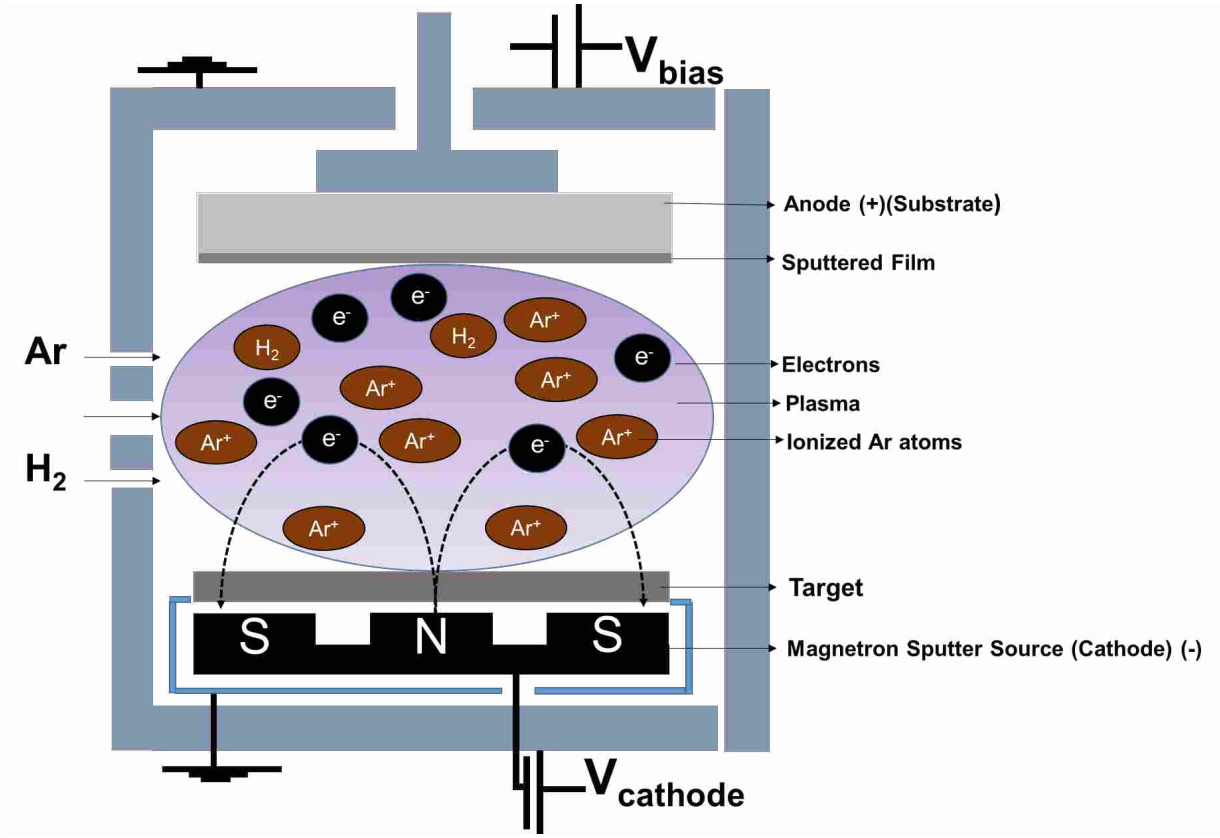

Figure 1.1. Schematic of the magnetron sputtering process.

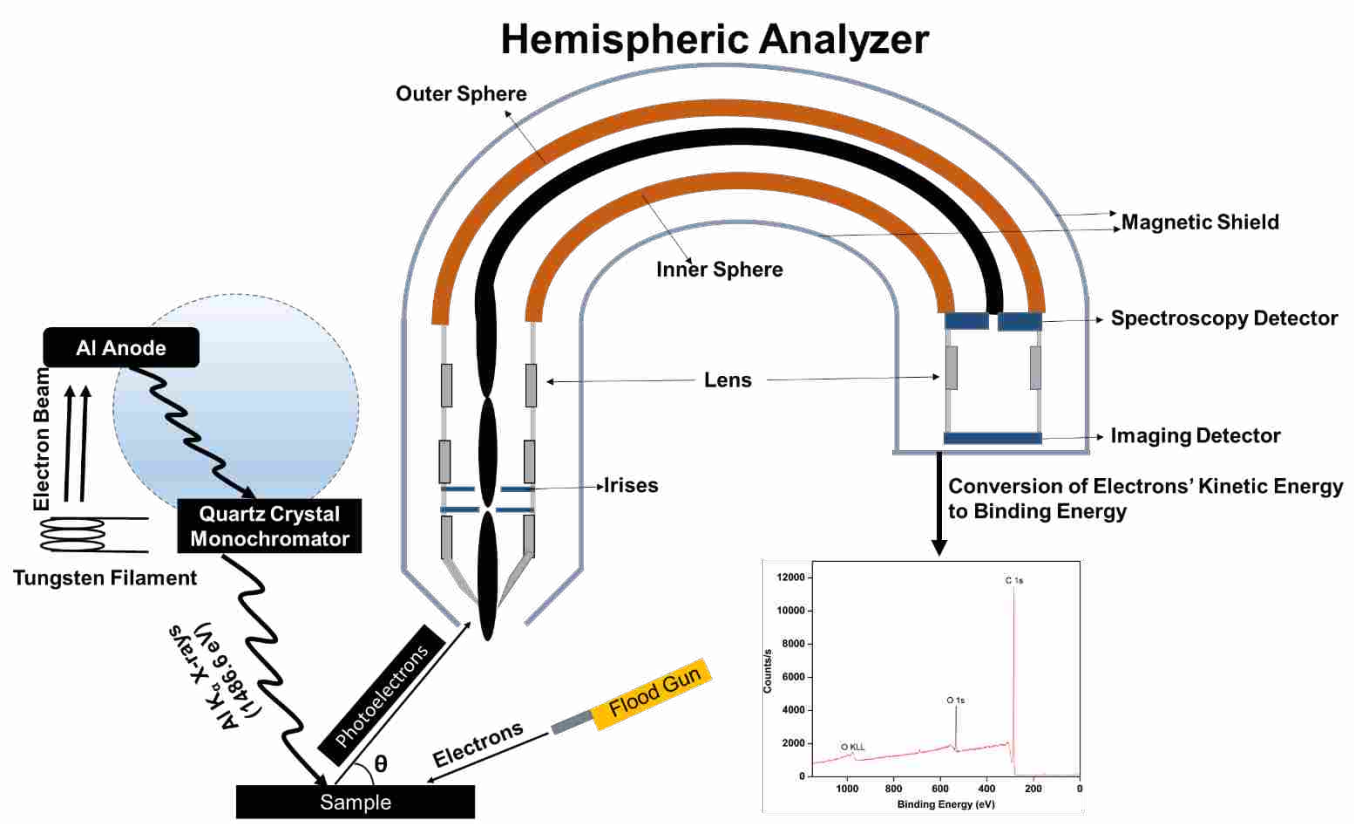

Figure 1.2. Schematic of working of X-ray photoelectron spectroscopy.

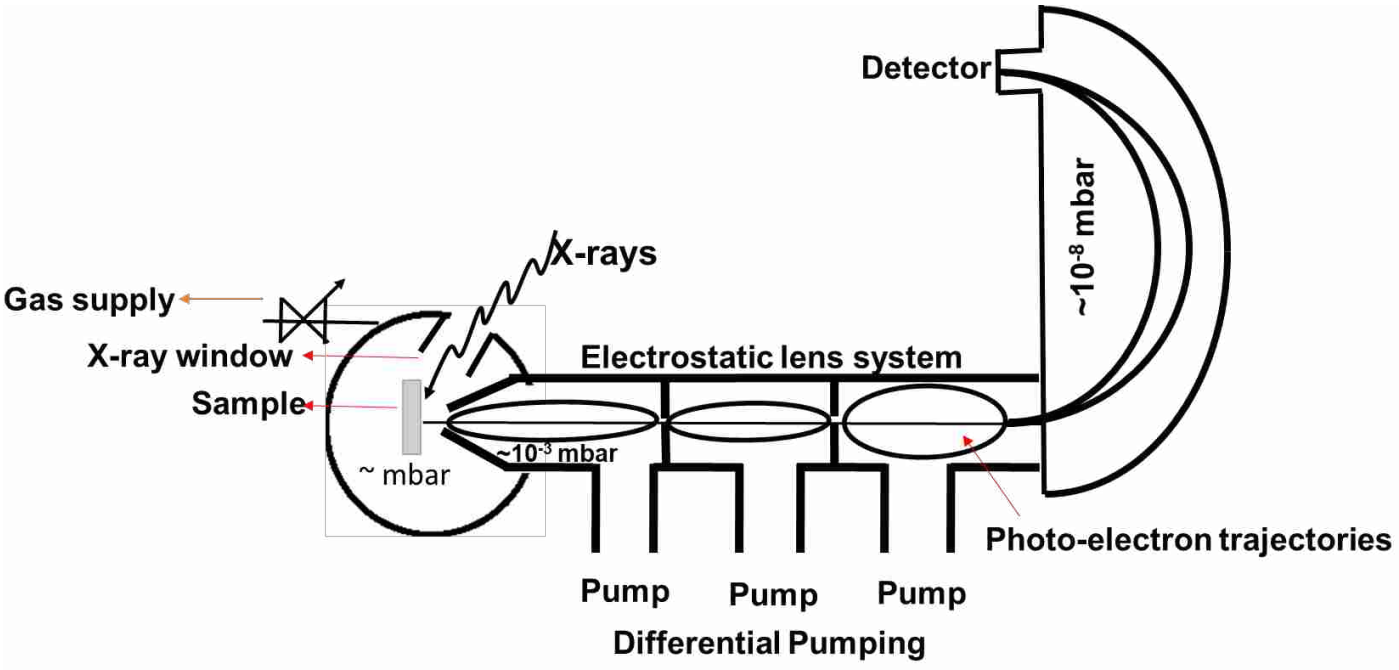

Figure 1.3. The schematic of differential pumping.

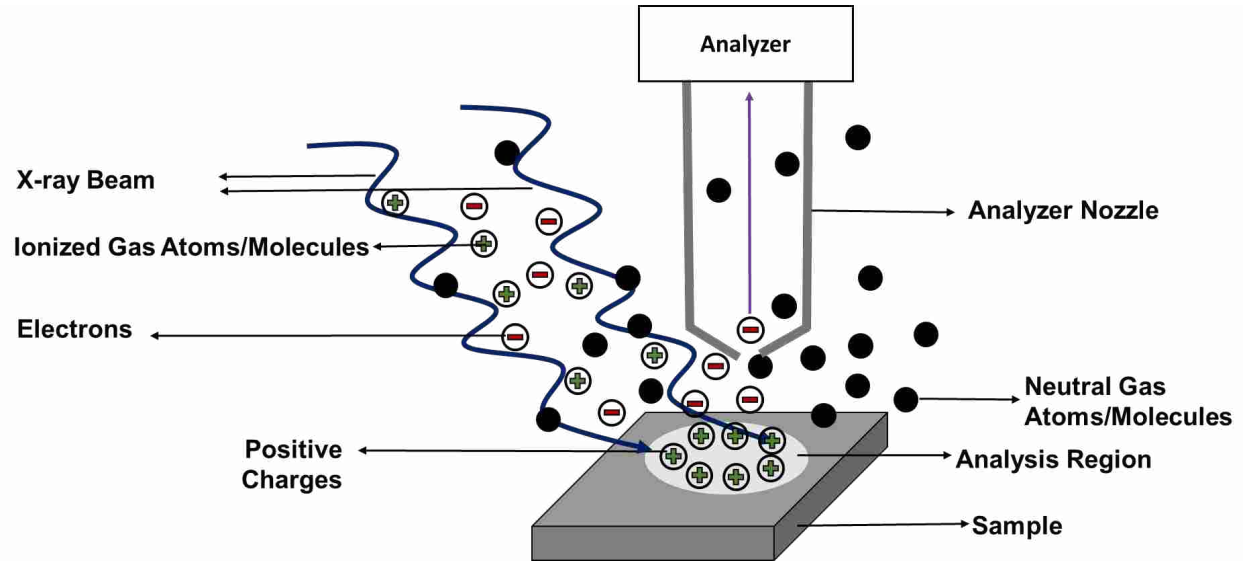

Figure 1.4. The schematic of environmental charge compensation.

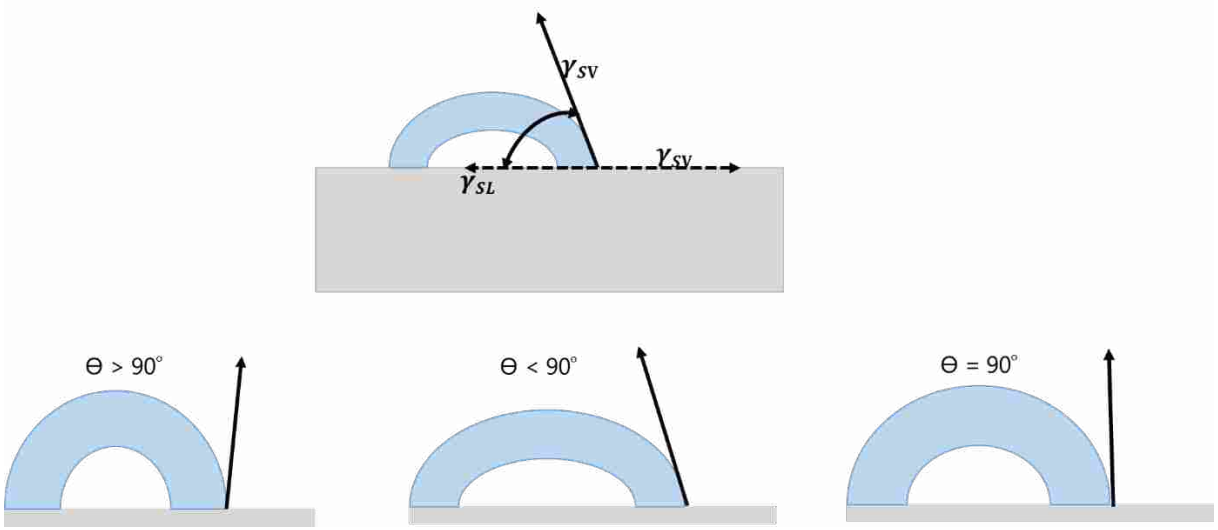

Figure 1.5. Schematic of wetting measurement.

1.7 References

1. Robertson, J., Diamond-like amorphous carbon. *Materials Science and Engineering: R: Reports* **2002,** *37* (4), 129-281.
2. Lockett, M. R.; Smith, L. M., Carbon Substrates: A Stable Foundation for Biomolecular Arrays. *Annual Review of Analytical Chemistry* **2015,** *8* (1), 263-285.
3. Robertson, J., Hard amorphous (diamond-like) carbons. *Progress in Solid State Chemistry* **1991,** *21* (4), 199-333.
4. Aisenberg, S.; Chabot, R., Ion-beam deposition of thin films of diamondlike carbon. *Journal of Applied Physics* **1971,** *42* (7), 2953-2958.
5. Spencer, E. G.; Schmidt, P. H.; Joy, D. C.; Sansalone, F. J., Ion-beam-deposited polycrystalline diamondlike films. *Applied Physics Letters* **1976,** *29* (2), 118-120.
6. Weissmantel, C.; Bewilogua, K.; Dietrich, D.; Erler, H. J.; Hinneberg, H. J.; Klose, S.; Nowick, W.; Reisse, G., Structure and properties of quasi-amorphous films prepared by ion beam techniques. *Thin Solid Films* **1980,** *72* (1), 19-32.
7. Mōri, T.; Namba, Y., Hard diamondlike carbon films deposited by ionized deposition of methane gas. *Journal of Vacuum Science and Technology A: Vacuum, Surfaces and Films* **1983,** *1* (1), 23-27.
8. Jansen, F.; Machonkin, M.; Kaplan, S.; Hark, S., The effects of hydrogenation on the properties of ion beam sputter deposited amorphous carbon. *Journal of Vacuum Science and Technology A: Vacuum, Surfaces and Films* **1985,** *3* (3), 605-609.
9. Logothetidis, S., Hydrogen-free amorphous carbon films approaching diamond prepared by magnetron sputtering. *Applied Physics Letters* **1996,** *69* (2), 158-160.
10. McKenzie, D. R., Tetrahedral bonding in amorphous carbon. *Reports on Progress in Physics* **1996,** *59* (12), 1611-1664.
11. Fallon, P. J.; Veerasamy, V. S.; Davis, C. A.; Robertson, J.; Amaratunga, G. A. J.; Milne, W. I.; Koskinen, J., Properties of filtered-ion-beam-deposited diamondlike carbon as a function of ion energy. *Physical Review B* **1993,** *48* (7), 4777-4782.
12. Voevodin, A. A.; Donley, M. S., Preparation of amorphous diamond-like carbon by pulsed laser deposition: A critical review. *Surface and Coatings Technology* **1996,** *82* (3), 199-213.
13. Davanloo, F.; Juengerman, E. M.; Jander, D. R.; Lee, T. J.; Collins, C. B., Amorphic diamond films produced by a laser plasma source. *Journal of Applied Physics* **1990,** *67* (4), 2081-2087.
14. Yang, W.; Auciello, O.; Butler, J. E.; Cai, W.; Carlisle, J. A.; Gerbi, J. E.; Gruen, D. M.; Knickerbocker, T.; Lasseter, T. L.; Russell, J. N.; Smith, L. M.; Hamers, R. J., DNA-modified nanocrystalline diamond thin-films as stable, biologically active substrates. *Nature Materials* **2002,** *1* (4), 253-257.
15. Angus, J. C.; Hayman, C. C., Low-pressure, metastable growth of diamond and "diamondlike" phases. *Science* **1988,** *241* (4868), 913-921.
16. Butler, J. E.; Windischmann, H., Developments in CVD-Diamond Synthesis During the Past Decade. *MRS Bulletin* **1998,** *23* (9), 22-27.
17. Rossnagel, S. M.; Russak, M. A.; Cuomo, J. J., Pressure and plasma effects on the properties of magnetron sputtered carbon films. *Journal of Vacuum Science and Technology A: Vacuum, Surfaces and Films* **1987,** *5* (4), 2150-2153.

18. Cho, N. H.; Krishnan, K. M.; Veirs, D. K.; Rubin, M. D.; Hopper, C. B.; Bhushan, B., Chemical structure and physical properties of diamond-like amorphous carbon films prepared by magnetron sputtering. *Journal of Materials Research* **1990,** *5* (11), 2543-2554.
19. Rubin, M.; Hopper, C. B.; Cho, N. H.; Bhushan, B., Optical and Mechanical Properties of DC Sputtered Carbon Films. *Journal of Materials Research* **1990,** *5* (11), 2538-2542.
20. Schwan, J.; Ulrich, S.; Roth, H.; Ehrhardt, H.; Silva, S. R. P.; Robertson, J.; Samlenski, R.; Brenn, R., Tetrahedral amorphous carbon films prepared by magnetron sputtering and dc ion plating. *Journal of Applied Physics* **1996,** *79* (3), 1416-1422.
21. Gissler, W.; Hammer, P.; Haupt, J., Hardness and elasticity of diamond-like carbon films prepared by ion-beam assisted sputter deposition. *Diamond and Related Materials* **1994,** *3* (4-6), 770-774.
22. Cushman, C. V.; Brüner, P.; Zakel, J.; Dahlquist, C.; Sturgell, B.; Grehl, T.; Lunt, B. M.; Banerjee, J.; Smith, N. J.; Linford, M. R., Low energy ion scattering (LEIS) of as-formed and chemically modified display glass and peak-fitting of the Al/Si LEIS peak envelope. *Applied Surface Science* **2018,** *455*, 18-31.
23. Mukhopadhyay, S. M., *Sample Preparation for Microscopic and Spectroscopic Characterization of Solid Surfaces and Films*. John Wiley & Sons, Inc: USA, 2003.
24. Chatterjee, S.; Singh, B.; Diwan, A.; Lee, Z. R.; Engelhard, M. H.; Terry, J.; Tolley, H. D.; Gallagher, N. B.; Linford, M. R., A perspective on two chemometrics tools: PCA and MCR, and introduction of a new one: Pattern recognition entropy (PRE), as applied to XPS and ToF-SIMS depth profiles of organic and inorganic materials. *Applied Surface Science* **2018,** *433*, 994-1017.
25. Chatterjee, S.; Major, G. H.; Paull, B.; Rodriguez, E. S.; Kaykhaii, M.; Linford, M. R., Using pattern recognition entropy to select mass chromatograms to prepare total ion current chromatograms from raw liquid chromatography–mass spectrometry data. *Journal of Chromatography A* **2018,** *1558*, 21-28.
26. Olivieri, G.; Giorgi, J. B.; Green, R. G.; Brown, M. A., 5 years of ambient pressure photoelectron spectroscopy (APPES) at the Swiss Light Source (SLS). *Journal of Electron Spectroscopy and Related Phenomena* **2017,** *216*, 1-16.
27. TAO, F., ZHU, Y.; , BERNASEK, S. L. , *Functionalization of Semiconductor Surfaces*. 1st ed.; John Wiley & Sons, Inc.: USA, 2012.
28. Yates Jr, J. T., A new opportunity in silicon-based microelectronics. *Science* **1998,** *279* (5349), 335-336.
29. Lin, Z.; Strother, T.; Cai, W.; Cao, X.; Smith, L. M.; Hamers, R. J., DNA attachment and hybridization at the silicon (100) surface. *Langmuir* **2002,** *18* (3), 788-796.
30. Yang, W.; Auciello, O.; Butler, J. E.; Cai, W.; Carlisle, J. A.; Gerbi, J. E.; Gruen, D. M.; Knickerbocker, T.; Lasseter, T. L.; Russell Jr, J. N.; Smith, L. M.; Hamers, R. J., DNA-modified nanocrystalline diamond thin-films as stable, biologically active substrates. *Nature Materials* **2002,** *1*, 253.
31. Stewart, M. P.; Buriak, J. M., Chemical and Biological Applications of Porous Silicon Technology. *Advanced Materials* **2000,** *12* (12), 859-869.
32. Maduraiveeran, G.; Sasidharan, M.; Ganesan, V., Electrochemical sensor and biosensor platforms based on advanced nanomaterials for biological and biomedical applications. *Biosensors and Bioelectronics* **2018,** *103*, 113-129.
33. Pasinszki, T.; Krebsz, M.; Tung, T. T.; Losic, D., Carbon Nanomaterial Based Biosensors for Non-Invasive Detection of Cancer and Disease Biomarkers for Clinical Diagnosis. *Sensors* **2017,** *17* (8), 1919.

34. Grieshaber, D.; MacKenzie, R.; Vörös, J.; Reimhult, E., Electrochemical Biosensors - Sensor Principles and Architectures. *Sensors* **2008,** *8* (3), 1400-1458.
35. Yates, J. T., A New Opportunity in Silicon-Based Microelectronics. *Science* **1998,** *279* (5349), 335-336.
36. Pasternack, R. M.; Rivillon Amy, S.; Chabal, Y. J., Attachment of 3-(Aminopropyl)triethoxysilane on Silicon Oxide Surfaces: Dependence on Solution Temperature. *Langmuir* **2008,** *24* (22), 12963-12971.
37. Zhu, Z.; Garcia-Gancedo, L.; Flewitt, A. J.; Xie, H.; Moussy, F.; Milne, W. I., A Critical Review of Glucose Biosensors Based on Carbon Nanomaterials: Carbon Nanotubes and Graphene. *Sensors* **2012,** *12* (5), 5996-6022.
38. Wang, J., Carbon-Nanotube Based Electrochemical Biosensors: A Review. *Electroanalysis* **2005,** *17* (1), 7-14.
39. Chan, H. N.; Tan, M. J. A.; Wu, H., Point-of-care testing: applications of 3D printing. *Lab on a Chip* **2017,** *17* (16), 2713-2739.
40. Fodor, S.; Read, J.; Pirrung, M.; Stryer, L.; Lu, A.; Solas, D., Light-directed, spatially addressable parallel chemical synthesis. *Science* **1991,** *251* (4995), 767-773.
41. Hughes, T. R.; Mao, M.; Jones, A. R.; Burchard, J.; Marton, M. J.; Shannon, K. W.; Lefkowitz, S. M.; Ziman, M.; Schelter, J. M.; Meyer, M. R.; Kobayashi, S.; Davis, C.; Dai, H.; He, Y. D.; Stephaniants, S. B.; Cavet, G.; Walker, W. L.; West, A.; Coffey, E.; Shoemaker, D. D.; Stoughton, R.; Blanchard, A. P.; Friend, S. H.; Linsley, P. S., Expression profiling using microarrays fabricated by an ink-jet oligonucleotide synthesizer. *Nature Biotechnology* **2001,** *19* (4), 342-347.
42. Manickam, A.; Singh, R.; McDermott, M. W.; Wood, N.; Bolouki, S.; Naraghi-Arani, P.; Johnson, K. A.; Kuimelis, R. G.; Schoolnik, G.; Hassibi, A., A Fully Integrated CMOS Fluorescence Biochip for DNA and RNA Testing. *IEEE Journal of Solid-State Circuits* **2017,** *52* (11), 2857-2870.
43. Augenlicht, L. H.; Kobrin, D., Cloning and Screening of Sequences Expressed in a Mouse Colon Tumor. *Cancer Research* **1982,** *42* (3), 1088-1093.
44. Butler, J. E., Enzyme-Linked Immunosorbent Assay. *Journal of Immunoassay* **2000,** *21* (2-3), 165-209.
45. Schmalzing, D.; Nashabeh, W., Capillary electrophoresis based immunoassays: A critical review. *ELECTROPHORESIS* **1997,** *18* (12-13), 2184-2193.
46. Diamandis, E. P.; van der Merwe, D.-E., Plasma Protein Profiling by Mass Spectrometry for Cancer Diagnosis: Opportunities and Limitations. *Clinical Cancer Research* **2005,** *11* (3), 963-965.
47. Widjojoatmodjo, M. N.; Fluit, A. C.; Torensma, R.; Verdonk, G. P.; Verhoef, J., The magnetic immuno polymerase chain reaction assay for direct detection of salmonellae in fecal samples. *Journal of Clinical Microbiology* **1992,** *30* (12), 3195-3199.
48. Davis, G., Electrochemical techniques for the development of amperometric biosensors. *Biosensors* **1985,** *1* (2), 161-178.
49. van der Schoot, B. H.; Bergveld, P., ISFET based enzyme sensors. *Biosensors* **1987,** *3* (3), 161-186.
50. Jang, B.; Cao, P.; Chevalier, A.; Ellington, A.; Hassibi, A. In *A CMOS fluorescent-based biosensor microarray*, 2009 IEEE International Solid-State Circuits Conference - Digest of Technical Papers, 8-12 Feb. 2009; 2009; pp 436-437,437a.

51. Schwartz, D. E.; Charbon, E.; Shepard, K. L., A Single-Photon Avalanche Diode Array for Fluorescence Lifetime Imaging Microscopy. *IEEE Journal of Solid-State Circuits* **2008,** *43* (11), 2546-2557.
52. K. D, W.; D. J, A.; J. F, H.; D. R, K.; K, N., Wireless implantable microsystems: high-density electronic interfaces to the nervous system. *Proceedings of the IEEE* **2004,** *92* (1), 76-97.
53. Derek, C. A.; Carlos, A. P. P.; Eliezer, S., Epidemiology of Severe Sepsis Around the World. *Endocrine, Metabolic & Immune Disorders - Drug Targets* **2006,** *6* (2), 207-212.
54. Mellhammar, L.; Wullt, S.; Lindberg, Å.; Lanbeck, P.; Christensson, B.; Linder, A., Sepsis Incidence: A Population-Based Study. *Open Forum Infectious Diseases* **2016,** *3* (4).
55. Qureshi, A.; Kang, W. P.; Davidson, J. L.; Gurbuz, Y., Review on carbon-derived, solid-state, micro and nano sensors for electrochemical sensing applications. *Diamond and Related Materials* **2009,** *18* (12), 1401-1420.
56. Etzioni, R.; Urban, N.; Ramsey, S.; McIntosh, M.; Schwartz, S.; Reid, B.; Radich, J.; Anderson, G.; Hartwell, L., The case for early detection. *Nature Reviews Cancer* **2003,** *3* (4), 243-252.
57. Srinivas, P. R.; Kramer, B. S.; Srivastava, S., Trends in biomarker research for cancer detection. *Lancet Oncology* **2001,** *2* (11), 698-704.
58. Wulfkuhle, J. D.; Liotta, L. A.; Petricoin, E. F., Proteomic applications for the early detection of cancer. *Nature Reviews Cancer* **2003,** *3* (4), 267-275.
59. Buriak, J. M., Organometallic chemistry on silicon and germanium surfaces. *Chemical Reviews* **2002,** *102* (5), 1271-1308.
60. Bousse, L.; Rooij, N. F. D.; Bergveld, P., Operation of chemically sensitive field-effect sensors as a function of the insulator-electrolyte interface. *IEEE Transactions on Electron Devices* **1983,** *30* (10), 1263-1270.
61. Linford, M. R.; Chidsey, C. E. D.; Fenter, P.; Eisenberger, P. M., Alkyl Monolayers on Silicon Prepared from 1-Alkenes and Hydrogen-Terminated Silicon. *Journal of the American Chemical Society* **1995,** *117* (11), 3145-3155.
62. Strother, T.; Cai, W.; Zhao, X.; Hamers, R. J.; Smith, L. M., Synthesis and characterization of DNA-modified silicon (111) surfaces. *Journal of the American Chemical Society* **2000,** *122* (6), 1205-1209.
63. Hashimoto, K.; Ito, K.; Ishimori, Y., Sequence-Specific Gene Detection with a Gold Electrode Modified with DNA Probes and an Electrochemically Active Dye. *Analytical Chemistry* **1994,** *66* (21), 3830-3833.
64. Millan, K. M.; Spurmanis, A. J.; Mikkelsen, S. R., Covalent immobilization of DNA onto glassy carbon electrodes. *Electroanalysis* **1992,** *4* (10), 929-932.
65. Kremsky, J. N.; Wooters, J. L.; Dougherty, J. P.; Meyers, R. E.; Collins, M.; Brown, E. L., Immobilization of DNA via oligonucleotides containing an aldehyde or carboxylic acid group at the 5' terminus. *Nucleic Acids Research* **1987,** *15* (7), 2891-2909.
66. Aissaoui, N.; Bergaoui, L.; Landoulsi, J.; Lambert, J.-F.; Boujday, S., Silane Layers on Silicon Surfaces: Mechanism of Interaction, Stability, and Influence on Protein Adsorption. *Langmuir* **2012,** *28* (1), 656-665.
67. Phillips, M. F.; Lockett, M. R.; Rodesch, M. J.; Shortreed, M. R.; Cerrina, F.; Smith, L. M., In situ oligonucleotide synthesis on carbon materials: stable substrates for microarray fabrication. *Nucleic Acids Research* **2008,** *36* (1), e7-e7.
68. Radadia, A. D.; Stavis, C. J.; Carr, R.; Zeng, H.; King, W. P.; Carlisle, J. A.; Aksimentiev, A.; Hamers, R. J.; Bashir, R., Control of Nanoscale Environment to Improve Stability of

Immobilized Proteins on Diamond Surfaces. *Advanced Functional Materials* **2011,** *21* (6), 1040-1050.
69. Schoenfisch, M. H.; Pemberton, J. E., Air Stability of Alkanethiol Self-Assembled Monolayers on Silver and Gold Surfaces. *Journal of the American Chemical Society* **1998,** *120* (18), 4502-4513.
70. Horn, A. B.; Russell, D. A.; Shorthouse, L. J.; Simpson, T. R. E., Ageing of alkanethiol self-assembled monolayers. *Journal of the Chemical Society, Faraday Transactions* **1996,** *92* (23), 4759-4762.
71. Hutt, D. A.; Leggett, G. J., Influence of Adsorbate Ordering on Rates of UV Photooxidation of Self-Assembled Monolayers. *The Journal of Physical Chemistry* **1996,** *100* (16), 6657-6662.
72. Yang, G.; Amro, N. A.; Starkewolfe, Z. B.; Liu, G.-y., Molecular-Level Approach To Inhibit Degradations of Alkanethiol Self-Assembled Monolayers in Aqueous Media. *Langmuir* **2004,** *20* (10), 3995-4003.
73. Hsiao, V. K. S.; Waldeisen, J. R.; Zheng, Y.; Lloyd, P. F.; Bunning, T. J.; Huang, T. J., Aminopropyltriethoxysilane (APTES)-functionalized nanoporous polymeric gratings: Fabrication and application in biosensing. *Journal of Materials Chemistry* **2007,** *17* (46), 4896-4901.
74. Dietrich, P. M.; Streeck, C.; Glamsch, S.; Ehlert, C.; Lippitz, A.; Nutsch, A.; Kulak, N.; Beckhoff, B.; Unger, W. E. S., Quantification of Silane Molecules on Oxidized Silicon: Are there Options for a Traceable and Absolute Determination? *Analytical Chemistry* **2015,** *87* (19), 10117-10124.
75. Bansal, A.; Li, X.; Lauermann, I.; Lewis, N. S.; Yi, S. I.; Weinberg, W. H., Alkylation of Si Surfaces Using a Two-Step Halogenation/Grignard Route. *Journal of the American Chemical Society* **1996,** *118* (30), 7225-7226.
76. Hamers, R. J., Formation and Characterization of Organic Monolayers on Semiconductor Surfaces. *Annual Review of Analytical Chemistry* **2008,** *1* (1), 707-736.
77. Bent, S. F., Organic functionalization of group IV semiconductor surfaces: principles, examples, applications, and prospects. *Surface Science* **2002,** *500* (1), 879-903.
78. Filler, M. A.; Bent, S. F., The surface as molecular reagent: organic chemistry at the semiconductor interface. *Progress in Surface Science* **2003,** *73* (1), 1-56.
79. Bent, S. F.; Kachian, J. S.; Rodríguez-Reyes, J. C. F.; Teplyakov, A. V., Tuning the reactivity of semiconductor surfaces by functionalization with amines of different basicity. *Proceedings of the National Academy of Sciences* **2011,** *108* (3), 956-960.
80. Nebel, C. E.; Rezek, B.; Shin, D.; Uetsuka, H.; Yang, N., Diamond for bio-sensor applications. *Journal of Physics D: Applied Physics* **2007,** *40* (20), 6443-6466.
81. *Diamond Electrochemistry*. 1st ed.; Elsevier-BKC: Tokyo, 2004.
82. Lockett, M. R.; Smith, L. M., Attaching molecules to chlorinated and brominated amorphous carbon substrates via Grignard reactions. *Langmuir : the ACS journal of surfaces and colloids* **2009,** *25* (6), 3340-3343.
83. Nichols, B. M.; Butler, J. E.; Russell, J. N.; Hamers, R. J., Photochemical Functionalization of Hydrogen-Terminated Diamond Surfaces: A Structural and Mechanistic Study. *The Journal of Physical Chemistry B* **2005,** *109* (44), 20938-20947.
84. Härtl, A.; Schmich, E.; Garrido, J. A.; Hernando, J.; Catharino, S. C. R.; Walter, S.; Feulner, P.; Kromka, A.; Steinmüller, D.; Stutzmann, M., Protein-modified nanocrystalline diamond thin films for biosensor applications. *Nature Materials* **2004,** *3* (10), 736-742.
85. Nistor, P. A.; May, P. W., Diamond thin films: giving biomedical applications a new shine. *Journal of The Royal Society Interface* **2017,** *14* (134), 20170382.

86. Ahmed, R.; Nazari, M.; Hancock, B. L.; Simpson, J.; Engdahl, C.; Piner, E. L.; Holtz, M. W., Ultraviolet micro-Raman stress map of polycrystalline diamond grown selectively on silicon substrates using chemical vapor deposition. *Applied Physics Letters* **2018,** *112* (18), 181907.
87. May, P. W.; Regan, E. M.; Taylor, A.; Uney, J.; Dick, A. D.; McGeehan, J., Spatially controlling neuronal adhesion on CVD diamond. *Diamond and Related Materials* **2012,** *23*, 100-104.
88. Miller, J. B.; Brown, D. W., Photochemical modification of diamond surfaces. *Langmuir* **1996,** *12* (24), 5809-5817.
89. Ohtani, B.; Kim, Y. H.; Yano, T.; Hashimoto, K.; Fujishima, A.; Uosaki, K., Surface functionalization of doped CVD diamond via covalent bond. An XPS study on the formation of surface-bound quaternary pyridinium salt. *Chemistry Letters* **1998,** (9), 953-954.
90. Ando, T.; Yamamoto, K.; Kamo, M.; Sato, Y.; Takamatsu, Y.; Kawasaki, S.; Okino, F.; Touhara, H., Diffuse reflectance infrared Fourier-transform study of the direct thermal fluorination of diamond powder surfaces. *Journal of the Chemical Society, Faraday Transactions* **1995,** *91* (18), 3209-3212.
91. Phillips, M. F.; Lockett, M. R.; Rodesch, M. J.; Shortreed, M. R.; Cerrina, F.; Smith, L. M., In situ oligonucleotide synthesis on carbon materials: stable substrates for microarray fabrication. *Nucleic Acids Research* **2007,** *36* (1), e7-e7.
92. Sun, B.; Colavita, P. E.; Kim, H.; Lockett, M.; Marcus, M. S.; Smith, L. M.; Hamers, R. J., Covalent Photochemical Functionalization of Amorphous Carbon Thin Films for Integrated Real-Time Biosensing. *Langmuir* **2006,** *22* (23), 9598-9605.
93. Sreenivas, G.; Ang, S. S.; Fritsch, I.; Brown, W. D.; Gerhardt, G. A.; Woodward, D. J., Fabrication and Characterization of Sputtered-Carbon Microelectrode Arrays. *Analytical Chemistry* **1996,** *68* (11), 1858-1864.
94. Robertson, J., Properties of diamond-like carbon. *Surface and Coatings Technology* **1992,** *50* (3), 185-203.
95. Koidl, P.; Wild, C.; Dischler, B.; Wagner, J.; Ramsteiner, M., Plasma Deposition, Properties and Structure of Amorphous Hydrogenated Carbon Films, in Properties and Characterization of Amorphous Carbon Films. *Mater. Sci. Forum* **1990,** *52*, 41-69.
96. Tsai, H. C.; Bogy, D. B., Critical review characterization of diamondlike carbon films and their application as overcoats on thin-film media for magnetic recording. *Journal of Vacuum Science and Technology A: Vacuum, Surfaces and Films* **1987,** *5* (6), 3287-3312.
97. Lifshitz, Y., Diamond-like carbon - Present status. *Diamond and Related Materials* **1999,** *8* (8-9), 1659-1676.
98. Maalouf, R.; Chebib, H.; Saikali, Y.; Vittori, O.; Sigaud, M.; Garrelie, F.; Donnet, C.; Jaffrezic-Renault, N., Characterization of different diamond-like carbon electrodes for biosensor design. *Talanta* **2007,** *72* (1), 310-314.
99. Moon, J. M.; Park, S.; Lee, Y. K.; Sook Bang, G.; Hong, Y. K.; Park, C.; Cheol Jeon, I., Diamond-like carbon electrodes in electrochemical microgravimetry. *Journal of Electroanalytical Chemistry* **1999,** *464* (2), 230-237.
100. Broitman, E.; Hellgren, N.; Czigány, Z.; Twesten, R. D.; Luning, J.; Petrov, I.; Hultman, L.; Holloway, B. C., Structural and mechanical properties of diamond-like carbon films deposited by direct current magnetron sputtering. *Journal of Vacuum Science & Technology A* **2003,** *21* (4), 851-859.
101. Robertson, J., Amorphous carbon. *Current Opinion in Solid State and Materials Science* **1996,** *1* (4), 557-561.

102. Peiner, E.; Tibrewala, A.; Bandorf, R.; Biehl, S.; Lüthje, H.; Doering, L., Micro force sensor with piezoresistive amorphous carbon strain gauge. *Sensors and Actuators, A: Physical* **2006,** *130-131* (SPEC. ISS.), 75-82.
103. F G Celii, a.; Butler, J. E., Diamond Chemical Vapor Deposition. *Annual Review of Physical Chemistry* **1991,** *42* (1), 643-684.
104. Isono, Y.; Namazu, T.; Terayama, N., Development of AFM tensile test technique for evaluating mechanical properties of sub-micron thick DLC films. *Journal of Microelectromechanical Systems* **2006,** *15* (1), 169-180.
105. GOWARD, G. W., *J. Inst. Met.* **1970,** *31* (22).
106. Boone, D. H., Physical vapour deposition processes. *Materials Science and Technology* **1986,** *2* (3), 220-224.
107. Lundin, D.; Sarakinos, K., An introduction to thin film processing using high-power impulse magnetron sputtering. *Journal of Materials Research* **2012,** *27* (5), 780-792.
108. Bunshah, R. F., *Handbook of Deposition Technologies for Films and Coatings*. 2nd ed.; Noyes publication: Park Ridge, NJ, 1982.
109. Bouzakis, K.-D.; Michailidis, N., Physical Vapor Deposition (PVD). In *CIRP Encyclopedia of Production Engineering*, Int. Academy for Production, E.; Chatti, S.; Tolio, T., Eds. Springer Berlin Heidelberg: Berlin, Heidelberg, 2018; pp 1-8.
110. Hauert, R., A review of modified DLC coatings for biological applications. *Diamond and Related Materials* **2003,** *12* (3-7), 583-589.
111. Yang, G.; Liu, E.; Khun, N. W.; Jiang, S. P., Direct electrochemical response of glucose at nickel-doped diamond like carbon thin film electrodes. *Journal of Electroanalytical Chemistry* **2009,** *627* (1), 51-57.
112. Liu, H.; Ji, L.; Li, J.; Liu, S.; Liu, X.; Jiang, S., Magnetron sputtering Si interlayer: A protocol to prepare solid phase microextraction coatings on metal-based fiber. *Journal of Chromatography A* **2011,** *1218* (20), 2835-2840.
113. Rossnagel, S. M., Sputter deposition for semiconductor manufacturing. *IBM Journal of Research and Development* **1999,** *43* (1.2), 163-179.
114. Wang, H.; Madaan, N.; Bagley, J.; Diwan, A.; Liu, Y.; Davis, R. C.; Lunt, B. M.; Smith, S. J.; Linford, M. R., Spectroscopic ellipsometric modeling of a Bi–Te–Se write layer of an optical data storage device as guided by atomic force microscopy, scanning electron microscopy, and X-ray diffraction. *Thin Solid Films* **2014,** *569*, 124-130.
115. Wang, H.; Lunt, B. M.; Gates, R. J.; Asplund, M. C.; Shutthanandan, V.; Davis, R. C.; Linford, M. R., Carbon/Ternary Alloy/Carbon Optical Stack on Mylar as an Optical Data Storage Medium to Potentially Replace Magnetic Tape. *ACS Applied Materials & Interfaces* **2013,** *5* (17), 8407-8413.
116. Abbott, J.; Niederhauser, T. L.; Hansen, D. P.; Perkins, R. T.; Bell, D. A.; Bard, E. C.; Lunt, B. M.; Worthington, M. O.; Miller, C. M.; Hyatt, D. F.; Asplund, M. C.; Jiang, G.; Linford, M. R.; Vanfleet, R. R.; Davis, R. C., Carbon-Coated Tellurium for Optical Data Storage. *ACS Applied Materials & Interfaces* **2010,** *2* (8), 2373-2376.
117. Ohring, M., Chapter 5 - Plasma and Ion Beam Processing of Thin Films. In *Materials Science of Thin Films (Second Edition)*, Ohring, M., Ed. Academic Press: San Diego, 2002; pp 203-275.
118. Kelly, P. J.; Arnell, R. D., Magnetron sputtering: a review of recent developments and applications. *Vacuum* **2000,** *56* (3), 159-172.

119. Ellmer, K., Magnetron sputtering of transparent conductive zinc oxide: relation between the sputtering parameters and the electronic properties. *Journal of Physics D, Applied Physics* **2000,** *33* (4), R17-R32.
120. McLeod, P. S.; Hartsough, L. D., High-rate sputtering of aluminum for metallization of integrated circuits. *Journal of Vacuum Science and Technology* **1977,** *14* (1), 263-265.
121. Savvides, N., Deposition parameters and film properties of hydrogenated amorphous silicon prepared by high rate dc planar magnetron reactive sputtering. *Journal of Applied Physics* **1984,** *55* (12), 4232-4238.
122. Cuomo, J. J.; Doyle, J. P.; Bruley, J.; Liu, J. C., Sputter deposition of dense diamond-like carbon films at low temperature. *Applied Physics Letters* **1991,** *58* (5), 466-468.
123. Robbie, K.; Brett, M. J., Sculptured thin films and glancing angle deposition: Growth mechanics and applications. *Journal of Vacuum Science & Technology A* **1997,** *15* (3), 1460-1465.
124. Robbie, K.; Shafai, C.; Brett, M. J., Thin films with nanometer-scale pillar microstructure. *Journal of Materials Research* **1999,** *14* (7), 3158-3163.
125. Harris, K. D. B., M. J.; Smy, T. J.; Backhouse, C., Microchannel Surface Area Enhancement Using Porous Thin Films. *J Electrochem Soc* **2000,** *147* (5), 2002-2006.
126. Smith, D. O.; Cohen, M. S.; Weiss, G. P., Oblique-Incidence Anisotropy in Evaporated Permalloy Films. *Journal of Applied Physics* **1960,** *31* (10), 1755-1762.
127. Dick, B.; Brett, M. J.; Smy, T., Controlled growth of periodic pillars by glancing angle deposition. *Journal of Vacuum Science & Technology B: Microelectronics and Nanometer Structures Processing, Measurement, and Phenomena* **2003,** *21* (1), 23-28.
128. Savvides, N.; Window, B., Diamondlike amorphous carbon films prepared by magnetron sputtering of graphite. *Journal of Vacuum Science & Technology A* **1985,** *3* (6), 2386-2390.
129. Luo, J. K.; Fu, Y. Q.; Le, H. R.; Williams, J. A.; Spearing, S. M.; Milne, W. I., Diamond and diamond-like carbon MEMS. *Journal of Micromechanics and Microengineering* **2007,** *17* (7), S147-S163.
130. He, X. M.; Bardeau, J.-F.; Walter, K. C.; Nastasi, M., Characterization and enhanced properties of plasma immersion ion processed diamond-like carbon films. *Journal of Vacuum Science & Technology A* **1999,** *17* (5), 2525-2530.
131. Christou, C.; Barber, Z. H., Ionization of sputtered material in a planar magnetron discharge. *Journal of Vacuum Science & Technology A* **2000,** *18* (6), 2897-2907.
132. Rossnagel, S. M.; Hopwood, J., Metal ion deposition from ionized mangetron sputtering discharge. *Journal of Vacuum Science & Technology B: Microelectronics and Nanometer Structures Processing, Measurement, and Phenomena* **1994,** *12* (1), 449-453.
133. Helmersson, U.; Lattemann, M.; Bohlmark, J.; Ehiasarian, A. P.; Gudmundsson, J. T., Ionized physical vapor deposition (IPVD): A review of technology and applications. *Thin Solid Films* **2006,** *513* (1), 1-24.
134. Alami, J.; Persson, P. O. Å.; Music, D.; Gudmundsson, J. T.; Bohlmark, J.; Helmersson, U., Ion-assisted physical vapor deposition for enhanced film properties on nonflat surfaces. *Journal of Vacuum Science & Technology A* **2005,** *23* (2), 278-280.
135. Konstantinidis, S.; Nouvellon, C.; Dauchot, J. P.; Wautelet, M.; Hecq, M., RF amplified magnetron source for efficient titanium nitride deposition. *Surface and Coatings Technology* **2003,** *174-175*, 100-106.
136. Kouznetsov, V.; Macák, K.; Schneider, J. M.; Helmersson, U.; Petrov, I., A novel pulsed magnetron sputter technique utilizing very high target power densities. *Surface and Coatings Technology* **1999,** *122* (2), 290-293.

137. Sarakinos, K.; Alami, J.; Konstantinidis, S., High power pulsed magnetron sputtering: A review on scientific and engineering state of the art. *Surface and Coatings Technology* **2010,** *204* (11), 1661-1684.
138. Konstantinidis, S.; Dauchot, J. P.; Ganciu, M.; Ricard, A.; Hecq, M., Influence of pulse duration on the plasma characteristics in high-power pulsed magnetron discharges. *Journal of Applied Physics* **2006,** *99* (1), 013307.
139. Alami, J.; Sarakinos, K.; Uslu, F.; Wuttig, M., On the relationship between the peak target current and the morphology of chromium nitride thin films deposited by reactive high power pulsed magnetron sputtering. *Journal of Physics D: Applied Physics* **2008,** *42* (1), 015304.
140. Bohlmark, J.; Lattemann, M.; Gudmundsson, J. T.; Ehiasarian, A. P.; Aranda Gonzalvo, Y.; Brenning, N.; Helmersson, U., The ion energy distributions and ion flux composition from a high power impulse magnetron sputtering discharge. *Thin Solid Films* **2006,** *515* (4), 1522-1526.
141. Bohlmark, J.; Alami, J.; Christou, C.; Ehiasarian, A. P.; Helmersson, U., Ionization of sputtered metals in high power pulsed magnetron sputtering. *Journal of Vacuum Science & Technology A* **2005,** *23* (1), 18-22.
142. Gudmundsson, J. T.; Sigurjonsson, P.; Larsson, P.; Lundin, D.; Helmersson, U., On the electron energy in the high power impulse magnetron sputtering discharge. *Journal of Applied Physics* **2009,** *105* (12), 123302.
143. Bohlmark, J.; Gudmundsson, J. T.; Alami, J.; Latteman, M.; Helmersson, U., Spatial electron density distribution in a high-power pulsed magnetron discharge. *IEEE Transactions on Plasma Science* **2005,** *33* (2), 346-347.
144. Gudmundsson, J. T., The high power impulse magnetron sputtering discharge as an ionized physical vapor deposition tool. *Vacuum* **2010,** *84* (12), 1360-1364.
145. Vlček, J.; Kudláček, P.; Burcalová, K.; Musil, J., Ion flux characteristics in high-power pulsed magnetron sputtering discharges. *Europhysics Letters (EPL)* **2007,** *77* (4), 45002.
146. Samuelsson, M.; Lundin, D.; Jensen, J.; Raadu, M. A.; Gudmundsson, J. T.; Helmersson, U., On the film density using high power impulse magnetron sputtering. *Surface and Coatings Technology* **2010,** *205* (2), 591-596.
147. Sittinger, V.; Ruske, F.; Werner, W.; Jacobs, C.; Szyszka, B.; Christie, D. J., High power pulsed magnetron sputtering of transparent conducting oxides. *Thin Solid Films* **2008,** *516* (17), 5847-5859.
148. Lattemann, M.; Helmersson, U.; Greene, J. E., Fully dense, non-faceted 111-textured high power impulse magnetron sputtering TiN films grown in the absence of substrate heating and bias. *Thin Solid Films* **2010,** *518* (21), 5978-5980.
149. Konstantinidis, S.; Dauchot, J. P.; Hecq, M., Titanium oxide thin films deposited by high-power impulse magnetron sputtering. *Thin Solid Films* **2006,** *515* (3), 1182-1186.
150. Alami, J.; Eklund, P.; Andersson, J. M.; Lattemann, M.; Wallin, E.; Bohlmark, J.; Persson, P.; Helmersson, U., Phase tailoring of Ta thin films by highly ionized pulsed magnetron sputtering. *Thin Solid Films* **2007,** *515* (7), 3434-3438.
151. Ehiasarian, A. P.; Hovsepian, P. E.; Hultman, L.; Helmersson, U., Comparison of microstructure and mechanical properties of chromium nitride-based coatings deposited by high power impulse magnetron sputtering and by the combined steered cathodic arc/unbalanced magnetron technique. *Thin Solid Films* **2004,** *457* (2), 270-277.
152. Ehiasarian, A. P.; Wen, J. G.; Petrov, I., Interface microstructure engineering by high power impulse magnetron sputtering for the enhancement of adhesion. *Journal of Applied Physics* **2007,** *101* (5), 054301.

153. Wallin, E.; Selinder, T. I.; Elfwing, M.; Helmersson, U., Synthesis of α-Al2 O3 thin films using reactive high-power impulse magnetron sputtering. *EPL (Europhysics Letters)* **2008,** *82* (3), 36002.
154. Siemroth, P.; Schülke, T., Copper metallization in microelectronics using filtered vacuum arc deposition — principles and technological development. *Surface and Coatings Technology* **2000,** *133-134*, 106-113.
155. Christie, D. J., Target material pathways model for high power pulsed magnetron sputtering. *Journal of Vacuum Science & Technology A* **2005,** *23* (2), 330-335.
156. Mishra, A.; Kelly, P. J.; Bradley, J. W., The evolution of the plasma potential in a HiPIMS discharge and its relationship to deposition rate. *Plasma Sources Science and Technology* **2010,** *19* (4), 045014.
157. Banu, M.; Radoi, A.; Simion, M.; Kusko, M. In *Reproducible functionalization of silicon substrates intended for biomedical applications*, 2016 International Semiconductor Conference (CAS), 10-12 Oct. 2016; 2016; pp 151-154.
158. T. Franklin; Bernasek, S., In *Functionalization of Semiconductor Surfaces* John Wiley and Sons: USA, 2012; pp 402-423.
159. Majoul, N.; Aouida, S.; Bessaïs, B., Progress of porous silicon APTES-functionalization by FTIR investigations. *Applied Surface Science* **2015,** *331*, 388-391.
160. Kim, J.; Seidler, P.; Wan, L. S.; Fill, C., Formation, structure, and reactivity of amino-terminated organic films on silicon substrates. *Journal of Colloid and Interface Science* **2009,** *329* (1), 114-119.
161. Mathieu, H. J., Bioengineered material surfaces for medical applications. *Surface and Interface Analysis* **2001,** *32* (1), 3-9.
162. Cui, F. Z.; Li, D. J., A review of investigations on biocompatibility of diamond-like carbon and carbon nitride films. *Surface and Coatings Technology* **2000,** *131* (1), 481-487.
163. Colavita, P. E.; Sun, B.; Wang, X.; Hamers, R. J., Influence of Surface Termination and Electronic Structure on the Photochemical Grafting of Alkenes to Carbon Surfaces. *The Journal of Physical Chemistry C* **2009,** *113* (4), 1526-1535.
164. Szunerits, S.; Boukherroub, R., Different strategies for functionalization of diamond surfaces. *Journal of Solid State Electrochemistry* **2008,** *12* (10), 1205-1218.
165. Tsubota, T.; Hirabayashi, O.; Ida, S.; Nagaoka, S.; Nagata, M.; Matsumoto, Y., Abstraction of hydrogen atoms on diamond surface using benzoyl peroxide as a radical initiator. *Diamond and Related Materials* **2002,** *11* (7), 1374-1378.
166. Ida, S.; Tsubota, T.; Tanii, S.; Nagata, M.; Matsumoto, Y., Chemical Modification of the Diamond Surface Using Benzoyl Peroxide and Dicarboxylic Acids. *Langmuir* **2003,** *19* (23), 9693-9698.
167. Miller, J. B., Amines and thiols on diamond surfaces. *Surface Science* **1999,** *439* (1), 21-33.
168. Liu, Y.; Gu, Z.; Margrave, J. L.; Khabashesku, V. N., Functionalization of Nanoscale Diamond Powder: Fluoro-, Alkyl-, Amino-, and Amino Acid-Nanodiamond Derivatives. *Chemistry of Materials* **2004,** *16* (20), 3924-3930.
169. Sotowa, K.-I.; Amamoto, T.; Sobana, A.; Kusakabe, K.; Imato, T., Effect of treatment temperature on the amination of chlorinated diamond. *Diamond and Related Materials* **2004,** *13* (1), 145-150.

170. Kuo, T. C.; McCreery, R. L.; Swain, G. M., Electrochemical Modification of Boron-Doped Chemical Vapor Deposited Diamond Surfaces with Covalently Bonded Monolayers. *Electrochemical and Solid-State Letters* **1999,** *2* (6), 288-290.
171. Allongue, P.; Delamar, M.; Desbat, B.; Fagebaume, O.; Hitmi, R.; Pinson, J.; Savéant, J.-M., Covalent Modification of Carbon Surfaces by Aryl Radicals Generated from the Electrochemical Reduction of Diazonium Salts. *Journal of the American Chemical Society* **1997,** *119* (1), 201-207.
172. Strother, T.; Knickerbocker, T.; Russell, J. N.; Butler, J. E.; Smith, L. M.; Hamers, R. J., Photochemical Functionalization of Diamond Films. *Langmuir* **2002,** *18* (4), 968-971.
173. Clare, T. L.; Clare, B. H.; Nichols, B. M.; Abbott, N. L.; Hamers, R. J., Functional Monolayers for Improved Resistance to Protein Adsorption: Oligo(ethylene glycol)-Modified Silicon and Diamond Surfaces. *Langmuir* **2005,** *21* (14), 6344-6355.
174. Ohta, R.; Saito, N.; Inoue, Y.; Sugimura, H.; Takai, O., Organosilane self-assembled monolayers directly linked to the diamond surfaces. *Journal of Vacuum Science & Technology A* **2004,** *22* (5), 2005-2009.
175. Gallardo, I.; Pinson, J.; Vilà, N., Spontaneous Attachment of Amines to Carbon and Metallic Surfaces. *The Journal of Physical Chemistry B* **2006,** *110* (39), 19521-19529.
176. Singh, P.; Campidelli, S.; Giordani, S.; Bonifazi, D.; Bianco, A.; Prato, M., Organic functionalisation and characterisation of single-walled carbon nanotubes. *Chemical Society Reviews* **2009,** *38* (8), 2214-2230.
177. Colavita, P. E.; Sun, B.; Tse, K.-Y.; Hamers, R. J., Photochemical Grafting of n-Alkenes onto Carbon Surfaces: the Role of Photoelectron Ejection. *Journal of the American Chemical Society* **2007,** *129* (44), 13554-13565.
178. Rosso, M.; Arafat, A.; Schroën, K.; Giesbers, M.; Roper, C. S.; Maboudian, R.; Zuilhof, H., Covalent Attachment of Organic Monolayers to Silicon Carbide Surfaces. *Langmuir* **2008,** *24* (8), 4007-4012.
179. Evans, M. J. B.; Halliop, E.; Liang, S.; MacDonald, J. A. F., The effect of chlorination on surface properties of activated carbon. *Carbon* **1998,** *36* (11), 1677-1682.
180. Papirer, E.; Lacroix, R.; Donnet, J.-B.; Nanse, G.; Fioux, P., XPS Study of the halogenation of carbon black-part 1. Bromination. *Carbon* **1994,** *32* (7), 1341-1358.
181. Rezek, B.; Shin, D.; Nebel, C. E., Properties of Hybridized DNA Arrays on Single-Crystalline Undoped and Boron-Doped (100) Diamonds Studied by Atomic Force Microscopy in Electrolytes. *Langmuir* **2007,** *23* (14), 7626-7633.
182. Singh, B.; Diwan, A.; Jain, V.; Herrera-Gomez, A.; Terry, J.; Linford, M. R., Uniqueness plots: A simple graphical tool for identifying poor peak fits in X-ray photoelectron spectroscopy. *Applied Surface Science* **2016,** *387*, 155-162.
183. Gupta, V.; Ganegoda, H.; Engelhard, M. H.; Terry, J.; Linford, M. R., Assigning Oxidation States to Organic Compounds via Predictions from X-ray Photoelectron Spectroscopy: A Discussion of Approaches and Recommended Improvements. *Journal of Chemical Education* **2014,** *91* (2), 232-238.
184. Zhang, S.; Li, L.; Kumar, A., *Materials characterization techniques*. CRC Press: Boca Raton, 2009.
185. Cushman, C. V.; Brüner, P.; Zakel, J.; Major, G. H.; Lunt, B. M.; Smith, N. J.; Grehl, T.; Linford, M. R., Low energy ion scattering (LEIS). A practical introduction to its theory, instrumentation, and applications. *Analytical Methods* **2016,** *8* (17), 3419-3439.

186. Fadley, C. S.; Baird, R. J.; Siekhaus, W.; Novakov, T.; Bergström, S. Å. L., Surface analysis and angular distributions in x-ray photoelectron spectroscopy. *Journal of Electron Spectroscopy and Related Phenomena* **1974,** *4* (2), 93-137.
187. Swingle, R. S., Quantitative surface analysis by x-ray photoelectron spectroscopy (ESCA). *Analytical Chemistry* **1975,** *47* (1), 21-24.
188. Powell, C. J.; Larson, P. E., Quantitative surface analysis by X-ray photoelectron spectroscopy. *Applications of Surface Science* **1978,** *1* (2), 186-201.
189. Siegbahn Karl Manne, G.; Price William, C.; Turner David, W., A Discussion on photoelectron spectroscopy - Electron spectroscopy for chemical analysis (e.s.c.a.). *Philosophical Transactions of the Royal Society of London. Series A, Mathematical and Physical Sciences* **1970,** *268* (1184), 33-57.
190. van der heide, P., *X-ray Photoelectron Spectroscopy. An Introduction to Principles and Practices.* 1 ed.; John Wiley & Sons: New York, 2012; p 1-264.
191. Watts, J. F.; Wolstenholme, J., *An Introduction to Surface Analysis by XPS and AES*. John Wiley & Sons: New York, 2014.
192. Powell, C. J., New data resources and applications for AES and XPS. *J. Surf. Anal.* **2014,** *20* (3), 155-160.
193. Linford, M. R., An introduction to convolution with a few comments beforehand on XPS. *Vacuum Technology & Coatings* **2014,** *June* 25-32.
194. Shah, D. P., D. I.; Roychowdhury, T.; Rayner, G. R.; O'Toole, N.; Baer, D. R.; Linford, M. R., A Tutorial on Interpreting X-ray Photoelectron Spectroscopy (XPS) Survey Spectra: Questions on Spectra from the Atomic Layer Deposition (ALD) of Al2O3 on Silicon. *J. Vac. Sci. Technol. B* **2018,** *Submitted*.
195. Jain, V.; Biesinger, M. C.; Linford, M. R., The Gaussian-Lorentzian Sum, Product, and Convolution (Voigt) functions in the context of peak fitting X-ray photoelectron spectroscopy (XPS) narrow scans. *Applied Surface Science* **2018,** *447*, 548-553.
196. Singh, B.; Hesse, R.; Linford, M. R., Good Practices for XPS (and other Types of) Peak Fitting. *Vac. Techno. Coat* **2015,** *December* (12), 25-31.
197. Ganegoda, H.; Jensen, D. S.; Olive, D.; L.;, C.; Serge, C. U.; Linford, M. R.; Terry, J., Photoemission studies of fluorine functionalized porous graphitic carbon. *J. Appl. Phys.* **2012,** *111* (053705), 1-6.
198. Gupta, V.; Ganegoda, H.; Engelhard, M. H.; Terry, J.; Linford, M. R., Assigning Oxidation States to Organic Compounds via Predictions from X-ray Photoelectron Spectroscopy: A Discussion of Approaches and Recommended Improvements. *Journal of Chemical Education* **2013,** *91* (2), 232-238.
199. Linford, M. R., The Gaussian-Lorentzian Sum, Product, and Convolution (Voigt) Functions Used in Peak Fitting XPS Narrow Scans, and an Introduction to the Impulse Function' *Vacuum Technology & Coating* July, **2014** pp 27-33.
200. McArthur, S. L. M., G.; Easton, C. D., Applications of XPS in biology and biointerface analysis. In *Surface Analysis and Techniques in Biology*, Smentkowski, V., Ed. Springer International: Berlin, Germany, 2014.
201. Salmeron, M.; Schlögl, R., Ambient pressure photoelectron spectroscopy: A new tool for surface science and nanotechnology. *Surf. Sci. Rep.* **2008,** *63* (4), 169-199.
202. Arble, C.; Jia, M.; Newberg, J. T., Lab-based ambient pressure X-ray photoelectron spectroscopy from past to present. *Surface Science Reports* **2018,** *73* (2), 37-57.

203. Karsloglu, O.; Nemsak, S.; Zegkinoglou, I.; Shavorskiy, A.; Hartl, M.; Salmassi, F.; Gullikson, E. M.; Ng, M. L.; Rameshan, C.; Rude, B.; Bianculli, D.; Cordones, A. A.; Axnanda, S.; Crumlin, E. J.; Ross, P. N.; Schneider, C. M.; Hussain, Z.; Liu, Z.; Fadley, C. S.; Bluhm, H., Aqueous solution/metal interfaces investigated in operando by photoelectron spectroscopy. *Faraday Discussions* **2015,** *180* (0), 35-53.
204. Cushman, C. V.; Dahlquist, C. T.; Dietrich, P. M.; Bahr, S.; Thißen, A.; Schaff, O.; Banerjee, J.; Smith, N. J.; Linford, M. R., Trends in Advanced XPS Instrumentation. 5. Near-Ambient Pressure XPS. *Vac. Techno. Coat* **2017,** *August*, 23-31.
205. Patel, D. I.; Roychowdhury, T.; Jain, V.; Shah, D.; Avval, T. G.; Chatterjee, S.; Bahr, S.; Dietrich, P.; Meyer, M.; Thißen, A.; Linford, M. R., Introduction to near ambient pressure-x-ray 2 photoelectron spectroscopy characterization of Q1 3 various materials *Surface Sceince Spectra* **2019,** *26*.
206. Synowicki, R. A.; Johs, B. D.; Martin, A. C., Optical properties of soda-lime float glass from spectroscopic ellipsometry. *Thin Solid Films* **2011,** *519* (9), 2907-2913.
207. N. Hilfiker, J.; Bungay, C. L.; Synowicki, R. A.; Tiwald, T. E.; Herzinger, C. M.; Johs, B.; Pribil, G. K.; Woollam, J. A., Progress in spectroscopic ellipsometry: Applications from vacuum ultraviolet to infrared. *Journal of Vacuum Science & Technology A* **2003,** *21* (4), 1103-1108.
208. Leibiger, G.; Gottschalch, V.; Riede, V.; Schubert, M.; Hilfiker, J. N.; Tiwald, T. E., Interband transitions and phonon modes in B x Ga 1 - x As ($0 < \sim x <\sim 0.03$) and GaN y As 1 - y ($0 < \sim y < \sim 0.037$): A comparison. *Physical Review B* **2003,** *67* (19), 195205.
209. Johnson, B. I.; Cushman, C. V.; Rowely, J.; Lunt, B. M.; Smith, N. J.; Martin, A.; Linford, M. R., Optical Constant of SiO2 from 196 - 1688 nm (0.735 - 6.33 ev) from 20, 40, 60 nm films of reactively sputtered SiO2 on Eagle XG® Glass by Spectroscopic Ellipsometry. *accepted Surface Science Spectra* **2017**.
210. Cushman, C. V.; Johnson, B. I.; Martin, A.; Lunt, B. M.; Smith, N. J.; Linford, M. R., Eagle XG® glass: Optical constants from 196 to 1688 nm (0.735–6.33 eV) by spectroscopic ellipsometry. *Surface Science Spectra* **2017,** *24* (2), 026001.
211. Singh, B.; Chatterjee, S.; Diwan, A.; Lee, Z. R. E., M. H.; Terry, J.; Tolley, H. D.; Gallagher, N. B.; Linford, M. R., A Perspective on Two Established Chemometrics Tools: PCA and MCR, and Introduction of a New One: the Information Content (Entropy), As Applied to XPS and ToF-SIMS Depth Profiles of Organic and Inorganic Materials. *accepted Applied Surface Science* **2017**
212. Cushman, C. V.; Zakel, J.; Sturgell, B. S.; Major, G. I.; Lunt, B. M.; Brüner, P.; Grehl, T.; Smith, N. J.; Linford, M. R., Time-of-flight secondary ion mass spectrometry of wet and dry chemically treated display glass surfaces. *Journal of the American Ceramic Society* **2017,** *2017*, 1-15.
213. Zhang, F.; Gates, R. J.; Smentkowski, V. S.; Natarajan, S.; Gale, B. K.; Watt, R. K.; Asplund, M. C.; Linford, M. R., Direct adsorption and detection of proteins, including ferritin, onto microlens array patterned bioarrays. *Journal of the American Chemical Society* **2007,** *129* (30), 9252-+.
214. Tyler, B. J.; Rayal, G.; Castner, D. G., Multivariate Analysis Strategies for Processing ToF-SIMS Images of Biomaterials. *Biomaterials* **2007,** *28* (15), 2412-2423.
215. Lee, J. L. S.; Gilmore, I. S.; Fletcher, I. W.; Seah, M. P., Multivariate image analysis strategies for ToF-SIMS images with topography. *Surface and Interface Analysis* **2009,** *41* (8), 653-665.

216. Yang, L.; Lua, Y.-Y.; Jiang, G.; Tyler, B. J.; Linford, M. R., Multivariate Analysis of TOF-SIMS Spectra of Monolayers on Scribed Silicon. *Analytical Chemistry* **2005,** *77* (14), 4654-4661.
217. Pei, L.; Jiang, G.; Davis, R. C.; Shaver, J. M.; Smentkowski, V. S.; Asplund, M. C.; Linford, M. R., Laser activation-modification of semiconductor surfaces (LAMSS) of 1-alkenes on silicon: A ToF-SIMS, chemometrics, and AFM analysis. *Applied Surface Science* **2007,** *253* (12), 5375-5386.
218. Crist, V., Advanced Peak-Fitting of Monochromatic XPS Spectra. *Surface Analysis* **1998,** *4*, 428-434.
219. Madaan, N.; Diwan, A.; Linford, M. R., Fluorine plasma treatment of bare and nitrilotris(methylene)triphosphonic acid (NP) protected aluminum: an XPS and ToF-SIMS study. *Surface and Interface Analysis* **2015,** *47* (1), 56-62.
220. Sherwood, P. M. A., Curve fitting in surface analysis and the effect of background inclusion in the fitting process. *Journal of Vacuum Science & Technology A: Vacuum, Surfaces, and Films* **1996,** *14* (3), 1424-1432.
221. Singh, B.; Velazquez, D.; Terry, J.; Linford, M. R., Comparison of the equivalent width, the autocorrelation width, and the variance as figures of merit for XPS narrow scans. *Journal of Electron Spectroscopy and Related Phenomena* **2014,** *197*, 112-117.
222. Singh, B.; Velazquez, D.; Terry, J.; Linford, M. R., The equivalent width as a figure of merit for XPS narrow scans. *Journal of Electron Spectroscopy and Related Phenomena* **2014,** *197*, 56-63.
223. Zhang, G.; Sun, S.; Yang, D.; Dodelet, J.-P.; Sacher, E., The surface analytical characterization of carbon fibers functionalized by H2SO4/HNO3 treatment. *Carbon* **2008,** *46* (2), 196-205.
224. Okpalugo, T. I. T.; Papakonstantinou, P.; Murphy, H.; McLaughlin, J.; Brown, N. M. D., High resolution XPS characterization of chemical functionalised MWCNTs and SWCNTs. *Carbon* **2005,** *43* (1), 153-161.
225. Singh, B.; M.R., L., An Introduction to the Equivalent Width and the Autocorrelation Width. . *Vacuum Coating & Technology* October, 2015.
226. Crist, B. V., Advanced Peak-Fitting of Monochromatic XPS Spectra. *Journal of Surface Analysis* **1998,** *4* (3), 428-433.
227. Aronniemi, M.; Sainio, J.; Lahtinen, J., Chemical state quantification of iron and chromium oxides using XPS: the effect of the background subtraction method. *Surface Science* **2005,** *578* (1), 108-123.
228. Singh, B.; Hesse, R.; Linford, M. R., Good Practices for XPS (and other Types of) Peak Fitting. Use Chi Squared, Use the Abbe Criterion, Show the Sum of Fit Components, Show the (Normalized) Residuals, Choose an Appropriate Background, Estimate Fit Parameter Uncertainties, Limit the Number of Fit Parameters, Use Information from Other Techniques, and Use Common Sense. *Vacuum Technology and Coating* December, 2015.
229. Singh, B.; Gomez, A., H.; Terry, J.; Linford, M., R. , Good Practices for XPS Peak Fitting, II' *Vacuum Technology & Coating* August 2016.
230. Hesse, R.; Chasse, T.; Streubel, P.; Szargan, R., Error estimation in peak-shape analysis of XPS core-level spectra using UNIFIT 2003: how significant are the results of peak fits? *Surface and Interface Analysis* **2004,** *36* (10), 1373-1383.
231. Hesse, R.; Chasse, T.; Szargan, R., Peak shape analysis of core level photoelectron spectra using UNIFIT for WINDOWS. *Fresenius Journal of Analytical Chemistry* **1999,** *365* (1-3), 48-54.

232. Hesse, R.; Streubel, P.; Szargan, R., Product or sum: comparative tests of Voigt, and product or sum of Gaussian and Lorentzian functions in the fitting of synthetic Voigt-based X-ray photoelectron spectra. *Surface and Interface Analysis* **2007,** *39* (5), 381-391.
233. Charles, C.; Leclerc, G.; Pireaux, J.-J.; Rasson, J.-P., Introduction to wavelet applications in surface spectroscopies. *Surface and Interface Analysis* **2004,** *36* (1), 49-60.
234. Charles, C.; Leclerc, G.; Louette, P.; Rasson, J.-P.; Pireaux, J.-J., Noise filtering and deconvolution of XPS data by wavelets and Fourier transform. *Surface and Interface Analysis* **2004,** *36* (1), 71-80.
235. Chatterjee, S.; Singh, B.; Diwan, A.; Lee, Z. R.; Engelhard, M. H.; Terry, J.; Tolley, H. D.; Gallagher, N. B.; Linford, M. R., A perspective on two chemometrics tools: PCA and MCR, and introduction of a new one: Pattern recognition entropy (PRE), as applied to XPS and ToF-SIMS depth profiles of organic and inorganic materials. *Applied Surface Science* **2018,** *433*, 994-1017.
236. Castle, J. E.; Chapman-Kpodo, H.; Proctor, A.; Salvi, A. M., Curve-fitting in XPS using extrinsic and intrinsic background structure. *Journal of Electron Spectroscopy and Related Phenomena* **2000,** *106* (1), 65-80.
237. Shirley, D. A., High-Resolution X-Ray Photoemission Spectrum of the Valence Bands of Gold. *Physical Review B* **1972,** *5* (12), 4709-4714.
238. Fairley, N. CasaXPS, http://www.casaxps.com/help_manual/manual_updates/peak_fitting_in_xps.pdf.
239. Huhtamäki, T.; Tian, X.; Korhonen, J. T.; Ras, R. H. A., Surface-wetting characterization using contact-angle measurements. *Nature Protocols* **2018,** *13* (7), 1521-1538.
240. Shi, Z.; Zhang, Y.; Liu, M.; Hanaor, D. A. H.; Gan, Y., Dynamic contact angle hysteresis in liquid bridges. *Colloids and Surfaces A: Physicochemical and Engineering Aspects* **2018,** *555*, 365-371.
241. Lodge, R. A.; Bhushan, B., Wetting properties of human hair by means of dynamic contact angle measurement. *Journal of Applied Polymer Science* **2006,** *102* (6), 5255-5265.
242. Nguyen, C. V.; Chao, K.-J.; Stevens, R. M. D.; Delzeit, L.; Cassell, A.; Han, J.; Meyyappan, M., Carbon nanotube tip probes: stability and lateral resolution in scanning probe microscopy and application to surface science in semiconductors. *Nanotechnology* **2001,** *12* (3), 363-367.
243. Saini, G.; Trenchevska, O.; Howell, L. J.; Boyd, J. G.; Smith, D. P.; Jain, V.; Linford, M. R., Performance Comparison of Three Chemical Vapor Deposited Aminosilanes in Peptide Synthesis: Effects of Silane on Peptide Stability and Purity. *Langmuir* **2018,** *34* (40), 11925-11932.

CHAPTER 2: Differences in Reactivity Between HiPIMS and DC Magnetron Sputtered Carbon for Bioarrays

2.1 Statement of Attribution

This Document is originally submitted as Varun Jain, Tuhin Roychowdhury, Robert G. Kuimelis, Matthew R. Linford. Differences in Reactivity between HiPIMS and DC Magnetron Sputtered Carbon for Bioarrays, *Vacuum Coating & technology*, **2019** (submitted)

2.2 Abstract

Stable substrates that allow covalent modification are useful in bioarrays. Diamond like carbon (DLC) is an amorphous form of carbon with a significant fraction of sp^3 bonds. In general, it enjoys high hardness, chemical inertness, and optical transparency. It can be deposited by various chemical (CVD) and physical (PVD) vapor deposition methods, including sputtering, which is an industrially important PVD method. DLC has previously been used as a substrate for bioarrays. Here we investigate carbon sputtered by conventional direct current magnetron sputtering (DCMS) and by the newer high power impulse magnetron sputtering (HiPIMS) as substrates for bioarrays. Scanning electron microscopy (SEM) showed that HiPIMS produced more compact and smoother (featureless) films. X-ray photoelectron spectroscopy (XPS) revealed chemical differences between the two types of carbon surfaces. Stability tests were performed on the carbon films. Two functionalization schemes were then investigated, each with a range of amines. The first consisted of amidation of the surface by activation with 1-ethyl-3-(3-dimethylaminopropyl) carbodiimide (EDC) and *N*-hydroxy sulfosuccinamide (sulfo-NHS), and the second consisted of activation via halogenation with PCl_5 or PBr_5 followed by subsequent amination. The resulting surfaces were characterized by SEM, X-ray photoelectron spectroscopy (XPS), atomic force microscopy (AFM), ellipsometry, and wetting. HiPIMS-deposited carbon showed higher levels of amidation. On the

other hand, the DCMS surface showed greater functionalization in the halogenation/amination route. These results are consistent with the higher level of oxidized carbon on the HiPIMS surface.

Key Words: Sputtering, carbon, bioarray, magnetron, HiPIMS, DCMS

2.3 Introduction

Effective and early diagnostics through the detection of biological events and species plays an important role in the clinical treatment of various diseases.[1-8] Therefore, there is a need for advanced platforms that are selective, sensitive, cost-effective, easy to miniaturize and fabricate, and provide high throughput and speed.[6-7, 9] Electrochemical and optical bioarrays are examples of platforms that can provide point-of-care treatment, e.g., for sepsis.[9-10] These biosensors can be applied to large numbers and types of samples including various body fluids, food samples, cell cultures, and environmental samples.[7-8, 11]

Bioarrays are planar substrates that allow biomolecule attachment and detection in a massively parallel fashion.[12] The fabrication of bioarrays involves (i) a substrate onto which biomolecules are attached, i.e. the interface, (ii) biomolecules of interest, and (iii) a functionalization chemistry for immobilizing the biomolecules onto the substrate.[7, 12] This area of research has seen much activity since the introduction of the first high-density peptide arrays (bioarrays) in the early 1990s.[7-8, 12,] Since then, array technology has expanded to include oligonucleotides, carbohydrates, proteins like lectins and antibodies, and even cell lysates.[12] The Southern blot is one of the oldest examples of a quantitative DNA detection method.[12-13] Other traditional assays, which have the disadvantages of being time-consuming, expensive, and requiring highly trained operators, include enzyme-linked immunosorbent assays[7, 14] and radioimmunoassays.[15]

Historically, many, if not most, bioarrays have involved glass or gold with their respective silane- or thiol-based attachment chemistries. However, the stabilities of these materials are questionable at elevated temperatures, at pH values greater than 10, and in some cases to organic solvents and even to air.[16-18] This has limited the development of the resulting integrated biosensors; the degradation of interface materials in bioarrays has been an issue for many years, Hence, there is a need for chemically stable surfaces in bioarrays. Accordingly, there has been an interest in group IV materials as substrates,[19-21] as well as robust attachment chemistries on other materials.[22] By virtue of their biocompatibility, and also their semiconducting, electrical, chemical, and mechanical properties,[23-24] various carbon-based materials, e.g., carbon nanotubes, carbon quantum-dots, graphene (sp^2), and diamond (sp^3), have also been investigated as substrates for bioarrays.[7, 12, 25-27] In particular, because of its high mechanical hardness, inertness, and versatility for attachment of biomolecules by direct covalent bond formation,[12] diamond is arguably a better candidate for bioarrays than glass, silicon, or gold.[12, 25, 28-31] However, diamond materials and films can be challenging to create/deposit. Diamond-like carbon (DLC) is a non-crystalline, amorphous form of carbon that contains a high degree of sp^3 character.[32] DLC shows good chemical inertness, resistance to air oxidation, mechanical hardness, semiconducting properties, and biocompatibility,[25, 30-31] It can be deposited as a thin film by both physical (PVD) and chemical vapor (CVD) deposition at room temperature.[22, 30, 33-34] and it can be reproducibly immobilized with biomolecules through stable carbon-carbon covalent bonds.[12, 28-29] These attributes make DLC a good choice as an interface for the construction of biosensors.

PVD techniques that have been used to deposit DLC include cathodic arc deposition, ion (and ion-assisted) deposition methods, plasma deposition, pulsed laser deposition, and sputtering.[25] Of these, sputtering is the most commonly used industrial process for the deposition

of DLC**.** Because sputtering is relatively inexpensive and can be scaled up, it is a method of choice industrially. The deposition rate in sputtering can be controlled by the plasma power, gas pressure, and, most importantly, the deposition time. Sputtering is mostly independent of the condition and geometry of the substrate.[30, 35] The most common forms of sputtering use direct current (DC) or radio frequency (RF) power supplies to sputter carbon under an Ar plasma. In magnetron sputtering (MS), magnets are placed behind the cathode to increase the path lengths of the electrons, increasing the degree of ionization of the plasma.[30] Sputtering can also be performed by HiPIMS (high power impulse magnetron sputtering), which is a newer technique. HiPIMS is a pulsed magnetron sputtering method in which the peak power typically exceeds the time-averaged power by two orders of magnitude".[36-38] HiPIMS imparts a high power density in the range of few kilowatts/cm^2 while maintaining the time-averaged power to watts/cm^2 to protect the target.[39] HiPIMS combines normal magnetron sputtering with a pulsed plasma. This generates a highly ionized plasma and consequently, a high number of ionized, sputtered atoms,[40] which facilitates reactively deposited material, smoother films, and greater film density.[41, 42] Thus, HiPIMS allows control of film phase composition, microstructure, morphology, and mechanical properties**.**[42] HiPIMS has been used to improve the adhesion of deposited films, which in turn makes possible the deposition of uniforms films on complex shapes. HiPIMS allows lower temperature depositions. However, HiPIMS has the disadvantage of a lower deposition rate.[35] Both DCMS and HiPIMS carbon films are substrates that deserve exploration for the covalent attachment of biomolecules.

Covalent functionalization provides an important way of altering the chemical, physical, and electronic properties of surfaces, e.g., in bioarrays.[43-44] The chemical modification of a substrate is often necessary to achieve the desired orientation and association of biomolecules.[45-

[46] Covalent attachment of biomolecules is especially important where applications require long incubation times, repeated washing, and/or exposure to harsh chemical environments. A number of covalent functionalization chemistries have been developed for carbon-based materials. These have been based on peroxide radical initiators,[33, 47] gas-phase halogenation,[48-50] electrochemical reduction of diazonium salts,[51-52] the UV-assisted and thermal attachment of alkenes,[10, 53-56] and the attachment of primary and secondary amines through electrochemical oxidation.[57] Amidation or esterification of single-walled carbon nanotubes has been demonstrated via both acid chlorides and carbodiimide activation.[58] Solution-based chlorination and bromination activates carbon-based substrates without the need for gas-phase or ultrahigh vacuum methods.[49, 59-62] The oxidation state of a carbon substrate, e.g., (i) hydrocarbon (C-C), (ii) ether (C-O), (iii) carbonyl (C=O), and (iv) carboxyl (O=C-O), determines its reactivity with other organic molecules.[10, 28, 62-67]

The purpose of this study is to compare DCMS and HiPIMS sputtered carbon films as substrates for bioarrays. We first evaluated the stability of these carbon layers under conditions that mimic the polymerase chain reaction (PCR). Two schemes were then employed to functionalize these surfaces with amines, which should lead to stable, covalent attachment of these reagents: amidation of the carboxyl moieties (O=C-O) on the carbon surfaces through an activating agent (**Figure 2.1**, left), and (ii) halogenation of the hydrogenated/hydrocarbon (CH-CH/C-C) moieties on the surfaces, or other groups that might react under the conditions explored, followed by amination of the halogenated surfaces (**Figure 2.1**, right). These functionalizations were followed by X-ray photoelectron spectroscopy (XPS) and wetting. The conclusions drawn from these studies suggest that there are both structural and chemical differences between HiPIMS and DCMS sputtered carbon. Structurally, HiPIMS carbon is somewhat smoother than DCMS carbon, and it can be functionalized to a greater degree via our activation/amidation approach, which

suggests that it has more carboxyl groups on it. Indeed, XPS shows that the atom % oxygen and amount of chemically shifted (carboxyl) carbon are higher on the HiPIMS surfaces. In contrast, DCMS carbon shows a greater degree of halogenation and consequently amination, which suggests it possesses more C-H type moieties. This latter observation is consistent with the more reduced state of the DCMS carbon that is suggested by XPS. Both surfaces show a higher degree of chemisorption than non-specific adsorption.

2.4 Materials and Methods

2.4.1 Reagents

2.4.1.1 Stability Testing

Stability testing was done in a commercial Tris buffer 10X (pH 8.4) (Fisher Scientific, Hampton, USA).

2.4.1.2. Activation/Amidation

All of the water-soluble amines (ethanolamine (EA), diethylenetriamine (DETA), polyallylamine (PAM), branched polyethyleneamine (PEI), and poly(diallyldimethyl)ammonium chloride (PAC)), and water-insoluble amines (octadecylamine (ODA), benzylamine (BA), 4-methoxybenzylamine (MBA), and 2,2,3,3,4,4,4-heptafluorobutylamine (HFA)) and coupling agents (1-ethyl-3-(3-dimethylaminopropyl) carbodiimide (EDC) and *N*-hydroxy sulfosuccinamide (sulfo-NHS)) were purchased from Sigma Aldrich (St. Louis, MO), except for EA and sulfo-NHS, which were obtained from Alfa Aeser (Haverhill, MA). Deionized (DI) water and chloroform (Fisher Chemicals, Hampton, USA) were used as solvents to dissolve the water-soluble and water-insoluble amines, respectively. Concentrated HCl was obtained from Fisher Scientific. (Hampton, USA). (See figure 2.2 for structures of amines and coupling agents)

2.4.1.3 Halogenation/Amination

Phosphorus pentachloride (PCl_5), phosphorus pentabromide (PBr_5), and dibenzoyl peroxide were obtained from Sigma Aldrich. Solvents used for this functionalization included benzene (EMD Millipore Corporation, Burlington, USA), deionized water (house source, 18 MΩ), and dimethyl sulfoxide (DMSO) (Sigma Aldrich).

2.4.2 Methods

2.4.2.1 Substrate Preparation

Carbon was magnetron sputtered in DC and HiPIMS modes on native oxide-terminated 4″ Si(100)/SiO_2 wafers in a PVD-75 system from the Kurt J. Lesker Company (Jefferson Hills, PA, USA). The sputtering time was 4 h, the working pressure was 7 mTorr, and the base pressure was $2.3x10^{-2}$ mTorr. For the DC mode the power was 400 W, and for HiPIMS it was 125 W.

2.4.2.2 Stability Testing of the Carbon Films

We evaluated the stability of sputtered carbon under conditions relevant to the polymerase chain reaction (PCR). Here, we immersed 1” x 1” pieces of carbon-coated silicon in heated water and Tris buffer at different temperatures and for different amounts of time. (see Table 2.1)

Table 2.1. Conditions used in the stability studies reported in this work.

Solvent	Temperature	Time(s)
Water	55 °C	0 - 4 h
	95 °C	0 - 4 h
Tris Buffer (pH – 8.4)	55 °C	0 - 4 h
	95 °C	0 - 4 h

2.4.2.3 Functionalization of DCMS and HiPIMS Carbon Surfaces

Activation/Amidation

Pieces of carbon-coated silicon (ca. 1" x 1" in^2) were first activated with a solution of 0.1 M EDC and 0.05 M sulfo-NHS in water for 10 min and then dried with a jet of nitrogen, after which they were immersed in a 0.1 M solution of an amine in water or $CHCl_3$ for 2 h. Control experiments were performed in the same manner, except without the EDC/sulfo-NHS activation. For the samples treated with the water-soluble amines, work up was performed by sonication in DI water containing a few drops of HCl (conc.). For the samples treated with the water-insoluble amines, work up was performed by sonication in $CHCl_3$, which also contained a few drops of HCl (conc.). Finally, the samples were washed with their respective solvents (water or chloroform), dried with a jet of nitrogen gas, and stored under vacuum to limit contamination prior to characterization.

Halogenation/Amination

Pieces of silicon (1" x 1") sputtered with carbon were first placed in 100 mM PCl_5 (for the chlorination reaction) or 100 mM PBr_5 (for the bromination reaction) in anhydrous benzene with a catalytic amount of benzoyl peroxide (15 mg). The reaction vessels were then purged with nitrogen, sealed, and incubated at 80° for 2 h (bromination) or 100° for 1 h (chlorination). After this literature-based approach,[29] the substrates were rinsed with benzene, followed by ethanol, and then dried under a stream of nitrogen. In our work, there were a few modifications to this previously reported protocol: (i) the earlier study described the modification of carbon-coated gold on glass, (ii) prior to halogenation, the sputtered carbon surface was not treated with a hydrogen plasma, and (iii) no amination was performed in the previous work. For amination, samples were treated with a 0.1 M solution of the amines in dimethylsulfoxide (DMSO). The work-up after

amination was done by sonicating the samples in DMSO with few added drops of HCl (conc.). Finally, the samples were rinsed with DI water. They were then dried with a jet of nitrogen and stored under vacuum to limit contamination prior to characterization.

2.4.2.4 Surface Characterization

Surfaces were characterized by X-ray photoelectron spectroscopy (SSX-100, Service Physics Inc., Bend, OR, USA) in a high vacuum system ($P < 5 \times 10^{-8}$ Torr) equipped with a load-lock for sample introduction, a monochromatized Al Kα source (1486.6 eV), and a hemispherical analyzer with a multichannel detector. The (nominal) pass energy was 100 eV. Sputtered, thin carbon films were imaged using scanning electron microscopy (SEM) (FEI Helios NanoLabTM 600 DualBeam (FIB/SEM), ThermoFisher Scientific, Waltham, MA, USA). Advancing water contact angles ($\theta_a(H_2O)$) were measured using a water contact angle goniometer (Model No. 100-00, ramé-hart, Mountain Lakes, NJ, USA). Atomic force microscopy (AFM) (Model No. Dimension^{TM} 3100, Digital Instruments, Santa Barbara, CA, USA) step height measurements performed in tapping mode were used to determine film thicknesses. As described previously, to create a step for the film thickness measurements, we drew a line with a felt pen, deposited a film around and over it, and finally rinsed away the mark from the pen (and the film above it) with an organic solvent.[68] AFM was also used to measure surface roughness.

Standard deviations shown in all the figures (2.5 to 2.8) in this chapter were calculated from measurements on three or more samples of each type of surface.

2.5 Results and Discussion

2.5.1 Characterization of DCMS and HiPIMS Sputtered Carbon

Carbon films were sputtered per the instrument parameters listed in Table 2.2. These conditions consistently yielded moderately thick films of 140 ± 10 nm (DCMS) and 120 ± 10 nm (HiPIMS), as determined by atomic force microscopy (AFM) step height measurements. Both types of surfaces were quite smooth by AFM: 1.53 ± 0.27 nm (DCMS) and 1.20 ± 0.55 nm (HiPIMS), as measured over 10 x 10 μm^2 areas (each of these AFM values is the result of 12 measurements: three different spots analyzed on four different sputtered surfaces). Scanning electron microscopy (SEM) images (3 μm x 3 μm) of both types of carbon surfaces were essentially featureless. (See Supporting Information Figure A 1.1 for AFM and SEM images.)

Table 2.2. Parameters used for deposition of films and their thickness.

Type of Carbon	Sputtering Time (h)	Power (W)	Pressure (mTorr)	Thickness (nm)
DCMS	4	400	7	130 - 150
HiPIMS	4	125	7	110 - 130

Wetting measurements reflect surface chemistry. Clean, bare Si(100)/SiO_2 has high hydrophilicity, i.e., a low advancing water contact angle: $\Theta_a(H_2O)$ <10º. Both types of sputtered carbon had higher water contact angles, where the water contact angle of HiPIMS carbon (43.15 ± 3.07) was a little less than that of the DCMS carbon (49.35 ± 3.22). XPS was also used to characterize the carbon surfaces. As shown in Figure 3, the survey spectra[69-70] of both forms of

carbon are dominated by C 1s (largest), O 1s (moderate), and O KLL Auger (smaller) signals. Dividing the C 1s and O 1s peak areas from the survey spectra by the instrument sensitivity factors and normalizing gave the percent carbon and oxygen values listed in Table 2.3. Of course these measurements assume that the elements are uniformly distributed with depth into the sample, which may not be the case here. That is, the outermost surface of the sample may be more oxidized than the bulk – any carbon radicals (dangling bonds) left at the surface at the end of the deposition would be expected to react with oxygen in the chamber or in the air. In any case, Table 2.3 suggests that the HiPIMS surface is significantly enriched in oxygen compared to the DCMS carbon surface. The wetting results noted above are also consistent with the HiPIMS surfaces having greater oxygen content than the DCMS carbon surface. As will be demonstrated below, this difference in oxygen content appears to control and define the reactivities of these sputtered surfaces. The trace F 1s, Si 2s, and Si 2p signals in the survey spectra in Figure 2.3 are attributed to small amounts of surface contamination.

Table 2.3. Atomic compositions and ratios of O 1s/C 1s for HiPIMS and DCMS carbon, as obtained from the respective XPS survey scans. The averages and standard deviations (for Carbon % and Oxygen %) in this table were obtained from more than 10 different sputtered HiPIMS surfaces and 10 different sputtered DCMS surfaces.

Type of Carbon	O 1s/C 1s	Carbon %	Oxygen %
HiPIMS	0.23 ± 0.01	81.27 ± 1.0	18.73 ± 1.0
DCMS	0.122 ± 0.002	89.1 ± 0.2	10.9 ± 0.2

The C 1s narrow scans from HiPIMS and DCMS carbon (Figure 2.4) were visually inspected prior to any peak fitting. It was immediately obvious here that the HiPIMS C 1s narrow scan has a larger shoulder/area at higher binding energy than the DCMS carbon surface, which is

consistent with the carbon on the HiPIMS surface being, in general, in a higher oxidation state. (Note that the shoulder on the HiPIMS C 1s signal is not present in the corresponding O 1s signal, suggesting that the shape of this C 1s narrow scan is the result of chemical effects and not differential charging.) Peak fitting of the C 1s narrow scans of the HiPIMS and DCMS carbon surfaces provided additional evidence for the more oxidized nature of the HiPIMS surface. For these fits, Shirley backgrounds were originally chosen because of the 'steps' in the backgrounds and also because of the expected, moderately conducting nature of the materials (the carbon samples were expected to have some sp^2 character).[71] Reasonable fits were then obtained using Gaussian-Lorentzian product (GLP) functions with 30% Lorentzian character (note that the GLP line shape is quite similar to a pure Gaussian line shape).[72] The degree of Lorentzian character in the peaks was chosen by setting it at 0%, 10%, 20%, 30%, …, where 30% gave the best fit to the peak envelopes. The position of the lowest energy (aliphatic, C-C/C-H, C(0)) component was allowed to vary, but the positions of the higher energy peaks were constrained, per literature precedent,[73-74]] to be at +1.5 eV, e.g., alcoholic carbon (C(I)), +3.0 eV, e.g., carbonyl carbon (C(II)), and +4.5 eV, e.g., carboxyl carbon (C(III)), relative to this signal. While some asymmetry, both for sample and instrumental reasons, would be expected, it was ignored. The widths of the peaks in each fit were constrained to have the same value, but this value was not fixed. The resulting best fits to these narrow scans gave peak widths of 2.05 and 2.01 eV (nearly the same value) for the HiPIMS and DCMS carbon, respectively. The fitted narrow scans in Figure 2.4 clearly indicate a substantially higher amount of carboxyl carbon in the HiPIMS carbon (6.0 % vs. 1.1 % in the DCMS carbon) and a much large fraction of aliphatic carbon in the DCMS carbon (80.9 % vs. 62.3 % for the HiPIMS carbon). However, when we calculated the amount of oxygen that would correspond to the oxidized carbon predicted in the fits, the predicted amount of oxygen

exceeded the amounts derived from the survey scan in Table 2.3. (In these calculations and also those that follow, we assumed half of the carbon was due to C-OH and half to C-O-C in the first oxidation state of carbon, C(I), which gave an O:C ratio of 2:3, we assumed a 1:1 O:C ratio for the second oxidation state (C(II)) of carbon, and for the third oxidation state (C(III)) we assumed a 2:1 O:C ratio.

A second attempt involving Tougaard backgrounds and asymmetric Lorentzian line shapes (LA line shapes) with the same widths in each fit was then made to peak fit the HiPIMS and DCMS C 1s narrow scans.[75-76] In this approach, it was possible to adjust the two exponents in the generalized Lorentzian (LA) line shape until the predicted and experimental amounts of oxygen for the HiPIMS and DCMS carbon samples were in reasonable agreement. The resulting fits are shown in Figure 2.4 Note that the exponents for the LA line shape used to fit the DCMS carbon are larger than those for the line shape used to model the HiPIMS carbon, which gives the line shape for the HiPIMS carbon greater tailing. This result is consistent with greater conductivity for the HiPIMS carbon. Ultimately, these fits suggested that there is approximately twice as much carboxyl carbon on the HiPIMS carbon surface compared to the DCMS carbon surface.

2.5.2 Stability of the Sputtered Carbon Surfaces

The stability of DCMS and HiPIMS sputtered carbon surfaces was monitored by XPS and wetting after immersion in 55 °C and 95 °C water and 55 °C and 95 °C Tris butter. Figure 2.5 shows the areas of the C 1s, O 1s, and Si 2p peaks, and water contact angle, for DCMS and HiPIMS carbon surfaces after immersion in 95 °C Tris buffer for 0 - 4 h. These results suggest that the sputtered carbon enjoys quite good stability (see Supporting Information Figures A 1.2 – 1.4 for the results of the other stability tests).

2.5.3 Functionalization of HiPIMS and DCMS Surfaces

Functionalization of HiPIMS and DCMS carbon surfaces was explored in two ways we designate as: (i) activation/amidation and (ii) halogenation/amination (see **Figure 2.1**). Each step in these synthetic processes was followed by XPS and wetting. In both cases, control experiments were performed, i.e., attempts to react the surfaces with amines without prior surface activation.

2.5.3.1 Carbon Functionalization by Activation/Amidation

Carboxyl groups on DCMS and HiPIMS carbon surfaces were activated with EDC and sulfo-NHS under conditions that were expected to create reactive (sulfo-NHS) esters. These activated surfaces were then treated with amines to form amides.[77] Control experiments to determine the degree of non-specific adsorption were also performed in which unactivated surfaces (blank samples) were directly exposed to the amines.

Reactivity of DCMS and HiPIMS Carbon to Activation/Amidation

Amidation of DCMS and HiPIMS carbon was undertaken by activating carboxyl groups on these surfaces with EDC and sulfo-NHS. Since the fraction of oxygenated carbon atoms and carboxyl groups (see Figures 2.3 and 2.4, and Table 2.3) was higher for the HiPIMS carbon, it was expected that the degree of functionalization would be greater for the HiPIMS carbon in the activation/amidation approach (it was). Figure 2.6 shows the XPS and wetting characterization of the surfaces after the reactions between EDC/sulfo-NHS-activated DCMS and HiPIMS carbon for a series of different amines. The following trends are observed:

i. As expected, the HiPIMS carbon consistently shows a greater degree of functionalization with the amines than the DCMS carbon (compare the red bars in Figure 2.6, panels a and b).

ii. The degree of functionalization (amidation) is consistently greater on the EDC/sulfo-NHS-activated surfaces (red bars) than on the non-activated surfaces (green bars, no EDC/sulfo-NHS activation). The only exception here is for the PAC, which is a polymer containing quaternary amines. Here, the red and green bars corresponding to the activated and non-activated surfaces are essentially the same to within experimental error. These results are consistent with the fact that the quaternary amine should not be able to react with either type of surface. (See Figure 2.6, panels a and b.)

iii. The polymers with reactive functional groups (PAM and PEI have primary amines) react to a much greater extent than the PAC (see previous comment), which is consistent with the fact that they bring a larger number of reactive groups to the surface. (See Figure 2.6, panels a and b.)

iv. The amount of fluorine is higher on the HiPIMS carbon surface than the DCMS surface after the reaction with the fluorinated amine (HFA). (See Figure 2.6, panels a and b.)

v. The water-soluble reagents consistently react to a greater extent than the water-insoluble reagents on both types of carbon surfaces. Non-specific adsorption is also greater for the water-soluble reagents, which may be related to the fact that they have more polar groups and may therefore interact more strongly with the surfaces. (See Figure 2.6, panels a and b.)

vi. In general, after the reactions with the amines, the differences in wetting, θa(H2O) values, between the activated and non-activated surfaces are not large (10° or less). (See Figure 2.6, panels c and d.)

vii. For the activated surfaces, the θa(H2O) values are higher for the water-insoluble amines (this seems reasonable – they are non-polar), while the θa(H2O) values are lower for the

water-soluble amines (this also seems reasonable – they are polar). (See Figure 2.6, panels c and d.)

These observations and results are consistent with a higher density of carboxyl groups available at the HiPIMS surface for activation with EDC/sulfo-NHS and subsequent reaction with amines.

2.5.3.2 Carbon Functionalization by Halogenation/Amination

DCMS and HiPIMS carbon surfaces were activated via halogenation.[29] These surfaces were then reacted, presumably through nucleophilic displacement chemistry, with various water-soluble and water-insoluble amines. Control experiments to determine the degree of non-specific adsorption were also performed in which unactivated surfaces were exposed directly to the amines.

Halogenation (Chlorination and Bromination) of DCMS and HiPIMS Carbon

The chlorination and bromination of DCMS and HiPIMS carbon was followed by XPS and contact angle goniometry. From Figure 2.7, we observe that:

i. There is no Cl or Br by XPS prior to halogenation.

ii. Noticeable amounts of Cl and Br are present after halogenation.

iii. The degree of halogenation with both Cl and Br is greater on the DCMS carbon than the HiPIMS carbon.

iv. The water contact angles of both types of carbon surfaces increase after both bromination and chlorination. The $\theta_a(H_2O)$ values for the DCMS carbon are a little larger than those for the HiPIMS carbon. However, this may simply be a reflection of the somewhat larger value of $\theta_a(H_2O)$ on the unfunctionalized DCMS surface.

v. The chlorinated surface is a little more hydrophobic than the brominated surface. However, this is not exactly a fair comparison because the degree of halogenation is also higher on the chlorinated surface.

These results suggest that the expected chlorination and bromination occur on both types of sputtered carbon surfaces.

Reactivity of DCMS and HiPIMS Carbon in Halogenation/Amination

As previously noted, DCMS and HiPIMS carbon surfaces could be halogenated (chlorinated or brominated). Both types of surfaces were then reacted with amines. The appearance of N 1s XPS signals on the resulting surfaces indicated that both the chlorinated and the brominated surfaces reacted with amines, presumably via a nucleophilic displacement of the halogen. However, a greater degree of amination was observed on the chlorinated surfaces. This outcome appears to be due, at least in part, to the higher amount of chlorination obtained on the DCMS and HiPIMS carbon surfaces. Nevertheless, we now focus on the reactivity of chlorinated DCMS and HiPIMS carbon. The results of these reactions are summarized in Figure 8 from which we make the following observations.

i. The atom % chlorine on the surfaces goes down after all the reactions between the chlorinated carbon surfaces and the amines, which suggests that the expected reactions are occurring. In general, this decrease in chlorine concentration is greater for the water-soluble amines and in particular for the water-soluble primary amine-containing polymers (PAM and PEI). This latter result is consistent with the large numbers of reactive primary amines in these reagents. (See Figure 2.8, panels a and b.)

ii. More nitrogen is consistently deposited onto the DCMS carbon surface than the HiPIMS surface. This observation is, again, consistent with the lower concentration of oxygen on the DCMS carbon surface (see Figures 2.4 and 2.8).

iii. The decrease in chlorine concentration on the carbon surfaces is smallest for the PAC polymer. As previously noted, PAC is a quaternary amine and therefore not able to act as

a nucleophile. The decrease in chlorine concentration is also relatively small for the octadecylamine (ODA) reaction. This latter result may be due to the fact that ODA is a relatively large reagent that blocks surface sites, i.e., limits surface reactivity. (See Figure 2.8, panels a and b.)

iv. After the reaction with the fluorinated amine (HFA), the amount of fluorine is higher on the DCMS carbon than the HiPIMS surface. Also, the amount of fluorine is greater on the activated surfaces than the unactivated ones, which is again consistent with the fact that a reaction is occurring on the activated surfaces and only non-specific adsorption taking place on the unactivated ones. (See Figure 2.8, panels a and b.)

v. After reactions of the chlorinated DCMS and HiPIMS carbon surfaces with the water-insoluble amines, the $\theta_a(H_2O)$ values for the surfaces stay roughly constant in a way that is consistent with the chemistry of the amine adsorbate. For example, the reaction with methoxybenzylamine (MBA), which has a polar methoxy group at the top of the molecule, leads to a small decrease in the $\theta_a(H_2O)$ value, while the reaction with octadecylamine (ODA) leads to a small increase in it. It may come as a surprise that the reaction of heptafluorobutylamine (HFA) with the chlorinated surfaces leads to a decrease in the $\theta_a(H_2O)$ value of the surface. It appears here that the hydrophobicity that is no doubt introduced by the short (three-carbon) perfluorinated chain in the molecule is counterbalanced by the introduction of an amine group at the surface, which is capable of hydrogen bonding. (See Figure 2.8, panels c and d.)

vi. Increases in the $\theta_a(H_2O)$ values are observed after the control reactions of the bare (unchlorinated) carbon surfaces with the water-insoluble amines. These results suggest some degree on non-specific adsorption of the non-polar reagents to the carbon surfaces.

The water contact angles of these surfaces are smaller than those of the chlorinated surfaces that reacted with the water-insoluble amines. (See Figure 2.8, panels c and d.)

vii. After reactions of the chlorinated DCMS and HiPIMS carbon surfaces with the water-soluble amines, the $\theta_a(H_2O)$ values for the surfaces decrease in a way that is consistent with the chemisorption of polar molecules. (See Figure 2.8, panels c and d.)

viii. Decreases in the $\theta_a(H_2O)$ values are also observed after the control reactions of the bare (unchlorinated) carbon surfaces with the water-insoluble amines. These water contact angle values are lower than those from the reactions with the chlorinated surfaces. However, the $\theta_a(H_2O)$ values of the bare chlorinated surfaces are also quite a bit higher than the contact angles of the bare carbon surfaces. (See Figure 2.8, panels c and d.)

2.6 Conclusions

Two types of sputtered carbon surfaces (deposited by DCMS and HiPIMS sputtering) were compared vis-à-vis amine functionalization with two different synthetic routes. The carbon surfaces were first characterized by XPS and wetting. XPS showed a clear difference in the amount of oxygen at these surfaces, with the HiPIMS surfaces being the more oxidized of the two. The general shapes of the C 1s narrow scans, along with peak fitting of them, suggested that the fraction of carboxyl groups on the HiPIMS surfaces was greater than the fraction on the DCMS surface. Both types of carbon surfaces showed good stability in a hot buffer. The first amine-coupling chemistry studied in this work consisted of surface activation by EDC/sulfo-NHS to create active esters followed by the direct reaction with a series of amines. Both small molecule and polymeric amines were explored. As expected, the degree of surface functionalization was greater on the HiPIMS surface. The second coupling chemistry consisted of surface halogenation followed by a reaction with an amine. Primary amine containing polymers reacted very effectively with the

activated surfaces. There was little difference between the activated and unactivated surfaces in their interactions with a quaternary amine-containing polymer. The other control reactions also showed some non-specific adsorption to the surfaces. Overall, these results suggest ways for controlling the chemisorption of amines to different types of sputtered carbon surfaces. The resulting surfaces are expected to serve as a good starting point for electrochemical sensors and/or bioarrays.

2.7 Acknowledgements

We acknowledge the Department of Chemistry and Biochemistry and College of Physical and Mathematical Sciences at Brigham Young University for their support of this work.

2.8 Funding

We thank InSilixa Inc. (Sunnyvale, CA, USA) for their generous support of this work.

2.9 Figures

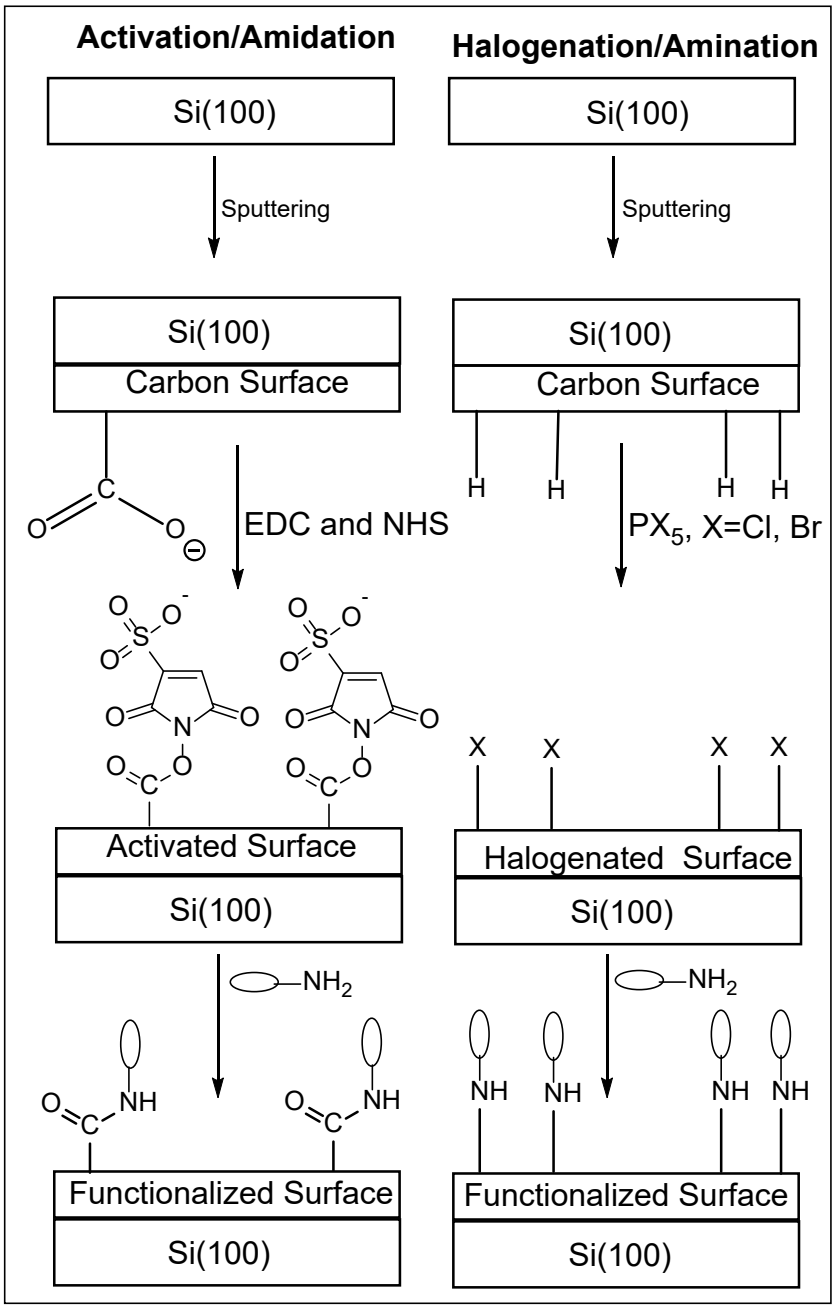

Figure 2.1. Representation of the functionalization strategies employed in this work: activation/amidation route (left), halogenation/amination route (right).

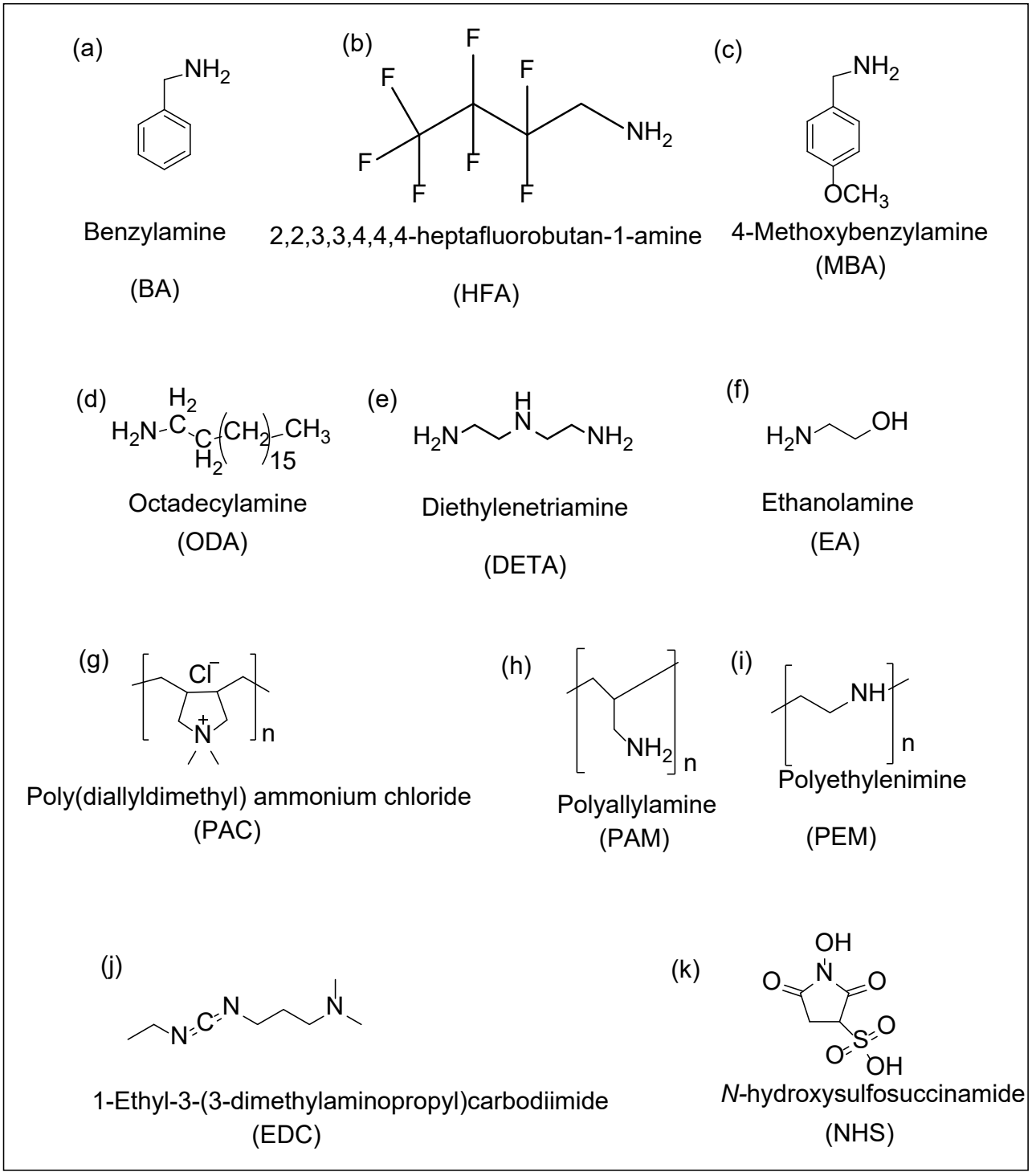

Figure 2.2. Amine adsorbates used for activation/amidation and halogenation/amination. Coupling agents used for activation before amidation in activation/amidation route.

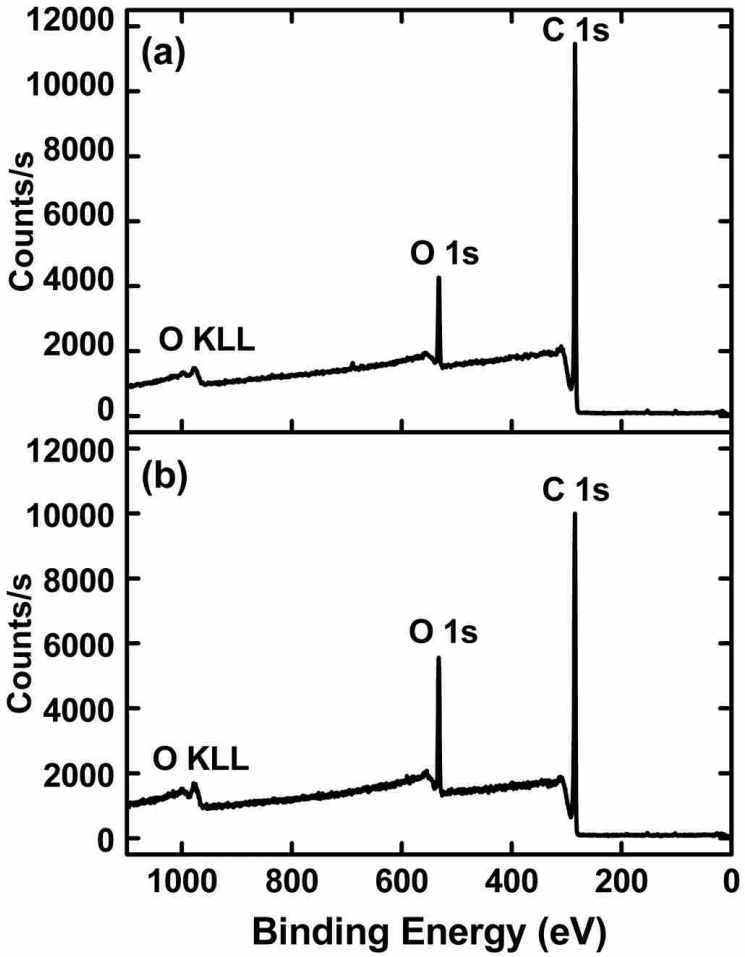

Figure 2.3. XPS survey scans of (a) DCMS and (b) HiPIMS sputtered carbon.

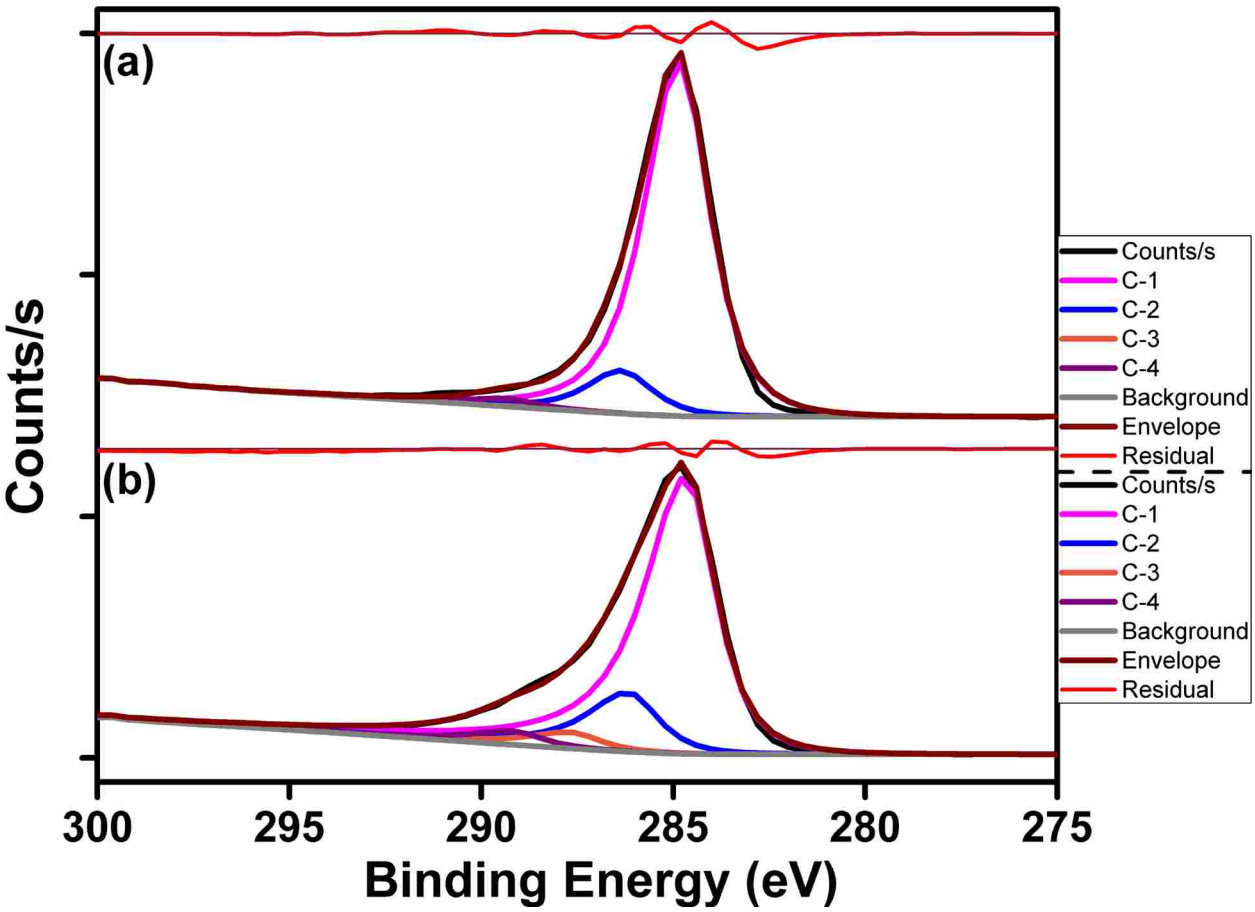

Figure 2.4. Peak fitting of C 1s narrow scans. (a) DCMS carbon as fit with LA(1.6,2.0,0) line shapes of FWHM 1.87 eV, and (b) HiPIMS carbon as fit with LA(1.0,1.2,0) synthetic line shapes of FWHM 1.82 eV. The first and second parameters in the LA line shape are the exponents of the Lorentzian function on the high and low binding energy side of the peak, respectively. The third parameter is a measure of the width of the Gaussian with which the generalized Lorentzian is convolved – because this parameter is zero here, there was no convolution with a Gaussian in these line shapes, which would have created a Voigt-type line shape.

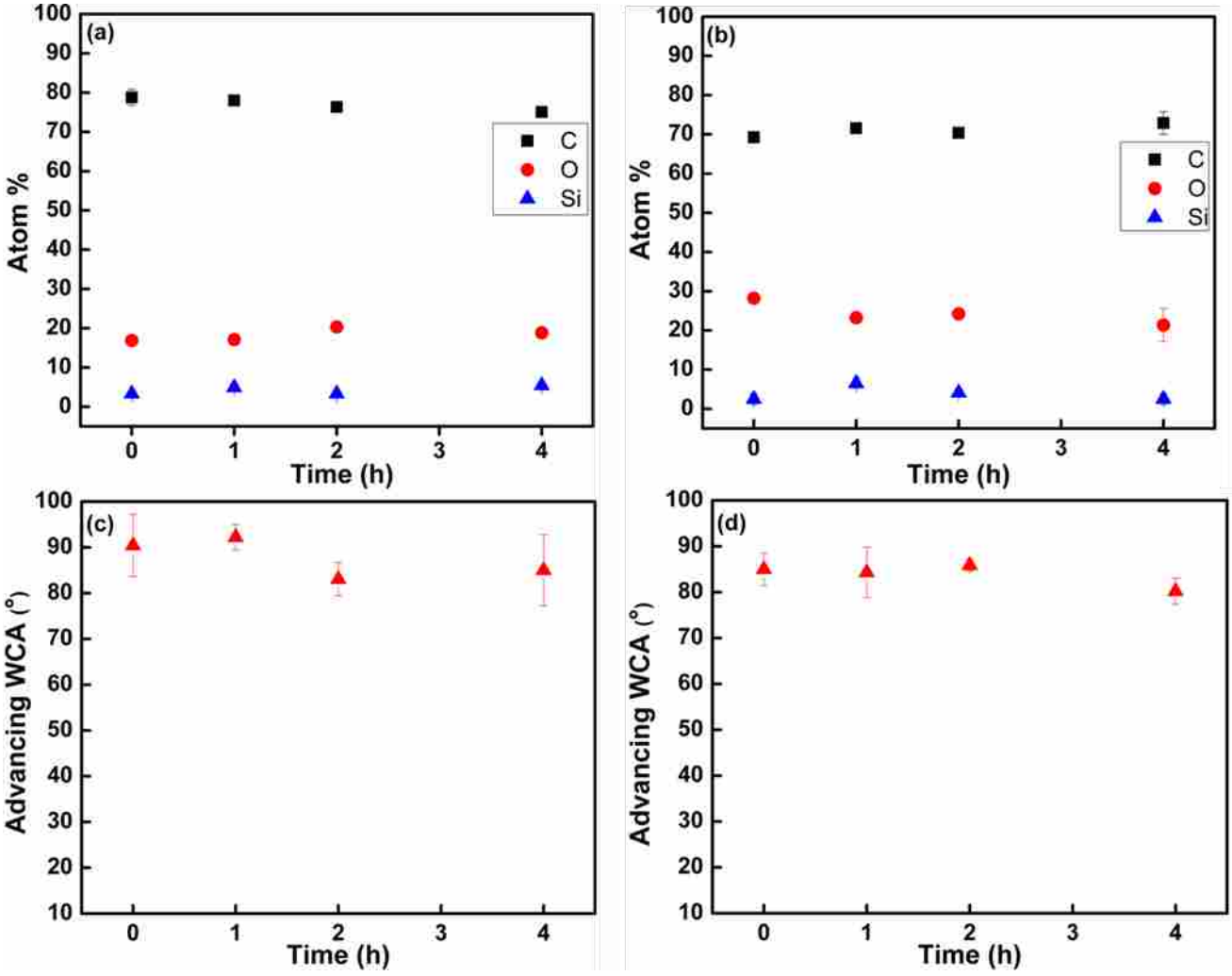

Figure 2.5. Results of stability tests from sputtered carbon surfaces after their immersion in Tris buffer at 95 °C for various amounts of time. (a) Composition of DCMS carbon by XPS. (b) Composition of HiPIMS carbon by XPS. (c) Wetting of DCMS carbon surface. (d) Wetting of DCMS carbon surface. (d) Wetting of HiPIMS carbon surface.

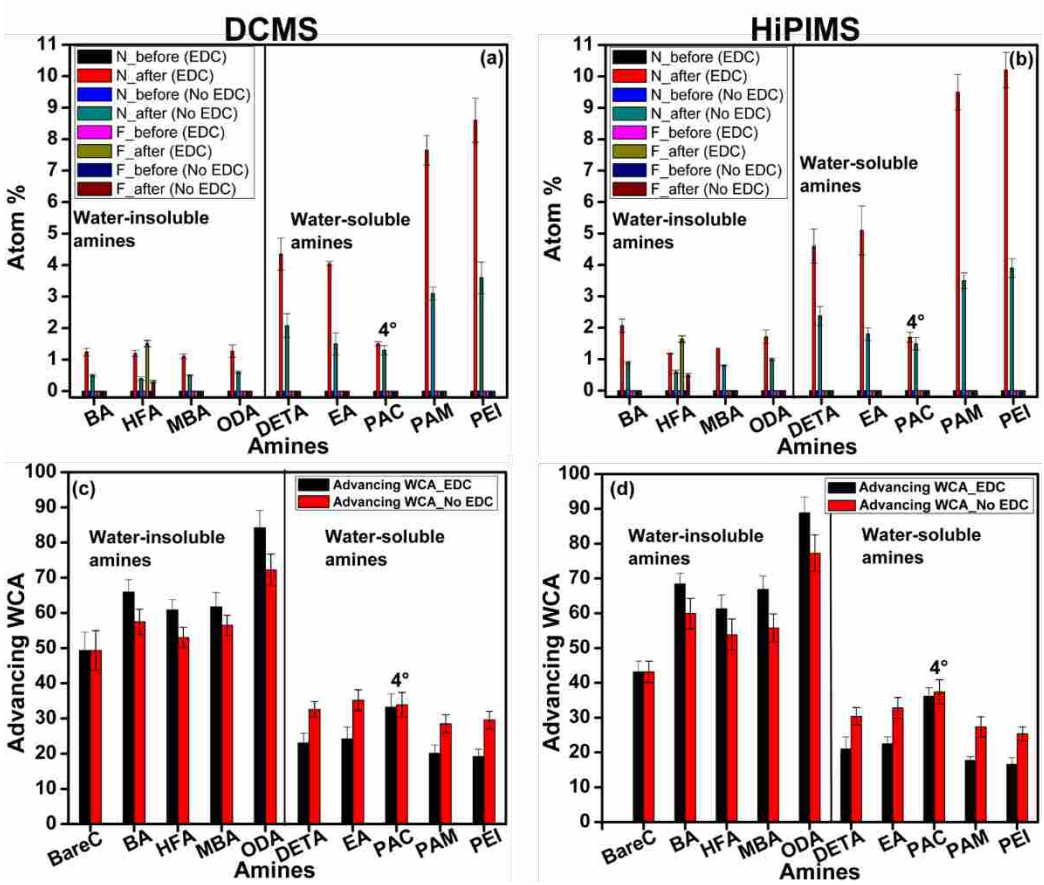

Figure 2.6. Comparison of amidation on activated (with EDC/sulfo-NHS) vs. unactivated (no EDC/sulfo-NHS) DCMS and HiPIMS carbon surfaces for a series of amines. Surface elemental compositions of (a) DCMS and (b) HiPIMS carbon by XPS, and advancing water contact angles of (c) DCMS and (d) HiPIMS carbon.

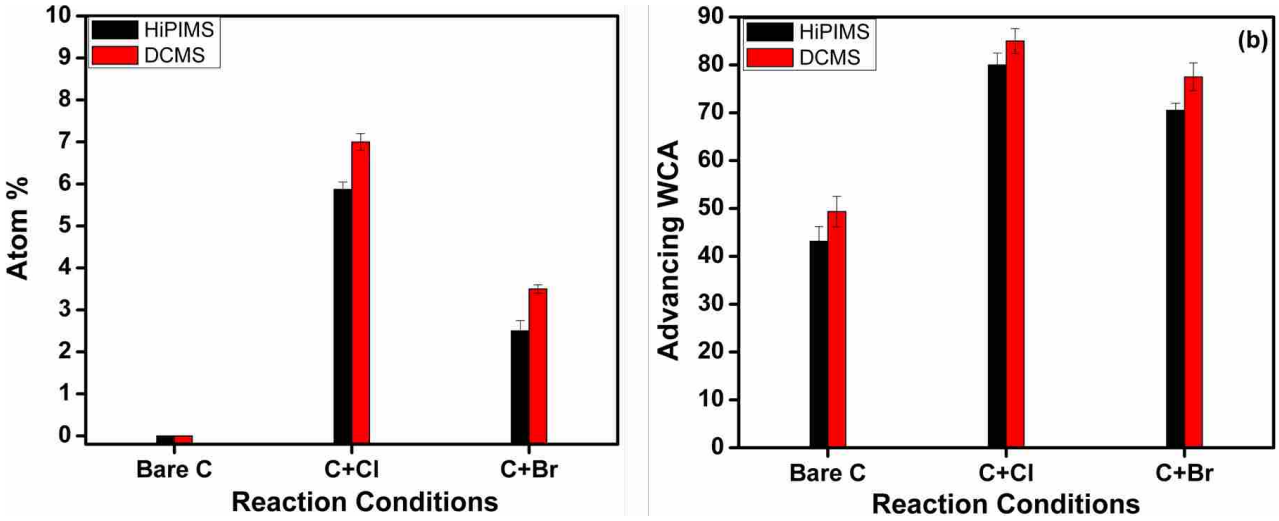

Figure 2.7. Characterization of DCMS and HiPIMS carbon surfaces before (Bare) and after chlorination (C+Cl) and bromination (C+Br) by (a) XPS and (b) wetting.

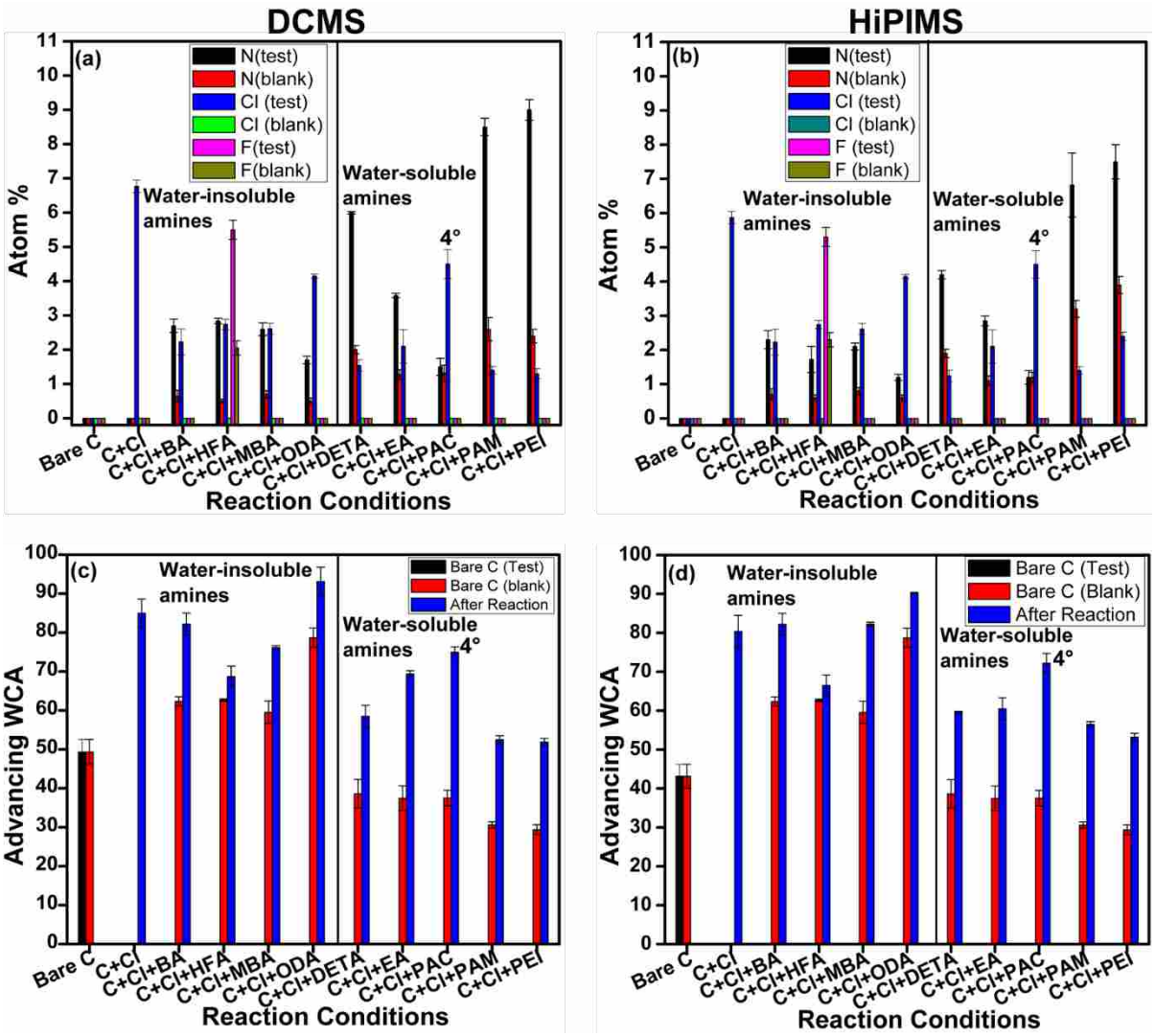

Figure 2.8. Comparison of amination on chlorinated and unchlorinated (unactivated) DCMS and HiPIMS carbon surfaces. Surface elemental compositions of (a) DCMS and (b) HiPIMS carbon by XPS, and advancing water contact angles of (c) DCMS and (d) HiPIMS carbon.

2.10 References

1. TAO, F., ZHU, Y.; , BERNASEK, S. L. , *Functionalization of Semiconductor Surfaces*. 1st ed.; John Wiley & Sons, Inc.: USA, 2012.
2. Yates Jr, J. T., A new opportunity in silicon-based microelectronics. *Science* **1998,** *279* (5349), 335-336.
3. Lin, Z.; Strother, T.; Cai, W.; Cao, X.; Smith, L. M.; Hamers, R. J., DNA attachment and hybridization at the silicon (100) surface. *Langmuir* **2002,** *18* (3), 788-796.
4. Yang, W.; Auciello, O.; Butler, J. E.; Cai, W.; Carlisle, J. A.; Gerbi, J. E.; Gruen, D. M.; Knickerbocker, T.; Lasseter, T. L.; Russell Jr, J. N.; Smith, L. M.; Hamers, R. J., DNA-modified nanocrystalline diamond thin-films as stable, biologically active substrates. *Nature Materials* **2002,** *1*, 253.
5. Stewart, M. P.; Buriak, J. M., Chemical and Biological Applications of Porous Silicon Technology. *Advanced Materials* **2000,** *12* (12), 859-869.
6. Maduraiveeran, G.; Sasidharan, M.; Ganesan, V., Electrochemical sensor and biosensor platforms based on advanced nanomaterials for biological and biomedical applications. *Biosensors and Bioelectronics* **2018,** *103*, 113-129.
7. Pasinszki, T.; Krebsz, M.; Tung, T. T.; Losic, D., Carbon Nanomaterial Based Biosensors for Non-Invasive Detection of Cancer and Disease Biomarkers for Clinical Diagnosis. *Sensors* **2017,** *17* (8), 1919.
8. Grieshaber, D.; MacKenzie, R.; Vörös, J.; Reimhult, E., Electrochemical Biosensors - Sensor Principles and Architectures. *Sensors* **2008,** *8* (3), 1400-1458.
9. Manickam, A.; Singh, R.; McDermott, M. W.; Wood, N.; Bolouki, S.; Naraghi-Arani, P.; Johnson, K. A.; Kuimelis, R. G.; Schoolnik, G.; Hassibi, A., A Fully Integrated CMOS Fluorescence Biochip for DNA and RNA Testing. *IEEE Journal of Solid-State Circuits* **2017,** *52* (11), 2857-2870.
10. Rosso, M.; Arafat, A.; Schroën, K.; Giesbers, M.; Roper, C. S.; Maboudian, R.; Zuilhof, H., Covalent Attachment of Organic Monolayers to Silicon Carbide Surfaces. *Langmuir* **2008,** *24* (8), 4007-4012.
11. K. D, W.; D. J, A.; J. F, H.; D. R, K.; K, N., Wireless implantable microsystems: high-density electronic interfaces to the nervous system. *Proceedings of the IEEE* **2004,** *92* (1), 76-97.
12. Lockett, M. R.; Smith, L. M., Carbon Substrates: A Stable Foundation for Biomolecular Arrays. *Annual Review of Analytical Chemistry* **2015,** *8* (1), 263-285.
13. Augenlicht, L. H.; Kobrin, D., Cloning and Screening of Sequences Expressed in a Mouse Colon Tumor. *Cancer Research* **1982,** *42* (3), 1088-1093.
14. Goldsmith, S. J., Radioimmunoassay: Review of basic principles. *Seminars in Nuclear Medicine* **1975,** *5* (2), 125-152.
15. Butler, J. E., Enzyme-Linked Immunosorbent Assay. *Journal of Immunoassay* **2000,** *21* (2-3), 165-209.
16. Aissaoui, N.; Bergaoui, L.; Landoulsi, J.; Lambert, J.-F.; Boujday, S., Silane Layers on Silicon Surfaces: Mechanism of Interaction, Stability, and Influence on Protein Adsorption. *Langmuir* **2012,** *28* (1), 656-665.
17. Phillips, M. F.; Lockett, M. R.; Rodesch, M. J.; Shortreed, M. R.; Cerrina, F.; Smith, L. M., In situ oligonucleotide synthesis on carbon materials: stable substrates for microarray fabrication. *Nucleic Acids Research* **2008,** *36* (1), e7-e7.

18. Radadia, A. D.; Stavis, C. J.; Carr, R.; Zeng, H.; King, W. P.; Carlisle, J. A.; Aksimentiev, A.; Hamers, R. J.; Bashir, R., Control of Nanoscale Environment to Improve Stability of Immobilized Proteins on Diamond Surfaces. *Advanced Functional Materials* **2011,** *21* (6), 1040-1050.
19. Hsiao, V. K. S.; Waldeisen, J. R.; Zheng, Y.; Lloyd, P. F.; Bunning, T. J.; Huang, T. J., Aminopropyltriethoxysilane (APTES)-functionalized nanoporous polymeric gratings: Fabrication and application in biosensing. *Journal of Materials Chemistry* **2007,** *17* (46), 4896-4901.
20. Dietrich, P. M.; Streeck, C.; Glamsch, S.; Ehlert, C.; Lippitz, A.; Nutsch, A.; Kulak, N.; Beckhoff, B.; Unger, W. E. S., Quantification of Silane Molecules on Oxidized Silicon: Are there Options for a Traceable and Absolute Determination? *Analytical Chemistry* **2015,** *87* (19), 10117-10124.
21. Wagner, P.; Nock, S.; Spudich, J. A.; Volkmuth, W. D.; Chu, S.; Cicero, R. L.; Wade, C. P.; Linford, M. R.; Chidsey, C., E.. Bioreactive self-assembled monolayers on hydrogen-passivated Si(111) as a new class of atomically flat substrates for biological scanning probe microscopy. *Journal of Structural Biology* **1997,** *119* (2), 189-201.
22. Attavar, S.; Diwekar, M.; Linford, M. R.; Davis, M. A.; Blair, S., Passivation of aluminum with alkyl phosphonic acids for biochip applications. *Applied Surface Science* **2010,** *256* (23), 7146-7150.
23. Hamers, R. J., Formation and Characterization of Organic Monolayers on Semiconductor Surfaces. *Annual Review of Analytical Chemistry* **2008,** *1* (1), 707-736.
24. Bent, S. F.; Kachian, J. S.; Rodríguez-Reyes, J. C. F.; Teplyakov, A. V., Tuning the reactivity of semiconductor surfaces by functionalization with amines of different basicity. *Proceedings of the National Academy of Sciences* **2011,** *108* (3), 956-960.
25. Qureshi, A.; Kang, W. P.; Davidson, J. L.; Gurbuz, Y., Review on carbon-derived, solid-state, micro and nano sensors for electrochemical sensing applications. *Diamond and Related Materials* **2009,** *18* (12), 1401-1420.
26. Henke, A. H.; Saunders, T. P.; Pedersen, J. A.; Hamers, R. J., Enhancing Electrochemical Efficiency of Hydroxyl Radical Formation on Diamond Electrodes by Functionalization with Hydrophobic Monolayers. *Langmuir* **2019,** *35* (6), 2153-2163.
27. Filler, M. A.; Bent, S. F., The surface as molecular reagent: organic chemistry at the semiconductor interface. *Progress in Surface Science* **2003,** *73* (1), 1-56.
28. Nichols, B. M.; Butler, J. E.; Russell, J. N.; Hamers, R. J., Photochemical Functionalization of Hydrogen-Terminated Diamond Surfaces: A Structural and Mechanistic Study. *The Journal of Physical Chemistry B* **2005,** *109* (44), 20938-20947.
29. Lockett, M. R.; Smith, L. M., Attaching Molecules to Chlorinated and Brominated Amorphous Carbon Substrates via Grignard Reactions. *Langmuir* **2009,** *25* (6), 3340-3343.
30. Robertson, J., Diamond-like amorphous carbon. *Materials Science and Engineering: R: Reports* **2002,** *37* (4), 129-281.
31. Maia, F. C. B.; Samad, R. E.; Bettini, J.; Freitas, R. O.; Vieira Junior, N. D.; Souza-Neto, N. M., Synthesis of diamond-like phase from graphite by ultrafast laser driven dynamical compression. *Scientific Reports* **2015,** *5*, 11812.
32. Robertson, J., Amorphous carbon. *Current Opinion in Solid State and Materials Science* **1996,** *1* (4), 557-561.
33. Tsubota, T.; Hirabayashi, O.; Ida, S.; Nagaoka, S.; Nagata, M.; Matsumoto, Y., Abstraction of hydrogen atoms on diamond surface using benzoyl peroxide as a radical initiator. *Diamond and Related Materials* **2002,** *11* (7), 1374-1378.

34. Nistor, P. A.; May, P. W., Diamond thin films: giving biomedical applications a new shine. *Journal of The Royal Society Interface* **2017,** *14* (134), 20170382.
35. Lundin, D.; Sarakinos, K., An introduction to thin film processing using high-power impulse magnetron sputtering. *Journal of Materials Research* **2012,** *27* (5), 780-792.
36. Kouznetsov, V.; Macák, K.; Schneider, J. M.; Helmersson, U.; Petrov, I., A novel pulsed magnetron sputter technique utilizing very high target power densities. *Surface and Coatings Technology* **1999,** *122* (2), 290-293.
37. Helmersson, U.; Lattemann, M.; Bohlmark, J.; Ehiasarian, A. P.; Gudmundsson, J. T., Ionized physical vapor deposition (IPVD): A review of technology and applications. *Thin Solid Films* **2006,** *513* (1), 1-24.
38. Gudmundsson, J. T.; Brenning, N.; Lundin, D.; Helmersson, U., High power impulse magnetron sputtering discharge. *Journal of Vacuum Science & Technology A* **2012,** *30* (3), 030801.
39. Sarakinos, K.; Alami, J.; Konstantinidis, S., High power pulsed magnetron sputtering: A review on scientific and engineering state of the art. *Surface and Coatings Technology* **2010,** *204* (11), 1661-1684.
40. Bohlmark, J.; Lattemann, M.; Gudmundsson, J. T.; Ehiasarian, A. P.; Aranda Gonzalvo, Y.; Brenning, N.; Helmersson, U., The ion energy distributions and ion flux composition from a high power impulse magnetron sputtering discharge. *Thin Solid Films* **2006,** *515* (4), 1522-1526.
41. Samuelsson, M.; Lundin, D.; Jensen, J.; Raadu, M. A.; Gudmundsson, J. T.; Helmersson, U., On the film density using high power impulse magnetron sputtering. *Surface and Coatings Technology* **2010,** *205* (2), 591-596.
42. Sittinger, V.; Ruske, F.; Werner, W.; Jacobs, C.; Szyszka, B.; Christie, D. J., High power pulsed magnetron sputtering of transparent conducting oxides. *Thin Solid Films* **2008,** *516* (17), 5847-5859.
43. Banu, M.; Radoi, A.; Simion, M.; Kusko, M. In *Reproducible functionalization of silicon substrates intended for biomedical applications*, 2016 International Semiconductor Conference (CAS), 10-12 Oct. 2016; 2016; pp 151-154.
44. T. Franklin; Bernasek, S., In *Functionalization of Semiconductor Surfaces* John Wiley and Sons: USA, 2012; pp 402-423.
45. Majoul, N.; Aouida, S.; Bessaïs, B., Progress of porous silicon APTES-functionalization by FTIR investigations. *Applied Surface Science* **2015,** *331*, 388-391.
46. Kim, J.; Seidler, P.; Wan, L. S.; Fill, C., Formation, structure, and reactivity of amino-terminated organic films on silicon substrates. *Journal of Colloid and Interface Science* **2009,** *329* (1), 114-119.
47. Ida, S.; Tsubota, T.; Tanii, S.; Nagata, M.; Matsumoto, Y., Chemical Modification of the Diamond Surface Using Benzoyl Peroxide and Dicarboxylic Acids. *Langmuir* **2003,** *19* (23), 9693-9698.
48. Miller, J. B., Amines and thiols on diamond surfaces. *Surface Science* **1999,** *439* (1), 21-33.
49. Liu, Y.; Gu, Z.; Margrave, J. L.; Khabashesku, V. N., Functionalization of Nanoscale Diamond Powder: Fluoro-, Alkyl-, Amino-, and Amino Acid-Nanodiamond Derivatives. *Chemistry of Materials* **2004,** *16* (20), 3924-3930.
50. Sotowa, K.-I.; Amamoto, T.; Sobana, A.; Kusakabe, K.; Imato, T., Effect of treatment temperature on the amination of chlorinated diamond. *Diamond and Related Materials* **2004,** *13* (1), 145-150.

51. Allongue, P.; Delamar, M.; Desbat, B.; Fagebaume, O.; Hitmi, R.; Pinson, J.; Savéant, J.-M., Covalent Modification of Carbon Surfaces by Aryl Radicals Generated from the Electrochemical Reduction of Diazonium Salts. *Journal of the American Chemical Society* **1997,** *119* (1), 201-207.
52. Kuo, T. M., R.; Swain, G. , Covalent Modification of Carbon Surfaces by Aryl Radicals Generated from the Electrochemical Reduction of Diazonium Salts. *Electrochem. Solid State Lett.* **1999,** *2*, 288–290.
53. Strother, T.; Knickerbocker, T.; Russell, J. N.; Butler, J. E.; Smith, L. M.; Hamers, R. J., Photochemical Functionalization of Diamond Films. *Langmuir* **2002,** *18* (4), 968-971.
54. Clare, T. L.; Clare, B. H.; Nichols, B. M.; Abbott, N. L.; Hamers, R. J., Functional Monolayers for Improved Resistance to Protein Adsorption: Oligo(ethylene glycol)-Modified Silicon and Diamond Surfaces. *Langmuir* **2005,** *21* (14), 6344-6355.
55. Ohta, R.; Saito, N.; Inoue, Y.; Sugimura, H.; Takai, O., Organosilane self-assembled monolayers directly linked to the diamond surfaces. *Journal of Vacuum Science & Technology A* **2004,** *22* (5), 2005-2009.
56. Colavita, P. E.; Sun, B.; Tse, K.-Y.; Hamers, R. J., Photochemical Grafting of n-Alkenes onto Carbon Surfaces: the Role of Photoelectron Ejection. *Journal of the American Chemical Society* **2007,** *129* (44), 13554-13565.
57. Gallardo, I.; Pinson, J.; Vilà, N., Spontaneous Attachment of Amines to Carbon and Metallic Surfaces. *The Journal of Physical Chemistry B* **2006,** *110* (39), 19521-19529.
58. Hamon, M. A.; Chen, J.; Hu, H.; Chen, Y.; Itkis, M. E.; Rao, A. M.; Eklund, P. C.; Haddon, R. C., Dissolution of Single-Walled Carbon Nanotubes. *Advanced Materials* **1999,** *11* (10), 834-840.
59. Mickelson, E. T.; Huffman, C. B.; Rinzler, A. G.; Smalley, R. E.; Hauge, R. H.; Margrave, J. L., Fluorination of single-wall carbon nanotubes. *Chemical Physics Letters* **1998,** *296* (1), 188-194.
60. Evans, M. J. B.; Halliop, E.; Liang, S.; MacDonald, J. A. F., The effect of chlorination on surface properties of activated carbon. *Carbon* **1998,** *36* (11), 1677-1682.
61. Linford, M. R.; Chidsey, C. E. D., Surface Functionalization of Alkyl Monolayers by Free-Radical Activation: Gas-Phase Photochlorination with Cl2. *Langmuir* **2002,** *18* (16), 6217-6221.
62. Cicero, R. L. W., P.; Linford, M.R.; Hawker, C.J.; Waymouth, R.M.; Chidsey, C.E.D, Functionalization of Alkyl Monolayers on Surfaces with Diverse Amines: Photochemical Chlorosulfonation Followed by Sulfonamide Formation. *Polymer Preprints* **1997,** *38*, 904-905.
63. Colavita, P. E.; Sun, B.; Wang, X.; Hamers, R. J., Influence of Surface Termination and Electronic Structure on the Photochemical Grafting of Alkenes to Carbon Surfaces. *The Journal of Physical Chemistry C* **2009,** *113* (4), 1526-1535.
64. Rezek, B.; Shin, D.; Nebel, C. E., Properties of Hybridized DNA Arrays on Single-Crystalline Undoped and Boron-Doped (100) Diamonds Studied by Atomic Force Microscopy in Electrolytes. *Langmuir* **2007,** *23* (14), 7626-7633.
65. Singh, B.; Diwan, A.; Jain, V.; Herrera-Gomez, A.; Terry, J.; Linford, M. R., Uniqueness plots: A simple graphical tool for identifying poor peak fits in X-ray photoelectron spectroscopy. *Applied Surface Science* **2016,** *387*, 155-162.
66. Gupta, V.; Ganegoda, H.; Engelhard, M. H.; Terry, J.; Linford, M. R., Assigning Oxidation States to Organic Compounds via Predictions from X-ray Photoelectron Spectroscopy: A Discussion of Approaches and Recommended Improvements. *Journal of Chemical Education* **2014,** *91* (2), 232-238.

67. Szunerits, S.; Boukherroub, R., Different strategies for functionalization of diamond surfaces. *Journal of Solid State Electrochemistry* **2008,** *12* (10), 1205-1218.
68. Abbott, J.; Niederhauser, T. L.; Hansen, D. P.; Perkins, R. T.; Bell, D. A.; Bard, E. C.; Lunt, B. M.; Worthington, M. O.; Miller, C. M.; Hyatt, D. F.; Asplund, M. C.; Jiang, G.; Linford, M. R.; Vanfleet, R. R.; Davis, R. C., Carbon-Coated Tellurium for Optical Data Storage. *ACS Applied Materials & Interfaces* **2010,** *2* (8), 2373-2376.
69. Shah, D.; Patel, D. I.; Roychowdhury, T.; Rayner, G. B.; O'Toole, N.; Baer, D. R.; Linford, M. R., Tutorial on interpreting x-ray photoelectron spectroscopy survey spectra: Questions and answers on spectra from the atomic layer deposition of Al2O3 on silicon. *Journal of Vacuum Science & Technology B* **2018,** *36* (6), 062902.
70. Tougaard, S., Improved XPS analysis by visual inspection of the survey spectrum. *Surface and Interface Analysis* **2018,** *50* (6), 657-666.
71. Shirley, D. A., High-Resolution X-Ray Photoemission Spectrum of the Valence Bands of Gold. *Physical Review B* **1972,** *5* (12), 4709-4714.
72. Jain, V.; Biesinger, M. C.; Linford, M. R., The Gaussian-Lorentzian Sum, Product, and Convolution (Voigt) functions in the context of peak fitting X-ray photoelectron spectroscopy (XPS) narrow scans. *Applied Surface Science* **2018,** *447*, 548-553.
73. Lua, Y.-Y.; Fillmore, W. J. J.; Yang, L.; Lee, M. V.; Savage, P. B.; Asplund, M. C.; Linford, M. R., First Reaction of a Bare Silicon Surface with Acid Chlorides and a One-Step Preparation of Acid Chloride Terminated Monolayers on Scribed Silicon. *Langmuir* **2005,** *21* (6), 2093-2097.
74. George, G. A., High resolution XPS of organic polymers—the scienta ESCA 300 data base. G. Beamson and D. Briggs. John Wiley & Sons, Ltd, Chichester, 1992. Pp. 295, price £65.00. ISBN 0-471-93592-1. *Polymer International* **1994,** *33* (4), 439-440.
75. Tougaard, S., Universality Classes of Inelastic Electron Scattering Cross-sections. *Surface and Interface Analysis* **1997,** *25* (3), 137-154.
76. Patel, D. I.; Bahr, S.; Dietrich, P.; Meyer, M.; Thißen, A.; Linford, M. R., Argon gas, by near-ambient pressure XPS. *surface science spectra* **2019,** *26*.
77. Bart, J.; Tiggelaar, R.; Yang, M.; Schlautmann, S.; Zuilhof, H.; Gardeniers, H., Room-temperature intermediate layer bonding for microfluidic devices. *Lab on a Chip* **2009,** *9* (24), 3481-3488.

CHAPTER 3: The Gaussian-Lorentzian Sum, Product, and Convolution (Voigt) Functions in the Context of Peak Fitting X-ray Photoelectron Spectroscopy (XPS) Narrow Scans

3.1. Statement of Attribution

This document was originally published as Varun Jain, Mark C. Biesinger, and Matthew R. Linford. The Gaussian-Lorentzian Sum, Product, and Convolution (Voigt) functions in the context of peak fitting X-ray photoelectron spectroscopy (XPS) narrow scans. *Applied Surface Science*, **2018**, *447*, 548-553.[1]

It has undergone two minor revisions, prior to publication.

3.2. Abstract

X-ray photoelectron spectroscopy (XPS) is arguably the most important vacuum technique for surface chemical analysis, and peak fitting is an indispensable part of XPS data analysis. Functions that have been widely explored and used in XPS peak fitting include the Gaussian, Lorentzian, Gaussian-Lorentzian sum (GLS), Gaussian-Lorentzian product (GLP), and Voigt functions, where the Voigt function is a convolution of a Gaussian and a Lorentzian function. In this article we discuss these functions from a graphical perspective. Arguments based on convolution and the Central Limit Theorem are made to justify the use of functions that are intermediate between pure Gaussians and pure Lorentzians in XPS peak fitting. Mathematical forms for the GLS and GLP functions are presented with a mixing parameter *m*. Plots are shown for GLS and GLP functions with mixing parameters ranging from 0 to 1. There are fundamental differences between the GLS and GLP functions. The GLS function better follows the 'wings' of the Lorentzian, while these 'wings' are suppressed in the GLP. That is, these two functions are not interchangeable. The GLS and GLP functions are compared to the Voigt function, where the GLS

is shown to be a decent approximation of it. Practically, both the GLS and the GLP functions can be useful for XPS peak fitting. Examples of the uses of these functions are provided herein.

Key words: XPS, GLS, GLP, Voigt function, Gaussian function, Lorentzian function

3.3. Introduction

X-ray photoelectron spectroscopy (XPS) is arguably the most popular and important high vacuum surface analytical tool.[2] It is unique in being highly surface sensitive, quantitative, and available in many laboratories and facilities, providing the elemental compositions of all the elements except helium and hydrogen, and yielding chemical/oxidation state information about the elements it detects.[3] Important decisions in the laboratory and in industry are made based on XPS results,[4] where much of the key information derived from XPS is based on peak fitting narrow (high resolution) scans. Indeed, as explained by Sherwood, peak fitting is an indispensable part of XPS data analysis because the chemical shifts that provide the rich chemical information available through the technique and the widths of the fit components have comparable values.[5] For many years XPS practitioners have employed a variety of functions/peak shapes in their fitting. These have included pure Lorentzians, which model the fundamental/theoretical line shape, pure Gaussians, which often model amorphous materials well, e.g., polymers and glasses, Gaussian-Lorentzian sum and product functions, which consist of either the sum[6] or product[5] of these two functions, Voigt functions, which are the convolutions of Gaussian and Lorentzian functions, and other more complex functions, including the Doniach-Sunjic line shape.[7] Asymmetry must often be added to fit components/peaks to model conducting materials.[8]

In this paper we discuss five functions that have been widely explored and used in XPS peak fitting: the Gaussian function, the Lorentzian function, the Gaussian-Lorentzian sum function (GLS), the Gaussian-Lorentzian product (GLP) function, and the Voigt function, which is a

convolution of Gaussian and Lorentzian functions. A primary goal of this work is to compare the GLS and GLP functions. Indeed, different software packages for XPS peak fitting have different mathematical functions available in them. Thus, it is important to understand these synthetic line shapes, i.e., to know where they are best used and how to apply them. Arguments based on convolution and the Central Limit Theorem are made to justify the use of functions that are intermediate between pure Gaussians and pure Lorentzians in XPS peak fitting. This is illustrated graphically by showing the results of the repeated convolution of a rectangle (slit) function with itself. Mathematical forms for the GLS and GLP functions are presented, where they each contain a mixing parameter, m, that ranges from 0 to 1. Plots are shown for the GLS and GLP functions with different values of the mixing parameter. The GLS function better follows the 'wings' of the Lorentzian, while, because of the more compact nature of the Gaussian function, these 'wings' are suppressed in the GLP. The GLS and GLP are compared to the Voigt function, where the GLS is shown to be the better approximation of it. Thus, there are fundamental differences between the GLS and GLP functions, i.e., they are not interchangeable. As shown below, both have their place in XPS peak fitting.

Finally, while peak fitting plays a central role in the work up and interpretation of XPS data, the use of other statistical tools and mathematical analyses of XPS peaks and data are also important.[9, 10] These include chi squared, calculating and showing the residuals, showing the sum of the fit components, the Abbe criterion,[11-13] uniqueness plots,[14] peak smoothing/denoising, e.g., by wavelets,[15, 16] chemometrics tools such as principal component analysis, multivariate curve resolution, and pattern recognition entropy,[17] and width functions.[18,19]

3.4. Results and Discussions

1. Basic theory of convolution and the GLS and GLP functions

When peak fitting an XPS narrow scan, one generally selects a baseline first followed by a series of peaks (usually synthetic fit components) that represents the chemical/oxidation states[3] of an element. We noted above that some of the most common functions chosen to represent symmetric XPS signals are the Gaussian, Lorentzian, Gaussian-Lorentzian sum (GLS), Gaussian-Lorentzian product (GLP), and Voigt functions. We now discuss these functions in some detail.

Gaussian and Lorentzian functions play extremely important roles in science, where their general mathematical expressions are given here in Equations 3.1 and 3.2, respectively.[20, 21, 13]

(1) $$G(x;F,E,h) = h * exp\left[-4ln2\,\frac{(x-E)^2}{F^2}\right] \qquad (3.1)$$

(2) $$L(x;F,E,h) = \frac{h}{\left[1+4\frac{(x-E)^2}{F^2}\right]} \qquad (3.2)$$

These Gaussian and Lorentzian functions are graphed in Figures 3.1 and 3.2, respectively, with the following parameters: h = 1 (the functions have a height of one), E = 0 (the functions are centered at the origin), and F = 1 (the functions have a width of one). Note that Equations 3.1 and 3.2 and many of those below follow the formatting of Fairley.[20] Obviously both functions are symmetric about their center points. They also have finite integrals and are localized – they do not have exceedingly large tails or other components that extend out to a significant degree. The Gaussian curve is the classic 'bell-shaped' or 'normal' curve/distribution. The Lorentzian is somewhat narrower around its maximum and it extends out a little more than the Gaussian on its sides, i.e., the Lorentzian has 'wings'. Any serious physical scientist should know the difference between these two functions, be able to recognize their shapes, and be comfortable working with them.

In the theory of X-ray photoelectron spectroscopy, natural line shapes are generally assumed to be Lorentzian. There are, however, reasons why this line shape may not be observed

experimentally. There will be some line width of the X-rays that excite the photoelectrons, i.e., they won't be perfectly monochromatic. The photoelectrons will travel through a spectrometer that will broaden signals to some degree. The elements in question within a sample may be in heterogeneous environments (disorder broadening), and the emission of the photoelectrons may be perturbed by vibrations in the material (phonon broadening), which is temperature dependent. For a more detailed discussion of these concepts, see Briggs and Grant's book on Surface Analysis.[20] One can think of at least some of these broadening mechanisms as being convolutions of the natural, Lorentzian, line shape with other functions, often Gaussians. (MRL previously published a tutorial article on convolution in Vacuum Technology & Coating. This document is included in the Supporting Information of this article.[22]) In mathematics, the Central Limit Theorem states that it will often be the case that if a function is repeatedly convolved with itself, or if a series of functions are convolved together, the resulting function will increasingly resemble a Gaussian. This function will also become increasingly smooth and broad. We now illustrate these concepts with the slit function, S(x), shown in Figure 3.3. This function is important enough to be referred to in other ways, including as $\Pi(x)$, Rect(x), or simply as the rectangle function.[23] S(x) is an important window, or apodization, function in signal processing, i.e., it has a value of zero outside of a specific interval. In addition, there are a number of interesting relationships between S(x) and other common functions in signal processing, e.g., it can be derived from the unit step function, $\theta(x)$ (Equation 3.3), where S(x) is the product of $\theta(½ - x)$ and $\theta(x + ½)$ (see Equation 3.4). Note that it rarely matters how functions like $\theta(x)$ and S(x) are defined at their transition points. For example, if we redefined $\theta(x)$ as 1 for $x > 0$ and 0 for $x \leq 0$, it would only differ from the definition in Equation 3.3 by a null function, i.e., for all practical purposes these functions will behave identically.

(3) $$UnitStep(x) = \theta(x) = \begin{cases} 1\ for\ x \geq 0 \\ 0\ for\ x < 0 \end{cases} \quad (3.3)$$

(4) $$S(x) = \theta(\tfrac{1}{2} - x)\theta(x + \tfrac{1}{2}) = \begin{cases} 1\ for\ x \leq \frac{1}{2} \\ 0\ for\ x > \frac{1}{2} \end{cases} \quad (3.4)$$

Now, if we convolve S(x) with itself (S(x)*S(x)) we get the triangle function, T(x), as shown in Figure 3.4. (Note that the triangle function may also be represented as Λ(x).) Of course this function is still somewhat angular – it consists of line segments, however it can be argued that it is beginning to resemble a Gaussian function and that it does so to a greater degree than S(x). It also seems to be getting smoother. That is, would you rather drive over bumps on a road shaped like the features in Figure 3.3 or Figure 3.4? A more advanced justification for stating that T(x) is smoother than s(x) is to note that it only takes one derivative to reduce S(x) to delta (impulse) functions, while it takes two derivatives to reduce T(x) to these types of functions. Finally, note that the convolution of S(x) with itself, T(x), is broader that S(x), i.e., S(x) has non-zero values between -½ and ½, while, T(x) has non-zero values between -1 and 1.

We now convolve T(x) with itself, where T(x)*T(x) = T(x)*S(x))*S(x) = S(x)*S(x)*S(x)*S(x). The resulting function is shown in Figure 3.5 Consistent with the Central Limit Theorem it is starting to look rather Gaussian-like – this function is smoother and broader than its predecessor in Figure 3.4. Thus, it would be reasonable to expect that it would require more derivatives to reduce T(x)*T(x) to a series of impulse functions than T(x) or S(x). All of this is to argue for the reasonableness of stating that when a set of photoelectrons, which may inherently have a Lorentzian line shape, is perturbed by a spectrometer and/or the broadening mechanisms mentioned above, one would expect the final signal to have at least some Gaussian character. Thus,

the recommendation[4] that the C 1s fit components of polymers be modeled as 100% Gaussians or 90:10 Gaussian:Lorentzian mixes seems reasonable because polymers will often exist in rather heterogeneous environments, i.e., their chains can often be approximated as random coils, which will correspond to a variety of bond angles and chemical environments for the different chemical groups/moieties within the polymer. However, the photoemission spectra in this example were collected on an older XPS instrument. In general, newer instruments produce signals with more Lorentzian character, i.e., this suggestion is no longer entirely current. Also, peaks generated from polymeric materials with newer instruments generally show some asymmetry in their shapes.

A more advanced and precise mathematical justification for the peak broadening mechanisms discussed herein is to note that variances add under convolution. That is, for two functions f and g with standard deviation σ_f and σ_g, their convolution (f*g) has a variance σ_{f*g} given by:

$$\sigma_{f*g}^2 = \sigma_f^2 + \sigma_g^2 \qquad (3.5)$$

For example, the convolution of a Gaussian with a second Gaussian is yet an additional Gaussian, where according to Equation 3.5, this new Gaussian will be broader than either of the original Gaussians.

So we have argued that it is plausible that many of the components of XPS narrow scans will be best defined and fit by peaks that have both Gaussian and Lorentzian character. Mathematically, the 'purest' way to handle this problem is to use a Voigt function, which is the convolution of a Gaussian and a Lorentzian. Historically, however, this convolution was found to be computationally expensive so many of the earlier XPS fitting packages used one of two approximations for it: the Gaussian-Lorentzian sum (GLS) or the Gaussian-Lorentzian product (GLP) function. These functions remain relevant today because (i) there are still a number of fitting

packages that provide the GLS and/or the GLP functions as options, (ii) there is a great deal of Literature precedent for the use of both of these functions, and (iii) these functions work – both the Literature and the examples provided below show that both the GLS and the GLP remain useful and relevant in peak fitting. Indeed, it is an active area of research to determine which synthetic function is most appropriate in different situations.

The GLS function has the following form:

(6) $$GLS(x;F,E,m,h) = h * (1-m)exp\left[-4ln2\frac{(x-E)^2}{F^2}\right] + \frac{h*m}{\left[1+4\frac{(x-E)^2}{F^2}\right]} \qquad (3.6)$$

Notice that the first and second terms in this function are the Gaussian and Lorentzian functions in Equations 3.1 and 3.2 weighted by a mixing parameter, *m*. That is, for *m* = 0, 3.6 reduces to Equation 3.1, a Gaussian, and for *m* = 1, Equation 3.6 reduces to Equation 3.2, a Lorentzian. Obviously, by varying *m* from 0 to 1 we can proceed from a pure Gaussian to a pure Lorentzian function. Clearly, *m* could be a parameter in an algorithm used to fit XPS narrow scans. Figure 3.6 shows the GLS function (Equation 3.6) for three values of *m*: *m* = 0 (the blue/bottom line), which (again) is a Gaussian, *m* = 1 (the green/top line), which is a Lorentzian, and *m* = 0.5 (the red/middle line), which runs between the other two functions. Figure 3.7 goes a little further, zooming in on the region where the Gaussian and Lorentzian functions differ and showing results for *m* = 0, 0.1, 0.3, 0.5, 0.7, and 1. It is clear that the GLS allows variation in a reasonable way between a pure Gaussian and a pure Lorentzian function.

The GLP function is defined in Equation 3.7. As expected from its name, it consists of the product of a Gaussian and a Lorentzian function. As was the case for the GLS, the GLP contains a mixing parameter, *m*, and values of *m* = 0 and *m* = 1 in Equation 3.7 yield pure Gaussian (Equation 3.1) and pure Lorentzian functions (Equation 3.2), respectively.

(7) $$GLP(x;F,E,m,h) = h * exp\left[-4ln2(1-m)\frac{(x-E)^2}{F^2}\right] * \frac{1}{\left[1+4m\frac{(x-E)^2}{F^2}\right]} \qquad (3.7)$$

At this point, it may appear that the GLS and GLP functions are interchangeable, but this is not the case. Figure 3.8 shows the GLP function for m = 0, 0.5, and 1. It is clear here that while the m = 0.5 GLS function was approximately in the middle of the pure Gaussian and Lorentzian functions (see Figure 3.6), the m = 0.5 GLP function differs only slightly from the pure Gaussian. The obvious reason for this is that, as suggested above, the Gaussian function is 'more contained' than the Lorentzian function – it goes to zero faster. As a result, when the Lorentzian and Gaussian functions in Figure 3.8 are multiplied together, the 'wings' of the Lorentzian are multiplied by values that are quite close to zero with the result that they largely disappear. These conclusions are further confirmed in Figure 3.9, which shows an enlarged view of the m = 0.5 GLP function and also of the m = 0.9 GLP function. A priori, one might expect that a mixing parameter of 0.9 would yield a GLP function that would rather closely resemble/follow a pure Lorentzian function. However, even at m = 0.9 the GLP function only appears to be about half way between the pure Gaussian and pure Lorentzian, where this representation/extension of the function still poorly represents the 'wings' of the Lorentzian, cf., Figure 3.7.

For comparison to the use of m in this work, four XPS instrument manufacturers and an XPS software company were surveyed to determined how they handle the mixing parameter in the Gaussian-Lorentzian mixture functions in their software. Four of the companies: CasaXPS (UK), Kratos (Manchester, England), Specs (Berlin, Germany), and ThermoFisher (East Grinstead, UK), use m = 0 for the pure Gaussian and m = 1 for the pure Lorentzian. Interestingly, the default peak for peak fitting in the software package of one of these XPS companies is a GLP with m = 0.3. Figure 3.8 suggests that this synthetic peak shape is very nearly a Gaussian. Also, m is presented in two of these software packages as a percentage running from 0 to 100 (see, for example, the peak fits in the Supporting Information that were performed in CasaXPS). However, PHI

(Chanhassen, MN) takes the opposite approach, using $m = 0$ for its pure Lorentzian. Beamson and Briggs similarly used a GLS with $m = 0$ corresponding to a pure Lorentzian and $m = 1$ to a pure Gaussian.[24]

Around 1980, the GLP function was recommended in the literature for XPS narrow scan peak fitting.[25] This suggestion appears to have been relatively influential. However, a later paper in 2007 by Hesse, Streubel, and Szargan[13] did not confirm the previous recommendation. In their analyses of synthetic, Voigt-based XPS spectra, i.e., they did not use real data, the GLS function mathematically/theoretically outperformed the GLP. In their work, Hesse and coworkers plotted the GLS with m = 0.5, the GLP with m = 0.5, and the Voigt function, all with widths of 2. This plot is reproduced in Figure 3.10, albeit with the peaks shifted to the origin so they can be better compared to the peaks in the other figures in this document. The Voigt function (yellow line) is the widest of the three functions. The red line just inside it is the GLS function. Obviously the GLS function approximates the Voigt function quite well. The lowest line in Figure 3.10 is the GLP. It is clearly a less adequate approximation of the Voigt function. In 2003, Fairley also discussed this issue, noting, as had Hesse, the significant decrease of the Lorentzian's wings when it is multiplied by a Gaussian.[20,11]

2. Practical applications of the GLP and its comparisons to the GLS function

At this point one might argue that the GLS should be favored and the GLP deprecated, where the mathematical reasoning outlined and cited here is supportive of this position. However, at some point, the most important test of a synthetic line shape is not the theory behind it but rather its effectiveness in fitting real data. As shown in this section, the GLP appears to more effectively fit some XPS narrow scans, which indicates that it remains a useful synthetic line shape for XPS narrow scan analysis. Modern XPS instruments have seen an increase in energy resolution for both

the spectrometer and X-ray source. As the spectral resolution contribution from the spectrometer and source, which are both Gaussian in shape, decreases, an increase in the resolution contribution from the core-line, which is Lorentzian in shape, is seen (barring other effects as mentioned earlier).

The three examples below illustrate the use of the GLP in XPS narrow scan analysis. The spectra and fits corresponding to these analyses, which were performed in CasaXPS, are in the Supporting Information. Note that 'GL' and 'SGL' in CasaXPS are the same as GLP and GLS, respectively, in this work.

i. The first example shows a Mo 3d spectrum from a sample of MoO_3. The two signals here are the Mo $3d_{5/2}$ and $3d_{3/2}$ peaks. They are expected to be mostly Gaussian in nature and are due to spin-orbit splitting. These same peaks with the same Shirley background and similar background endpoints were best fit with a GLP with m = 29 and a GLS with m = 5. The fit residual values for these fits were very similar: 2.539 and 2.699, respectively. The fitting functions here do not differ much from pure Gaussians, and for all practical purposes the fits are identical.

ii. The second example shows the S 2p spectrum from MoS_2. These spin-orbit signals (the S $2p_{3/2}$ and $2p_{1/2}$) are expected to have more Lorentzian character than the signals in the previous example. Best fits to these peaks were obtained with a GLP with m = 62 and a fit residual value of 1.758 and a GLS with m = 17 and a fit residual value of 2.079. Here the GLS is not able to fit the data as well as the GLP.

iii. The third example is the Cu $2p_{3/2}$ signal from a sample of sputter-cleaned metallic copper. Best fits to this peak were obtained with a GLP with m = 60 and a fit residual of 3.931 and a GLS

with m = 80 and a fit residual of 1.804. The GLS does a very poor job here and is unable to fit this experimental line shape. Quantitation with the GLS here would be problematic.

Thus we see the practical value of having multiple synthetic line shapes at our disposal for XPS narrow scan analysis.

3.5. Conclusions

In this article we have discussed a series of line shapes that are important for XPS peak fitting. These include the Gaussian, Lorentzian, GLS, GLP, and Voigt functions, which are discussed and/or presented symbolically in the context of signal processing mathematics, e.g., convolution. Plots of the GLS and GLP are shown with different values of the mixing parameter, *m*. The parameter *m* is used differently by different XPS hardware and/or software companies. Plots of the GLS show that it is a better mathematical representation of a function that is intermediate between a pure Gaussian and a pure Lorentzian. The GLS also appears to be a better approximation of the Voigt function. Because of the more compact nature of the Gaussian, the GLP does not have significant 'wings', and for low values of *m* it is a rather close approximation of a pure Gaussian. Nevertheless, as illustrated with three examples, the GLP is also a useful synthetic line shape for XPS narrow scan peak fitting.

3.6. Acknowledgments

In February, 2014 one of the authors of this work (MRL) wrote an article in a trade/technical magazine, Vacuum Technology & Coating (VT&C), on 'The Gaussian-Lorentzian Sum, Product, and Convolution (Voigt) Functions Used in Peak Fitting XPS Narrow Scans, and an Introduction to the Impulse Function". [26] After publishing this article, MRL posted a copy of it to his Research Gate page, where, according to Wikipedia, Research Gate is: "a social networking site for scientists and researchers to share papers, ask and answer questions, and find

collaborators." He had not anticipated that this article would receive any special attention. However, as of Mar. 15, 2018 it had received 4137 reads – far more than most of his other articles. This unexpected and enthusiastic response prompted this submission. Accordingly, with the permission of Vacuum Technology & Coating, we present this article, which has been reformatted for this journal, reedited, and more thoroughly referenced. VT&C also approved the use of another of MRL's articles in the Supporting Information. Varun Jain, one of MRL's graduate students, took on the task of adapting the original article. His contributions have been significant. Note that the position taken by MRL in the VT&C article was that the GLP should be avoided for mathematical reasons. This article represents his/our latest thinking on this topic.

3.7. Figures

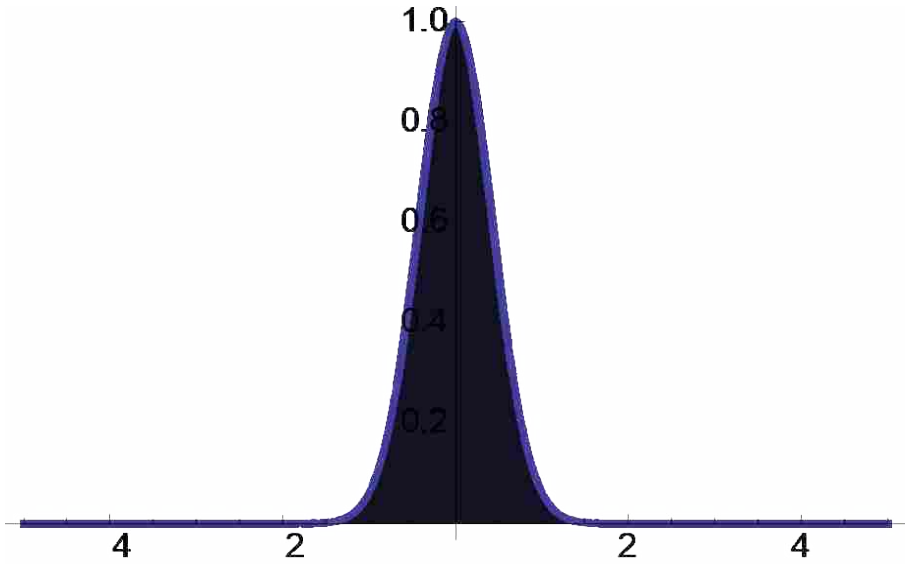

Figure 3.1. The Gaussian function from Equation 3.1 with parameters h = 1, E = 0, and F = 1.

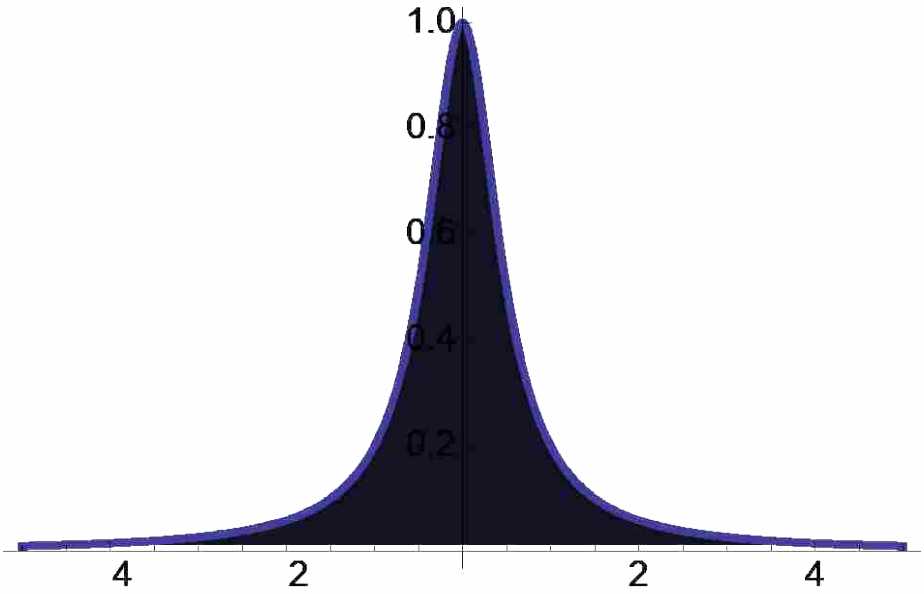

Figure 3.2. The Lorentzian from Equation 3.2 with parameters h = 1, E = 0, and F = 1.

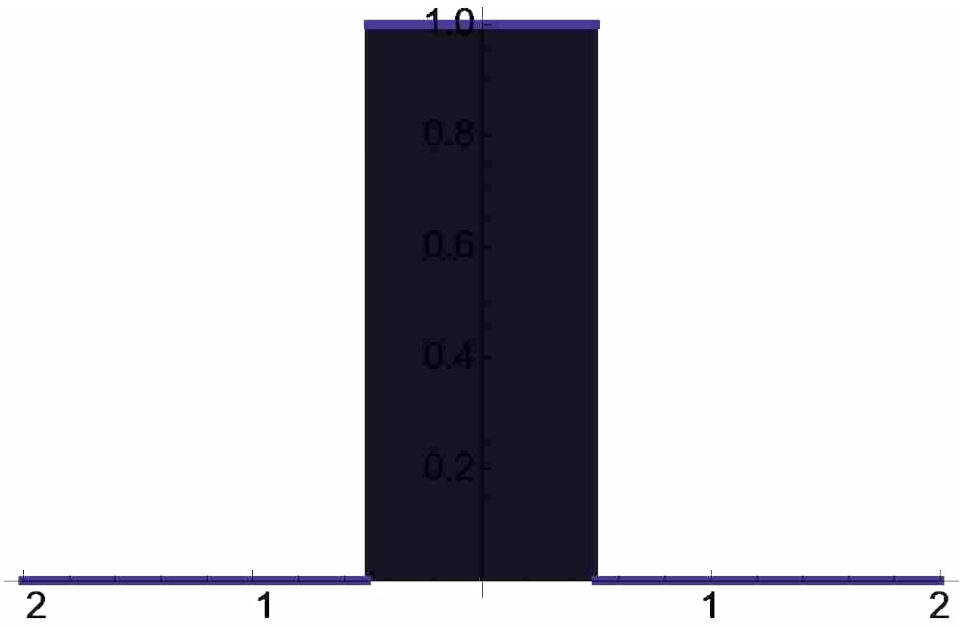

Figure 3.3. Graph of the slit function, S(x), with a width of 1.

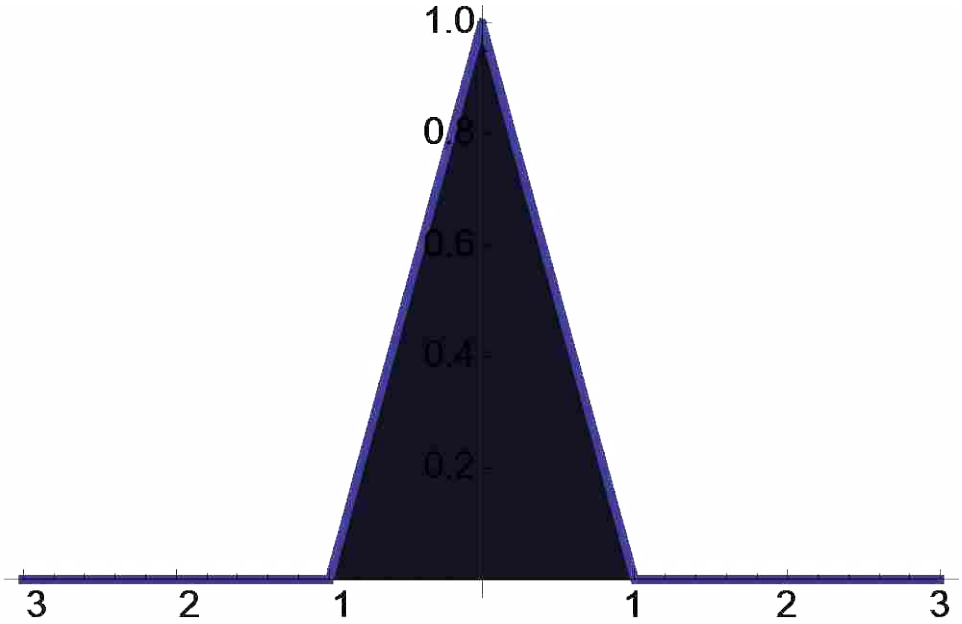

Figure 3.4. Convolution of the slit function in Equation 3.4, with itself (S(x)*S(x)) forming a triangle function, T(x).

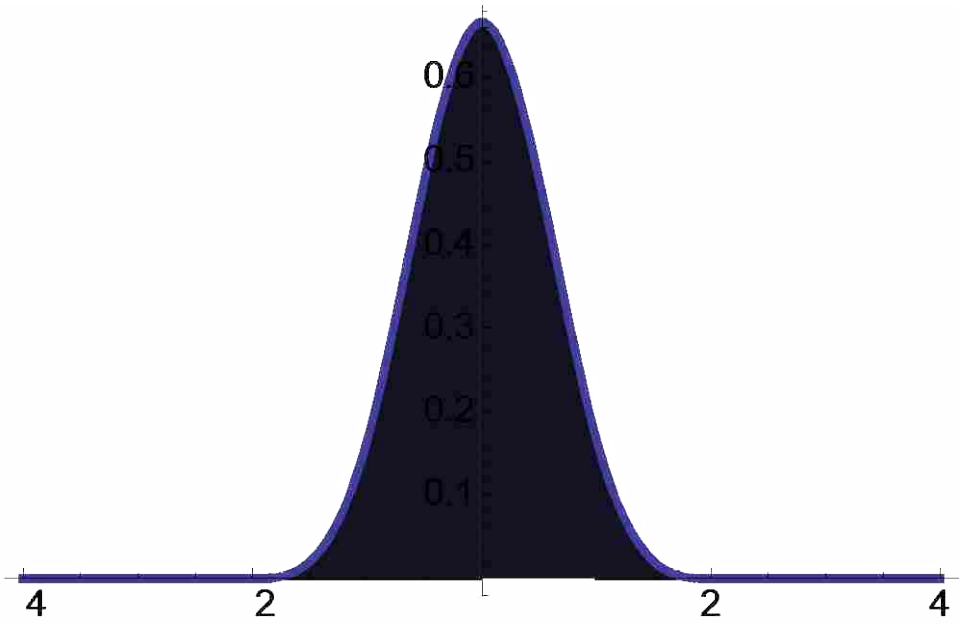

Figure 3.5. Convolution of the triangle function with itself (T(x)*T(x)) forming a function that appears rather Gaussian-like.

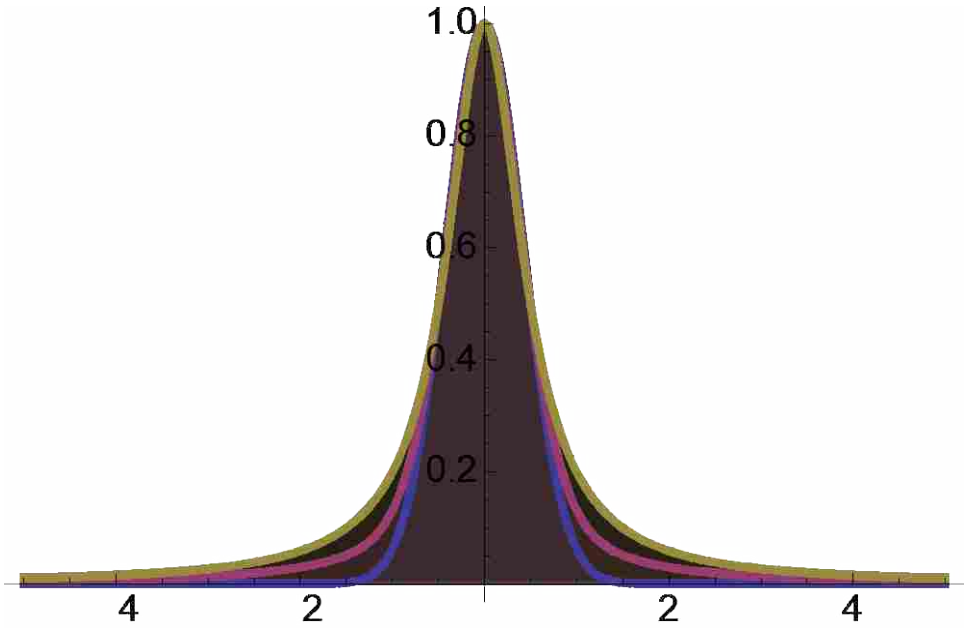

Figure 3.6. Graph of the GLS function (Equation 3.5) with parameters h = 1, E = 0, and F = 1 for m = 0 (bottom, blue line), m = 0.5 (middle, red line), and m = 1 (top, green line).

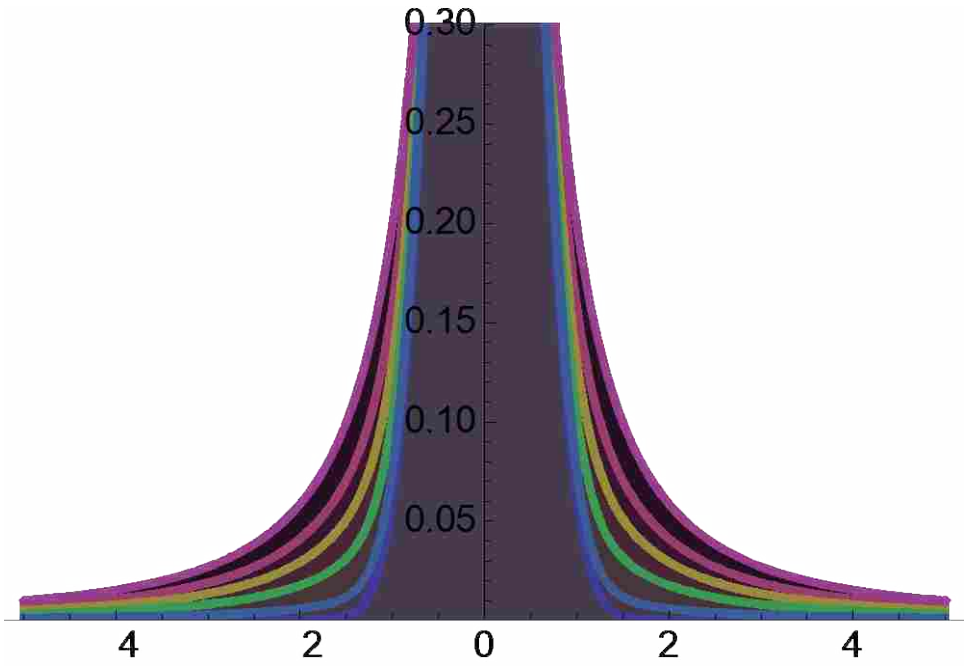

Figure 3.7. Graph of the GLS function (Equation 3.3) with parameters h = 1, E = 0, and F = 1 for (from bottom to top) m = 0, 0.1, 0.3, 0.5, 0.7, and 1.

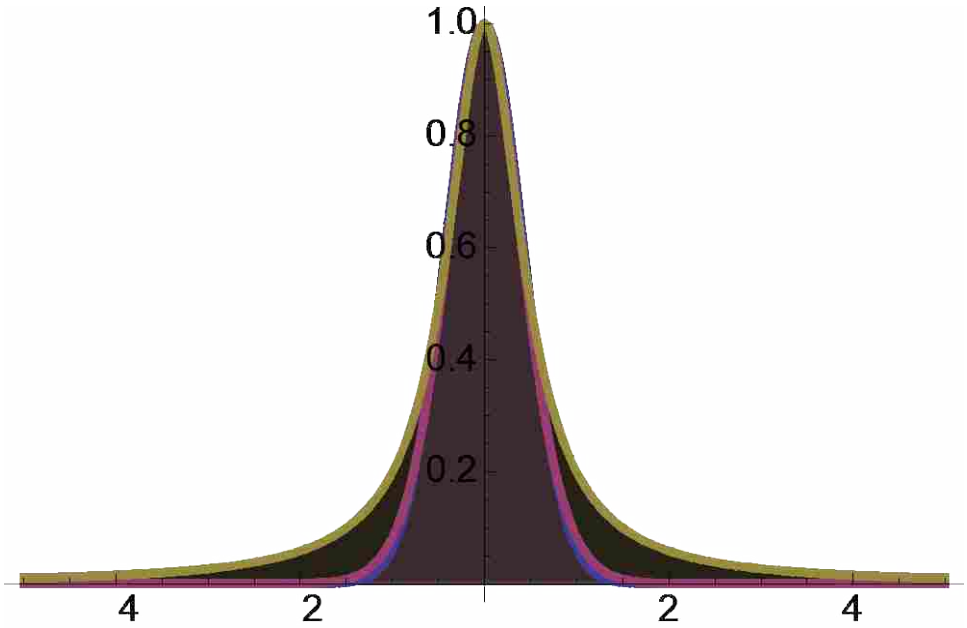

Figure 3.8. Graph of the GLP function (Equation 3.6) with parameters h = 1, E = 0, and F = 1 for m = 0 (bottom, blue line), m = 0.5 (middle, red line), and m = 1 (top, green line).

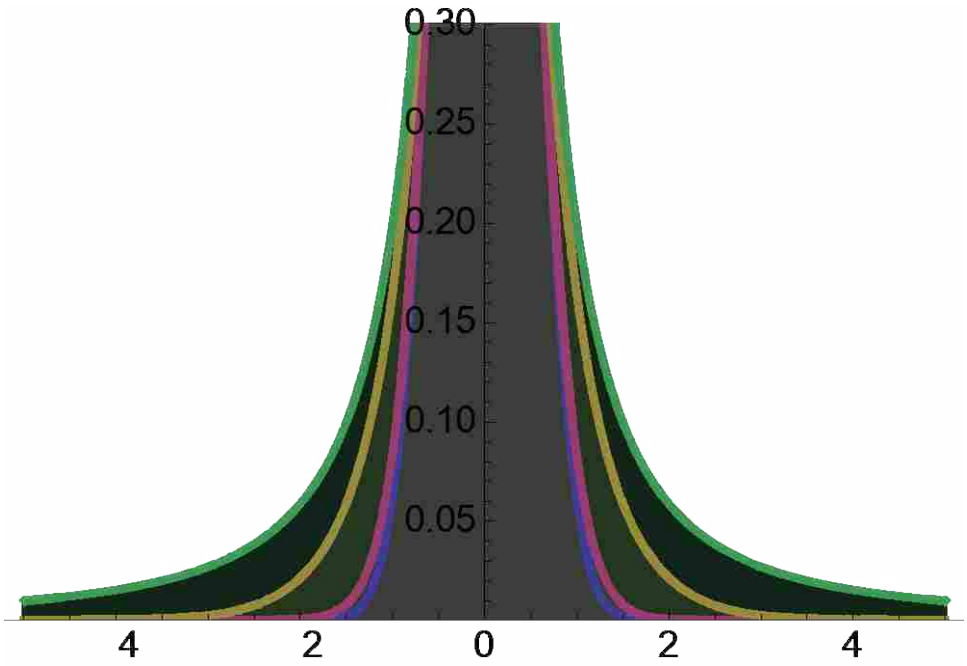

Figure 3.9. Graph of the GLP function (Equation 3.6) with parameters h = 1, E = 0, and F = 1 for, going from bottom to top, m = 0 (blue line), m = 0.5 (red line), m = 0.9 (yellow line), and m = 1 (green line).

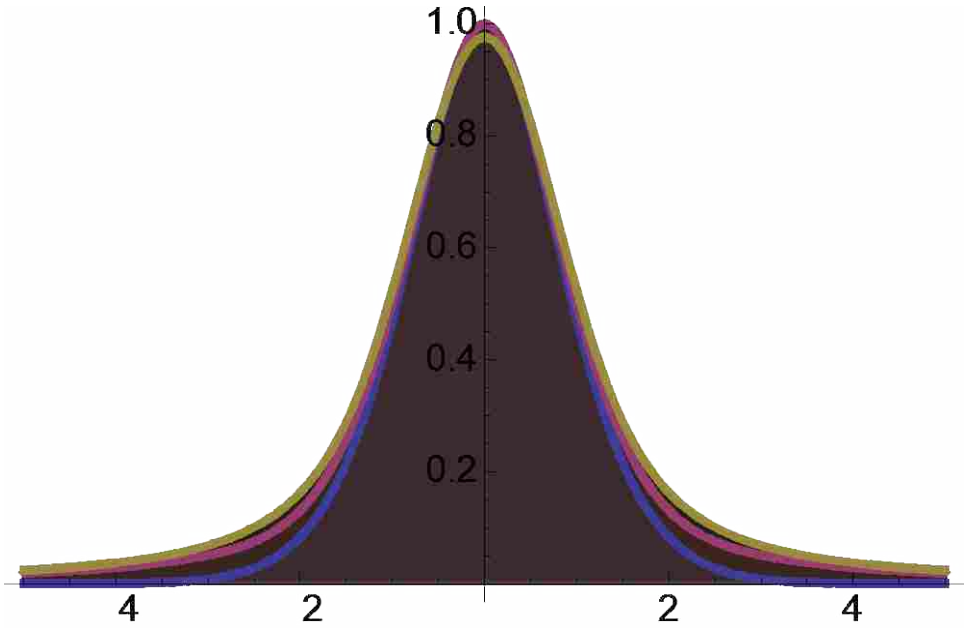

Figure 3.10. Graphs of the GLS function with m = 0.5 (red line), the GLP function with m = 0.5 (blue line), and the Voigt function (yellow line). All three functions have widths of 2 and are centered at the origin. The Voigt function here is the convolution of a Gaussian function with a width of 1.3 and a Lorentzian function with the same width. A figure similar to this one previously appeared in paper by Hesse and coworkers.[12]

3.8. References

1. Jain, V.; Biesinger, M. C.; Linford, M. R., The Gaussian-Lorentzian Sum, Product, and Convolution (Voigt) functions in the context of peak fitting X-ray photoelectron spectroscopy (XPS) narrow scans. *Applied Surface Science* **2018,** *447*, 548-553.
2. Watts, J. F.; Wolstenholme, J., *An Introduction to Surface Analysis by XPS and AES*. John Wiley & Sons, Ltd: Chichester, UK, 2005.
3. Gupta, V.; Ganegoda, H.; Engelhard, M. H.; Terry, J.; Linford, M. R., Assigning Oxidation States to Organic Compounds via Predictions from X-ray Photoelectron Spectroscopy: A Discussion of Approaches and Recommended Improvements. *Journal of Chemical Education* **2014,** *91* (2), 232-238.
4. Crist, B. V., Advanced Peak-Fitting of Monochromatic XPS Spectra. *Journal of Surface Analysis* **1998,** *4* (3), 428-433.
5. Sherwood, P. M. A., Curve fitting in surface analysis and the effect of background inclusion in the fitting process. *Journal of Vacuum Science & Technology A: Vacuum, Surfaces, and Films* **1996,** *14* (3), 1424-1432.
6. Beamson, G.; Briggs, D., High-Resolution Monochromated X-Ray Photoelectron-Spectroscopy of Organic Polymers - a Comparison between Solid-State Data for Organic Polymers and Gas-Phase Data for Small Molecules. *Molecular Physics* **1992,** *76* (4), 919-936.
7. Doniach, S.; Sunjic, M., Many-electron singularity in X-ray photoemission and X-ray line spectra from metals. *Journal of Physics C: Solid State Physics* **1970,** *3* (2), 285.
8. Ganegoda, H.; Jensen, D. S.; Olive, D.; Cheng, L. D.; Segre, C. U.; Linford, M. R.; Terry, J., Photoemission studies of fluorine functionalized porous graphitic carbon. *Journal of Applied Physics* **2012,** *111* (5).
9. Singh, B.; Hesse, R.; Linford, M. R., Good Practices for XPS (and other Types of) Peak Fitting. Use Chi Squared, Use the Abbe Criterion, Show the Sum of Fit Components, Show the (Normalized) Residuals, Choose an Appropriate Background, Estimate Fit Parameter Uncertainties, Limit the Number of Fit Parameters, Use Information from Other Techniques, and Use Common Sense. *Vacuum Technology and Coating* December, 2015.
10. Singh, B.; Gomez, A., H.; Terry, J.; Linford, M., R. , Good Practices for XPS Peak Fitting, II' *Vacuum Technology & Coating* August 2016.
11. Hesse, R.; Chasse, T.; Streubel, P.; Szargan, R., Error estimation in peak-shape analysis of XPS core-level spectra using UNIFIT 2003: how significant are the results of peak fits? *Surface and Interface Analysis* **2004,** *36* (10), 1373-1383.
12. Hesse, R.; Chasse, T.; Szargan, R., Peak shape analysis of core level photoelectron spectra using UNIFIT for WINDOWS. *Fresenius Journal of Analytical Chemistry* **1999,** *365* (1-3), 48-54.
13. Hesse, R.; Streubel, P.; Szargan, R., Product or sum: comparative tests of Voigt, and product or sum of Gaussian and Lorentzian functions in the fitting of synthetic Voigt-based X-ray photoelectron spectra. *Surface and Interface Analysis* **2007,** *39* (5), 381-391.
14. Singh, B.; Diwan, A.; Jain, V.; Herrera-Gomez, A.; Terry, J.; Linford, M. R., Uniqueness plots: A simple graphical tool for identifying poor peak fits in X-ray photoelectron spectroscopy. *Applied Surface Science* **2016,** *387*, 155-162.
15. Charles, C.; Leclerc, G.; Pireaux, J.-J.; Rasson, J.-P., Introduction to wavelet applications in surface spectroscopies. *Surface and Interface Analysis* **2004,** *36* (1), 49-60.

16. Charles, C.; Leclerc, G.; Louette, P.; Rasson, J.-P.; Pireaux, J.-J., Noise filtering and deconvolution of XPS data by wavelets and Fourier transform. *Surface and Interface Analysis* **2004,** *36* (1), 71-80.
17. Chatterjee, S.; Singh, B.; Diwan, A.; Lee, Z. R.; Engelhard, M. H.; Terry, J.; Tolley, H. D.; Gallagher, N. B.; Linford, M. R., A perspective on two chemometrics tools: PCA and MCR, and introduction of a new one: Pattern recognition entropy (PRE), as applied to XPS and ToF-SIMS depth profiles of organic and inorganic materials. *Applied Surface Science* **2018,** *433*, 994-1017.
18. Singh, B.; Velazquez, D.; Terry, J.; Linford, M. R., Comparison of the equivalent width, the autocorrelation width, and the variance as figures of merit for XPS narrow scans. *Journal of Electron Spectroscopy and Related Phenomena* **2014,** *197*, 112-117.
19. Singh, B.; Velazquez, D.; Terry, J.; Linford, M. R., The equivalent width as a figure of merit for XPS narrow scans. *Journal of Electron Spectroscopy and Related Phenomena* **2014,** *197*, 56-63.
20. Fairley, N., In Surface Analysis by Auger and X-Ray Photoelectron Spectroscopy. Briggs, D.; Grant, J. T., Eds. IM Publications: UK, 2003; pp 397-403.
21. Fairley, N., Peak Fitting in XPS, www.casaxps.com. UK, **2006**.
22. Linford, M. R., An Introduction to Convolution with a Few Comments Beforehand on XPS' Vacuum Technology & Coating, . *Vacuum Technology & Coating* June, June, 2014, pp 25-31.
23. Bracewell, R. N., *Fourier Transform and Its Applications* 3rd ed.; Mcraw-Hill Companies: USA, 1999.
24. Beamson, G.; Briggs, D., High Resolution XPS of Organic Polymers-The Scienta ESCA300 Database. Wiley Interscience: USA, 1992; p 31.
25. Sherwood, P. M. A., *Practical Surface Analysis*. John Wiley Chichester, England **1983**.
26. Linford, M. R., The Gaussian-Lorentzian Sum, Product, and Convolution (Voigt) Functions Used in Peak Fitting XPS Narrow Scans, and an Introduction to the Impulse Function' Vacuum Technology & Coating. *Vacuum Technology & Coating* July, 2014 pp 27-33.

CHAPTER 4: Performance Comparison of Three Chemical Vapor Deposited Aminosilanes in Peptide Synthesis: Effects of Silane on Peptide Stability and Purity

4.1 Statement of Attribution

This document was originally published as Gaurav Saini, Olgica Trenchevska, Loren J. Howell, James G. Boyd, David P. Smith, Varun Jain, Matthew R. Linford. Performance Comparison of Three Chemical Vapor Deposited Aminosilanes in Peptide Synthesis: Effects of Silane on Peptide Stability and Purity. *Langmuir*, **2018**, *34*, 11925−11932.[1] I contributed as a co-author in this publication. My contribution includes the XPS analysis/peak fitting of surfaces modified through the chemical vapor deposition of three aminosilanes. Here, I am including the full paper to provide a context for what I did.

4.2 Abstract

Silicon oxide substrates underwent gas phase functionalization with various aminosilanes, and the resulting surfaces were evaluated for their suitability as a solid support for solid phase peptide synthesis (SPPS). APTES (3-aminopropyltriethoxysilane), APDEMS (3-aminopropyldiethoxymethylsilane) and APDIPES (3-aminopropyldiisopropylethoxysilane) were individually applied to thermal oxide-terminated silicon substrates via gas-phase deposition. Coated surfaces were characterized by spectroscopic ellipsometry (SE), contact angle goniometry, X-ray photoelectron spectroscopy (XPS), atomic force microscopy (AFM), and spectrophotometry. Model oligopeptides with 16 residues were synthesized on the amino surfaces, and the chemical stabilities of the resulting surfaces were evaluated against a stringent side chain deprotection (SCD) step, which contained trifluoroacetic acid (TFA) and trifluoromethanesulfonic acid (TFMSA). Functionalized surface thickness loss during SCD was most acute for APDIPES and the observed relative stability order was APTES > APDEMS > APDIPES. Amino surfaces

were evaluated for compatibility with stepwise peptide synthesis where complete deprotection and coupling cycles is paramount. Model trimer syntheses indicated that routine capping of unreacted amines with acetic anhydride significantly increased purity as measured by MALDI-MS. An inverse correlation between the amine loading density and peptide purity was observed. In general, peptide purity was highest for the lowest amine density APDIPES surface.

4.3 Introduction

Surface immobilization of a probe is a critical step in the fabrication of a biosensor. Different biomolecules such as DNA[2-4], RNA[5], proteins[6], peptides[7], lipids[8], and carbohydrates[9] have been used as probes in biosensors. Peptide-based biosensors have been used in a number of applications *e.g.*, analyses of protein-protein[10] and protein-peptide[11] interactions, and characterization of antibody binding.[12] Solid phase peptide synthesis (SPPS) is the method of choice for the chemical synthesis of peptides at both research and industrial scales.[13-15] For the synthesis of peptide arrays on planar substrates, silicon,[16-17] glass,[18] and plastic[19] have been used effectively. All these substrates require surface modification in the form of a chemical handle or linker with which to anchor the nascent peptide. A variety of functional groups have been investigated to modify these substrates' surfaces and make them reactive towards subsequent coupling. Epoxy/N-hydroxysuccinimide ester-functionalized surfaces have been used to print aminooxy-labeled peptides on glass slides.[20] Aldehyde-functionalized surfaces have been used to conjugate biomolecules such as hydrazide-modified streptavidin and aminooxy-labeled peptides to glass.[21-22] The use of amine surfaces in peptide synthesis is also widely reported.[23-24] Researchers have also used semicarbazide surfaces in the fabrication of peptide arrays and for peptide functionalization.[25-26] In one study, glyoxylyl peptides were used to print peptide arrays on semicarbazide-modified glass substrate.[27] Thiolated molecules have been used to modify gold

surface to immobilize biomolecules. For example, self-assembled monolayers of alkanethiolates have been used to introduce maleimide functional groups onto gold. These groups were subsequently used for peptide and carbohydrate immobilization.[28]

Among the various functionalities mentioned above, amine-modified surfaces are most commonly used because of the reactivity of the nucleophilic amine towards a diverse range of functional groups. Indeed, a variety of amine surfaces have been used in a wide spectrum of applications including immobilization of oligonucleotides,[29] carbohydrates,[30] peptides,[26, 31-32] and in the fabrication of biosensors.[33-34] For example, 3-aminopropyltrimethoxysilane has been used for peptide synthesis on porous silicon,[35] a polymeric amino coating synthesized from amino-terminated poly(ethylene glycol) methacrylate (PEGMA)/methyl methacrylate was used to synthesize a combinatorial peptide library on a glass slide,[36] and a polyamidoamine (PAMAM) dendrimer amino coating was used to immobilize carbohydrates on gold surfaces.[30]

Here, we report the use of aminosilane coatings for peptide synthesis on silicon oxide terminated silicon substrate. We synthesized three different aminosilane coatings and determined the effects of their structures/properties on the quality of peptide synthesis. These aminosilanes are 3-aminopropyltriethoxysilane (APTES), 3-aminopropyldiethoxymethylsilane (APDEMS), and 3-aminopropyldiisopropylethoxysilane (APDIPES), which are expected to produce coatings with different morphologies and chemical properties due to the different numbers of attachment points/surface reactive groups they contain: three for APTES, two for APDEMS, and one for APDIPES. Gas phase deposition of these aminosilanes was used as it often provides better control of reproducibility and homogeneity of the coating than solution phase deposition.[37-43] Matrix-assisted laser desorption ionization mass spectrometry (MALDI-MS) was used to measure the purity of peptides synthesized on these aminosilane surfaces. The effect of acetic anhydride (Ac_2O)

capping of unreacted amine groups during peptide synthesis on peptide product purity was also determined. Finally, we show that the three aminosilane surfaces have different degrees of chemical stability to trifluoroacetic acid/trifluoromethanesulfonic acid (TFA/TFMSA), a reagent commonly used for side chain deprotection (SCD) following SPPS. To our knowledge, no previous work has reported a performance comparison of these aminosilane anchor molecules in peptide synthesis. We believe that this work is important because it demonstrates the impact of surface properties of three aminosilane coatings on probe purity which is a crucial parameter in peptide microarray fabrication.

4.4 Experimental Section

4.4.1 Materials and Chemicals

Single side polished silicon wafers (P/B doped, <100> orientation, 1-100 ohm-cm resistivity) containing ~250 nm thick thermal SiO2 coating were purchased from a standard supplier. All tert-butyloxycarbonyl (Boc) protected amino acids (purity ≥ 99 %) were purchased from IRIS Biotech GmbH, Germany. Amino acid coupling reagents N,N'-diisopropylcarbodimide (DIC), 1-hydroxybenzotriazole, diisopropylethylamine (DIEA), and 1-[Bis(dimethylamino)methylene]-1H-1,2,3-triazolo[4,5-b]pyridinium3-oxide hexafluorophosphate (HATU) were from Sigma-Aldrich, USA, and IRIS Biotech, respectively. N-methylpyrrolidone (NMP) was purchased from VWR, USA. Reagents for the colorimetric assay sulfo-SDTB (sulfosuccinimidyl-4-O-(4,4'-dimethoxytrityl) butyrate), and dimethylformaminde (DMF), isopropyl alcohol (IPA) and perchloric acid were purchased from BioWorld, OH, USA and Sigma-Aldrich, USA, respectively. Photoresist formulation reagents bis-(4-tert-butylphenyl)iodonium triflate, isopropylthioxanthone, and propylene glycol monomethyl ether acetate were purchased from Sigma-Aldrich, USA and Integrated Micro Materials, USA, respectively. Methyl isobutyl

ketone was purchased from Sigma-Aldrich, USA. Aminosilanes APTES (>99%), APDEMS (95%), and APDIPES (>99%) were purchased from Gelest, PA, USA. Side chain deprotection reagents trifluoroacetic acid (Protein Technologies, AZ, USA), dimethylsulfide, m-cresol and trifluoromethanesulfonic acid (TCI America), and thioanisole and 2,2'-(ethylenedioxy)diethanethiol (DODT, Sigma-Aldrich, USA) were used as received. Reagents for MALDI-MS analysis iodoacetonitrile (ICN) and (N-Succinimidyloxycarbonylmethyl)tris(2,4,6-trimethoxyphenyl)phosphonium bromide (TMPP-NHS) were purchased from Sigma-Aldrich, USA. Acetic anhydride capping reagents were purchased from Glen Research, VA, USA, and were mixed just prior to use.

4.4.2 Substrate Cleaning

Silicon substrates were cleaned in piranha solution (66% conc. H2SO4:34% H2O2) at 85°C for 30 minutes before aminosilane functionalization. Caution: Piranha solution is extremely acidic and should be handled with care. After piranha solution treatment, silicon substrates were rinsed with copious amounts of water and spin dried (8" wafer) or blow dried with nitrogen (2.5 x 2.0 and 7.0 x 7.0 cm silicon coupons).

4.4.3 Aminosilane Functionalization

Chemical functionalization of piranha-cleaned silicon substrates with aminosilanes was carried out via gas-phase deposition in a chemical vapor deposition system from Yield Engineering Systems, CA. In this tool, the chemical reagent is injected into an externally heated reaction vessel (connected to the reaction chamber through a pneumatic valve) until a set chamber pressure, called the base pressure, is achieved. The injected chemical evaporates inside the reaction vessel and is introduced into the chamber in vapor form. In our work, the chamber temperature, base pressure and aminosilane injection volume were 150°C, 0.500 Torr, and 2 mL, respectively. The process

time for functionalization was 30 minutes. No surface dehydration was performed prior to aminosilane deposition. The CVD chamber was plasma cleaned between aminosilanes deposition to prevent contamination from previously used aminosilane. After each plasma cleaning, the chamber was pre-conditioned with the respective aminosilane by performing two mock runs without silicon wafer before the actual run.

4.4.4 Contact Angle Measurements

A Rame-Hart goniometer (Model 400) was used to measure the water contact angles of piranha-cleaned and aminosilane-functionalized substrates. The syringe was filled with 18.0 MΩ resistivity deionized water. The contact angle was measured using the static sessile drop method. Spectroscopic ellipsometry: Thicknesses of silicon oxide, and the aminosilane and peptide coatings were determined using an M2000V spectroscopic ellipsometer from the J. A. Woolam Co. (Lincoln, NE, USA) equipped with a 50W QTH lamp that generated wavelengths from 370-1000 nm. The substrate and coatings (SiO2, aminosilane, and peptide) were modeled using a three-layer Si/interface layer/SiO2 model as the optical constants of organic thin films and SiO2 are comparable to each other. The interface layer between the silicon and ca. 250 nm layer of thermal oxide was 12.5Å thick. Data acquisition was performed at three different angles of incidence i.e., 55, 60, and 65 degrees.

4.4.5 X-ray Photoelectron Spectroscopy

The atomic compositions of the surfaces were determined using an XPS instrument (Vacuum Generators 220i-XL) present at the Goldwater Materials Science Facility, Arizona State University, Tempe, USA. The instrument contains an Al Kα monochromatic X-ray source (1486.6 eV) with a hemispherical analyzer. The spot size for X-ray beam was 400 μ. The take-off angle

was 90 degrees. The dwell time for both survey and high resolution scans was 50 msec. The pass energies for survey scan and high resolution scan were 150 eV and 40 eV, respectively.

Every care was taken to minimize exposure of coated substrates to the atmosphere. After CVD, aminosilane-functionalized substrates were cooled down in a nitrogen atmosphere and packaged under a nitrogen atmosphere. The only air exposure to atmosphere was during loading into the XPS instrument.

4.5 Results and Discussion

4.5.1 Characterization of Aminosilane Coatings

Gas-phase deposited aminosilane coatings were analyzed by SE, contact angle goniometry, AFM, colorimetry, and XPS. The thicknesses of the APTES, APDEMS, and APDIPES coatings, as measured by SE, are 6.5±0.4 Å, 5.3±0.4 Å, and 6.2±0.3 Å, respectively. Each thickness is an average of eight measurements on two 8" wafers (four measurements on each wafer) that were silanized together in the CVD system. The APTES and APDIPES coatings are slightly thicker than the APDEMS coating. As shown in Figure 4.1, all three aminosilanes have the same number and types of atoms in the main chain but differ in the number of hydrolyzable ethoxy groups attached to silicon. APTES and APDEMS contain three and two ethoxy groups, respectively. In the presence of water APTES can form a network polymer and APDEMS can form linear polymer chains. APDIPES cannot polymerize as it contains only one ethoxy group. However, it has two bulky isopropyl groups that will contribute to the thickness of the coating in terms of the amount of mass sensed by SE. We think that the presence of two isopropyl groups outweighs APDIPES' inability to polymerize which is manifested as it having a thicker coating than APDEMS. Thus different degrees of polymerization on the surface, the number of possible attachment points, and the different side groups on the adsorbates all contribute to the observed thicknesses.

In contrast to the rather small differences in thickness by SE, the three aminosilanes exhibit remarkably different wetting properties. The WCA is lowest for the APTES coating (44±2°), relatively higher for APDEMS coating (60±1°) and highest for APDIPES coating (82±1°). These WCA values are the average of eight measurements on two 8" wafers (four measurements on each wafer). The WCA for the piranha cleaned substrate is less than 10° indicating a highly polar surface before CVD. Apart from different densities of polar amine groups on the surfaces (see Table 1), these aminosilanes differ in the amount of carbon bonded to silicon as side groups. APDEMS and APDIPES have one and six more carbon atoms than APTES, respectively. APTES also has a greater chance of producing a coating with residual silanol groups, which would result from hydrolyzed ethoxy groups. Therefore, the observed trend in WCA can be attributed to different concentrations of polar and nonpolar functional groups in the three aminosilane coatings.

Atomic force microscopy was used to determine the roughnesses of the three aminosilane-coated surfaces. The RMS roughness of the piranha-cleaned surface is 0.223 nm, and this value does not change much after functionalization with the aminosilanes. That is, the RMS roughnesses of the surfaces after APTES, APDEMS, and APDIPES functionalization are 0.239 nm, 0.239 nm, and 0.248 nm, respectively. This indicates that CVD of these aminosilanes results in smooth aminosilane films that are free of aggregates, as reported by Zhang et al.[38]

Table 4.1. Nitrogen content of three aminosilane coatings as measured by spectrophotometry and XPS.

Coating type	#NH_2 groups/cm^2 (spectrophotometry)	N1s/Si2p (XPS)
APDIPES	6.5±0.4E13	0.021±0.002
APDEMS	1.4±0.2E14	0.030±0.001
APTES	1.7±0.2E14	0.045±0.001

XPS of the coated silicon substrates was performed to confirm surface functionalization and determine respective nitrogen content.[44] A small but noticeable nitrogen peak is observed in the XPS spectra of all of the coated substrates (Figures 4.2, 4.7, and 4.12), which in each case confirms surface functionalization with aminosilane. The N1s/Si2p ratios for APTES, APDEMS, and APDIPES coated silicon substrates are 0.045, 0.030, and 0.021, respectively, indicating that the surface coverage is highest for the APTES coating, intermediate for the APDEMS coating and lowest for the APDIPES coating. This result is consistent with the fact that APTES and APDEMS can polymerize on the surface and deposit denser coatings. Conversely, APDIPES deposits a less dense coating as it is sterically hindered due to the presence of two bulky isopropyl groups, and has a single ethoxy group. Figure 4.2 to 4.16 represents all three survey scans from APDIPES, APTES, and APDEMS and high resolution scans of C 1s,O 1s, Si 2p, and N 1s.

High resolution N1s scans were used to obtain information on molecule orientation and interaction between functional groups in the aminosilane coatings. These N1s scans (Figures 4.6, 4.11, and 4.16) show the presence of protonated and unprotonated nitrogen in all three aminosilanes' coatings. The presence of protonated nitrogen indicates that some aminosilane molecules are possibly not oriented away from surface but rather that they electrostatically interact with the surface and neighboring silanols via primary amine groups. The remaining aminosilane molecules with unprotonated nitrogen atoms correspond to those molecules that don't interact with silanols and are oriented away from the surface. The three aminosilanes' coatings contain different percentages of protonated and unprotonated nitrogen. The percentage of unprotonated nitrogen is highest in APTES coating (81.6%) followed by APDIPES coating (75.0%), and lowest in APDEMS coating (69.7%). This implies that the APTES surface has the highest percentage and APDEMS surface has lowest percentage of molecules oriented away from surface.

The C1s/N1s XPS ratio of the APDIPES surface was used to determine potential adventitious carbon contamination. APDIPES is chosen because it is a simple surface that has carbon contributions from two isopropyl groups and three carbons in the main chain. This makes interpretation of the XPS data very straightforward. The C1s/N1s ratio for APDIPES surface is 10.7±1.3 which is 19% higher than the theoretical C/N ratio of 9.0. This indicates some inevitable adventitious carbon contamination due to the ex-situ nature of the technique.

The absolute concentrations of the reactive amine groups in the aminosilane coatings were determined by spectrophotometry. The silanol groups on the SiO_2 over-layer act as the reaction sites for aminosilane molecules. Thus, the concentration of silanols is likely to have an influence on the amine density of aminosilane coatings. Xu et al. have reported surface concentration of isolated silanols in planar silica to be 9.3E13/cm^2.[45] In addition to isolated silanols, the silica surface also contains geminal and vicinal silanols that will add to its total silanol content.[46] Considering all these facts, we assume the concentration of reactive silanols on our planar silica surface to be around 1.0E14/cm^2.

The surface amine densities of the three aminosilane coatings, along with their N1s/Si2p XPS ratios are displayed in Table 1. The surface amine densities of the three amino coatings follow the same order as the XPS N1s/Si2p ratio *i.e.*, APTES > APDEMS > APDIPES which again implies that among the three aminosilanes studied, APTES and APDIPES produce the most and least dense coatings, respectively. A reasonable agreement between the XPS and amine density data of APDIPES and APTES coatings is observed. However, slight disagreement in the XPS and amine density data of APDIPES and APDEMS, and APDEMS and APTES coatings is observed. One plausible explanation for this discrepancy could be the fact that different batches of Si/SiO_2

substrates that will likely differ in surface silanol concentration were used in the spectrophotometric and XPS measurements.

4.5.2 Chemical Stability

In SPPS with Boc amino acids, the residue side chains are protected with blocking groups that are stable during Boc removal and require treatment with a very strong acid for removal during the final side chain deprotection (SCD). Acids commonly used include TFMSA or anhydrous liquid hydrogen fluoride. If the surface chemistry is not stable during SCD, the peptides could detach from the surface and diffuse into the SCD mixture. Therefore, the stabilities of the APTES, APDEMS, and APDIPES aminosilane coatings were evaluated. A random dodecapeptide (12-mer) was synthesized using amino acids with no side chain protecting groups on a serine-glycine-serine-glycine (SGSG) tetrapeptide linker on the aminosilane-functionalized surfaces. The peptide-functionalized substrate was subjected three times to SCD in a TFA/TFMSA mixture, and the loss in coating thickness after side chain deprotection was measured. Figure 4.17 shows the total thicknesses of the peptide and aminosilane coatings before and after SCD. Noticeable decreases in coating thickness were observed after the first SCD treatment for all three aminosilane surfaces. This thickness loss is attributed to removal of the aminosilane coating and peptides from the surface, removal of serine side chain protecting group in the SGSG linker, and removal of the Boc group from the N terminus of the 12-mer. Subsequent losses during the second and third SCD treatments is due to removal of the aminosilane coating and peptides from the wafer surfaces. As evident from figure 4.17, the total percent thickness loss after three SCD treatments is lowest for the APTES surface, intermediate for the APDEMS surface, and highest for the APDIPES surface. Moreover, APTES and APDEMS show negligible thickness losses after a second SCD treatment, demonstrating that almost all of the side chain deprotected peptide remained covalently bound to

surface. These results indicate that the APTES and APDEMS surfaces are stable to 4.5 h treatment with TFA/TFMSA but the APDIPES coating is gradually degrading with loss of attached peptide. The differences in chemical stability of the three aminosilane coatings can be attributed to different degrees of surface attachment/crosslinking. APTES contains three ethoxy groups and can react to form up to three bonds with the surface and/or a crosslinked coating. APDEMS has two reactive ethoxy groups and is therefore more limited in its reactivity, and APDIPES can only bind to the surface through a single bond with no subsequent ability to crosslink.

In order to corroborate the thickness loss observed by ellipsometry, XPS was performed on peptide-functionalized APDIPES surfaces before and after the first SCD treatment. After SCD, the N1s/Si2p and C1s/Si2p ratio decrease by 56% and 42%, respectively, which is consistent with the SE results.

4.5.3 MALDI-MS Analysis

A primary objective of this work was to determine the effect of the surface properties of three aminosilane coatings on the efficiency of subsequent SPPS as judged by the purity of the final peptide product. To this end, four peptide dimers: serine-proline (SP), serine-leucine (SL), serine-valine (SV), and serine-phenylalanine (SF) were synthesized on four quadrants of 8" aminosilane-functionalized wafers. Before dimer synthesis, a glycine safety catch linker[47] (G-SCL) was coupled to a glycine-functionalized aminosilane surface to provide on-demand covalent detachment for MS analysis. After dimer synthesis and N-terminal labeling with TMPP-NHS ester, the SCL was activated with ICN. Subsequent treatment with gaseous ammonia cleaves the G-SCL bond forming a C-terminal glycine amide. Thus TMPP labeled trimers: SPG (figure 4.20), SLG, SVG, and SFG are the expected products to be detected by MALDI-MS. Ellipsometry was performed after dimer synthesis on the three aminosilane surfaces. Figure 4.18 shows the

thicknesses of the G-[cleavable linker-G]-X-S layers, where X is P, L, V, and F, as synthesized on the three aminosilane surfaces. The peptide coating is thickest for the APTES surface, somewhat thinner for the APDEMS surface, and thinnest for the APDIPES surface. This data correlates well with the surface amine density of the three aminosilane coatings reported in Table 1 *i.e.*, peptide coating thickness is directly proportional to surface amine density of the aminosilane coating. It is worth noting that almost a linear relationship between amine density and peptide coating thickness is observed for G-[cleavable linker-G]-X-S. However, this relationship deviates from linearity for the long 12 mer peptide synthesized for the chemical stability study. This is possibly due to the fact that steric effects don't play a significant role in short peptide synthesis but become substantial in long peptide synthesis.

4.5.4 Effect of Capping on Peptide Purity

The coupling reaction of surface amines with amino acids in peptide synthesis is not always quantitative. This can be attributed to steric hindrance, poor efficiency of the coupling reaction, or both. Uncoupled amines may react during the subsequent coupling cycle and form deletion products. Acetic anhydride capping of uncoupled amines is a common strategy employed in SPPS to truncate incompletely coupled chains and improve peptide purity.[13] In our work, the presence of unreacted amines on the surface after amino acid coupling was determined by measuring the thickness change due to acetic anhydride capping of uncoupled amines. Figure 4.19 shows the thickness change due to the acetic anhydride capping reaction after G and G-SCL couplings to three aminosilane surfaces. The thickness change is highest for the APTES surface, lower for the APDEMS surface, and lowest for the APDIPES surface. This indicates that the three amino surfaces contain different concentrations of unreacted amines after G and G-SCL coupling

reactions, and the unreacted amine density tracks with the original aminosilane loading as measured colorimetrically (Table 1).

4.5.5 Effect of the Aminosilane Coating on Peptide Purity

The three aminosilanes studied in this work have different chemical structures and are expected to produce coatings with different physicochemical properties. We were curious to determine whether certain coating properties such as amine density and homogeneity of the coating can affect peptide purity. APTES is reported to produce a heterogeneous coating because of its tendency to polymerize.[41] Polymerized APTES coating is likely to present partially buried amines and hydrogen bonded amines.[41] These amines may not be accessible initially for coupling but may become available later in a synthesis and produce impure peptides as a result. The APDEMS coating is expected to be less heterogeneous than the APTES coating. APDIPES cannot polymerize on the surface, and thus is expected to produce a more uniform and homogeneous coating than APTES and APDEMS. Additionally, the surface amine density of the APDIPES coating is much lower than that of the APTES and APDEMS coatings (Table 4.1) so amine groups in the APDIPES coating should be more dispersed and sterically less hindered than the amine groups in the APTES and APDEMS coatings.

To better understand the effects of the aminosilane coatings on peptide purity, uncapped amino surfaces were evaluated for probe purity. Table 4.2 reports the percent purities of the desired peptide for trimer-functionalized uncapped amino surfaces. This number is higher for the SPG, SLG, and SFG-functionalized APDIPES surfaces than the corresponding APTES and APDEMS surfaces, and it is comparable for the SVG-functionalized APDIPES and APTES surfaces. This result indicates that the APDIPES surface, in general, produces purer peptides than APTES and APDEMS surfaces.

Table 4.2. Peptide purity comparison of capped and uncapped syntheses on aminosilane surfaces.

Surface type	Percent purity			
	SPG	SLG	SVG	SFG
APTES (uncapped)	90.0±1.1	93.6±0.2	98.0±0.6	92.9±0.3
APTES (capped)	98.8±0.1	99.5±0.1	99.1±0.1	99.0±0.1
APDEMS (uncapped)	88.8±0.5	94.7±1.1	93.4±0.3	91.1±0.2
APDEMS (capped)	99.2±0.1	99.6±0.0	99.1±0.2	98.5±0.2
APDIPES (uncapped)	98.1±0.4	97.4±0.3	97.8±0.1	97.1±0.3
APDIPES (capped)	99.4±0.1	98.8±0.1	99.3±0.1	98.8±0.1

4.6 Summary and Conclusions

We have determined the merits and disadvantages of three different aminosilanes coatings as attachment layers in peptide synthesis on a Si/SiO_2 substrate. When choosing a substrate for SPPS one needs to consider both the stability of the support and efficiency of peptide synthesis on that support. The results shown here indicate that chemical stability of the peptide-functionalized aminosilane surface to harsh side chain deprotection treatment is proportional to expected degree of cross-linking in the aminosilane coating, *i.e.*, the APTES surface with its three possible attachment points/bonds is most stable, and the APDIPES surface is the least stable to SCD treatment. Unreacted (uncapped) amines in peptide synthesis lead to the formation of deletion products but capping of these amines substantially reduces the formation of deletion products. We also demonstrated that the surface homogeneity and/or amine density of the aminosilane coating impacts the purity of the synthesized peptide, though capping appears to negate this impact, at least in the example of short model peptides. In general, the purest probes are obtained on the more uniform APDIPES, the surface with the lowest density of amine groups. The stability of the

APDIPES surface to harsh acid treatment during SCD is a concern but this can be mitigated by limiting the time of acid exposure. Moreover, the SCD conditions used here are for Boc-based SPPS synthesis. The more widely used Fmoc-based SPPS synthesis approach employs milder SCD conditions that should greatly reduce the extent of surface peptide loss.

4.7 Figures

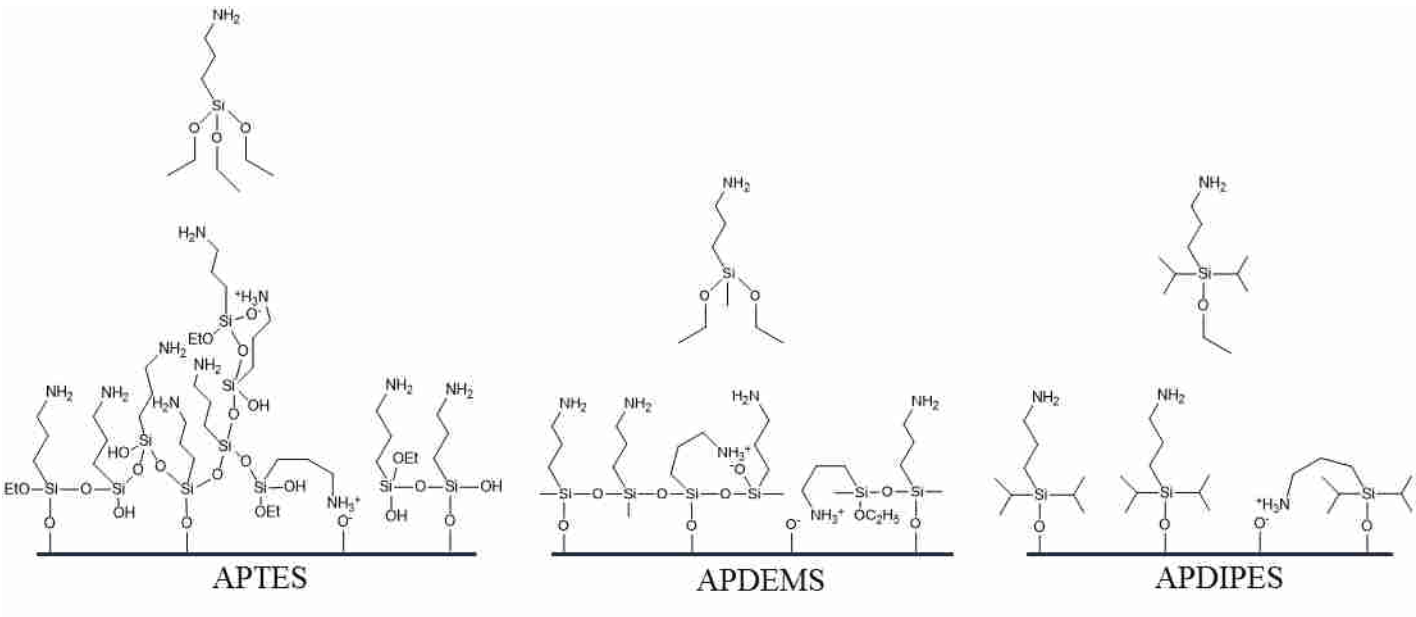

Figure 4.1. Structures of aminosilanes used for deposition.

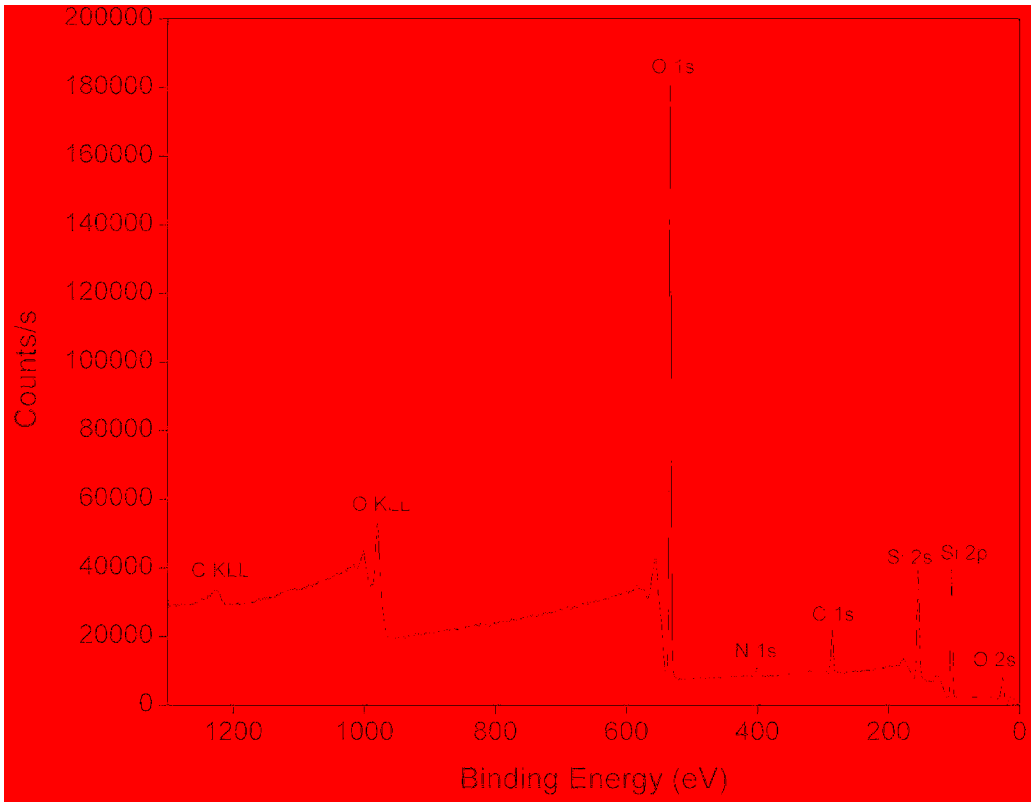

Figure 4.2. XPS survey spectrum of APTES-functionalized silicon substrate.

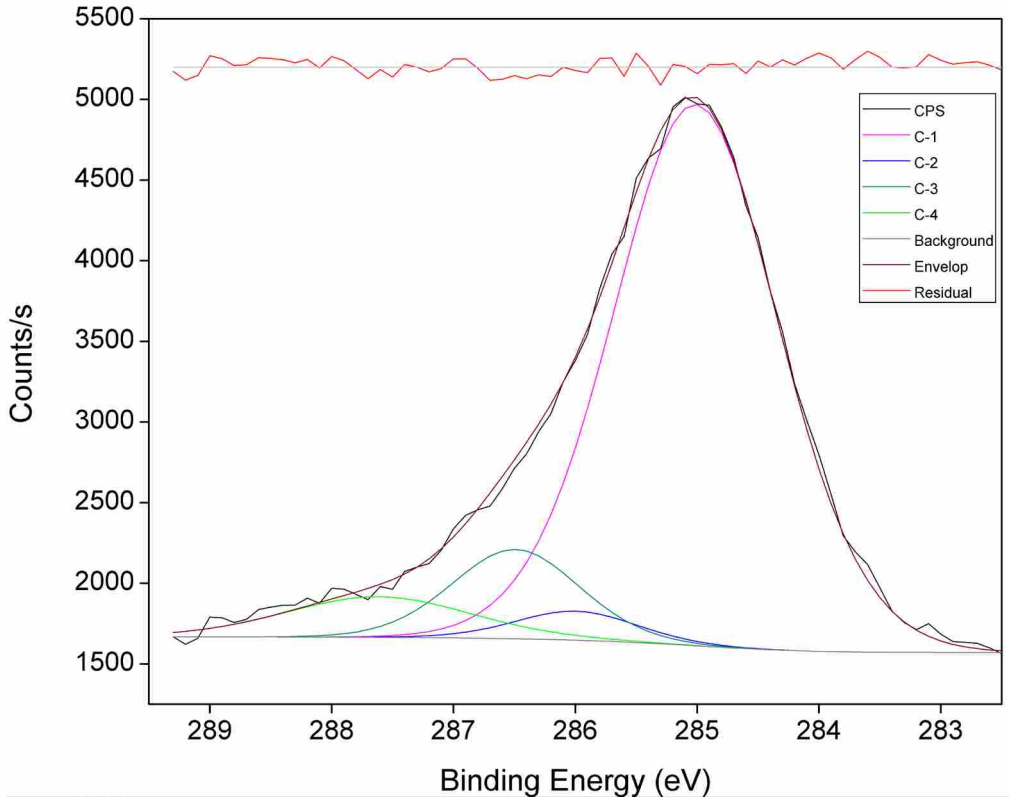

Figure 4.3. High resolution C 1s XPS scans of APTES-functionalized silicon. (We did not perform this peak fitting. It was done at a commercial analysis house.)

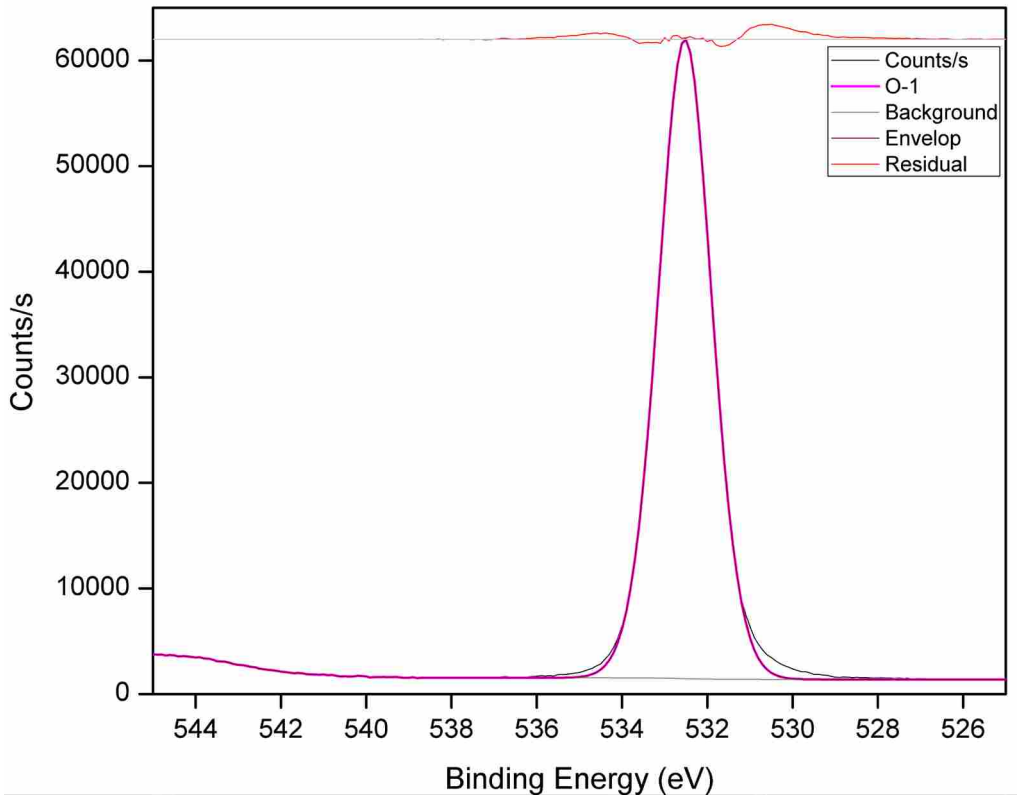

Figure 4.4. High resolution O 1s XPS scans of APTES-functionalized silicon. (We did not perform this peak fitting. It was done at a commercial analysis house.)

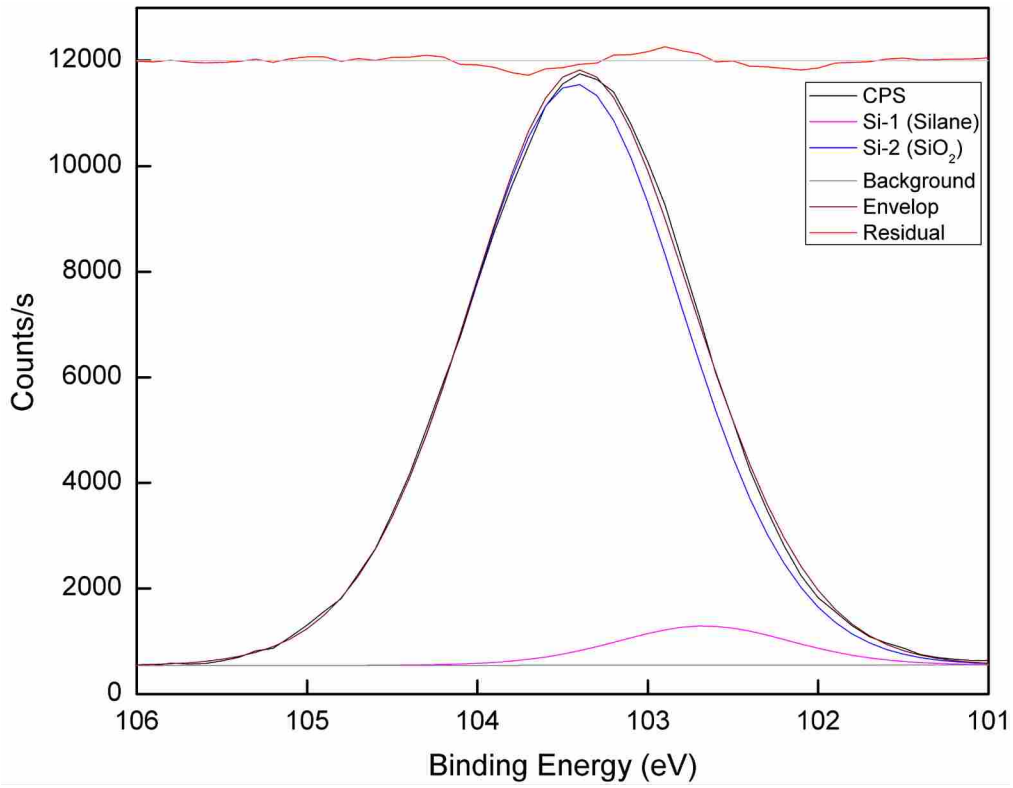

Figure 4.5. High resolution Si 2p XPS scans of APDEMS-functionalized silicon substrate. We did not fit the Si 2p narrow scan it was fitted at commercial agency.

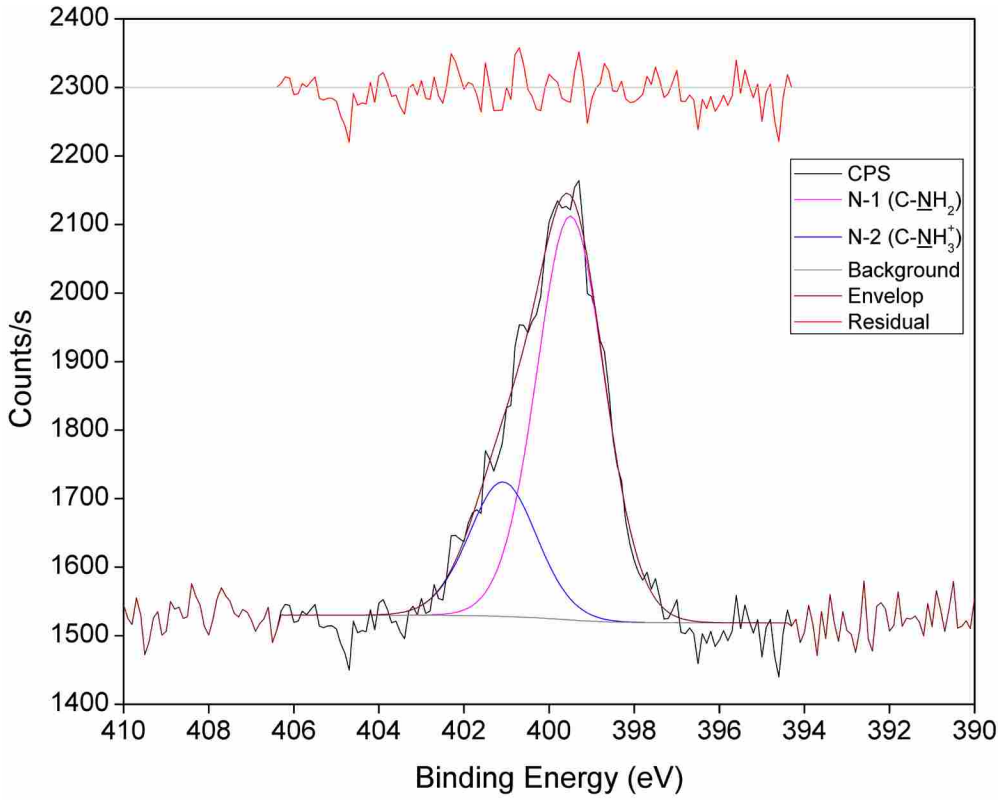

Figure 4.6. High resolution N 1s XPS scans of APTES-functionalized silicon substrate. The N 1s narrow scan was fit with Shirley background using Gaussian Lorentzian product function (GL) line shape with 30% Lorentzian and 70% Gaussian i.e. GL (30).

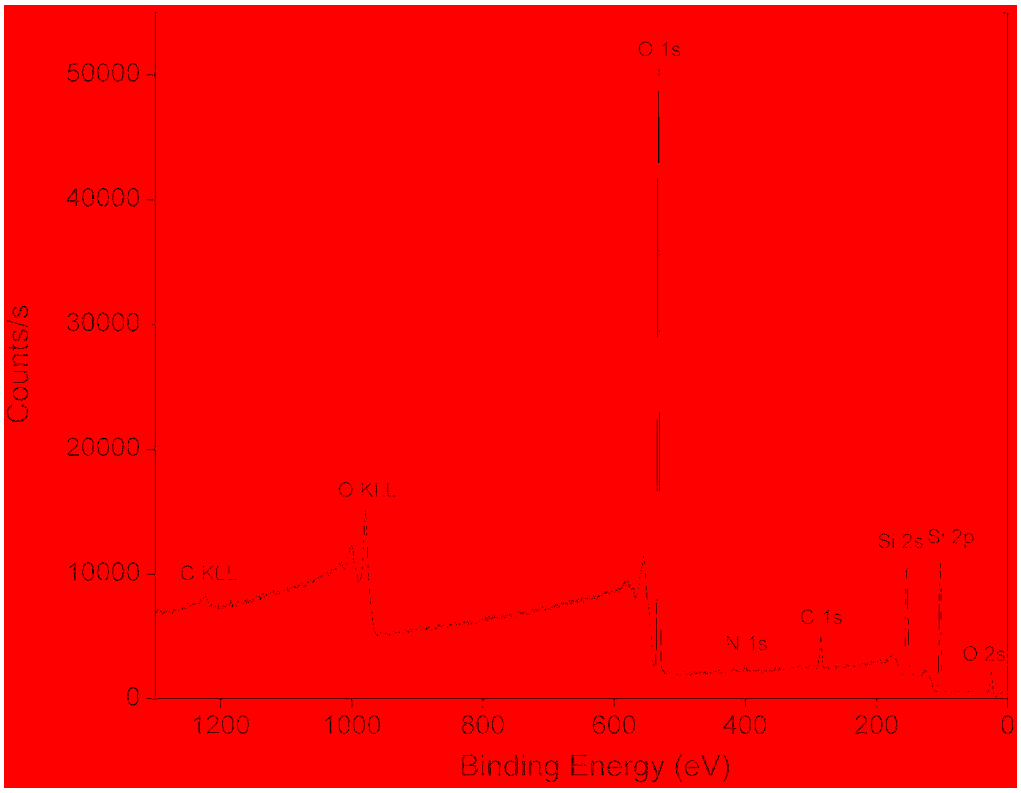

Figure 4.7. XPS survey spectrum of APDEMS-functionalized silicon substrate.

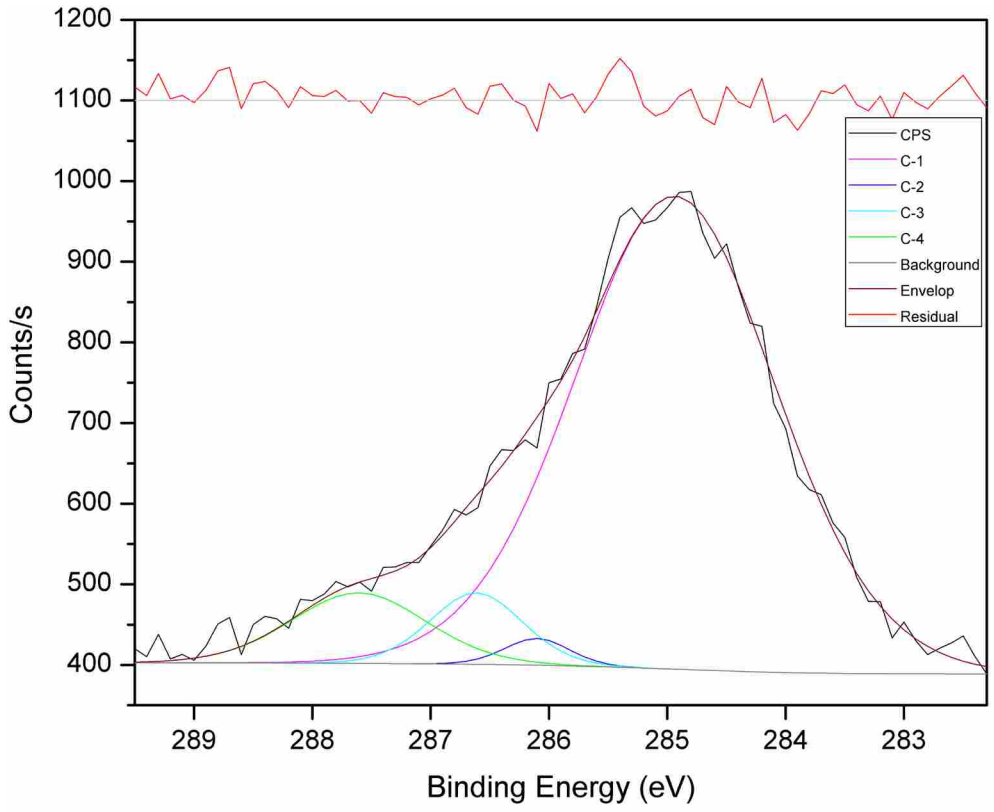

Figure 4.8. High resolution C 1s XPS scans of APDEMS-functionalized silicon substrate. (We did not perform this peak fitting. It was done at a commercial analysis house.)

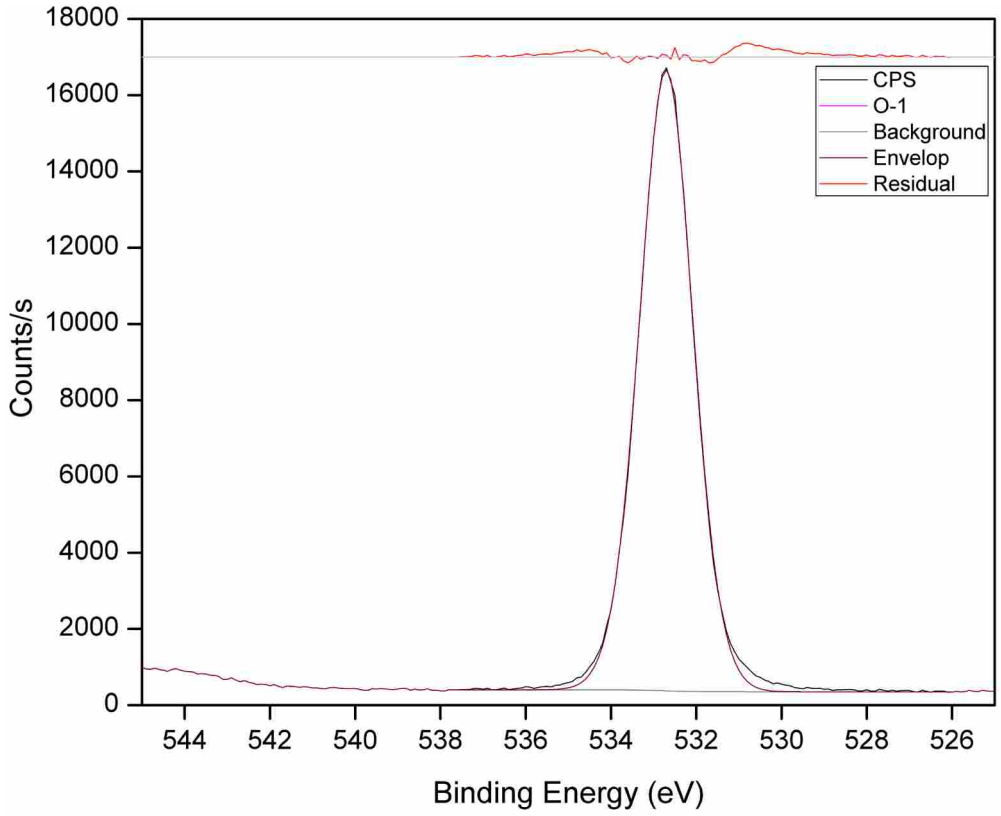

Figure 4.9. High resolution O 1s XPS scans of APDEMS-functionalized silicon substrate. (We did not perform this peak fitting. It was done at a commercial analysis house.)

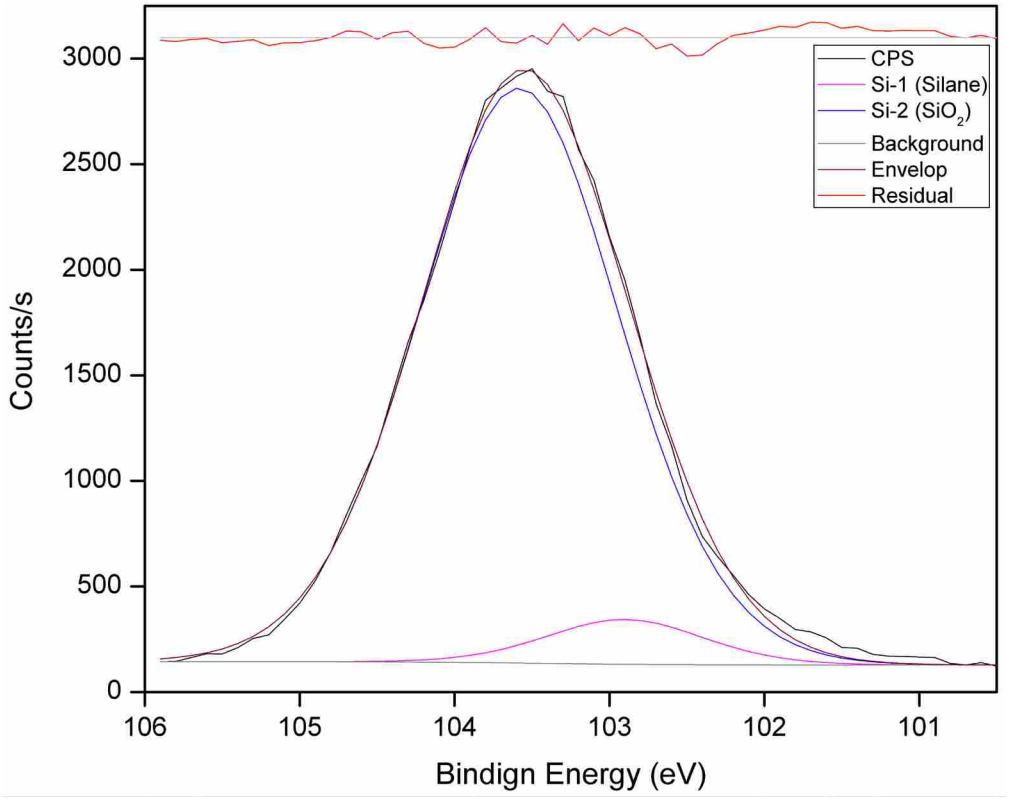

Figure 4.10. High resolution Si 2p (top) and N1s (bottom) XPS scans of APDEMS-functionalized silicon substrate. (We did not fit the Si 2p narrow scan it was fitted at commercial agency)

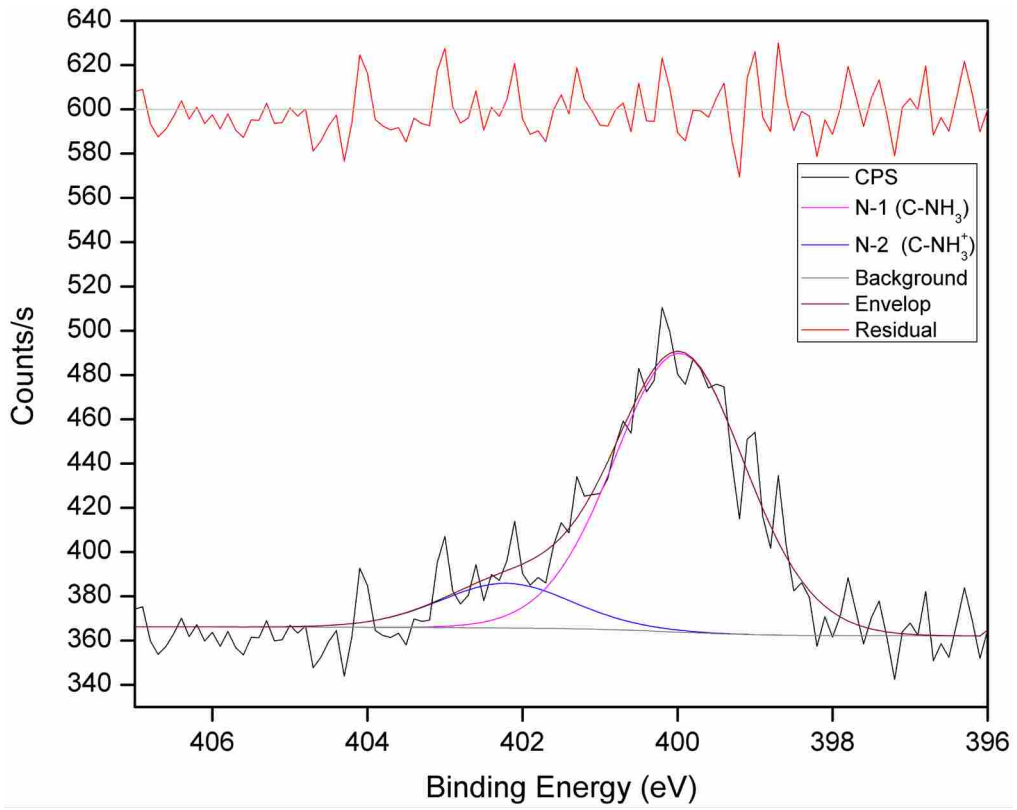

Figure 4.11. High resolution N 1s XPS scans of APDEMS-functionalized silicon substrate. The N 1s narrow scan was fit with Shirley background using Gaussian Lorentzian product function (GL) line shape with 30% Lorentzian and 70% Gaussian i.e. GL.

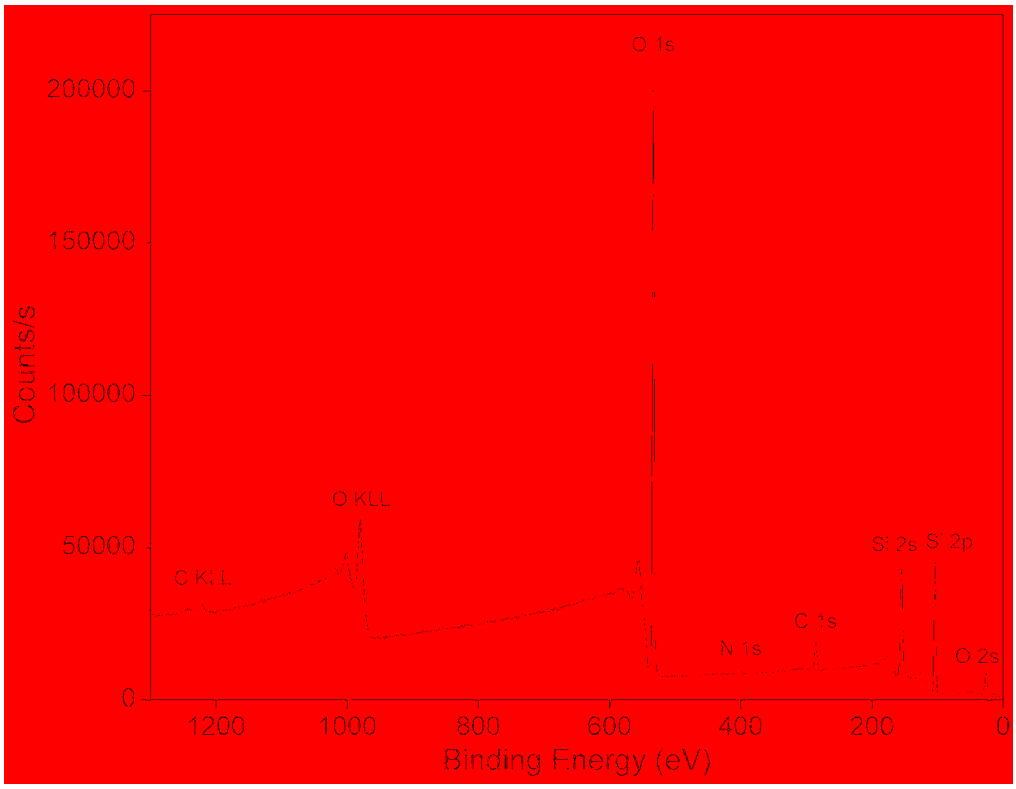

Figure 4.12. XPS survey spectrum of APDIPES-functionalized silicon substrate.

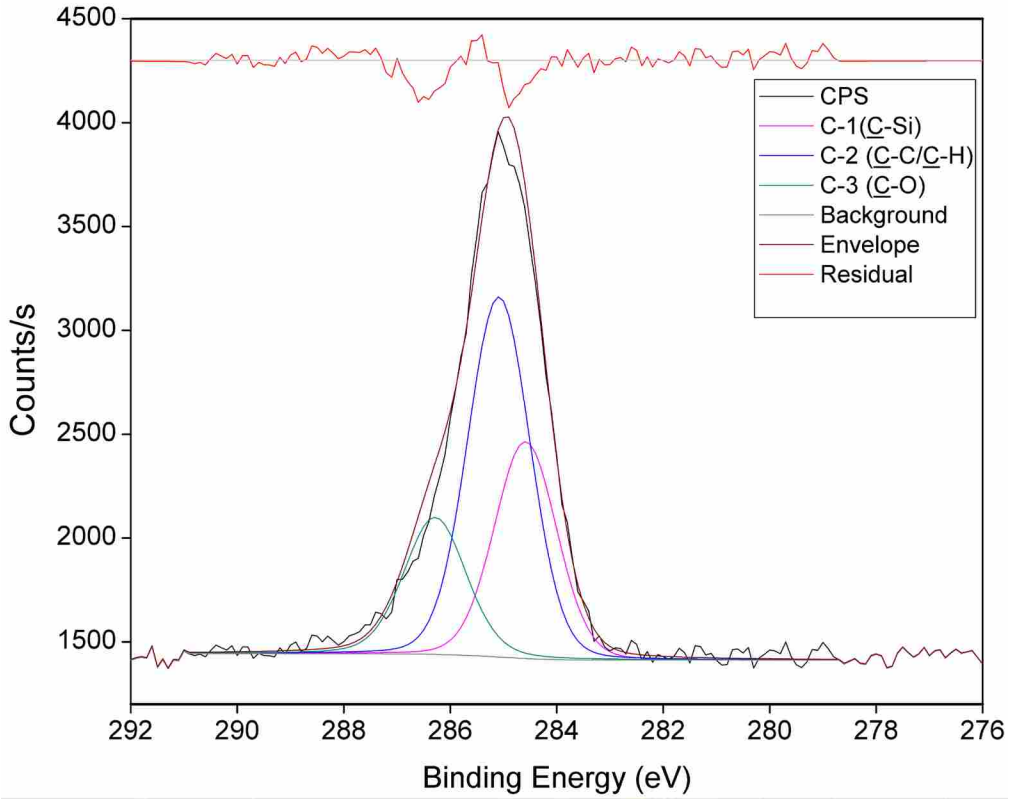

Figure 4.13. High resolution C 1s XPS scans of APDIPES-functionalized silicon substrate. The C 1s narrow scan was fit with Shirley background using Gaussian Lorentzian sum function (SGL) line shape with 10% Lorentzian and 90% Gaussian i.e. SGL.

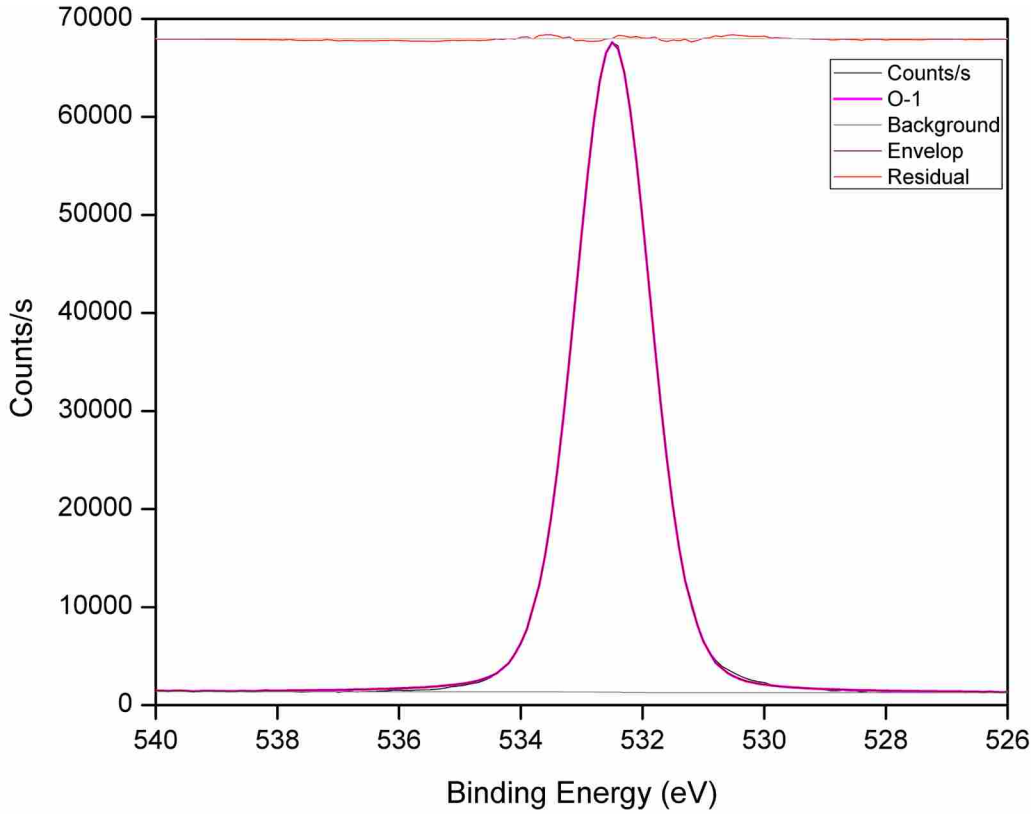

Figure 4.14. High resolution O 1s XPS scans of APDIPES-functionalized silicon substrate. Peak fitting was performed at commercial analysis house.)

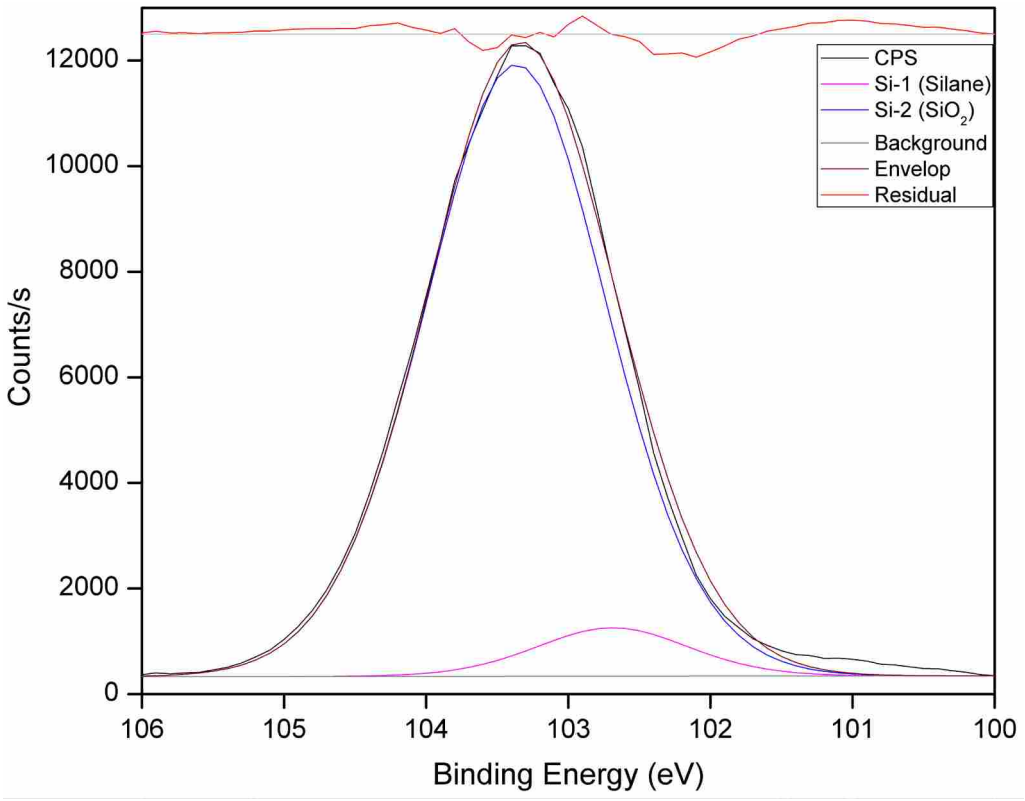

Figure 4.15. High resolution Si 2p XPS scans of APDIPES-functionalized silicon substrate.

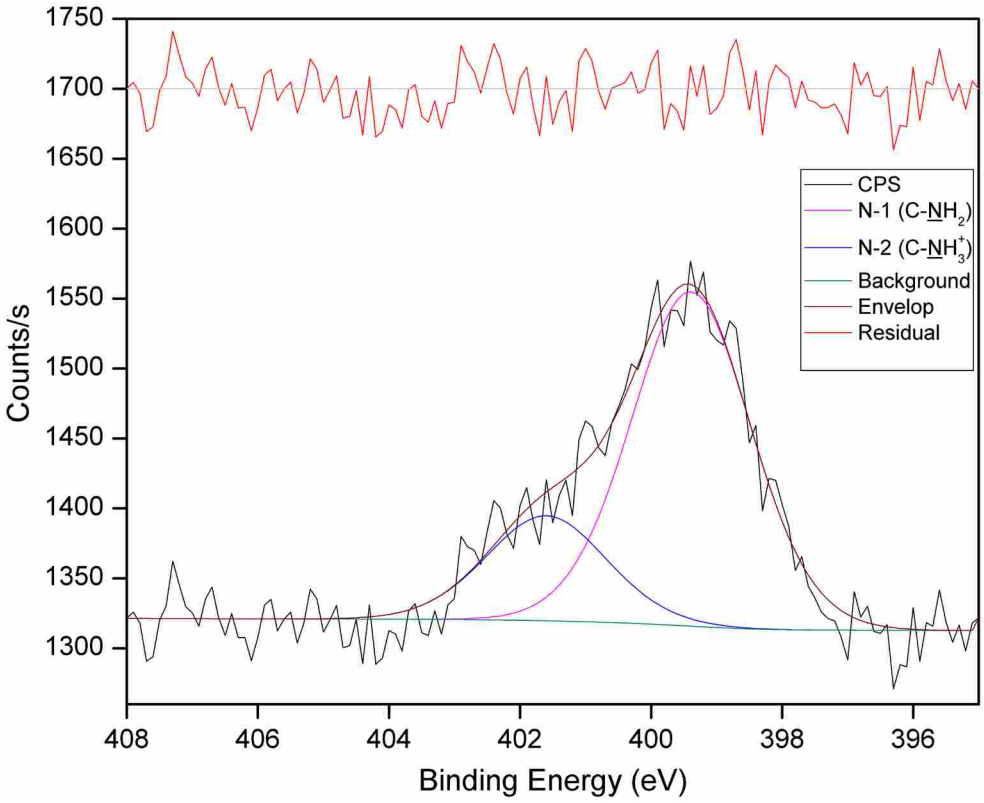

Figure 4.16. High resolution N 1s XPS scans of APDIPES-functionalized silicon substrate. The N 1s narrow scan was fit with Shirley background using Gaussian Lorentzian product function (GL) line shape with 30% Lorentzian and 70% Gaussian i.e. GL (30).

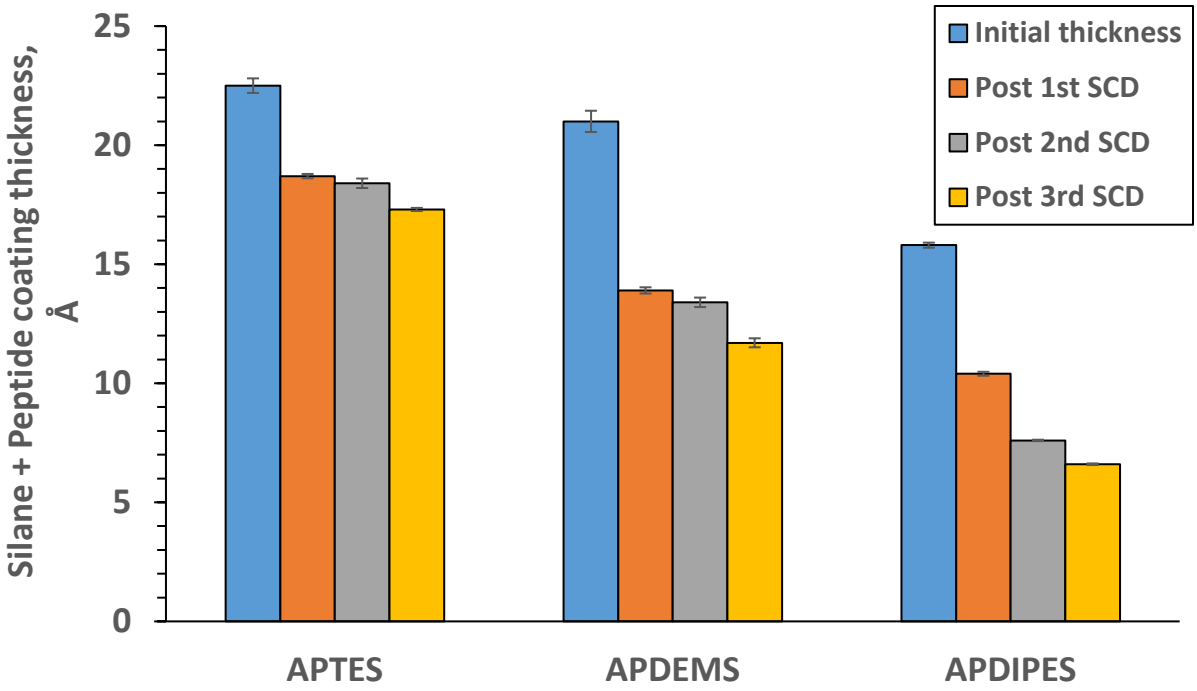

Figure 4.17 SE coating thickness of peptide-functionalized aminosilane surfaces before and after repetitive SCD treatments.

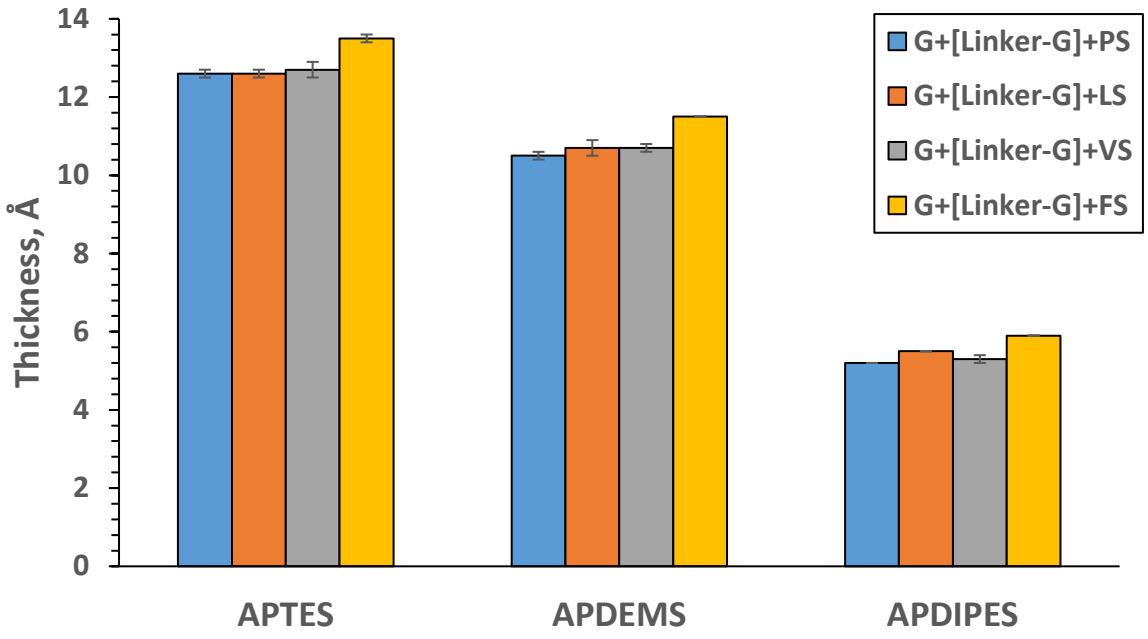

Figure 4.18 SE thickness increases by short model peptide coatings synthesized on three aminosilane surfaces. Highest amine density surface APTES shows the greatest magnitude increase.

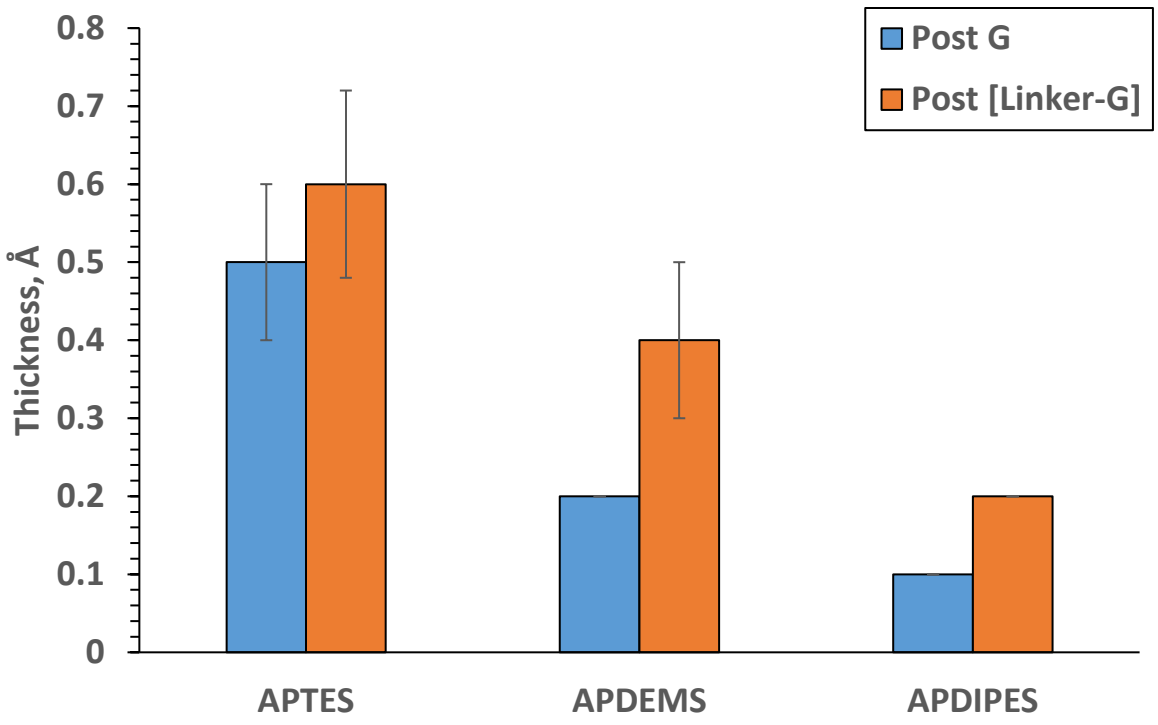

Figure 4.19 SE thickness increase due to acetic anhydride capping of unreacted amines after G and [Linker-G] coupling to three aminosilane surfaces.

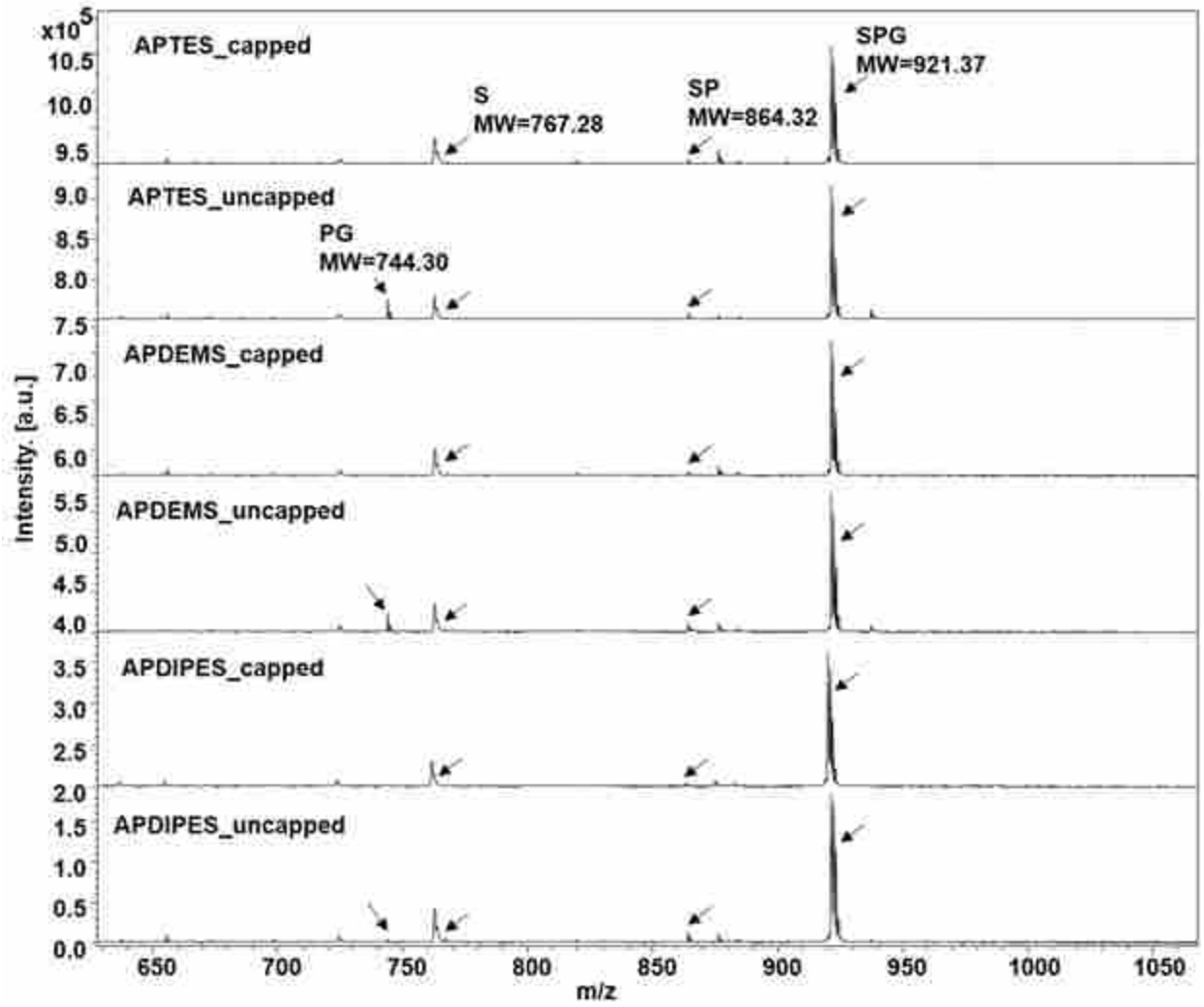

Figure 4.20 MALDI-MS spectra of G-[cleavable linker-G]-PS-functionalized capped and uncapped aminosilane surfaces. PG=TMPP-Pro-Gly amide, S=TMPP-Ser(Bzl) amide formed by NH_3 backbone cleavage, SPG=TMPP-Ser(OBzl)-Pro-Gly amide.

4.8 References

1. Saini, G.; Trenchevska, O.; Howell, L. J.; Boyd, J. G.; Smith, D. P.; Jain, V.; Linford, M. R., Performance Comparison of Three Chemical Vapor Deposited Aminosilanes in Peptide Synthesis: Effects of Silane on Peptide Stability and Purity. *Langmuir* **2018,** *34* (40), 11925-11932.
2. Igarashi C., M. A., Itoh Y., Subekti D. R. G., Takahashi S., Kamagata, K, DNA garden: A simple method for producing arrays of stretchable DNA for single-molecule fluorescence imaging of DNA binding proteins. *Bull Chem Soc Jpn* **2017,** *90* (1), 34-43.
3. Mei Chen, C. H., Danqun Huo, Huanbao Fa, Yanan Zhao, Caihong Shen, A sensitive electrochemical DNA biosensor based on three-dimensional nitrogen-doped graphene and Fe3O4 nanoparticles. *Sensors and Actuators B 239*, 421-429.
4. Ariga, K.; Mori, T.; Nakanishi, W.; Hill, J. P., Solid surface vs. liquid surface: nanoarchitectonics, molecular machines, and DNA origami. *Phys Chem Chem Phys* **2017,** *19* (35), 23658-23676.
5. Liu, R.; Wang, Q.; Li, Q.; Yang, X.; Wang, K.; Nie, W., Surface plasmon resonance biosensor for sensitive detection of microRNA and cancer cell using multiple signal amplification strategy. *Biosens Bioelectron* **2017,** *87*, 433-438.
6. Akyuz, E.; Baskan, K. S.; Tutem, E.; Apak, R., Novel Protein-Based Solid-Biosensor for Determining Pro-oxidant Activity of Phenolic Compounds. *J Agric Food Chem* **2017,** *65* (28), 5821-5830.
7. Puiu, M.; Bala, C., Peptide-based biosensors: From self-assembled interfaces to molecular probes in electrochemical assays. *Bioelectrochemistry* **2018,** *120*, 66-75.
8. Georgia-Paraskevi Nikoleli, D. P. N., Gennady Evtugynb,Tibor Hianik, Advances in lipid film based biosensors. *TrAC Trends in Analytical Chemistry* **2016,** *79*, 210-221.
9. Devillers, M.; Ahmad, L.; Korri-Youssoufi, H.; Salmon, L., Carbohydrate-based electrochemical biosensor for detection of a cancer biomarker in human plasma. *Biosens Bioelectron* **2017,** *96*, 178-185.
10. Chen Katz, L. L.-B., Shahar Rotem-Bamberger, Tiago Rito, Stefan G. D. Rüdiger, Assaf Friedler, Studying protein–protein interactions using peptide arrays. *Chem. Soc. Rev.* **2011,** *40*, 2131-2145.
11. Rothbart, S. B.; Krajewski, K.; Strahl, B. D.; Fuchs, S. M., Peptide microarrays to interrogate the "histone code". *Methods Enzymol* **2012,** *512*, 107-35.
12. Forsstrom, B.; Axnas, B. B.; Stengele, K. P.; Buhler, J.; Albert, T. J.; Richmond, T. A.; Hu, F. J.; Nilsson, P.; Hudson, E. P.; Rockberg, J.; Uhlen, M., Proteome-wide epitope mapping of antibodies using ultra-dense peptide arrays. *Mol Cell Proteomics* **2014,** *13* (6), 1585-97.
13. Coin, I.; Beyermann, M.; Bienert, M., Solid-phase peptide synthesis: from standard procedures to the synthesis of difficult sequences. *Nat Protoc* **2007,** *2* (12), 3247-56.
14. Bleczinski, C. F.; Richert, C., Solid-phase synthesis of cyclic peptide-DNA hybrids. *Org Lett* **2000,** *2* (12), 1697-700.
15. Merrifield, R. B., Solid-Phase Peptide Synthesis. 3. An Improved Synthesis of Bradykinin. *Biochemistry* **1964,** *3*, 1385-90.
16. Mosse, W. K.; Koppens, M. L.; Gengenbach, T. R.; Scanlon, D. B.; Gras, S. L.; Ducker, W. A., Peptides grafted from solids for the control of interfacial properties. *Langmuir* **2009,** *25* (3), 1488-94.

17. Price, J. V.; Tangsombatvisit, S.; Xu, G.; Yu, J.; Levy, D.; Baechler, E. C.; Gozani, O.; Varma, M.; Utz, P. J.; Liu, C. L., On silico peptide microarrays for high-resolution mapping of antibody epitopes and diverse protein-protein interactions. *Nat Med* **2012,** *18* (9), 1434-40.
18. Lei, Z. G., Jiaxue; Liu, Xia; Liu, Dianjun; Wang, Zhenxin, Poly(glycidyl methacrylate-co-2-hydroxyethyl methacrylate) Brushes as Peptide/Protein Microarray Substrate for Improving Protein Binding and Functionality. *Applied Materials & Interfaces* **2016,** *8* (16), 10174-10182.
19. Moschallski, M.; Baader, J.; Prucker, O.; Ruhe, J., Printed protein microarrays on unmodified plastic substrates. *Anal Chim Acta* **2010,** *671* (1-2), 92-8.
20. Ruwona, T. B.; McBride, R.; Chappel, R.; Head, S. R.; Ordoukhanian, P.; Burton, D. R.; Law, M., Optimization of peptide arrays for studying antibodies to hepatitis C virus continuous epitopes. *J Immunol Methods* **2014,** *402* (1-2), 35-42.
21. Andresen, H.; Bier, F. F., Peptide microarrays for serum antibody diagnostics. *Methods Mol Biol* **2009,** *509*, 123-34.
22. Salisbury, C. M.; Maly, D. J.; Ellman, J. A., Peptide microarrays for the determination of protease substrate specificity. *J Am Chem Soc* **2002,** *124* (50), 14868-70.
23. Jane Politi, S. Z., Ilaria Rea, Paolo Grieco, Alessandro Caliò, Amalia Luce, Michele Caraglia, and Luca De Stefano, Peptide Functionalization of Silicon for Detection and Classification of Prostatic Cells. *Journal of Sensors* **2017,** *2017*.
24. Pellois, J. P.; Zhou, X.; Srivannavit, O.; Zhou, T.; Gulari, E.; Gao, X., Individually addressable parallel peptide synthesis on microchips. *Nat Biotechnol* **2002,** *20* (9), 922-6.
25. Coffinier, Y.; Olivier, C.; Perzyna, A.; Grandidier, B.; Wallart, X.; Durand, J. O.; Melnyk, O.; Stievenard, D., Semicarbazide-functionalized Si(111) surfaces for the site-specific immobilization of peptides. *Langmuir* **2005,** *21* (4), 1489-96.
26. Duburcq, X.; Olivier, C.; Desmet, R.; Halasa, M.; Carion, O.; Grandidier, B.; Heim, T.; Stievenard, D.; Auriault, C.; Melnyk, O., Polypeptide semicarbazide glass slide microarrays: characterization and comparison with amine slides in serodetection studies. *Bioconjug Chem* **2004,** *15* (2), 317-25.
27. Melnyk, O.; Duburcq, X.; Olivier, C.; Urbes, F.; Auriault, C.; Gras-Masse, H., Peptide arrays for highly sensitive and specific antibody-binding fluorescence assays. *Bioconjug Chem* **2002,** *13* (4), 713-20.
28. Benjamin T. Houseman, E. S. G., and Milan Mrksich, Maleimide-Functionalized Self-Assembled Monolayers for the Preparation of Peptide and Carbohydrate Biochips. In *Langmuir*, 2003; Vol. 19, pp 1522-1531.
29. Joos, B.; Kuster, H.; Cone, R., Covalent attachment of hybridizable oligonucleotides to glass supports. *Anal Biochem* **1997,** *247* (1), 96-101.
30. Ogiso, M.; Kobayashi, J.; Imai, T.; Matsuoka, K.; Itoh, M.; Imamura, T.; Okada, T.; Miura, H.; Nishiyama, T.; Hatanaka, K.; Minoura, N., Carbohydrate immobilized on a dendrimer-coated colloidal gold surface for fabrication of a lectin-sensing device based on localized surface plasmon resonance spectroscopy. *Biosens Bioelectron* **2013,** *41*, 465-70.
31. Falsey, J. R.; Renil, M.; Park, S.; Li, S.; Lam, K. S., Peptide and small molecule microarray for high throughput cell adhesion and functional assays. *Bioconjug Chem* **2001,** *12* (3), 346-53.
32. Schirwitz, C.; Block, I.; Konig, K.; Nesterov, A.; Fernandez, S.; Felgenhauer, T.; Leibe, K.; Torralba, G.; Hausmann, M.; Lindenstruth, V.; Stadler, V.; Breitling, F.; Bischoff, F. R., Combinatorial peptide synthesis on a microchip. *Curr Protoc Protein Sci* **2009,** *Chapter 18*, Unit 18 2 18 2 1-13.

33. Sun, Y.; Wang, H.; Sun, C., Amperometric glucose biosensor based on layer-by-layer covalent attachment of AMWNTs and IO(4)(-)-oxidized GOx. *Biosens Bioelectron* **2008,** *24* (1), 22-8.
34. D.C.Tessier, S. B., M.Arbour, P.Roos, G.Pan, Improved surface sensing of DNA on gas-etched porous silicon. *Sensors and Actuators B* **2006,** *120* (1), 220-230.
35. Furbert, P.; Lu, C.; Winograd, N.; DeLouise, L., Label-free optical detection of peptide synthesis on a porous silicon scaffold/sensor. *Langmuir* **2008,** *24* (6), 2908-15.
36. Loeffler, F. F.; Foertsch, T. C.; Popov, R.; Mattes, D. S.; Schlageter, M.; Sedlmayr, M.; Ridder, B.; Dang, F. X.; von Bojnicic-Kninski, C.; Weber, L. K.; Fischer, A.; Greifenstein, J.; Bykovskaya, V.; Buliev, I.; Bischoff, F. R.; Hahn, L.; Meier, M. A.; Brase, S.; Powell, A. K.; Balaban, T. S.; Breitling, F.; Nesterov-Mueller, A., High-flexibility combinatorial peptide synthesis with laser-based transfer of monomers in solid matrix material. *Nat Commun* **2016,** *7*, 11844.
37. Liang YC, H. J., Zang PY, Kim JY, Hu W, Molecular layer deposition of APTES on silicon nanowire biosensors: Surface characterization, stability and pH response. *Applied Surface Science* **2014,** *322*, 202-208.
38. Zhang, F.; Sautter, K.; Larsen, A. M.; Findley, D. A.; Davis, R. C.; Samha, H.; Linford, M. R., Chemical vapor deposition of three aminosilanes on silicon dioxide: surface characterization, stability, effects of silane concentration, and cyanine dye adsorption. *Langmuir* **2010,** *26* (18), 14648-54.
39. Zheng-Zheng Liu, Q. W., Xin Liu, Jie-Qiong Bao, Effects of amino-terminated self-assembled monolayers on nucleation and growth of chemical vapor-deposited copper films. *Thin Solid Films* **2008,** *517* (2), 635-640.
40. Gupta, V.; Madaan, N.; Jensen, D. S.; Kunzler, S. C.; Linford, M. R., Hydrogen plasma treatment of silicon dioxide for improved silane deposition. *Langmuir* **2013,** *29* (11), 3604-9.
41. Mojun Zhu, M. Z. L., and Wei Chen, How to Prepare Reproducible, Homogeneous, and Hydrolytically Stable Aminosilane-derived Layers on Silica. *Langmuir* **2011,** *28* (1), 416-423.
42. Brian Dorvel, B. R. J., Ian Block, Patrick Mathias, Susan E. Clare, Brian Cunningham, Donald E. Bergstrom, Rashid Bashir, Vapor-Phase Deposition of Monofunctional Alkoxysilanes for Sub-Nanometer-Level Biointerfacing on Silicon Oxide Surfaces. *Advanced Functional Materials* **2009,** *20*, 87-95.
43. Fiorilli, S.; Rivolo, P.; Descrovi, E.; Ricciardi, C.; Pasquardini, L.; Lunelli, L.; Vanzetti, L.; Pederzolli, C.; Onida, B.; Garrone, E., Vapor-phase self-assembled monolayers of aminosilane on plasma-activated silicon substrates. *J Colloid Interface Sci* **2008,** *321* (1), 235-41.
44. David S. Jensen, S. S. K., Nitesh Madaan, Michael A. Vail, Andrew E. Dadson, Matthew R Linford, Silicon (100)/SiO2 by XPS. *Surface Science Spectra* **2013,** *20* (1), 36-42.
45. Ying Dong, S. V. P., Zhi Xu, Detection of Local Density Distribution of Isolated Silanol Groups on Planar Silica Surfaces Using Nonlinear Optical Molecular Probes. *Anal. chem.* **1998,** *70*, 4730-4735.
46. Zhuravlev, L. T., The surface chemistry of amorphous silica. Zhuravlev model. *Colloids and Surfaces* **2000,** *173*, 1-38.
47. Heidler, P.; Link, A., N-acyl-N-alkyl-sulfonamide anchors derived from Kenner's safety-catch linker: powerful tools in bioorganic and medicinal chemistry. *Bioorg Med Chem* **2005,** *13* (3), 585-99.

CHAPTER 5: Applications of Near-Ambient Pressure XPS (NAP-XPS) and XPS Peak Fitting in Material Characterization

5.1 Introduction

XPS is a well-developed technique for surface and material chemical analysis with many applications in research and industry, e.g., in semiconductors, polymers, cosmetics, medical, automobile, and aeronautics.[1] Conventional UHV-XPS requires fairly long times to analyze samples, especially when one considers sample introduction into a preparation chamber, pump down, transfer to the analysis chamber, pump down again, and finally the analysis.[2] Many sample analyses by XPS under ultra-high vacuum (UHV) are affected by different extents of degassing or charging due to their vacuum incompatibility and/or insulating nature. Traditional XPS instruments have systems, e.g., electron flood guns, for charge compensation, which includes differential charging. Near-ambient pressure (NAP) XPS represents a paradigm shift for the technique. NAP-XPS works at relatively high pressures,[3-5] which allows fast analysis of a wide variety of samples – it does not require special sample preparation that might include drying, freeze drying, flash freezing, and/or extensive pumping.[1] Samples that can now be rapidly analyzed by XPS include polymers, most other insulators, powders, liquids, gases, biological samples (both liquid and solid), porous materials, and complex devices like batteries. Typically, an NAP-XPS survey scan can be acquired in less than 5 min after the pump down begins. Hence, NAP-XPS is much faster than conventional UHV-XPS.[2] NAP-XPS has traditionally been available at synchrotrons and as a special add-on to some commercial or custom-built systems. However, until the instrument that was just introduced by SPECS (the EnviroESCA instrument), there has been no stand-alone, dedicated NAP-XPS instrument on the market.[1-2] This NAP-XPS instrument uses a series of electrostatic lenses and differential pumping to transfer the photoelectrons and decrease

the pressure from the sample to the detector, which results in an increase in the instrument count rate. NAP-XPS has a unique way of handling sample charging. It does not need a flood gun or similar device. Charge compensation in NAP-XPS works by ionization of the gas surrounding a sample, which is referred to as environmental charge compensation.

Here, in chapter 5, I discuss the characterization of different samples that would be challenging to analyze by conventional XPS. These materials include an aqueous solution of bovine serum albumin (BSA), polytetrafluoroethylene (PTFE), poly(γ-benzyl L-glutamate) (PBLG), human hair before and after different commercial treatments, and phosphate buffer saline (PBS) – both the solid and in solution. Data were collected with the NAP-XPS instrument from SPECS, GmbH, Germany. I analyzed the data sets we received from them to obtain and better understand the surface compositions of these materials.

Section 5.1.1: Bovine Serum Albumin (BSA), Aqueous Solution by Near-Ambient Pressure

5.1.1.1 Statement of Attribution

This document was originally published as Jain V.; Kjærvik, M.; Bahr, S.; Dietrich, P.; Meyer, M.; Thißen, A.; Linford, M. R. Bovine Serum Albumin (BSA), aqueous solution by near-ambient pressure (NAP-XPS). *Surface Science Spectra* (Accepted). Here, the whole document and all the figures are reproduced with the permission of AIP publishing. Data was collected at SPECS. I did all the peak fitting and data analysis.

Some information fields are omitted from this document to improve its readability in this format. We refer readers to the original document for a more complete description of the sample, instrument, and spectral features.

5.1.1.2 Abstract

Near ambient pressure – X-ray photoelectron spectroscopy (NAP-XPS) is a less traditional form of XPS that allows samples to be analyzed at relatively high pressures, i.e., at greater 2500 Pa. With NAP-XPS, XPS can probe moderately volatile liquids, biological samples, porous materials, and/or polymeric materials that outgas significantly. In this submission we show survey, C 1s, O 1s, and N 1s narrow scans from an aqueous solution of a common protein, bovine serum albumin (BSA). The C 1s peak envelope is well fit to four symmetric peaks of equal width that correspond to carbon bonded to carbon and hydrogen (C-1), carbon singly bonded to oxygen (C-2), carbonyl and/or amide carbon (C-3), and carboxyl carbon (C-4). Two possible peak fits are considered for the N 1s and O 1s peak envelopes. The N 1s signal is fit to four peaks that correspond to amine ($-NH_2$), amide ($O=C-NH_2$), ammonium ($-NH_3^+$), and $N_2(g)$ nitrogen, and alternatively to three peaks that correspond to amine, amide, and $N_2(g)$ nitrogen. The O 1s peak envelope is similarly fit to three and four components.

Keywords: Near-ambient pressure X-ray photoelectron spectroscopy, NAP-XPS, XPS, bovine serum albumin, BSA

5.1.1.3 Introduction

Here we present the near ambient pressure – X-ray photoelectron spectroscopy (NAP-XPS) characterization of an aqueous solution of a common protein: bovine serum albumin (BSA). This document is part of a series of submissions on NAP-XPS that has previously been introduced in this Journal.[6] Data were collected with the SPECS EnviroESCA instrument,[1, 7-10] where the liquid sample was analyzed directly without any sample preparation. Obviously, it is not possible to analyze aqueous solutions by traditional XPS under ultra-high vacuum.[11] The prospect of analyzing liquid-gas and solid-gas interfaces under near ambient pressure by NAP-XPS allows materials to be studied under more realistic conditions that should result in more relevant results. Other aqueous solutions, including those of RbCl, NaCl, and phosphate buffered saline (PBS), have previously been analyzed by NAP-XPS.[12,13]

Bovine serum albumin is a serum albumin protein obtained from cows. BSA has numerous biochemical applications including ELISA (enzyme-linked immunosorbent) assays,[14] immunoblots,[15] and immunohistochemistry.[16,17] It is also used as a protein concentration standard in laboratory experiments.[18, 19] The C 1s, O 1s, and N 1s narrow scans of the BSA aqueous solution were peak fit. The C 1s narrow scan was well fitted with four synthetic peaks of equal width. These peaks correspond to carbon bonded to carbon and hydrogen (C-1), carbon bonded once to oxygen (C-2), carbonyl and/or amide carbon (C-3), and carboxyl carbon (C-4).[20] The N 1s and O 1s peak envelopes were fitted in two different ways. That is, the N 1*s* peak envelope was fitted with a total of three synthetic components: C-$\underline{N}H_2$ (N-1), O=C-$\underline{N}H_2$ (N-2) and a signal from gaseous N_2 (N-3),[9, 21-22] or to four peaks: C-$\underline{N}H_2$ (N-1), O=C-$\underline{N}H_2$ (N-2), C-$\underline{N}H_3^+$ (N-3), and gaseous N_2 (N-4).[23,

[24] Similarly, the O 1s peak envelope could be fit to either three peaks: NH_2-C=O/O=C-O (O-1), O-C=O/liquid water (O-2), and gaseous water (O-3),[22, 23] or to four: NH_2-C=O (O-1), C-O-C/C-OH/O-C=O (O-2), O-C=O/liquid water (O-3), and gas phase water (O-4). [21, 24, 9] We prefer the fits with more peaks, as they should allow us to more fully represent the chemical speciation in the samples. All of the peak fitting reported herein was with CasaXPS using symmetric Gaussian-Lorentzian product (GLP) functions with 30% Lorentzian character on Tougaard backgrounds.[25] However, in the case of O 1*s*, the best fit (residual standard deviation) was obtained when the gas phase peak was fitted with a GLP with 60% Lorentzian character. In general, a gaseous species shows narrower photoemission signals than the same material in a condensed phase.[11] Also synthetic fit components in XPS peak fitting for a given phase usually have similar widths.[26, 27] Here, the N 1s and O 1s peak envelopes showed both gas phase (N_2(g) and H_2O(g), respectively) and liquid phase components. When the condensed phase portions of these narrow scans were fit to two synthetic peaks of equal width, this width was naturally greater than the width of the gas phase peak. When an additional synthetic peak was added to the condensed phase portion of these narrow scans, the peak widths of the gas phase and liquid phase components were constrained to be the same so that the liquid phase components would not be narrower than the gas phase ones.

Table 5.1.1.1. Spectral features of interest.

Figure number	**Element/ Transition**	**Peak Energy (eV)**	**Peak Width FWHM (eV)**	**Peak Area (eV x cts/s)**	**Sensitivity Factor**	**Concentration (at. %)**	**Peak Assignment**
5.1.1.1	C 1s	286	3.61	667.9	1	25.88	protein
5.1.1.1	N 1s	401	2.17	229	1.67	6.37	protein

5.1.1.1	O 1s	535	4.1	3613.1	2.47	67.75	protein
5.1.1.2	C 1s	285	1.47	182.9			-CH
5.1.1.2	5.1	286.2	1.47	149.9			C-O
5.1.1.2	C 1s	287.4	1.47	66.65			(C=O/O-C-O/N-C=O)
5.1.1.2	C 1s	288.6	1.47	100.7			(O-C=O)
5.1.1.3	N 1s	400	1.4	83.49			C-NH_2
5.1.1.3	N 1s	401	1.4	48.46			O=C-NH_2
5.1.1.3	N 1s	402.4	1.4	10.13			C-NH_3^+
5.1.1.3	N 1s	405.6	1.4	66.56			N_2
5.1.1.4	O 1s	531.1	1.44	114.3			NH-C=O
5.1.1.4	O 1s	532.4	1.44	521.9			O-C=O/C-OH
5.1.1.4	O 1s	533.3	1.44	729.4			H_2O and O=C-O
5.1.1.4	O 1s	535.3	1.44	1307.3			Gaseous H_2O
5.1.1.5	N 1s	400.3	1.67	117.8			C-NH_2
5.1.1.5	N 1s	401.7	1.67	12.39			O=C-NH_2
5.1.1.5	N 1s	405.6	1.41	66.4			N_2

5.1.1.6	O 1s	531.6	1.81	193			Oxygen from NH-C=O/O-C=O
5.1.1.6	O 1s	533	1.81	1211			Oxygen from O-C-O
5.1.1.6	O 1s	535.3	1.41	1273.4			Gaseous peak

5.1.1.4 Specimen Description

a. Host Material: Aqueous solution of a protein: bovine serum albumin (BSA)

b. CAS Registry #: 9048-46-8

c. Host Material Characteristics: homogeneous; liquid; amorphous; biological material; organic compound; Other. BSA is a serum albumin protein that is extracted from cows. Its isoelectric point in water at 25 °C is 4.7,24 and the pH of its 1% solution is 5.2-7.0.25

d. Chemical Name: Bovine serum albumin

e. Source: Sigma-Aldrich

f. Host Composition: BSA solution in water

g. Form: Solution/liquid

h. Structure: BSA is a large protein – it is composed of 583 amino acids, and its average molecular weight is 66430.3 kDa, as determined by electrospray ionization mass spectrometry.26

i. History & Significance: As mentioned in the Introduction, BSA has multiple uses in biochemistry.10- 15

j. As Received Condition: 0.05% BSA in water

k. Analyzed Region: Surface of the aqueous solution of BSA.

l. Ex Situ Preparation/Mounting: A liquid volume of 2-4 ml was transferred with a pipette into a watch glass, which was placed, together with an O-ring for mechanical stabilization, on a sample plate.

m. In Situ Preparation: None

n. Charge Control: Residual gas

o. Temp. During Analysis: 300K

p. Pressure During Analysis: 1200 Pa

q. Pre-analysis Beam Exposure: 30 s.

5.1.1.5 Instrument Settings

a. Manufacturer and Model: SPECS EnviroESCA

b. Analyzer Type: spherical sector

c. Detector: other 1D delay line detector (1D-DLD)

d. Number of Detector Elements: 25

e. Analyzer Mode: constant pass energy

f. Throughput (T=EN): N=0

g. Excitation Source Window: silicon nitride

h. Excitation Source: Al Kα monochromatic

i. Source Energy: 1486.6 eV

j. Source Strength: 42 W

k. Source Beam Size: 250 μm x 250 μm

l. Signal Mode: multichannel direct

m. Incident Angle: 55 ˚

n. Source-to-Analyzer Angle: 55 ˚

o. Emission Angle: 0 ˚

p. Specimen Azimuthal Angle: 0 ˚

q. Acceptance Angle from Analyzer Axis: 22 ˚

r. Analyzer Angular Acceptance Width: 44 ˚

s. Ion Gun: No ion gun was used

5.1.1.6 Data Analysis Methods

a. Energy Scale Correction: No correction

b. Recommended Energy Scale Shift: 0 eV

c. Peak Shape and Background Method: All peak fitting reported herein was with Gaussian-Lorentzian product (GLP) functions with 30% Lorentzian character, i.e., GLP(30) synthetic peaks, except in the case of the O 1s fit where a GLP(60) was employed. Universal polymer Tougaard backgrounds were used in all cases except for the N 1s fit, which used a linear background. All peak fitting was performed with CasaXPS (Casa Software Ltd., Version 2.3.18PR1.0).

d. Quantitation Method: Elemental compositions were calculated using the standard SPECS software.

Section 5.1.2: Polytetrafluoroethylene (PTFE), Aqueous Solution by Near-Ambient Pressure XPS

5.1.2.1 Statement of Attribution

This document was originally published as Jain V.; Bahr, S.; Dietrich, P.; Meyer, M.; Thißen, A.; Linford, M. R. Polytetrafluoroethylene, by near-ambient pressure XPS. *Surface Science Spectra*, **2019**, *26*. 014028. Here, the whole document and all the figures are reproduced with the permission of AIP publishing. Some of the information in this document was previously published in an application note produced by SPECS, GmbH (Berlin, Germany). It is used here with their permission. Data was collected at SPECS. I did all the peak fitting and data analysis.

Some information fields are omitted from this document to improve its readability in this format. We refer readers to the original document for complete sample, instrument information, and spectral features.

5.1.2.2 Abstract

Near ambient pressure X-ray photoelectron spectroscopy (NAP-XPS) is a less traditional form of XPS that allows samples to be analyzed at relatively high pressures, i.e., at greater than 1000 Pa. With NAP-XPS, XPS can analyze moderately volatile liquids, biological samples, porous materials, and/or polymeric materials that outgas significantly. Polytetrafluoroethylene (PTFE) is an important polymer with many applications in science and industry. It is an insulator that charges under X-ray illumination under high vacuum. In this submission, we show NAP-XPS spectra of PTFE. Survey spectra are shown at different background gas (air) pressures. These spectra contain F 2s, C 1s, O 1s, N 1s, F 1s, and F Auger signals. Also presented are F 1s narrow scans over a range of background pressures and illumination times. Peaks decrease in width, shift towards Literature values, and improve in shape with increasing background gas pressure.

Keywords: near-ambient pressure–x-ray photoelectron spectroscopy, NAP-XPS, XPS, polytetra-

fluoroethylene, PTFE.

5.1.2.3 Introduction

Here we present the near ambient pressure – X-ray photoelectron spectroscopy (NAP-XPS) characterization of polytetrafluoroethylene (PTFE). This document is part of a series of submissions on NAP-XPS being submitted to Surface Science Spectra. This set of articles and the NAP-XPS technique have previously been introduced in the journal.[6] Data were collected with the SPECS EnviroESCA instrument.[1, 7-8, 28] Some of the unique properties of PTFE include its low surface energy (hydrophobicity), chemical inertness, and thermal stability. Accordingly, it has many applications in science and technology, e.g., it is employed as a material for bearings, seals, and gaskets, it is a useful non-stick surface for cooking, and it has various applications in medical technology. In addition, PTFE vessels allow chemical reactions to be performed with caustic reagents. Some of these applications are made possible by the fact that PTFE can be machined.

Polytetrafluoroethylene (PTFE) is an insulator that charges under X-ray illumination at high vacuum. Accordingly, it requires charge compensation for analysis by conventional XPS. Here, we explore the effects of background gas pressure and analysis time on the NAP-XPS analysis of this material, where no external charge compensation was employed. Survey spectra obtained at $3x10^{-3}$, 100, 500, and 1000 Pa are presented (Figure 5.1.2.1 to 5.1.2.4). All of these survey scans show F 2s, C 1s, O 1s, N 1s, and F 1s photoelectron peaks, as well as the F Auger signals. As expected, the spectrum obtained at $3x10^{-3}$ Pa shows significant charging. F 1s narrow scans (peaks) obtained at $2.5x10^{-3}$, $5x10^{-3}$ 50, 100, 200, 500, 1000 Pa are also shown. At increasingly higher pressures, the peaks shift down towards their expected Literature values,[29] which suggests increasingly effective charge compensation. As indicated by their equivalent widths (EW),[30,31] the widths of these peaks decrease with increasing background pressure (Figure

5.1.2.5). Also shown are F 1*s* peaks obtained with different analysis times at pressures lower than 0.005 Pa (Figure 5.1.2.6). A peak shift towards higher binding energy is observed with increasing scan time. The EW values of these peaks remain large.

Table 5.1.2.1. Spectral features of interest.

Figure Number	**Element/ Transition**	**Peak Energy (eV)**	**Peak Width FWHM (eV)**	**Peak Area (eV x cts/s)**	**Sensitivity Factor**	**Concentration (at. %)**	**Peak Assignment**
5.1.2.1	F 2s	37.9	6.59	3314			valance band
5.1.2.1	C 1s	292.5	5.47	8231.2			[-CF_2-CF_2-]
5.1.2.1	O 1s	529.9	2.96	268.5			Residual oxygen gas
5.1.2.1	F 1s	682.9	5.18	49434.9			[-CF_2-CF_2-]
5.1.2.1*	F KLL	606.4	10.89	21974.8			[-CF_2-CF_2-]
5.1.2.1*	F KLL	583.4	4.14	5109.3			[-CF_2-CF_2-]
5.1.2.2	F 2s	35.5	5.32	4363			valance band
5.1.2.2	C 1s	292.5	2.75	14120.7			[-CF_2-CF_2-]
5.1.2.2	N 1s	402.5	4.59	1676.5			Residual nitrogen gas

5.1.2.2	O 1s	534.5	4.2	5198.1			Residual oxygen gas
5.1.2.2	F 1s	690.5	2.78	57530.5			[-CF_2-CF_2-]
5.1.2.2*	F KLL	596.6	8.9	37961.5			[-CF_2-CF_2-]
5.1.2.2*	F KLL	567.6	7.59	6231			[-CF_2-CF_2-]
5.1.2.3	F 2s	35.5	5.34	2548			valence band
5.1.2.3	C 1s	292.5	2.41	4653			[-CF_2-CF_2-]
5.1.2.3	N1s	404.5	2.33	5444			Residual nitrogen gas
5.1.2.3	O 1s	538.5	2.58	2700.5			Residual oxygen gas
5.1.2.3	F 1s	689.5	2.76	16464.8			[-CF_2-CF_2-]
5.1.2.3*	F KLL	597.6	8.81	5477			[-CF_2-CF_2-]
5.1.2.3*	F KLL	568.6	1.82	619.5			[-CF_2-CF_2-]
5.1.2.4	F 2s	35.5	4.38	777.9			valance band
5.1.2.4	C 1s	292.5	2.52	1236.9			[-CF_2-CF_2-]
5.1.2.4	N 1s	405.5	1.96	2149.7			Residual nitrogen gas
5.1.2.4	O 1s	539.5	2.36	942.9			Residual oxygen gas

5.1.2.4	F 1s	689.5	2.73	3253.2			[-CF_2-CF_2-]
5.1.2.4*	F KLL	596.6	4.99	1511.1			[-CF_2-CF_2-]
5.1.2.5	F 1s	689.7	2.42	5267.2			[-CF_2-CF_2-], at 500 Pa
5.1.2.5	F 1s	689.7	2.4	7101.7			[-CF_2-CF_2-], at 400 Pa
5.1.2.5	F 1s	689.7	2.56	10031.5			[-CF_2-CF_2-], at 300 Pa
5.1.2.5	F 1s	689.7	2.64	13341			[-CF_2-CF_2-], at 200 Pa
5.1.2.5	F 1s	689.7	2.85	18406.9			[-CF_2-CF_2-], at 100 Pa
5.1.2.5	F 1s	689.7	3.21	19563.7			[-CF_2-CF_2-], at 50 Pa
5.1.2.5	F 1s	689.7	6.36	23759.8			[-CF_2-CF_2-], at $5x10^{-3}$ Pa
5.1.2.6	F 1s	689.7	6.36	23662.4			[-CF_2-CF_2-], after 5 min illumination
5.1.2.6	F 1s	689.7	6.68	23267.7			[-CF_2-CF_2-], after 10 min illumination

5.1.2.6	F 1s	689.7	5.67	19873.9			[-CF_2-CF_2-], after 15 min illumination

∗ Peak energy for this Auger signal given as kinetic energy.

5.1.2.4 Specimen Description

a. Host Material: Polytetrafluoroethylene (PTFE)

b. CAS Registry #: 9002-84-0

c. Host Material Characteristics: homogeneous; solid; amorphous; polymer; Thin Film

d. Chemical Name: Polytetrafluoroethylene (PTFE)

e. Source: 0.5 mm foil from GuK GmbH (Berlin, Germany)

f. Host Composition: PTFE

g. Form: Solid

h. Structure: [-CF2-CF2-]n

i. History & Significance: PTFE is an important polymer with a wide variety of applications in science, engineering, and manufacturing.[32]

j. As Received Condition: Solid films

k. Analyzed Region: The film encountered by the X-ray beam

l. Ex Situ Preparation/Mounting: The film was cut into pieces and mounted to the sample plate of the instrument with carbon tape.

m. In Situ Preparation: None

n. Charge Control: Air was used for charge compensation/control at 50 Pa, 100 Pa, 200 Pa, 300 Pa, 400 Pa, 500 Pa and 1000 Pa. No background gas (traces of residual air) was used at 0.0025 Pa and 0.005 Pa.

o. Temp. During Analysis: 300K

p. Pressure During Analysis: 2.5x10-3, 5x10-3, 50, 100, 500, 1000 Pa

q. Pre-analysis Beam Exposure: 30 s.

5.1.2.5 Instrument Setting

a. Manufacturer and Model: Specs EnviroESCA

b. Analyzer Type: spherical sector

c. Detector: other 1D delay line detector (1D-DLD)

d. Number of Detector Elements: 25

e. Analyzer Mode: constant pass energy

f. Analyzer Pass Energy: 100 eV (survey spectrum) and 20 eV (narrow spectra)

g. Throughput ($T=E^N$): N=0

h. Excitation Source Window: silicon nitride

i. Excitation Source: Al K_α monochromatic

j. Source Energy: 1486.6 eV

k. Source Strength: 42 W

l. Source Beam Size: 250 µm x 250 µm

m. Signal Mode: multichannel direct

n. Incident Angle: 55°

o. Source-to-Analyzer Angle: 55°

p. Emission Angle: 0°

q. Specimen Azimuthal Angle: 0°

r. Acceptance Angle from Analyzer Axis: 0°

s. Analyzer Angular Acceptance Width: 44°

t. Ion Gun: No ion gun was used

5.1.2.6 Data Analysis Method

a. Energy scale correction: The energy shifts for the survey spectra at different pressure were calculated to make the C 1s energy 292.5 eV. For F 1s narrow scans at different pressure and at 0.005 Pa for different illumination time, the energy shifts were calculated to make F 1s peak at 689.7 eV.

b. Recommended energy scale shift: For survey spectra the energy shifts were, "Figure 5.1.2.1: -177.1 eV", "Figure 5.1.2.2: -15.5 eV", "Figure 5.1.2.3: -1.5 eV", "Figure 5.1.2.4: -0.5 eV". For F 1s narrow scan at different pressures, the energy shifts were: at "0.005 Pa: -91.9 eV", "50 Pa: -43.1 eV", "100 Pa: -25.5 eV", "200 Pa: -14.5 eV", "300 Pa: 9.5 eV", "400 Pa: -6.9 eV", 500 Pa: -4.9 eV" (Figure 5.1.2.5). For F 1s narrow scan at 0.005 Pa, for different illumination times, the energy shifts were- after "5 min: -91.9 eV", "10 min: -97.9 eV", 15 min: -103.9 eV" (Figure 5.1.2.6).

c. Peak shape and background method: Tougaard background were used for calculating peaks area, but otherwise no peak fitting was done.

5.1.2.7 Acknowledgements

Some of the information in this document was previously published in an application note produced by Specs, GmbH (Berlin, Germany). It is used here with their permission.

Section 5.1.3: Poly(γ-Benzyl L-Glutamate) (PBLG), by Near-Ambient Pressure XPS

5.1.3.1 Statement of Attribution

This document is originally published as Jain V.; Wheeler, J. J.; Ess, D. H.; Noack, S.; Vacogne C. D.; Scalaad, H.; Bahr, S.; Dietrich, P.; Meyer, M.; Thißen, A.; Linford, M. R. Poly(γ-Benzyl L-Glutamate) (PBLG), by near-ambient pressure XPS. *Surface Science Spectra* **2019** (Submitted). Here, all the data and figures are reproduced with the permission of AIP publishing. Data was collected at SPECS. I did all the peak fitting and data analysis.

Some information fields are omitted from this document to improve its readability in this format. We refer readers to the original document for complete sample, instrument information, and spectral features.

5.1.3.2 Abstract

Near ambient pressure X-ray photoelectron spectroscopy (NAP-XPS) is a less traditional form of XPS that allows samples to be analyzed at relatively high pressures, i.e., at greater than 2500 Pa. In this study, poly(γ-benzyl L-glutamate) (PBLG) with a molar mass of 11.3 kg/mol was analyzed by NAP-XPS; here we show the survey, C 1s, N 1s, and O 1s narrow scans of PBLG. The C 1s peak envelope was fitted in three different ways, to five, six, or seven synthetic peaks. In each fit, there was also a shake-up signal. The O 1s narrow scan was well fit with three peaks: C-O and C=O in a 1:2 ratio from the polymer, and a higher energy signal from water vapor. Mean-field Hartree-Fock orbital energy of a model monomer served as a guide to an additional fit of the C 1s envelope.

Keywords: Near-ambient pressure X-ray photoelectron spectroscopy, NAP-XPS, XPS, polymer, poly(γ-benzyl L-glutamate), PBLG

5.1.3.3 Introduction

Here we present the near ambient pressure – X-ray photoelectron spectroscopy (NAP-XPS) characterization of poly(γ-benzyl L-glutamate) (PBLG). This document is part of a series of papers on NAP-XPS being submitted to Surface Science Spectra. These articles and also the NAP-XPS technique have previously been introduced in this Journal.[6] Survey[33, 34] and narrow scans were collected with the SPECS EnviroESCA instrument.[2, 35-38]

PBLG is a polymer of γ-benzyl L-glutamic acid (N-carboxyanhydride). The number-average molar mass of the PBLG analyzed in this study is 11.3 kg/mol (corresponding to 51 repeat units).[39] This material appeared in an α-helical configuration held together by hydrogen bonds.[40] PBLG is frequently used to model biopolymers and α-helical polypeptides. It is also used to separate racemic materials in chromatography, for microencapsulation of pharmaceutically active hydrophobic liquids, and to improve the shatter resistance of plastics if it is blended with poly(vinyl chloride), poly(vinyl acetate), or their copolymers.[41-43]

XPS has previously been used to analyze proteins and polypeptides,[9, 21-22, 24, 44-45] e.g., human serum albumin (HSA) on diamond-like carbon[44] and bovine serum albumin in water.[46] XPS peak fitting has been performed in these analyses to determine the numbers and types of carbon, nitrogen, and oxygen atoms. Through peak fitting, the components/chemical states of the C 1s, O 1s, and N 1s envelopes can be speciated. For example, another study determined the molecular interaction between an antimicrobial peptide and the surface of silica nanoparticles via XPS peak fitting.[22]

In this study, we first fit the C 1s narrow scan of PBLG in three increasingly complex ways using literature precedent, i.e., per chemical shifts established in the literature.[47] These approaches are illustrated in Figure 5.1.3.1. In the first approach (Figure 5.1.3.1 a), the C 1s envelope was fit

to five synthetic peaks corresponding to: C-C/C-H, C-C(=O)O, C-O and C(=O)CNH at the same binding energy, C(=O)CNH, and C(=O)O. In the second approach (Figure 5.1.3.1b), the C 1s envelope was fit to six synthetic peaks, i.e., the same fit as the five-peak fit but the C-O and C(=O)CNH peaks were allowed to have different binding energies. In the third approach (Figure 5.1.3.1c), the C 1s envelope was fit to seven synthetic peaks, i.e., the same fit as the six-peak fit, but with the addition of a peak corresponding to additional hydrocarbon carbon, which may correspond to adventitious carbon or to additional C-C/C-H signal due to the orientation of the polymer. Only the results from the first approach are shown here because the results of the three methods were very similar. The literature precedent for these fits is based on established peak positions for aliphatic or aromatic carbon (C-C/C-H),[9, 21-22, 24, 44]secondarily shifted carbon (C-C(=O)O),[47, 48]carbon attached to oxygen or nitrogen through a single bond (C-O or C-NH),[9, 21-22, 24, 44, 47-48] carbon in a carbonyl or amide group (C=O or C(=O)NH),[9, 21-22, 24, 44] and carboxyl carbon (C(=O)O). [21, 47-48] Note that the relative areas of the synthetic peaks in the C 1s fit correspond to the number of carbon atoms in each chemical state. The C 1s fit also included a relatively broad synthetic peak to account for a shake-up signal, which is presumably from the aromatic ring in the polymer. The best fit to the C 1s envelope was determined based on the standard deviations of the residual to the fit. The widths of the synthetic peaks in the fits were constrained to have the same value (except the width of the shake-up signal). These widths were varied to obtain the best fit – ultimately, Gaussian-Lorentzian product functions with 30% Lorentzian character, i.e., GL(30) peaks, were emplyed.[49] Universal polymer Tougaard backgrounds were used for all the C 1s peak fitting, and also for the O 1s and N 1s fits described below.[25]

The O 1s envelope was fit with three synthetic peaks: two at lower energy attributable to the polymer (O-C=O (O-1) [9, 21, 44,22,47] and O=C-O/oxygen from adsorbed water (O-2) [44,21,14,47] in

close to a 2:1 area ratio) and a narrower, higher energy signal attributed to gaseous water.[47] The gas phase water signal was best fit with a GL(80) synthetic peak. Its lower width and greater Lorentzian character are consistent with it coming from a gas phase material. Neither the positions nor areas of these peaks were constrained in the fit, although the two 'polymer' peaks were fixed to have the same widths. Based on the structure of the polymer, the N 1s signal was fit to a single, synthetic GL(30) peak.

As a further guide to the peak fitting, the C 1s, O 1s, and N 1s orbital energies for the polymer were estimated using ab initio Hartree-Fock/6-31G** calculations in the Gaussian 09 program.[50] The model monomer used for PBLG is shown in Figure 5.1.3.2. This structure was optimized to its geometry equilibrium structure on the potential energy surface and confirmed to be a minimum energy structure with a vibrational frequency analysis. Hartree-Fock theory was selected because these mean field one-electron orbitals can be used to approximate one-electron ionization energies through Koopman's theorem. Also, Cumpson et al. and Zuilhof et al. showed that scaled Hartree-Fock orbital energies of small organic compounds provide reasonably accurate relative values for peak fitting purposes.[51, 52] Our synthetic spectrum/fit was generated based on the spacings between the Hartree-Fock calculated C 1s and O 1s energies (see Figure 5.1.3.7 and Figure 5.1.3.8). In these fits, (i) each calculated orbital energy corresponds to one peak in the synthetic spectrum (there were 3 and 12 components in the O 1s and C 1s synthetic spectra, respectively), (ii) the position of the lowest energy peak was allowed to vary, but all of the other peaks were constrained to have the positions predicted by the ab initio calculations, (iii) the widths of all the fit components were constrained to be the same, but this width was allowed to vary in the fit, (iv) the areas of all the fit components were constrained to be the same, and (v) neither the O 1s signal from vapor phase water nor the C 1s shake-up peak was calculated. Overall, the

Hartree-Fock calculated C 1s and O 1s spectra were in reasonable agreement with the experimental spectra. That is, for the C 1s fits, the residual standard deviations were 0.87, 0.86 and 0.80 for the three approaches described above, respectively, while with the Hartree-Fock analysis it was 1.57. For the O 1s fit the residual standard deviation is 1.00 with the literature-based approach and 1.15 with the Hartree-Fock analysis.

We also report the concentrations of atoms in the polymer as obtained from both survey and narrow scans. These calculations are entirely based on the C 1s, N 1s, and O 1s peaks; they exclude the small amount of signal from the Si 2s and 2p signals in the survey spectrum, which are presumably due to PDMS contamination, along with the O 1s and C 1s signal that would also be attributed to this PDMS, i.e., for PDMS we expect the Si:O:C ratio to be 1:1:2. The resulting, predicted concentrations are in reasonable agreement with theoretical values, i.e., we expect C, O, and N in a 12:3:1 ratio (75 at. % C, 18.75 at. % O, and 6.25 at. % N). From the narrow scans we obtained 74.2 at. % C, 19.61 at. % O, and 6.19 at. % N. The concentrations listed in the Spectral Features Table, which were obtained from the survey scan, are similar.

Table 5.1.3.1. Spectral features of interest.

Figure number	**Element/ Transition**	**Peak Energy (eV)**	**Peak Width FWHM (eV)**	**Peak Area (eV x cts/s)**	**Sensitivity Factor**	**Concentration (at. %)**	**Peak Assignment**
5.1.3.1	Si 2p	103	2.56	117.3	0.9	75.59	Carbon from PBLG

5.1.3.1	C 1s	286	2.78	7116.3	"1.0"	1.73	Si due to contamination
5.1.3.1	N 1s	401	2.47	1744	1.67	7.06	Nitrogen from PBLG
5.1.3.1	O 1s	536	2.49	10626.1	2.47	15.62	Oxygen from PBLG
5.1.3.1	O KLL	984	2.79	792.6			Oxygen Auger
5.1.3.2	C1s	285.4	1.1	675.2			C-C/C-H
5.1.3.2	C1s	286.2	1.1	97.9			C-C(=O)O
5.1.3.2	C1s	287.1	1.1	195.8			C-O, O=C-C-NH_2
5.1.3.2	C1s	288.7	1.1	97.9			C=O/C(=O)NH
5.1.3.2	C1s	289.7	1.1	97.9			C(=O)O
5.1.3.2	C1s	292.4	1.52	25.9			Shake-up peak
5.1.3.3	N 1s	400.7	1.15	155.5			O=C-C-NH_2
5.1.3.4	O 1s	532.7	1.37	495.9			C=O
5.1.3.4	O 1s	534.1	1.37	257			C-O

5.1.3.4	O 1s	535.9	0.57	1170.7			From water vapor
5.1.3.5	C1s	285.3	1.12	97.99			C-C/C-H
5.1.3.5	C1s	285.3	1.12	97.99			C-C/C-H
5.1.3.5	C1s	285.3	1.12	97.99			C-C/C-H
5.1.3.5	C1s	285.4	1.12	97.99			C-C/C-H
5.1.3.5	C1s	285.4	1.12	97.99			C-C/C-H
5.1.3.5	C1s	285.6	1.12	97.99			C-C/C-H
5.1.3.5	C1s	285.7	1.12	97.99			C-C/C-H
5.1.3.5	C1s	285.9	1.12	97.99			C-C(=O)O
5.1.3.5	C1s	287	1.12	97.99			C-O
5.1.3.5	C1s	287.2	1.12	97.99			O=C-C-NH_2
5.1.3.5	C1s	288.3	1.12	97.99			C=O/C(=O)NH
5.1.3.5	C1s	289.4	1.12	97.99			C(=O)O
5.1.3.5	O 1s	532.47	0.59	268.5			C=O (Carbonyl oxygen)
5.1.3.6	O 1s	532.72	1.45	268.5			C=O (Carboxyl oxygen)

5.1.3.6	O 1s	534.3	1.45	268.5			C-O
5.1.3.6	O 1s	535.9	1.45	1112.6			From water vapor

5.1.3.4 Specimen Description

a. Host Material: Poly(γ-benzyl L-glutamate) (PBLG)

b. CAS Registry #: 25014-27-1

c. Host Material Characteristics: homogeneous; solid; amorphous; polymer; Powder

d. Chemical Name: Poly(γ-benzyl L-glutamate)

e. Source: Synthesized in the Schlaad lab at the University of Potsdam, Germany.[39] Host Composition: PBLG (see labeled structure), 11.3 kg/mol

f. Form: Solid

g. Structure: See Figure 5.1.3.1

h. History & Significance: PBLG is a polymer of γ-benzyl L-glutamic acid, which is frequently used to model biopolymers and polypeptides.[41-43]

i. As Received Condition: Powder

j. Analyzed Region: Random region of a powder sample of the polymer encountered by the X-ray beam.

k. Ex Situ Preparation/Mounting: None

l. In Situ Preparation: N/A

m. Charge Control: Charge control through the gas atmosphere, i.e., water vapor, surrounding the sample.

n. Temp. During Analysis: 300K

o. Pressure During Analysis: 1000 Pa

p. Pre-analysis Beam Exposure: 30 s

5.1.3.5 Instrument Setting

a. Manufacturer and Model: SPECS EnviroESCA

b. Analyzer Type: spherical sector

c. Detector: other 1D delay line detector (1D-DLD)

d. Number of Detector Elements: 25

e. Analyzer Mode: constant pass energy

f. Analyzer Pass Energy: 100 eV (survey spectrum) and 30 eV (narrow spectra)

g. Throughput ($T=E^N$): N=0

h. Excitation Source Window: silicon nitride

i. Excitation Source: Al K_α monochromatic

j. Source Energy: 1486.6 eV

k. Source Strength: 42 W

l. Source Beam Size: 250 µm x 250 µm

m. Signal Mode: multichannel direct

n. Incident Angle: 55°

o. Source-to-Analyzer Angle: 55°

p. Emission Angle: 0°

q. Specimen Azimuthal Angle: 0°

r. Acceptance Angle from Analyzer Axis: 0°

s. Analyzer Angular Acceptance Width: 44°

t. Ion Gun: No ion gun was used

5.3.1.6 Data Analysis Method

a. Energy Scale Correction: No correction

b. Recommended Energy Scale Shift: 0

c. Peak Shape and Background Method: Peak fitting was performed with the CasaXPS software package (Casa Software Ltd., Version 2.3.18PR1.0). Hartree-Fock calculations were performed with a 6-31G** basis set using Gaussian 09 (Gaussian, Inc., Wallingford, CT). Universal polymer Tougaard backgrounds and synthetic Gaussian-Lorentzian product functions were used for all the fits.

d. Quantitation Method: Elemental compositions were calculated using the standard SPECS software.

Section 5.1.4: Human Hair, Untreated, Colored, Bleached, and/or Treated with a Conditioner, by Near-Ambient Pressure XPS

5.1.4.1 Statement of Attribution

This document was originally published as Jain V.; Bahr, S.; Dietrich, P.; Meyer, M.; Thißen, A.; Linford, M. R. Human Hair, Untreated, Colored, Bleached, and/or Treated with a Conditioner by near-ambient pressure (NAP-XPS). *Surface Science Spectra* (Accepted). Some of the information in this document was previously published in an application note produced by SPECS, GmbH (Berlin, Germany). It is used here with their permission. Data was collected at SPECS. I did all the peak fitting and data analysis. Here, all the data and figures are reproduced with the permission of AIP publishing.

Some information fields are omitted from this document to improve its readability in this format. We refer readers to the original document for complete sample, instrument information, and spectral features.

5.1.4.2 Abstract

Near ambient pressure – X-ray photoelectron spectroscopy (NAP-XPS) is a less traditional form of XPS that allows samples to be analyzed at relatively high pressures, i.e., at ca. 2500 Pa. With NAP-XPS, XPS can probe moderately volatile liquids, biological samples, porous materials, and/or polymeric materials that outgas significantly. Here, we show the NAP-XPS analysis of untreated/blank human hair, and human hair that has been colored (red) and treated with a commercial conditioner, or bleached and treated with a different conditioner. Survey spectra are shown of each material along with figures comparing their Si 2p, S 2p, and C 1s spectra. The survey spectrum of untreated hair shows S 2p, S 2s, C 1s, Ca 2p, N 1s, and O 1s peaks and corresponding O, N, and C Auger signals. The survey spectra of the colored and bleached hair

show significant Si 2s and Si 2p signals and reduced or eliminated S 2p and S 2s peaks, presumably due to deposition of dimethicone (polydimethylsiloxane) from the corresponding commercial hair treatment products. Narrow scans similarly indicate the deposition of a silicon-containing material on the two types of treated hair with a concomitant decrease in the intensity of the sulfur signals from the hair. Upon treatment, the C 1s envelope also changes – the chemically-shifted peak attributable to amide-type carbon disappears.

Keywords: Near-ambient pressure X-ray photoelectron spectroscopy, NAP-XPS, XPS, Hair

5.1.4.3 Introduction

Here we present near ambient pressure – X-ray photoelectron spectroscopy (NAP-XPS) characterization of three types of human hair: (1) untreated, (2) colored and conditioned, and (3) bleached and conditioned. This document is part of a series of submissions on NAP-XPS that is being submitted to Surface Science Spectra. This set of articles and the NAP-XPS technique have previously been introduced in this Journal.[6] Data were collected with the SPECS EnviroESCA instrument.[1, 7-10]

The XPS analysis of hair is important for understanding its outermost surface and also the effects of any surface treatments/modifications of it, where these results have implications for the cosmetic and forensic sciences. The analysis of hair by conventional XPS is complicated by its insulating nature and the fact that it is an organic material that can outgas. The samples studied in this work consisted of (1) untreated/blank hair, (2) hair that was colored (red) with a commercial dyeing agent and treated with a commercial conditioner, and (3) hair that was bleached with a commercial product and treated with a different commercial conditioner. Hair is a proteinaceous material, and the survey spectrum of the untreated hair shows the expected nitrogen (N 1s) and sulfur (S 2p and S 2s) signals.[33, 53-54] It also shows C 1s, Ca 2p, and O 1s peaks, along with the

expected O, N, and C Auger signals. After treatments with the commercial products, the XPS survey spectra revealed considerable Si 2s and Si 2p signals and decreased sulfur signals. The presence of silicon is attributed to residual dimethicone (polydimethylsiloxane), which is often included in commercial hair formulations. The high resolution C 1s spectrum of the untreated sample shows the presence of carbon species at higher binding energies (higher oxidation state[55]). The higher of these peaks is presumably due to amide-type carbon, which is expected to be present in hair.[56] These peaks disappear from the C 1s envelope after treatment with the conditioner. Indeed, the C 1s narrow scans of conditioned hair show signals at lower binding energy, which is consistent with the C-Si moieties in PDMS. [55,56,57] A comparison of the Si 2p, S 2p and C 1s narrow scans among three kinds of hair samples is shown below. The voltage shifts applied to the samples were similar to each other. The effect of these shifts was to move the maximum in the C 1s envelope to 285.0 eV.

Table 5.1.4.1. Spectral features of interest.

Figure Number	**Element/ Transition**	**Peak Energy (eV)**	**Peak Width FWHM (eV)**	**Peak Area (eV x cts/s)**	**Sensitivity Factor**	**Concentration (at. %)**	**Peak Assignment**
5.1.4.1	S 2p	160	2.91	1154.3	1.79	2.53	Untreated hair
5.1.4.1	S 2s	223	3.25	930.4			Untreated hair
5.1.4.1	C 1s	280	3.11	23728	“1.0”	75.33	Untreated hair

5.1.4.1	Ca 2p	343	3	1088.7			Untreated hair
5.1.4.1	N 1s	396	3.67	4534.4	1.67	7.84	Untreated hair
5.1.4.1	O 1s	527	3.26	11298.8	2.47	14.29	Untreated hair
5.1.4.1	O KLL	513.1*	10.71	2764			Untreated hair
5.1.4.1	O KLL	487.1*	4.67	736.4			Untreated hair
5.1.4.1	C KLL	265.1*	2.9	1005			Untreated hair
5.1.4.2	Si 2p	101.8	3.26	1741.9	0.91	8.73	Colored hair
5.1.4.2	Si 2s	152.8	3.64	1822			Colored hair
5.1.4.2	C 1s	283.8	3.3	14586.1	“1.0”	66.59	Colored hair
5.1.4.2	N 1s	401.8	5.69	1418.9	1.67	8.69	Colored hair
5.1.4.2	O 1s	531.8	3.25	7316.5	2.47	15.5	Colored hair
5.1.4.2	O KLL	503.3*	7.44	1480.1			Colored hair
5.1.4.2	N KLL	366.3*	8.63	841.6			Colored hair
5.1.4.2	C KLL	260.3*	8.25	702.6			Colored hair

5.1.4.3	Si 2p	100	3.51	3118.1	0.91	19.5	Bleached hair
5.1.4.3	Si 2s	151	3.99	3432.7			Bleached hair
5.1.4.3	C 1s	283	3.53	7185.7	“1.0”	50.56	Bleached hair
5.1.4.3	N 1s	400	4.28	2805	1.67	9.66	Bleached hair
5.1.4.3	O 1s	530	3.59	9135.9	2.47	20.28	Bleached hair
5.1.4.3	O KLL	506.1*	5.68	2332.9			Bleached hair
5.1.4.3	N KLL	368.1*	7.03	837.3			Bleached hair
5.1.4.3	C KLL	255.1*	2.45	907.5			Bleached hair
5.1.4.4	Si 2p	102.3	2.4	2437.2			Colored hair
5.1.4.4	Si 2s	153.7	3.08	2590			Colored hair
5.1.4.4	Si 2p	102.3	2.99	4614.8			Bleached hair
5.1.4.4	Si 2s	153.5	3.52	4676.4			Bleached hair

5.1.4.5	S 2p	163.6	2.3	400.9			Untreated hair
5.1.4.5	S 2p	167.4	2.21	117.6			Colored hair
5.1.4.5	S 2p	167	0.65	131.6			Bleached hair
5.1.4.6	C 1s	285	1.87	1210			Untreated hair (Due to C-C/C-H)
5.1.4.6	C 1s	286.5					Untreated hair (Due to C-N or C-O)
5.1.4.6	C 1s	288					Untreated hair (Due to amide/carboxyl groups)
5.1.4.6	C 1s	285	1.63	1677.8			Colored hair
5.1.4.6	C 1s	285	1.91	2286.1			Bleached hair
5.1.4.6	C 1s	283.5					Bleached hair (Due to C-Si)

* Kinetic energies of the Auger peaks.

5.1.4.4 Specimen Description

a. Host Material: Human hair

b. CAS Registry #: N/A

c. Host Material Characteristics: homogeneous; solid; amorphous; organic compound; Fiber

d. Chemical Name: N/A

e. Source: Untreated (01498), Colored (01499), Bleached (01500)

f. Host Composition:

g. Form: Solid

h. Structure: Proteinaceous fiber and polydimethylsiloxane coating.

i. History & Significance:

j. As Received Condition: As cut and/or treated.

k. Analyzed Region: Random region

l. Ex Situ Preparation/Mounting: Mounted to sample plate with carbon tape.

m. In Situ Preparation: N/A

n. Charge Control: Residual gas

o. Temp. During Analysis: 300K

p. Pressure During Analysis: 100 Pa

q. Pre-analysis Beam Exposure: 30 s

5.1.4.5 Instrument Setting

a. Manufacturer and Model: Specs EnviroESCA

b. Analyzer Type: spherical sector

c. Detector: other 1D delay line detector (1D-DLD)

d. Number of Detector Elements: 25

e. Analyzer Mode: constant pass energy

f. Analyzer Pass Energy: 100 eV (survey spectrum) and 20 eV (narrow spectra)

g. Throughput ($T=E^N$): N=0

h. Excitation Source Window: silicon nitride

i. Excitation Source: Al K_α monochromatic

j. Source Energy: 1486.6 eV

k. Source Strength: 42 W

l. Source Beam Size: 250 µm x 250 µm

m. Signal Mode: multichannel direct

n. Incident Angle: 55°

o. Source-to-Analyzer Angle: 55°

p. Emission Angle: 0°

q. Specimen Azimuthal Angle: 0°

r. Acceptance Angle from Analyzer Axis: 0°

s. Analyzer Angular Acceptance Width: 44°

t. Ion Gun: No ion gun was used

5.1.4.6 Data Analysis Method

a. Energy Scale Correction: The energy shifts for the different samples were calculated to make the C 1s energy 285.0 eV.

b. Recommended Energy Scale Shift: For untreated hair -15.8 eV, for colored hair -12.8 eV and for Bleached hair -13.6 eV

c. Peak Shape and Background Method: N/A

d. Quantitation Method: Elemental compositions were calculated using the standard SPECS software.

5.1.4.7 Acknowledgments

Some of the information in this document was previously published in an application note produced by SPECS, GmbH (Berlin, Germany). It is used here with their permission.

Section 5.1.5: Phosphate Buffered Saline (PBS). Aqueous Solution and Corresponding Solid by Near-Ambient Pressure XPS

5.1.5.1 Statement of Attribution

This document was originally submitted as Jain V.; Bahr, S.; Dietrich, P.; Meyer, M.; Thißen, A.; Linford, M. R. Phosphate Buffered Saline (PBS). Aqueous Solution and Corresponding Solid by near-ambient pressure XPS. *Surface Science Spectra* (Accepted). Data was collected at SPECS. I did all the peak fitting and data analysis. Here, all the data and figures are reproduced with the permission of AIP publishing.

5.1.5.2 Abstract

Near ambient pressure (NAP) XPS (NAP-XPS) is a less traditional form of XPS that allows samples to be analyzed at relatively high pressures, i.e., at ca. 10 mbar. With NAP-XPS, XPS can probe moderately volatile liquids, biological samples, porous materials, and/or polymeric materials that outgas significantly. Here we have used NAP-XPS to analyze phosphate buffer saline (PBS), a material that is widely used in biological research, in both its solid and solution form. Aqueous solutions are difficult, if not impossible, to analyze by conventional XPS. In particular, we show NAP-XPS survey, P 2p, P 2s, Cl 2p, Cl 2s, K 2p, O 1s, and Na 1s narrow, and valence band spectra of solid PBS. We also show the survey, Cl 2p narrow, and the valence band spectra from an aqueous solution of PBS.

Keywords: Near-ambient pressure X-ray photoelectron spectroscopy, NAP-XPS, XPS, PBS, phosphate buffered saline

5.1.5.3 Introduction

Here we present the near ambient pressure – X-ray photoelectron spectroscopy (NAP-XPS) characterization of solution of phosphate buffer saline (PBS) and its corresponding solid. This document is part of a series of submissions on NAP-XPS that is being submitted to Surface Science

Spectra. This set of articles and the NAP-XPS technique have previously been introduced in this Journal.[6] Data were collected with the Specs EnviroESCA instrument,[1, 7-10] where the liquid sample was analyzed directly without any sample preparation. Obviously, it is not possible to analyze aqueous solutions by traditional XPS under UHV.[11] Indeed, the prospect of analyzing liquid-gas and solid-gas interfaces under near ambient pressure by NAP-XPS allows materials to be studied under more realistic conditions that should result in more relevant results. Other aqueous solutions, including those of RbCl, NaCl, and bovine serum albumin (BSA), have previously been analyzed by NAP-XPS.[12,58]

In this submission we present NAP-XPS spectra of a solution of phosphate buffered saline (PBS) and its corresponding solid. PBS is an aqueous buffer that generally contains NaCl, NaH2PO4, KCl, and KH2PO4. It is important in biological research because it is isotonic and non-toxic to most cells. [59, 60] It has a large number of applications that include the detachment of clumped cells, dilution of cell culture solutions, and rinsing cell containers.[61, 62] For these types of biological applications, it is important to have high quality buffers.[63] The ability to analyze liquid-gas surfaces by photoelectron spectroscopy in a state closer to their native one opens up important opportunities for the analysis of solutions like PBS bovine serum albumin (BSA).[11,64]

Here, we show the NAP-XPS survey, P 2p, P 2s, Cl 2p, Cl 2s, K 2p, O 1s, and Na 1s narrow, and valence band spectra of solid PBS. We also show the survey spectrum, Cl 2p narrow scan, and valence band spectrum of an aqueous solution of PBS. Peak fits of some of these regions are shown, where this fitting was performed with CasaXPS. For the P 2p narrow scan, a reasonable fit was obtained with Gaussian-Lorentzian product functions with 30% Lorentzian character.[7] The separation of the spin-orbit P 2p3/2 (141.01 eV) and P 2p1/2 (142.01 eV) components in this fit were obtained from the Literature.[64] For the Cl 2p fit from the solid PBS, a reasonable fit was

obtained with Gaussian-Lorentzian sum functions with 20% Lorentzian character.[7] Note that changing the Gaussian-Lorentzian ratios in these fits by ca. 10% did not generally result in significant changes in the fits. The separation of the spin-orbit peaks in the Cl 2p fit (the Cl 2p3/2 peak at 207.4 eV and the Cl 2p1/2 peak at 209.4 eV) were obtained from the literature.[65] To fit the Cl 2p narrow scan obtained from the solution of PBS, all the parameters were the same as for the fit to the narrow scan of the solid, except for the synthetic line shape, which was a Gaussian-Lorentzian sum function with 10% Lorentzian character. In all the fits, the widths of the spin-orbit components were fixed to the same values, which is a fairly reasonable approximation because (i) the peaks usually do have similar widths, and (ii) they overlap to fairly large extent. For the fit to the Cl 2s signal, a single Gaussian-Lorentzian sum function with 50% Lorentzian character was used. Shirley backgrounds were used for all of the fits shown in this work. None of the spectra in this submission have been energy shifted.

Table 5.1.5.1. Spectral features of interest.

Figure Number	**Element/ Transition**	**Peak Energy (eV)**	**Peak Width FWHM (eV)**	**Peak Area (eV x cts/s)**	**Sensitivity Factor**	**Concentration (at. %)**	**Peak Assign ment**
5.1.5.1	Na 2p	39	3.13	1472.9			Solid PBS
5.1.5.1	Na 2s	72	3.18	2983			Solid PBS
5.1.5.1	P 2p	141	2.84	1934.1			Solid PBS

5.1.5.1	P 2s	199	3.28	1309.2			Solid PBS
5.1.5.1	Cl 2p	208	3.28	10646.9	…	…	Solid PBS
5.1.5.1	Cl 2s	278	3.62	5986.8	…	…	Solid PBS
5.1.5.1	C 1s	293	4.56	1877.9	…	…	Adventitious carbon
5.1.5.1	K 2p	302	4.61	2074.4			Solid PBS
5.1.5.1	K 2s	385	4.23	1406.4			Solid PBS
5.1.5.1	N 1s	412	3.71	1341.2			Nitrogen from air
5.1.5.1	Na KLL	506	3.52	24835.5			Solid PBS
5.1.5.1	O 1s	540	3.96	18363.5			Solid PBS
5.1.5.1	Na KLL	573	3.62	1605.7			Solid PBS
5.1.5.1	O KLL	978.5	5.68	3305.5			Solid PBS

5.1.5.1	Na 1s	1072.5	3.03	7690.1			Solid PBS
5.1.5.2	P $2p_{3/2}$	141.01	1.61	233.6			Solid PBS
5.1.5.2	P $2p_{1/2}$	142.01	1.61	116.8			Solid PBS
5.1.5.3	P 2s	198.8	2.11	227.9			Solid PBS
5.1.5.4	Cl $2p_{3/2}$	207.4	1.35	1433.6			Solid PBS
5.1.5.4	Cl $2p1_{/2}$	209.1	1.35	716.8			Solid PBS
5.1.5.5	Cl 2s	278.4	2.47	1095.6			Solid PBS
5.1.5.6	C 1s	294	3.79	1000.1			Adventitious carbon
5.1.5.6	K 2p	301	2.93	1546.1			Solid PBS
5.1.5.7	O 1s, O-1	539.7	3.11	3088.9			Solid PBS
5.1.5.7	O 1s, O-2	544.6	2.6	1077.5			Solid PBS

5.1.5.8	Na 1s	1080.4	2.31	4115			Solid PBS
5.1.5.9	Valance Band						Solid PBS
5.1.5.10	O 2s	26.3	3.67	508.7			Aqueous PBS
5.1.5.10	Na 2s	64.3	2.07	128.1			Aqueous PBS
5.1.5.10	Cl 2p	199.3	2.74	547.5			Aqueous PBS
5.1.5.10	C 1s	285.3	2.5	2197.6			Aqueous PBS
5.1.5.10	Na KLL	498.3	2.13	751.5			Aqueous PBS
5.1.5.10	O 1s	534.3	4.32	8537.7			Aqueous PBS
5.1.5.11	Cl $2p_{3/2}$	198.5	502.1	2.07			Aqueous PBS
5.1.5.11	Cl $2p_{1/2}$	200.5	251	2.07			Aqueous PBS
5.1.5.12	Valance Band						Aqueous PBS

5.1.5.4 Specimen Description

a. Host Material: PBS solid and PBS aqueous solution

b. CAS Registry #: MFCD00131855 (This is an MDL number)

c. Host Material Characteristics: homogeneous; solid; amorphous; inorganic compound; Other

d. Chemical Name: Phosphate buffered saline

e. Source: Sigma-Aldrich

f. Host Composition: NaCl, NaH2PO4, KCl, and KH2PO4 in water

g. Form: Solid, solution

h. Structure: N/A

i. History & Significance: PBS solutions are widely used in biological research.11, 12

j. As Received Condition: PBS tablet from Sigma-Aldrich

k. Analyzed Region: random

l. Ex Situ Preparation/Mounting: The solution was prepared in water and analyzed by XPS.

m. In Situ Preparation: To prepare PBS solution, tablets of PBS were dissolved in water.

n. Charge Control: Residual gas

o. Temp. During Analysis: 300K

p. Pressure During Analysis: PBS solid: 100 Pa (1 mbar), PBS solution: 800 Pa (8 mbar)

q. Pre-analysis Beam Exposure: 30 s.

5.1.5.5 Instrument Setting

a. Manufacturer and Model: Specs EnviroESCA

b. Analyzer Type: spherical sector

c. Detector: other 1D delay line detector (1D-DLD)

d. Number of Detector Elements: 25

e. Analyzer Mode: constant pass energy

f. Analyzer Pass Energy: 100 eV (survey spectrum) and 20 eV (narrow spectra)

g. Throughput (T=EN): N=0

h. Excitation Source Window: silicon nitride

i. Excitation Source: Al Kα monochromatic

j. Source Energy: 1486.6 eV

k. Source Strength: 42 W

l. Source Beam Size: 250 µm x 250 µm

m. Signal Mode: multichannel direct

n. Incident Angle: 55°

o. Source-to-Analyzer Angle: 55°

p. Emission Angle: 0°

q. Specimen Azimuthal Angle: 0°

r. Acceptance Angle from Analyzer Axis: 0°

s. Analyzer Angular Acceptance Width: 44°

t. Ion Gun: No ion gun was used

5.1.5.6 Data Analysis Method

a. Energy Scale Correction: No correction

b. Recommended Energy Scale Shift: 0 eV

c. Peak Shape and Background Method: GL (30) and U Poly Tougaard background was used.

d. Quantitation Method: N/A

5.2 Figures

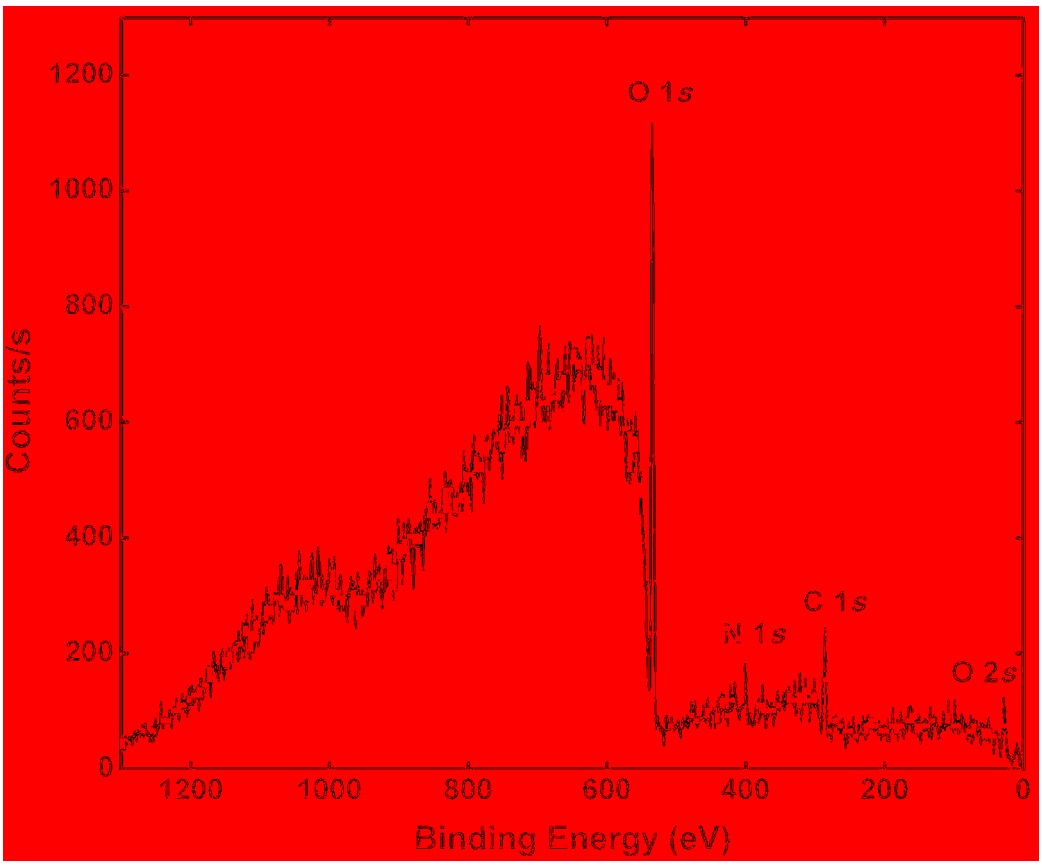

Figure 5.1.1.1. Survey scan of BSA.

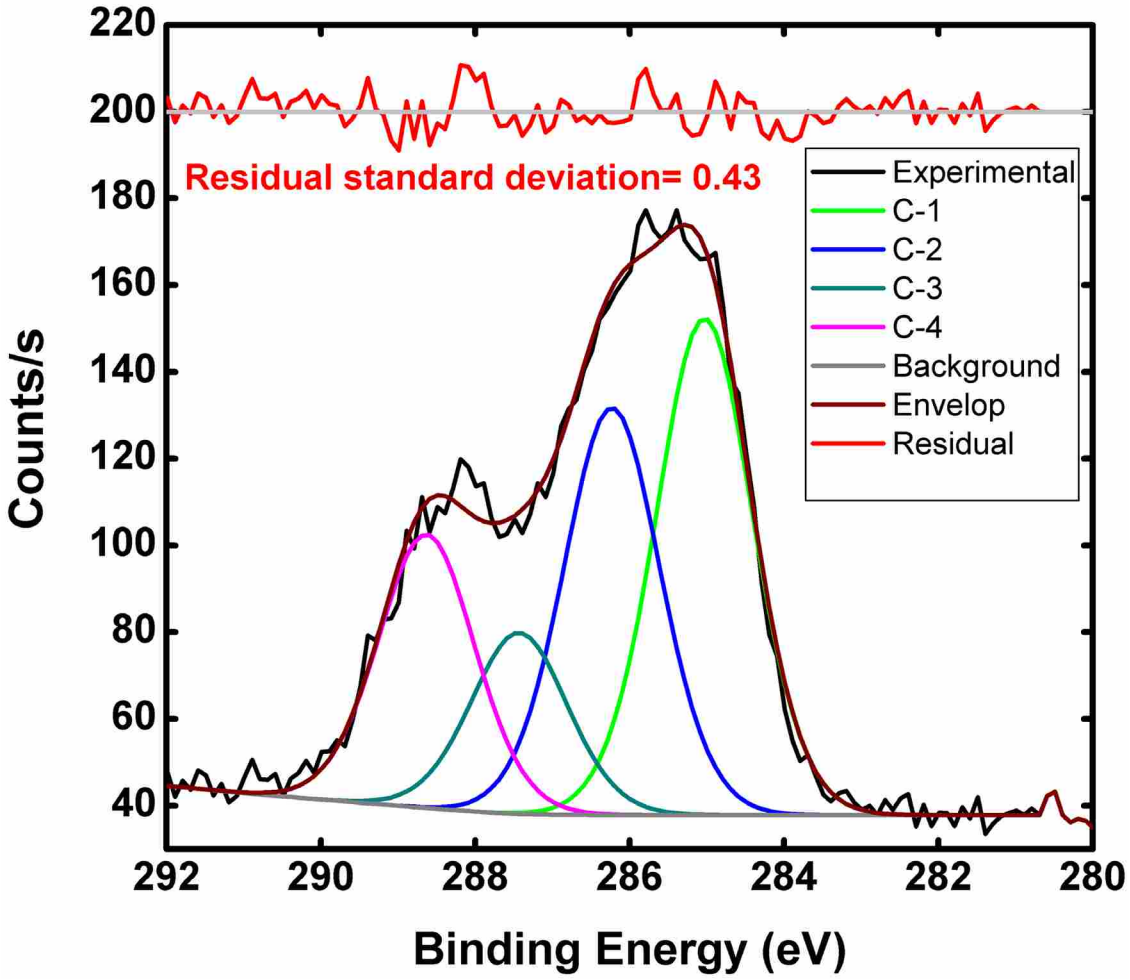

Figure 5.1.1.2. Peak fitting of C 1s peak envelope with 4 peaks.

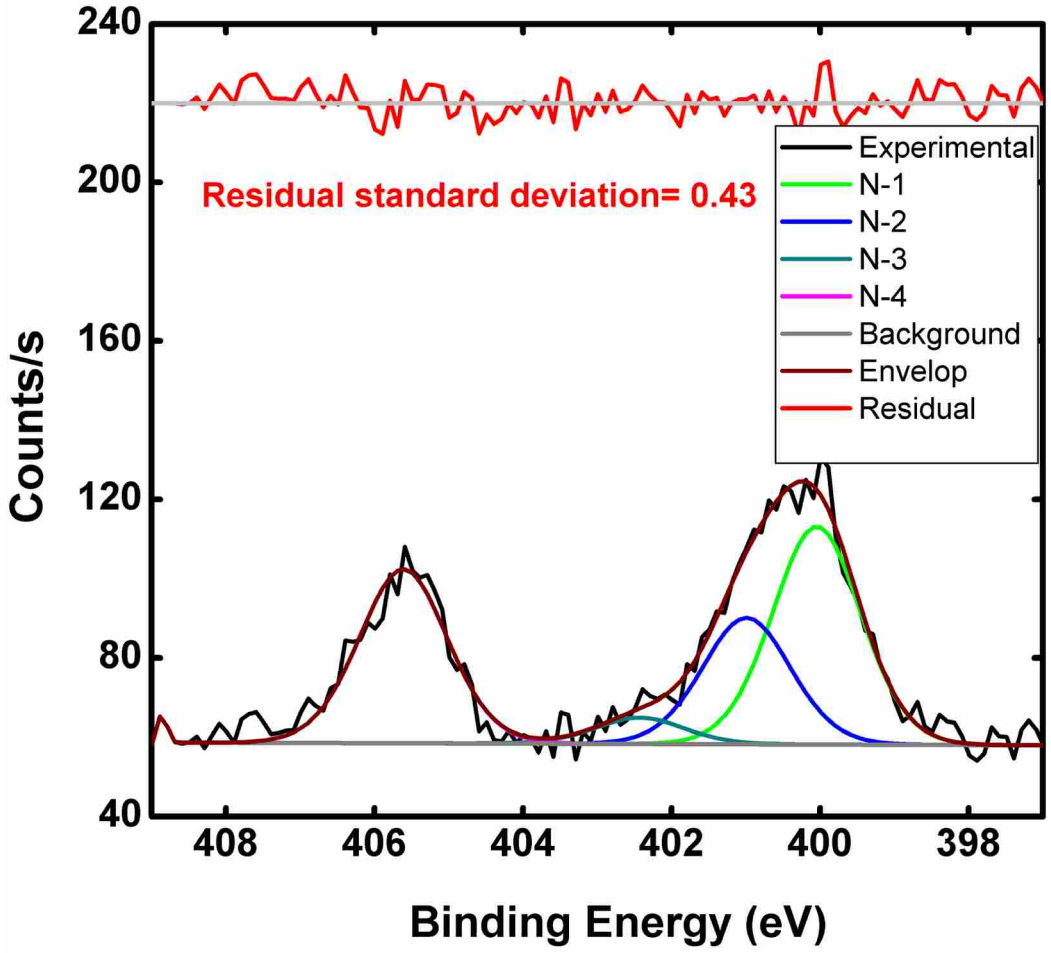

Figure 5.1.1.3. Peak fitting of N 1s envelope with 4 peaks.

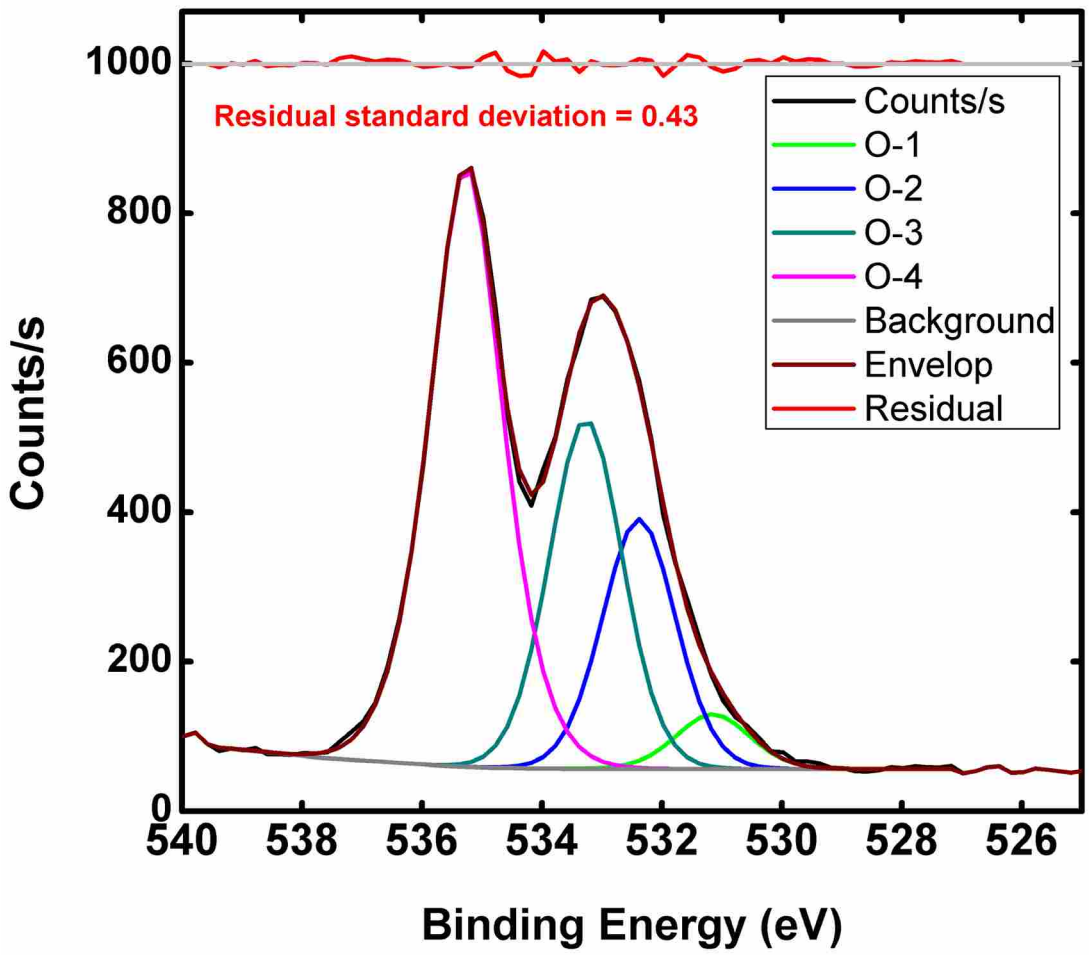

Figure 5.1.1.4. Peak fitting of O 1s envelope with 4 peaks.

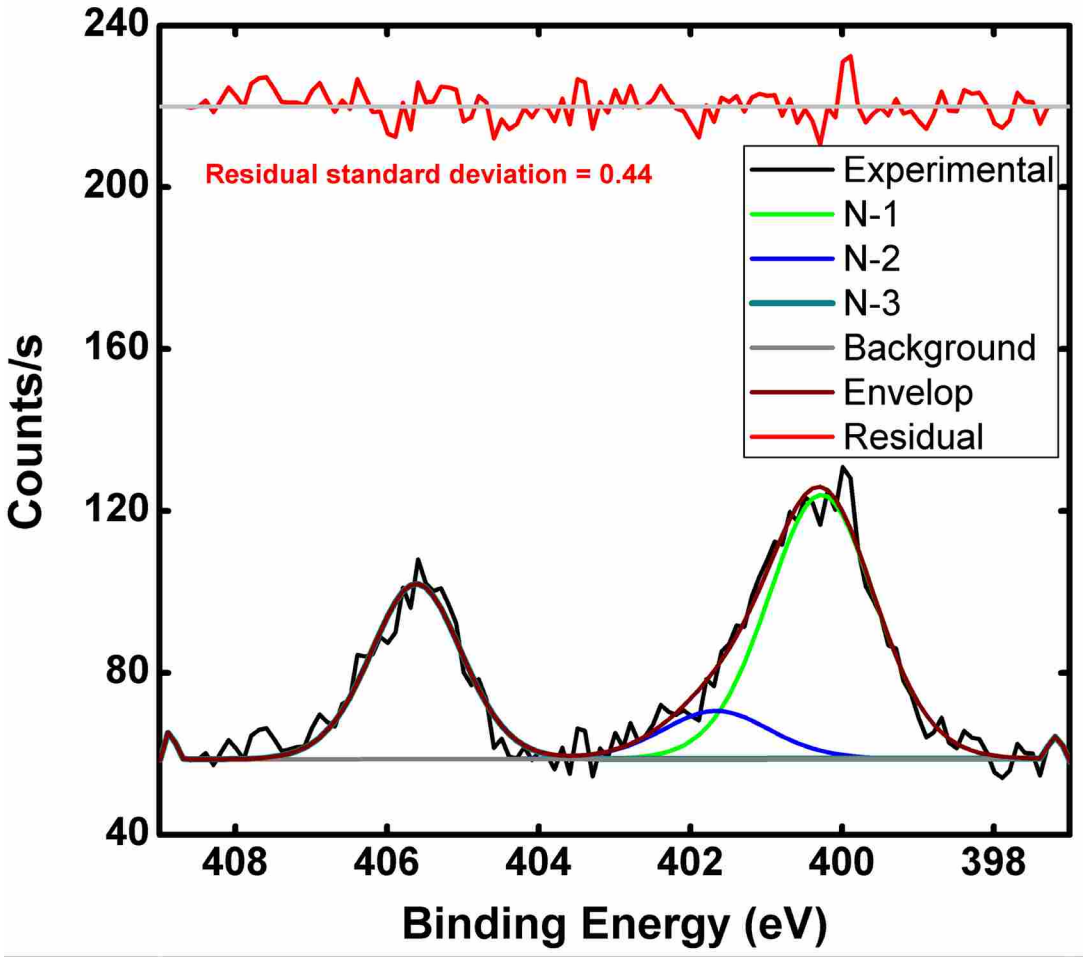

Figure 5.1.1.5. Peak fitting of N 1s envelope with 3 peaks.

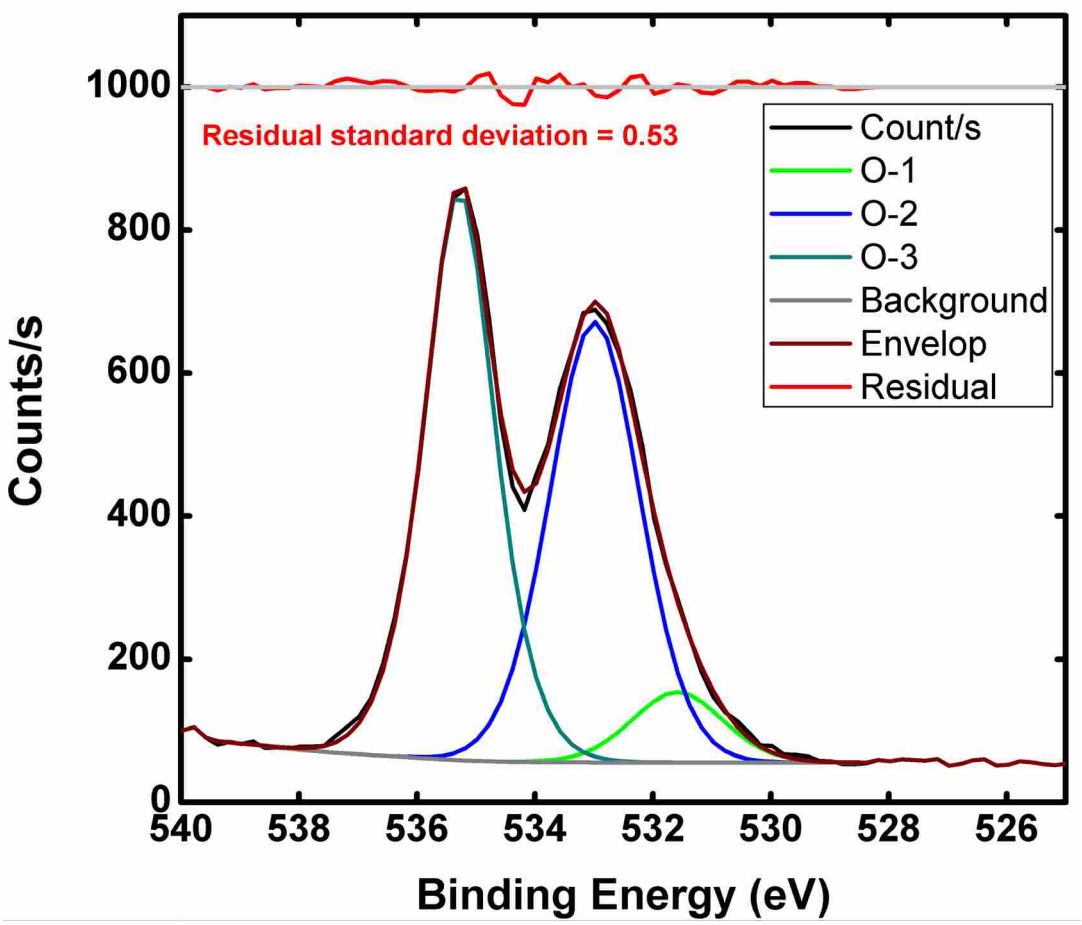

Figure 5.1.1.6. Peak fitting of O 1s narrow scan with 3 peaks.

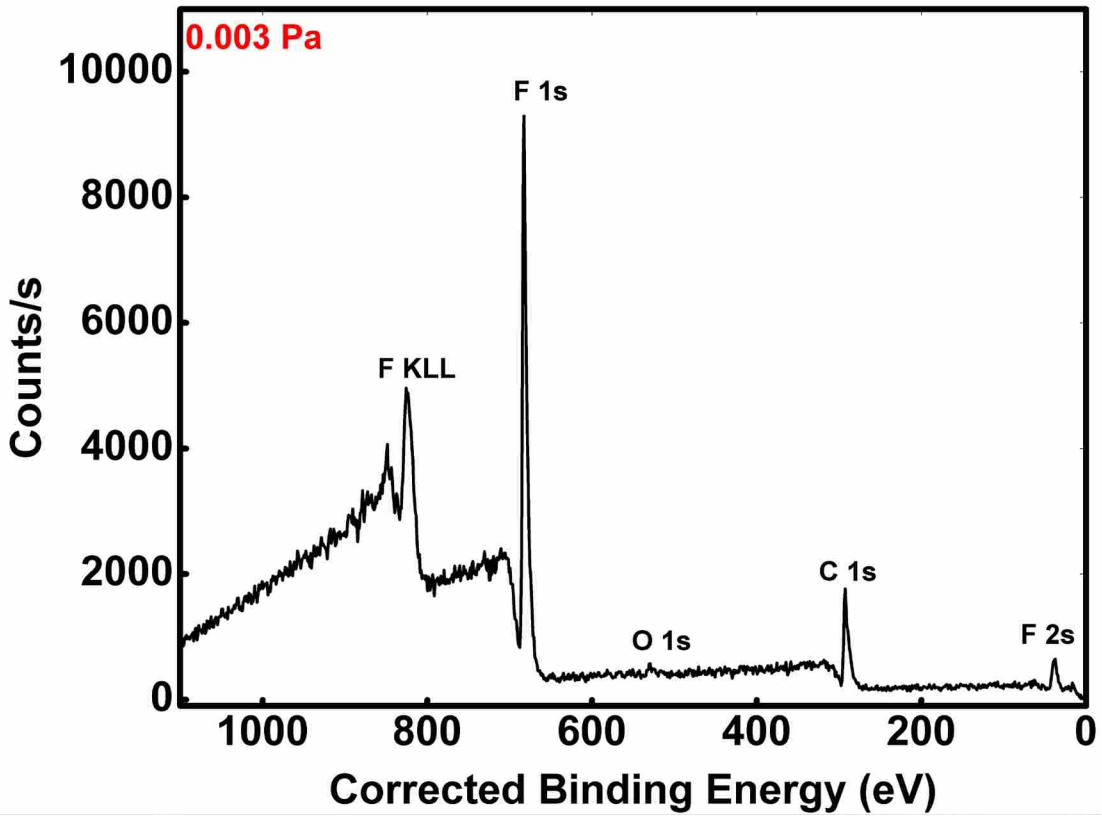

Figure 5.1.2.1. Survey scan of PTFE 1s at 0.003 Pa.

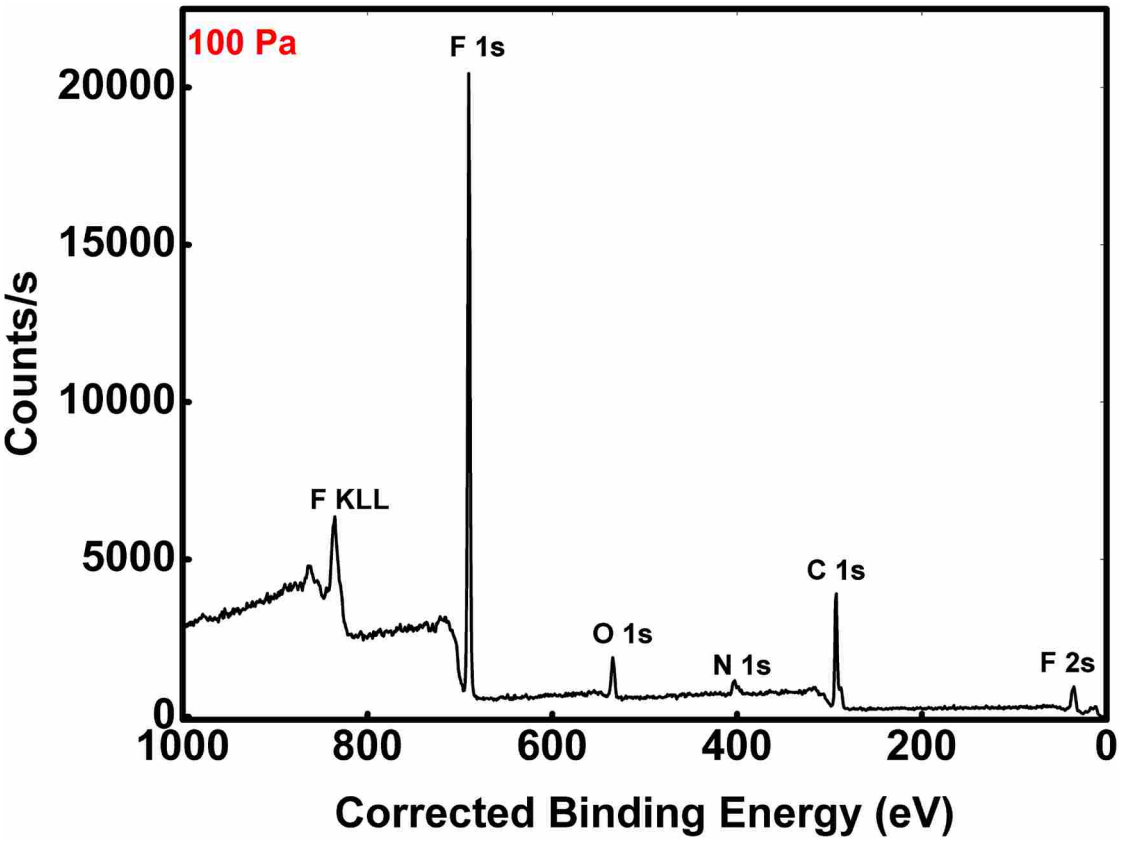

Figure 5.1.2.2. Survey scan of PTFE 1s at 100 Pa.

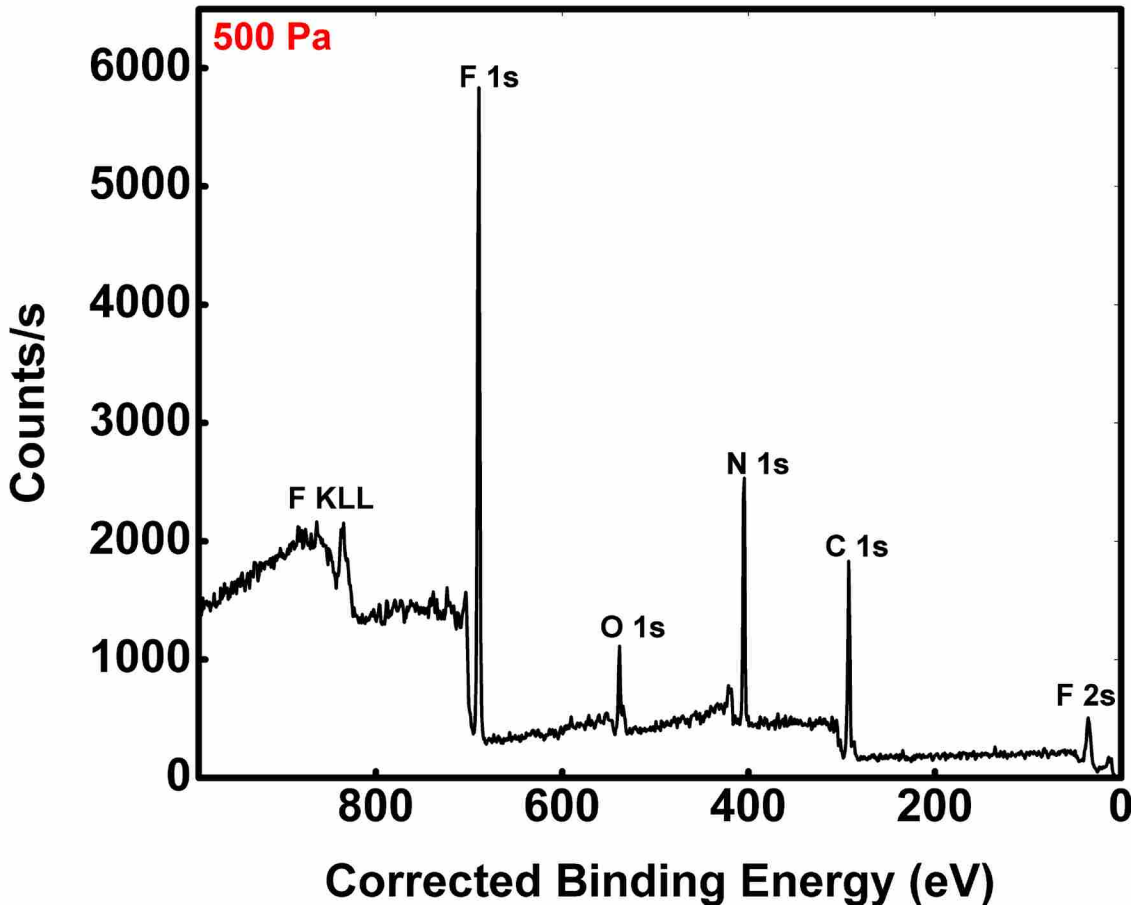

Figure 5.1.2.3. Survey scan of PTFE at 500 Pa.

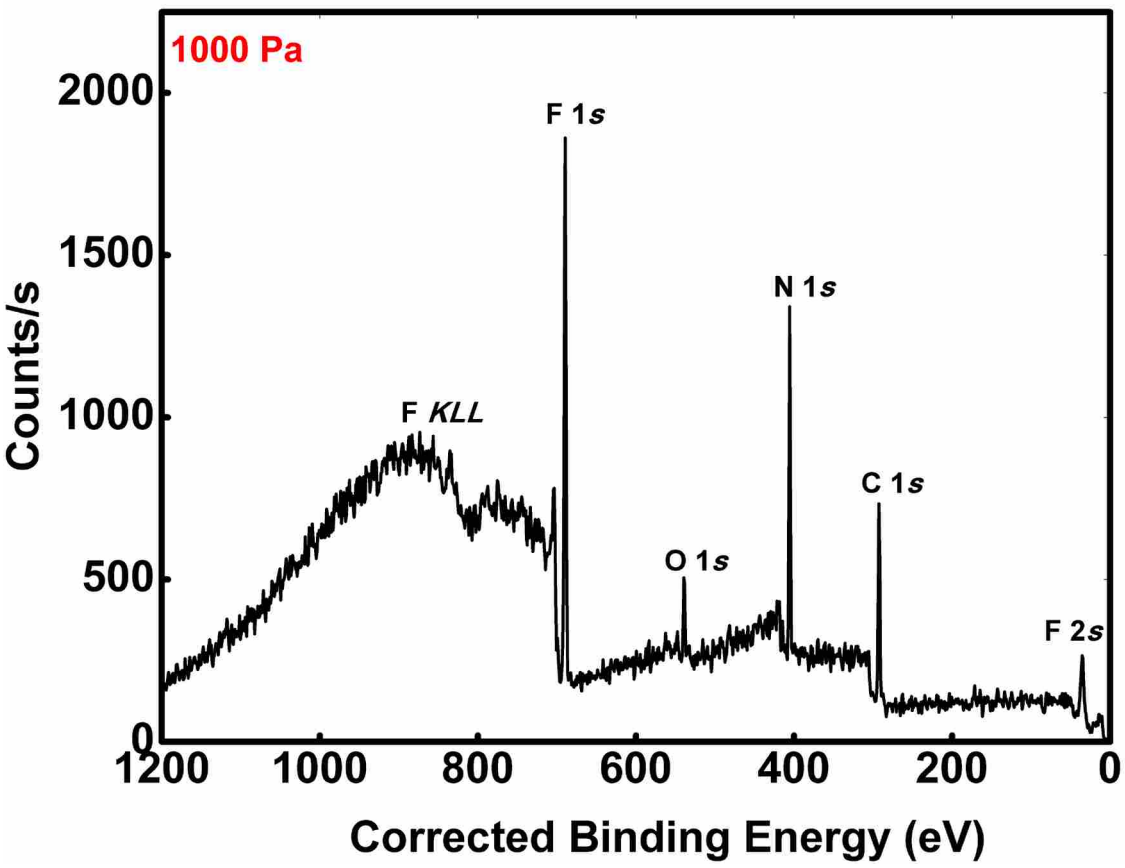

Figure 5.1.2.4. Survey scan of PTFE at 1000 Pa.

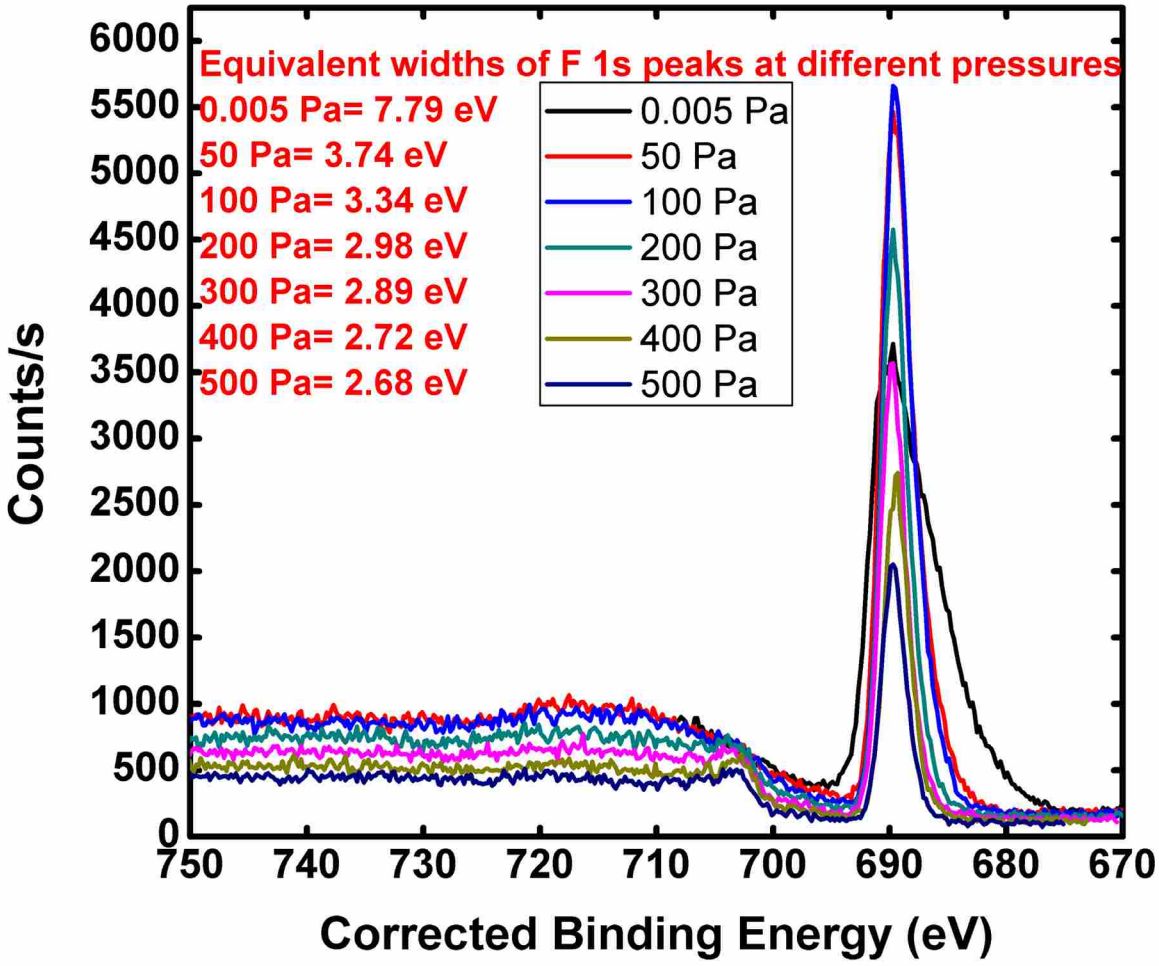

Figure 5.1.2.5. Narrow scans of F 1s at different pressures.

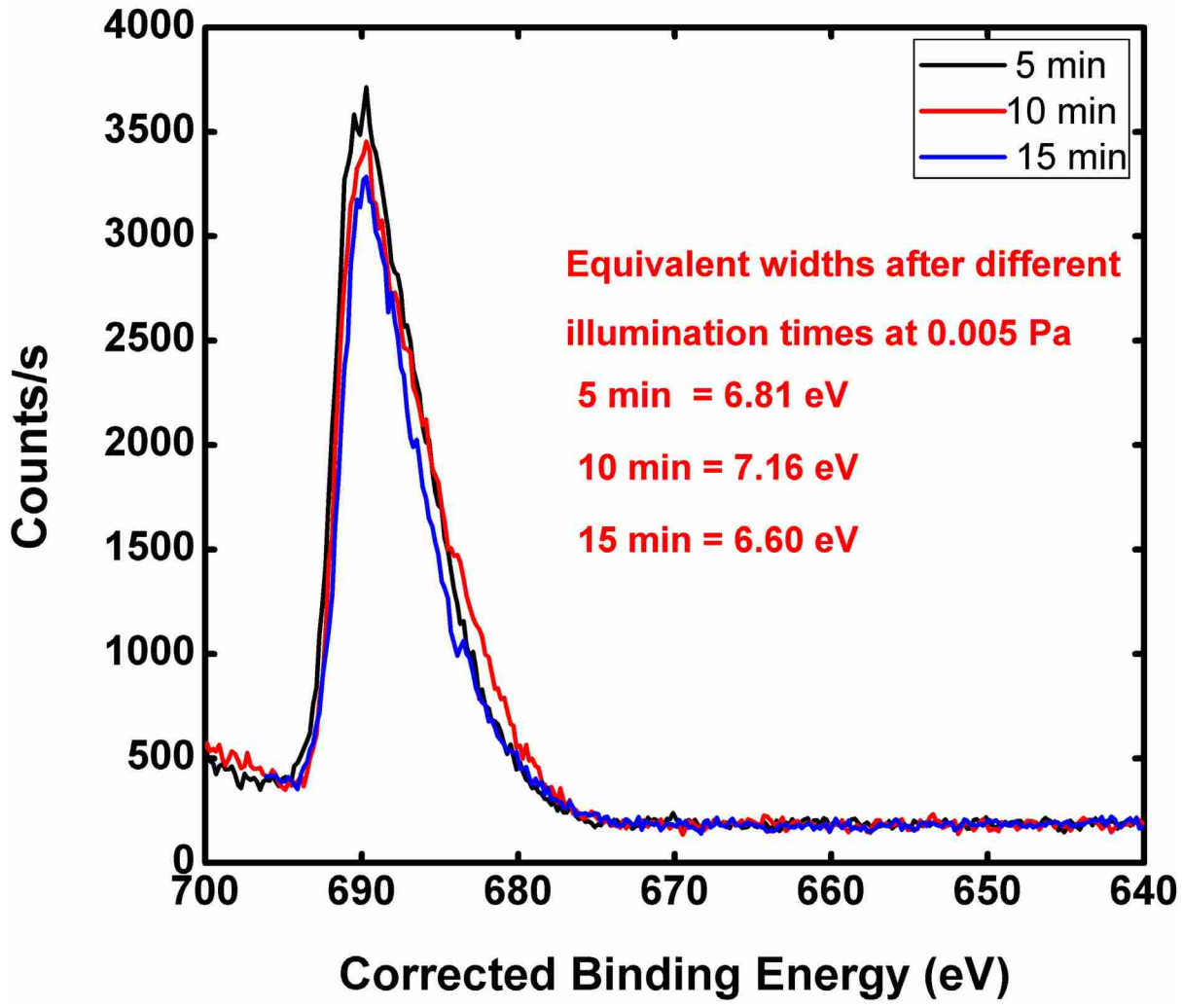

Figure 5.1.2.6. F 1s narrow scans at 0.005 Pa after different illumination times.

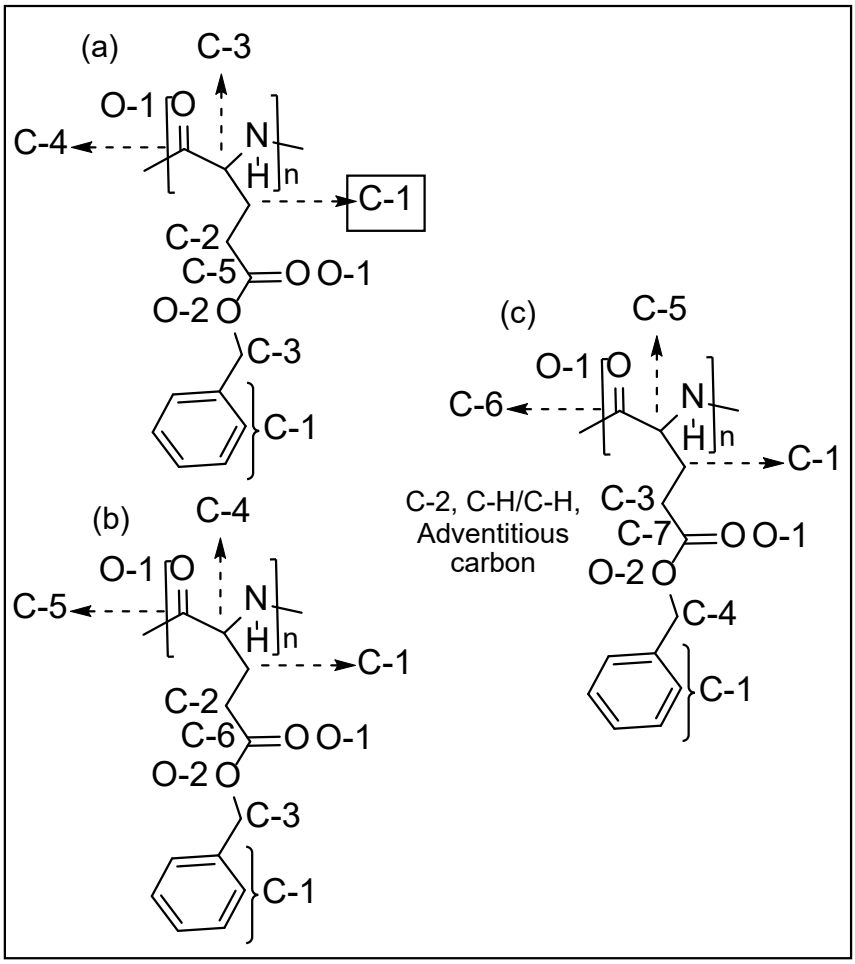

Figure 5.1.3.1. Representation of the three literature-based fitting approaches taken in this work: (a) five-, (b) six-, and (c) seven-peak approaches to fitting the C 1s narrow scan of PBLG.

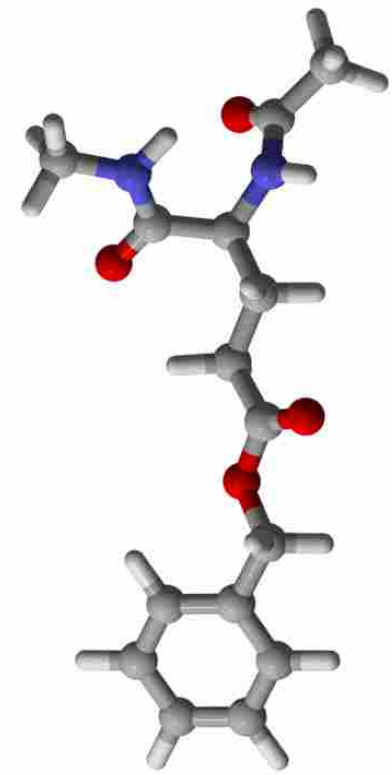

Figure 5.1.3.2. Structure of a model monomer unit that represents the repeat unit of PBLG. Grey, red, blue, and white balls represent C, O, N, and H respectively. The model monomer is terminated with C(O)H and –NMe2 groups. These extra atoms were not considered in the peak fitting/analysis described herein.

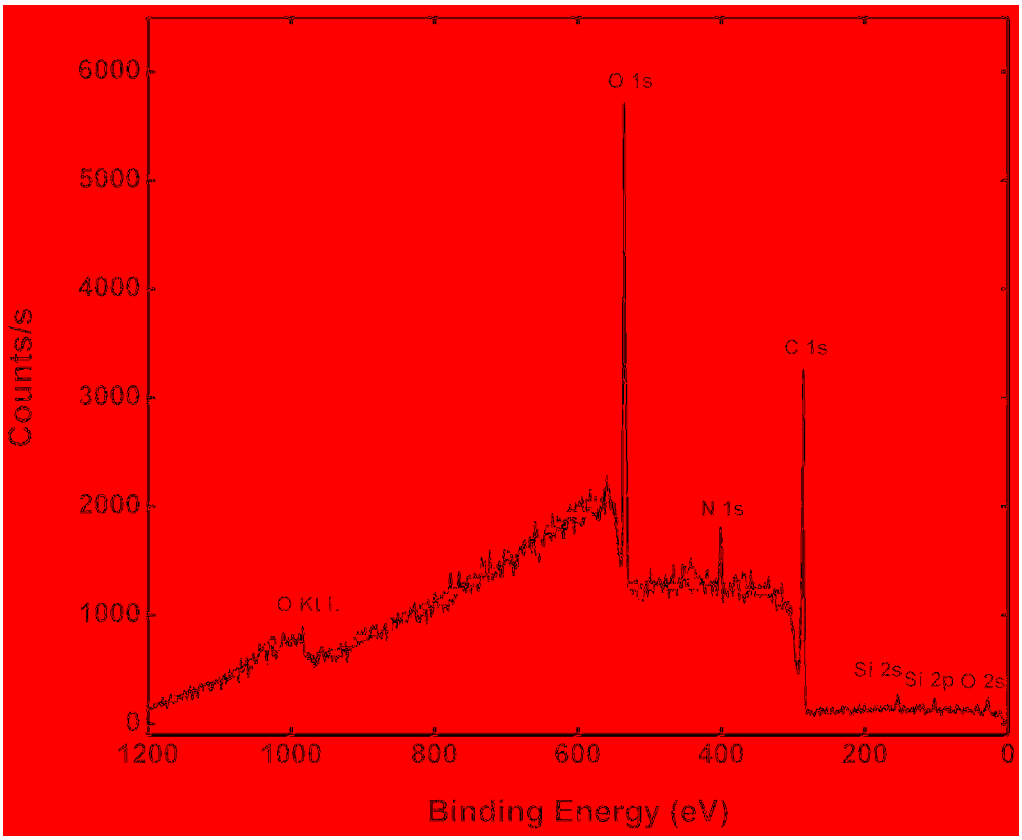

Figure 5.1.3.3. Survey scan of PBLG.

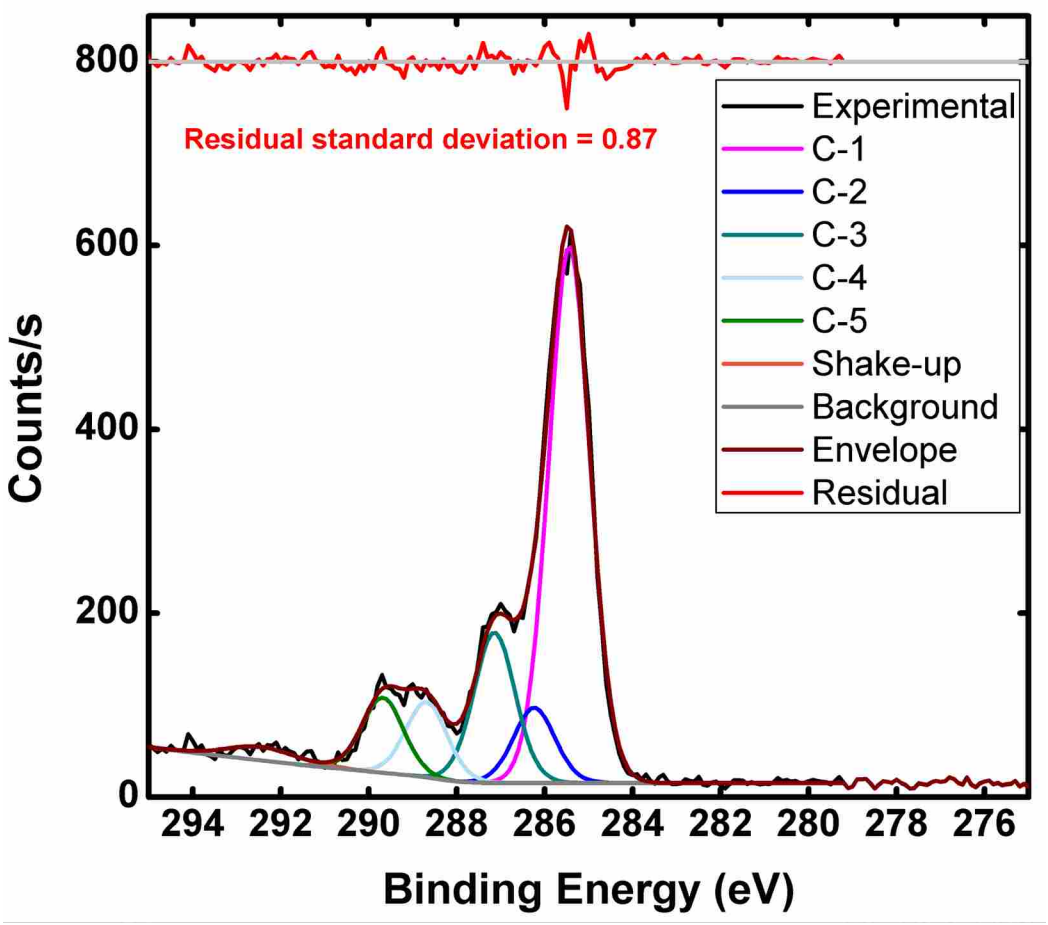

Figure 5.1.3.4. Peak fitting of C 1s envelope.

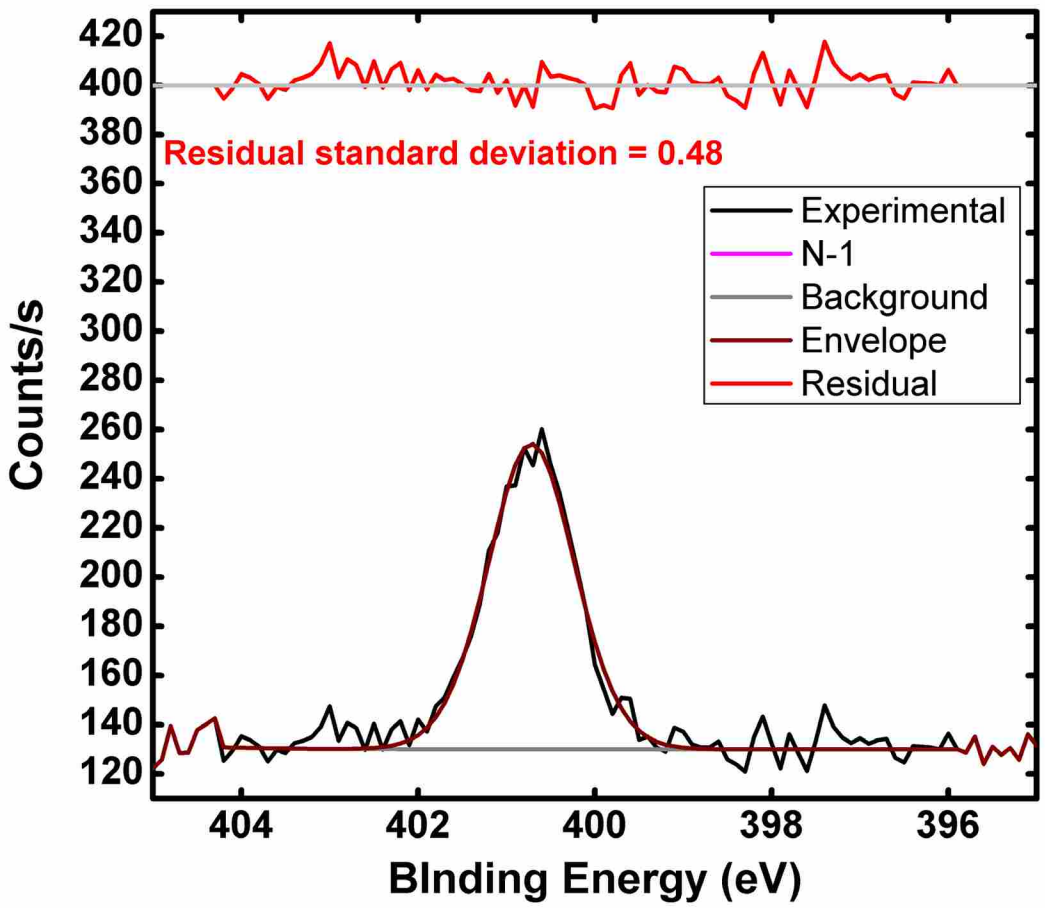

Figure 5.1.3.5. Peak fitting of N 1s envelope.

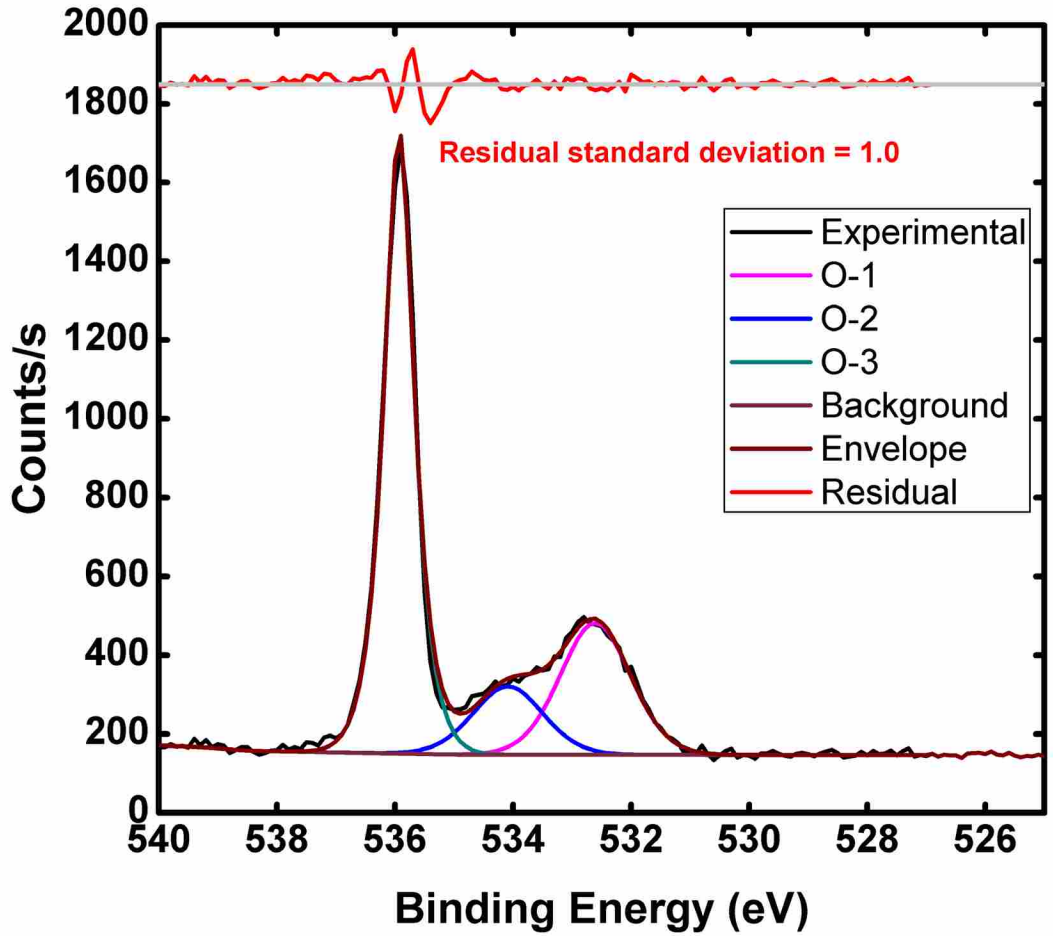

Figure 5.1.3.6. Peak fitting of O 1s envelope.

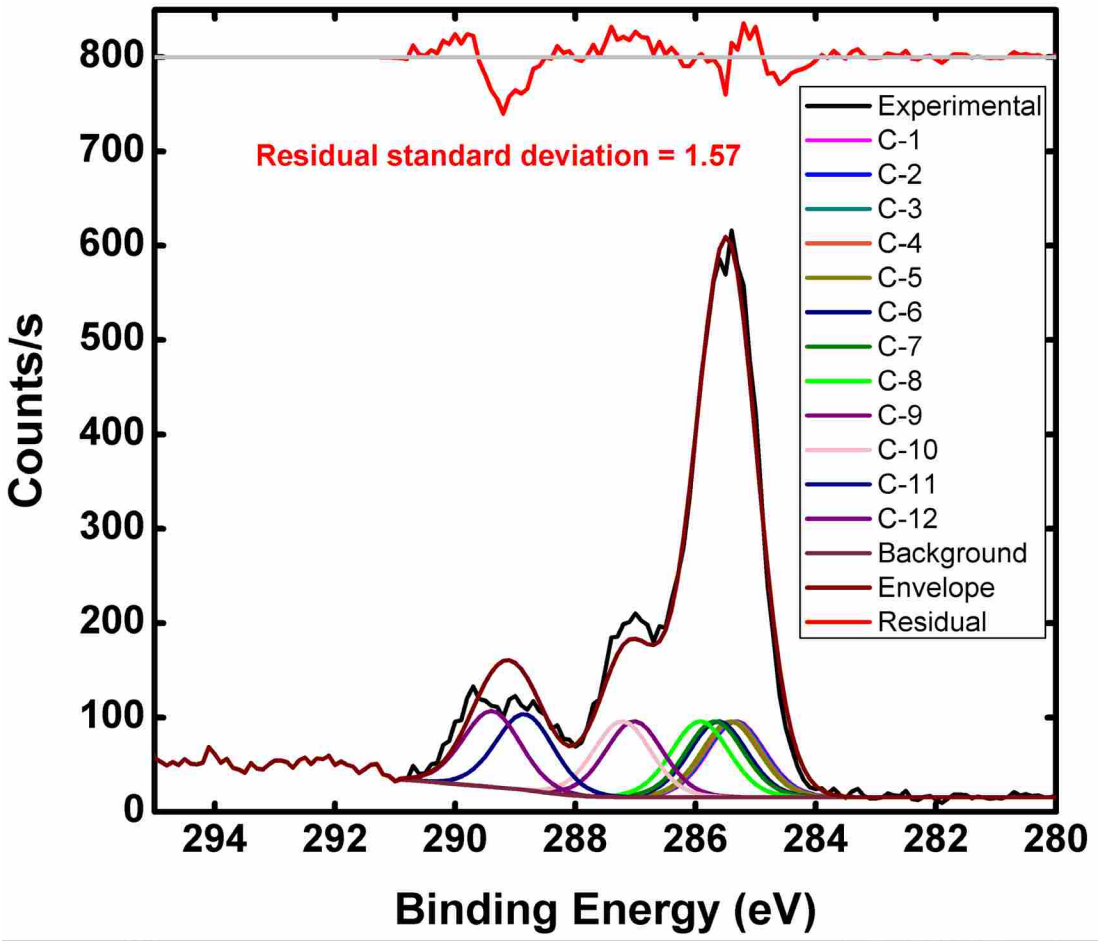

Figure 5.1.3.7. Peak fitting of C 1s envelope according to ab initio calculation.

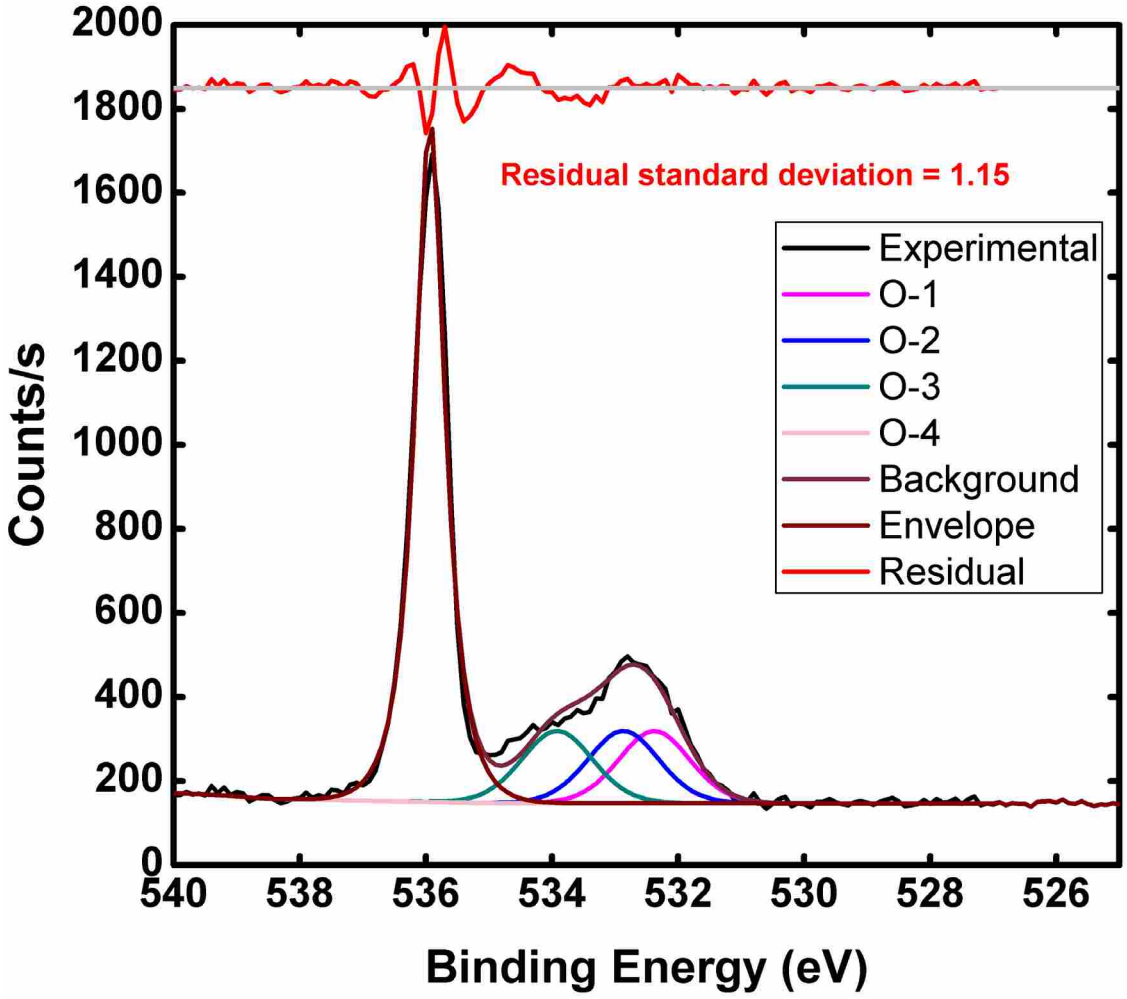

Figure 5.1.3.8. Peak fitting of O 1s envelope according to ab initio calculation.

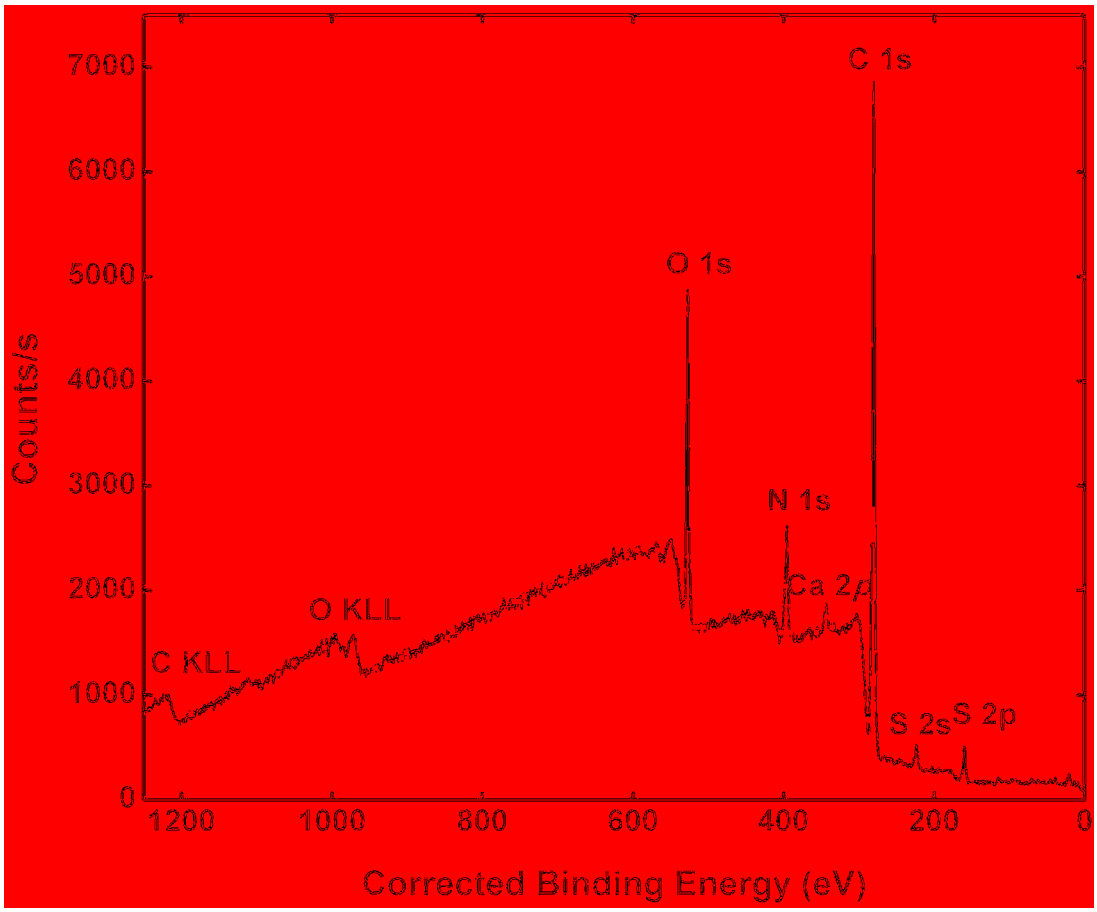

Figure 5.1.4.1. Survey scan of untreated hair.

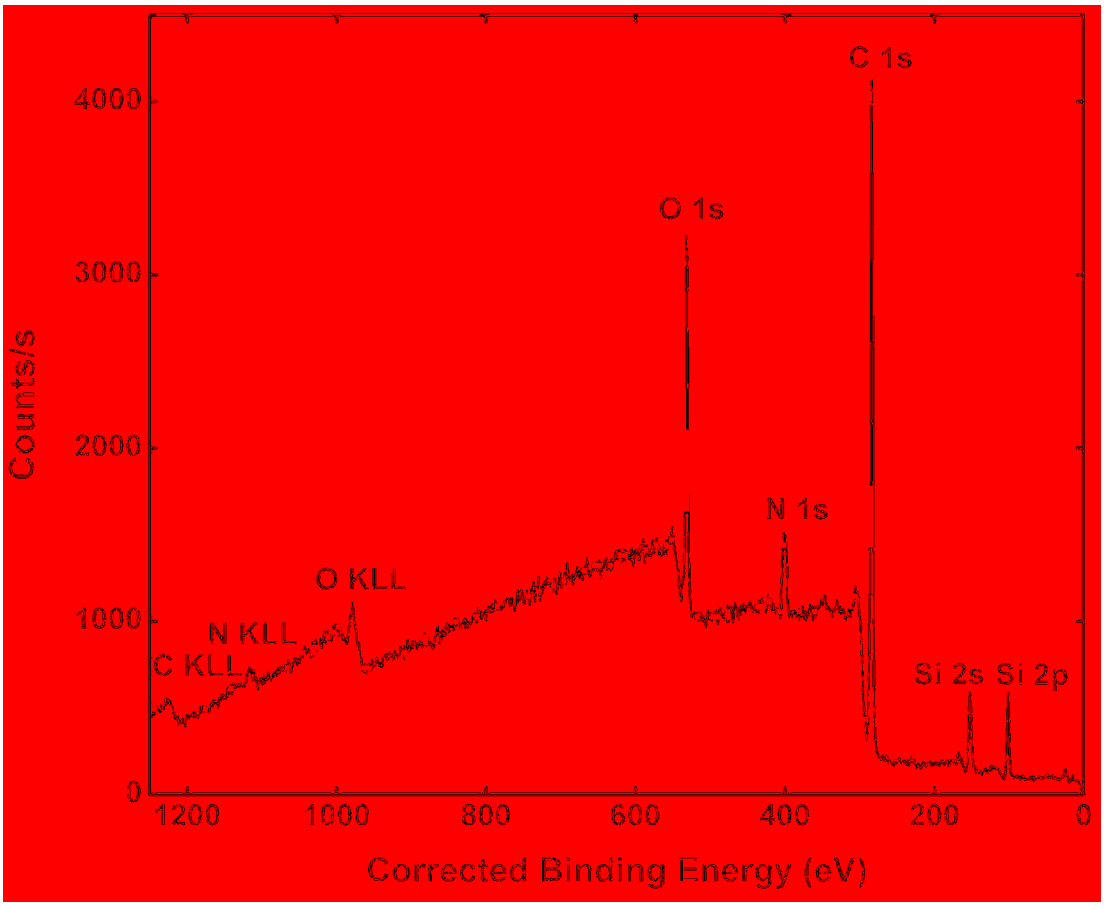

Figure 5.1.4.2. Survey scan of colored hair.

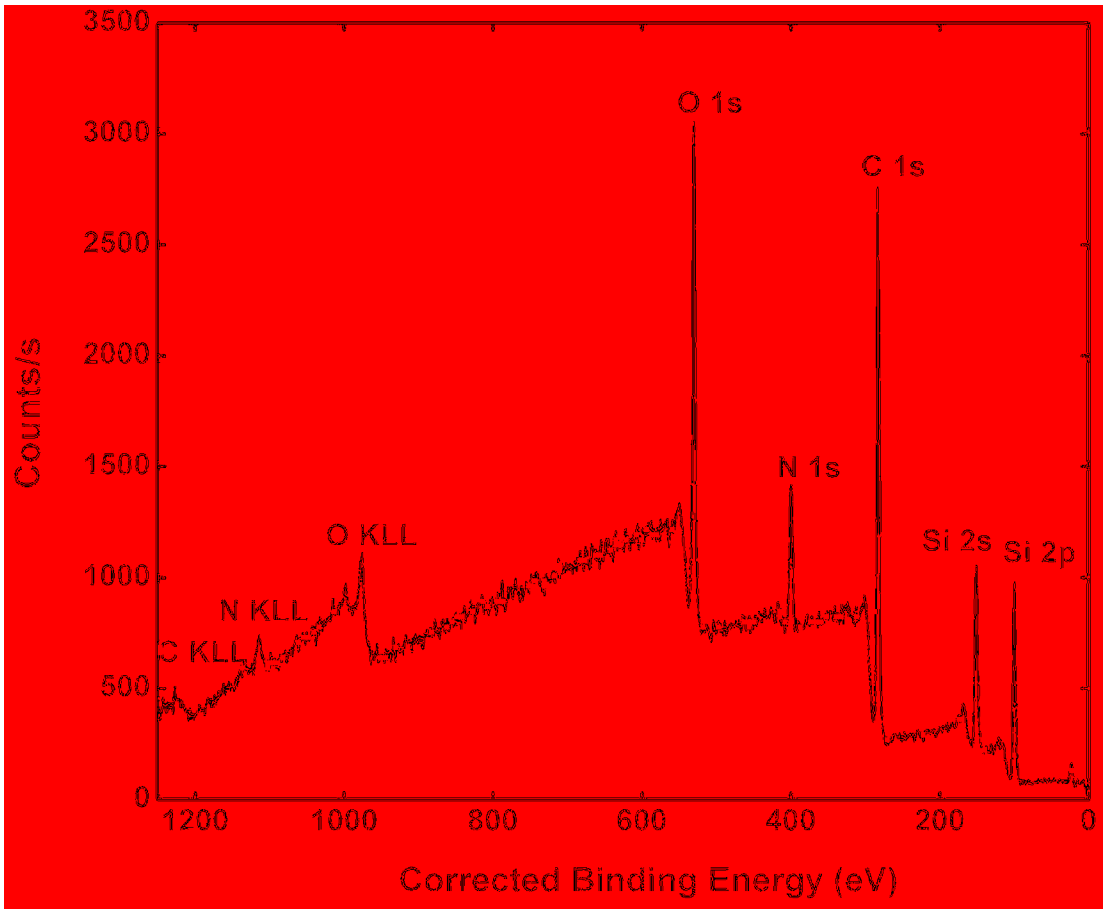

Figure 5.1.4.3. Survey scan of bleached hair.

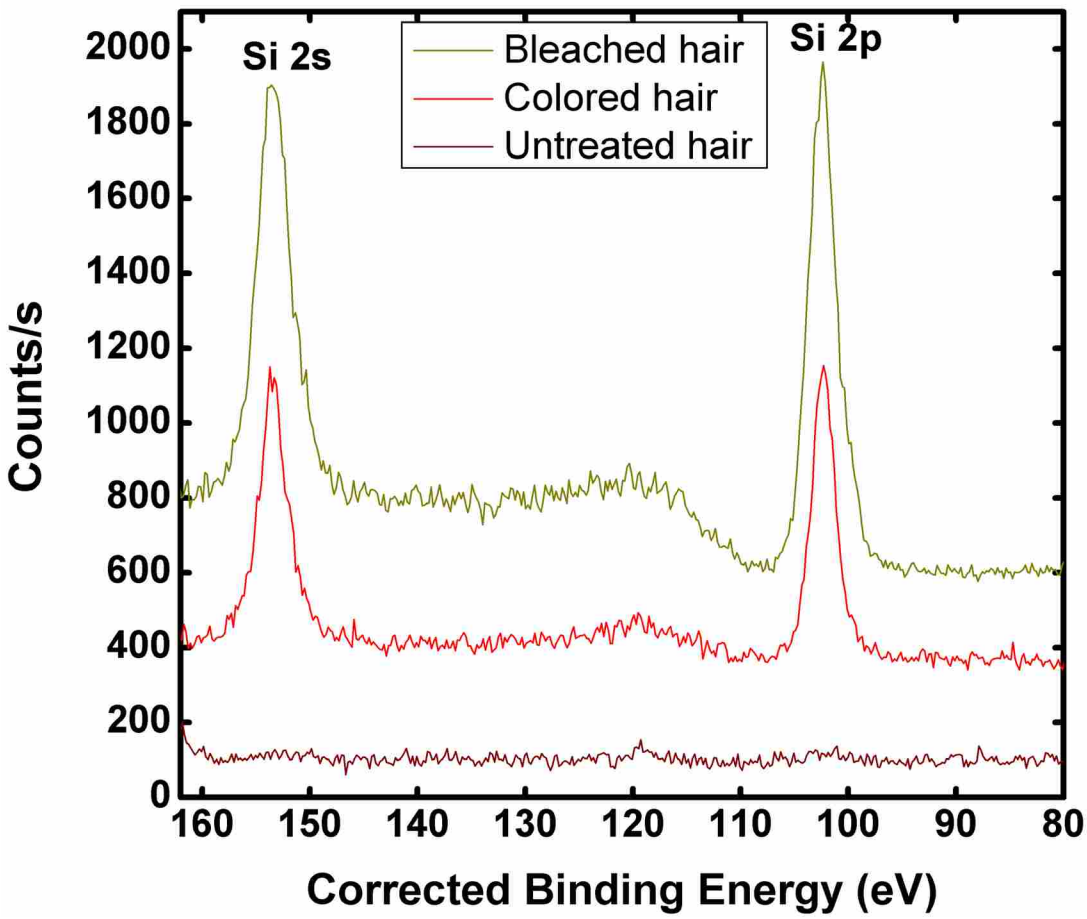

Figure 5.1.4.4. Comparison of Si 2p peaks.

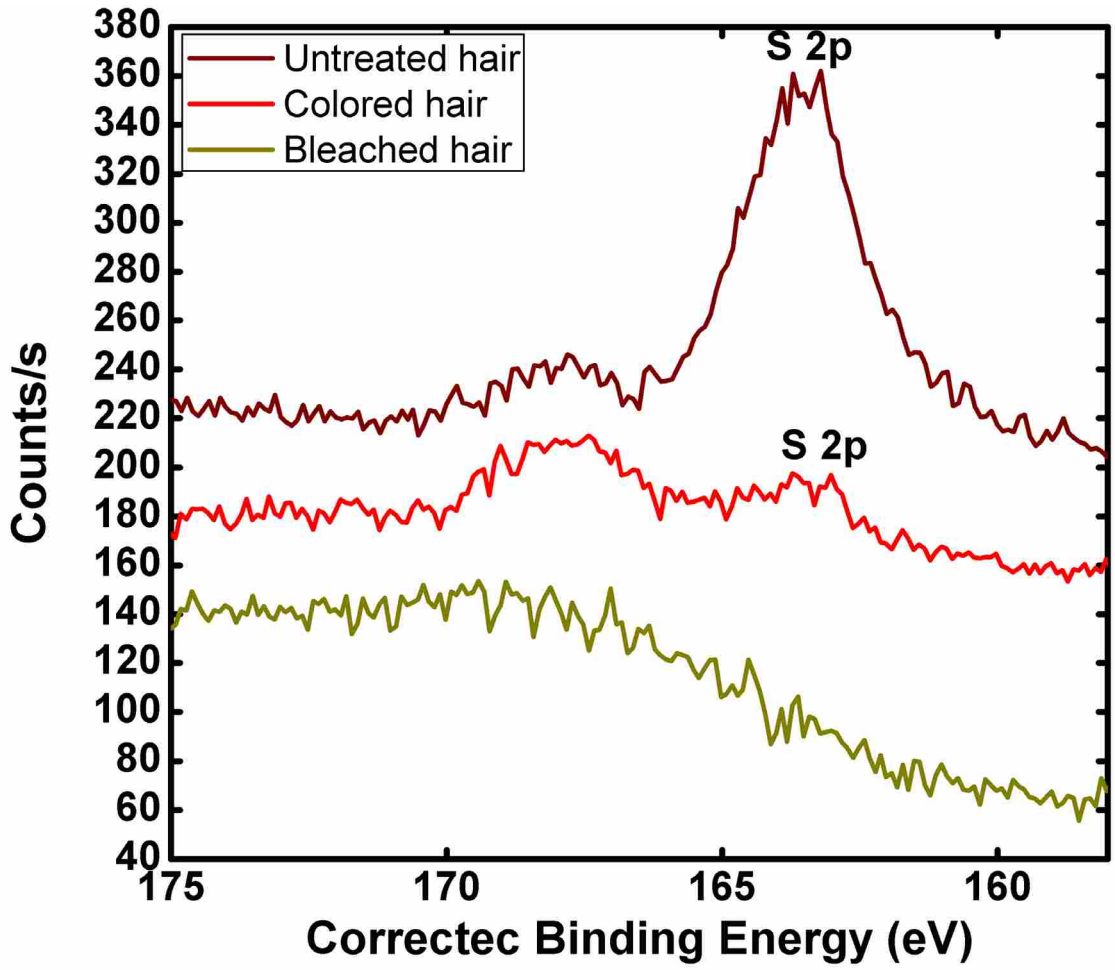

Figure 5.1.4.5. Comparison of S 2p peaks.

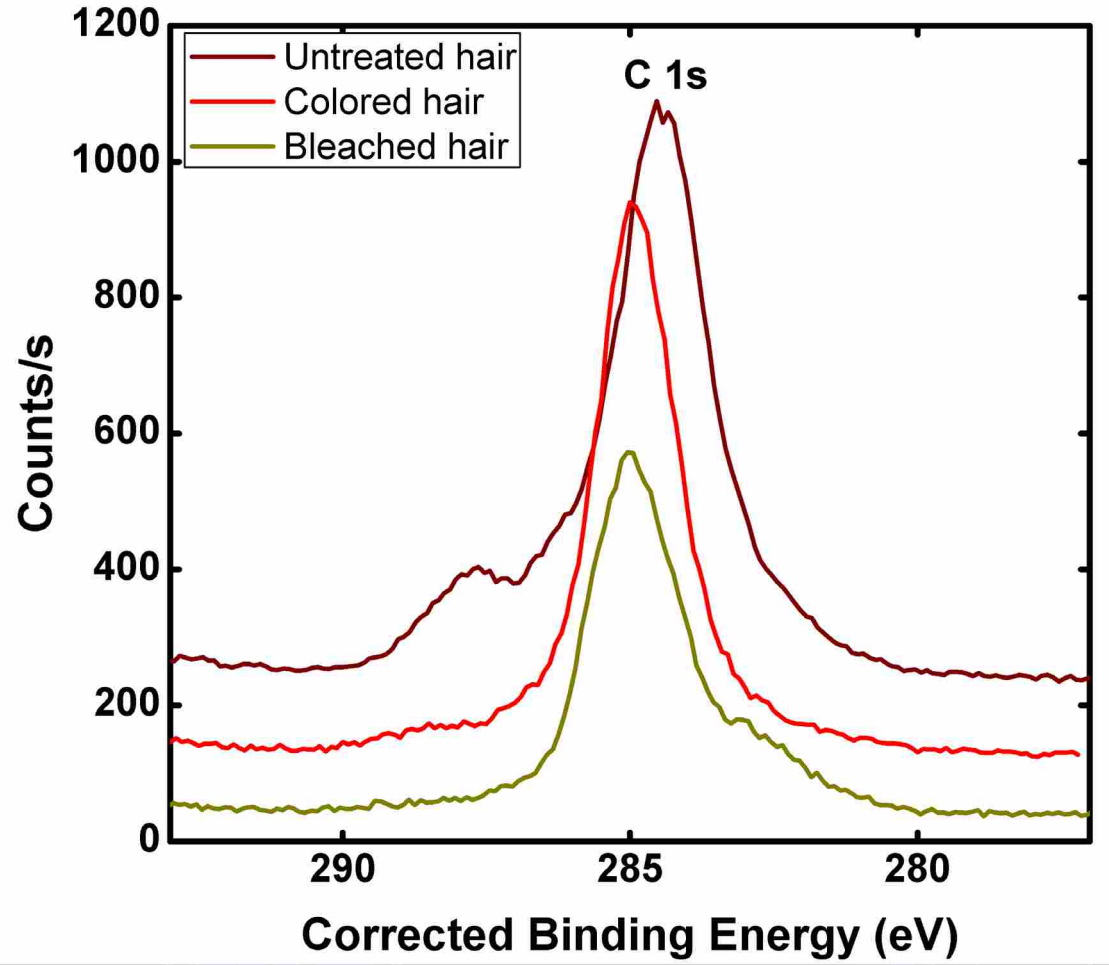

Figure 5.1.4.6. Comparison of C 1s peaks.

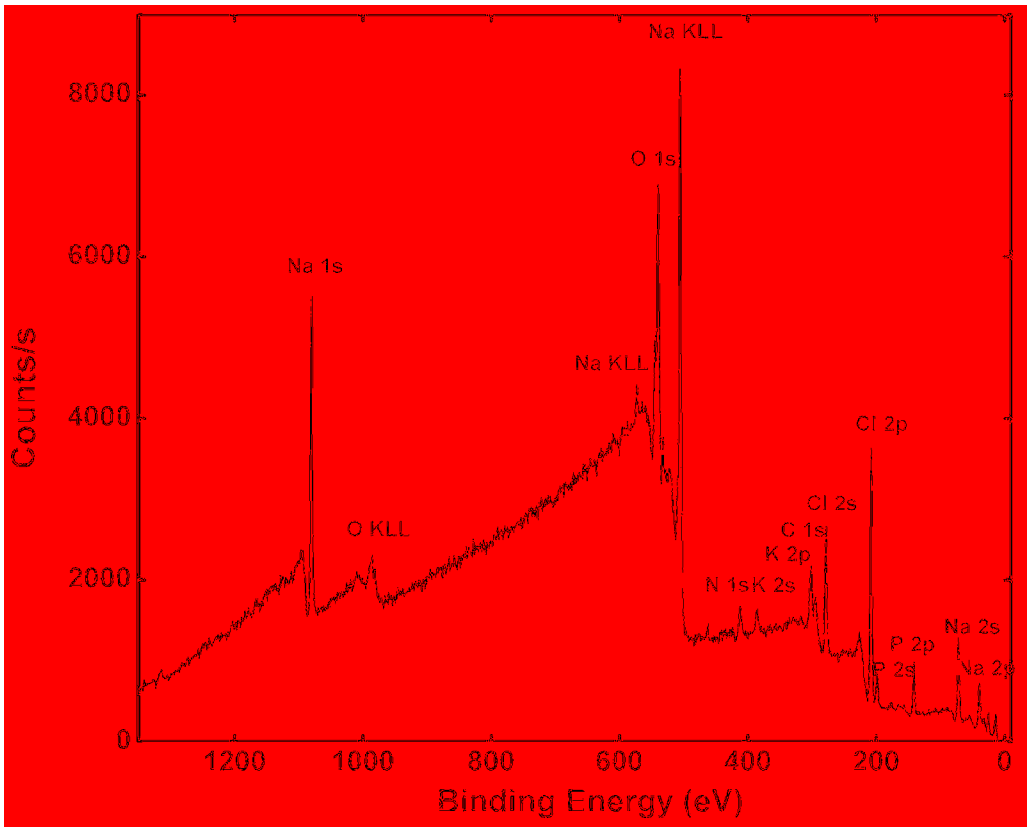

Figure 5.1.5.1. Survey scan of PBS solid.

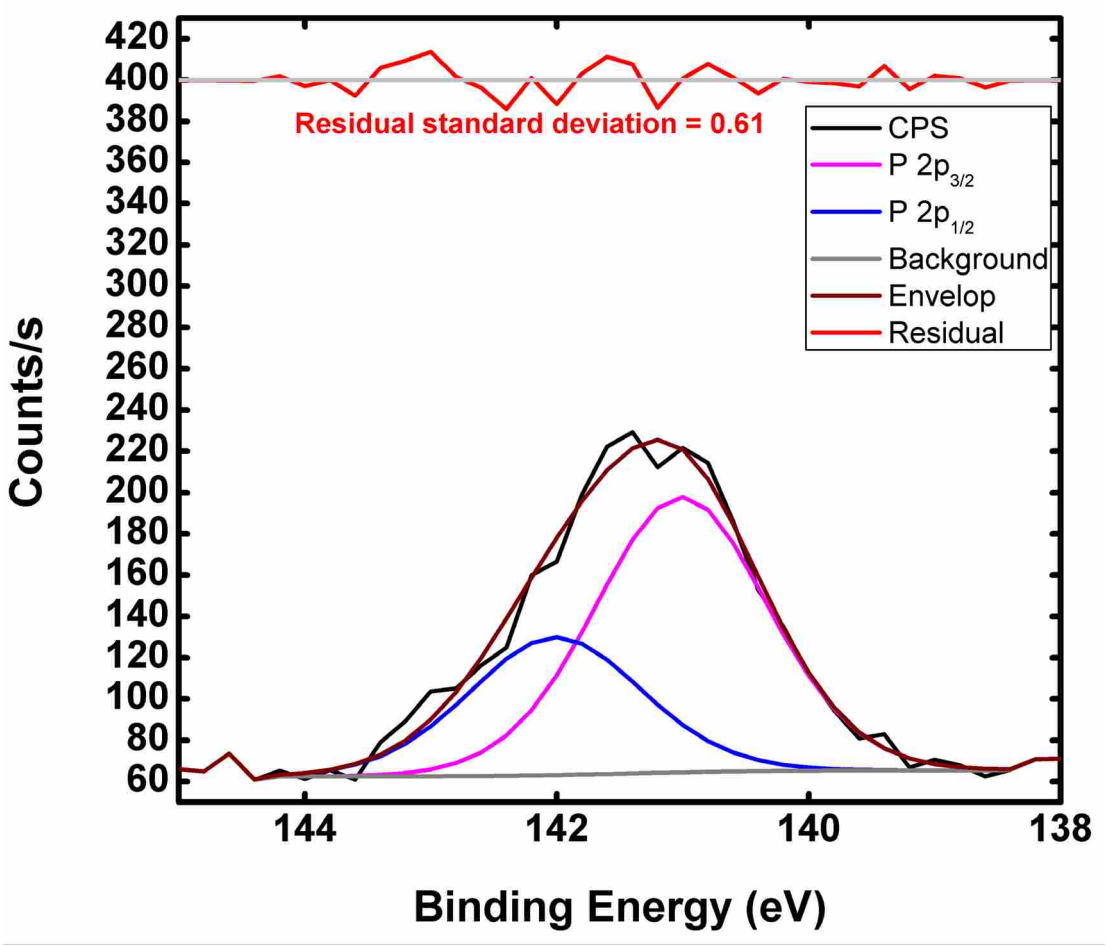

Figure 5.1.5.2. Peak fitting of P 2p peak envelope.

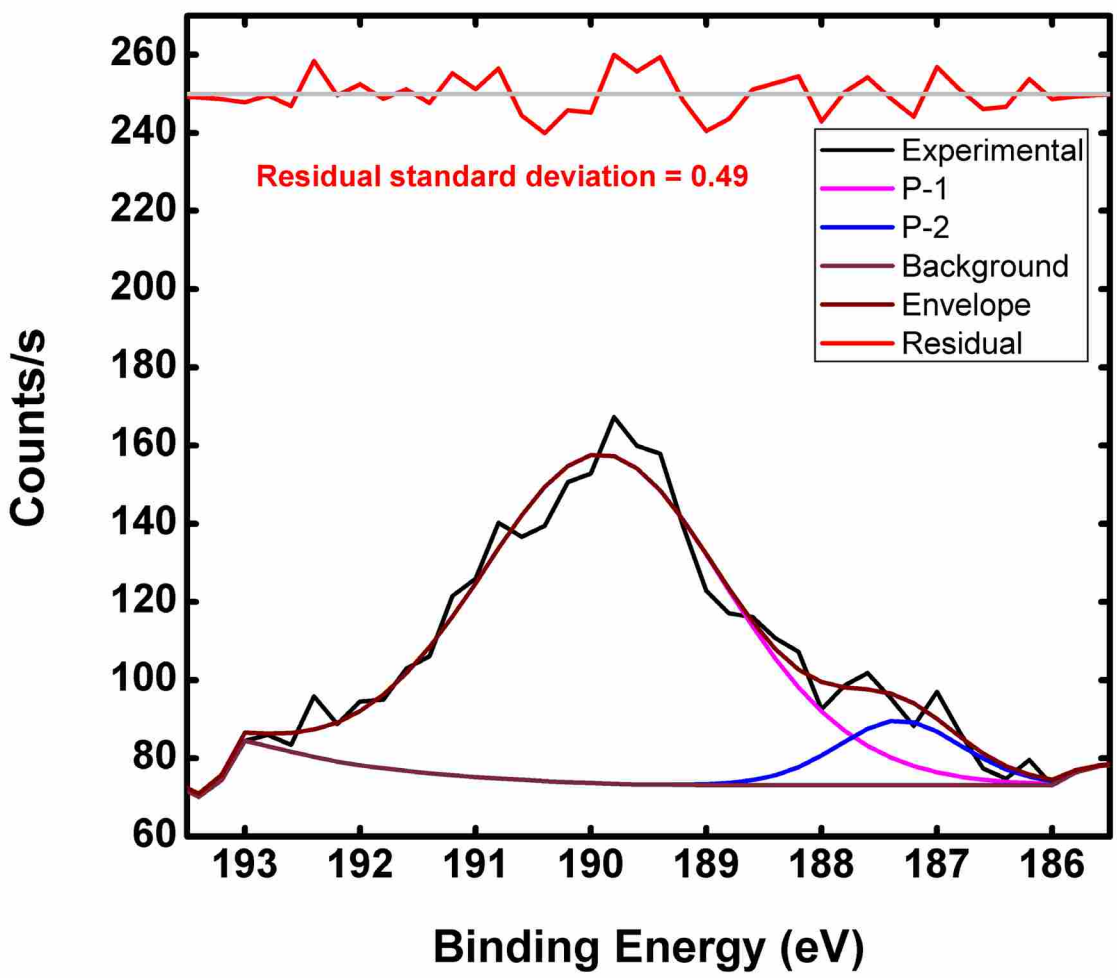

Figure 5.1.5.3. Peak fitting of P 2s peak envelope

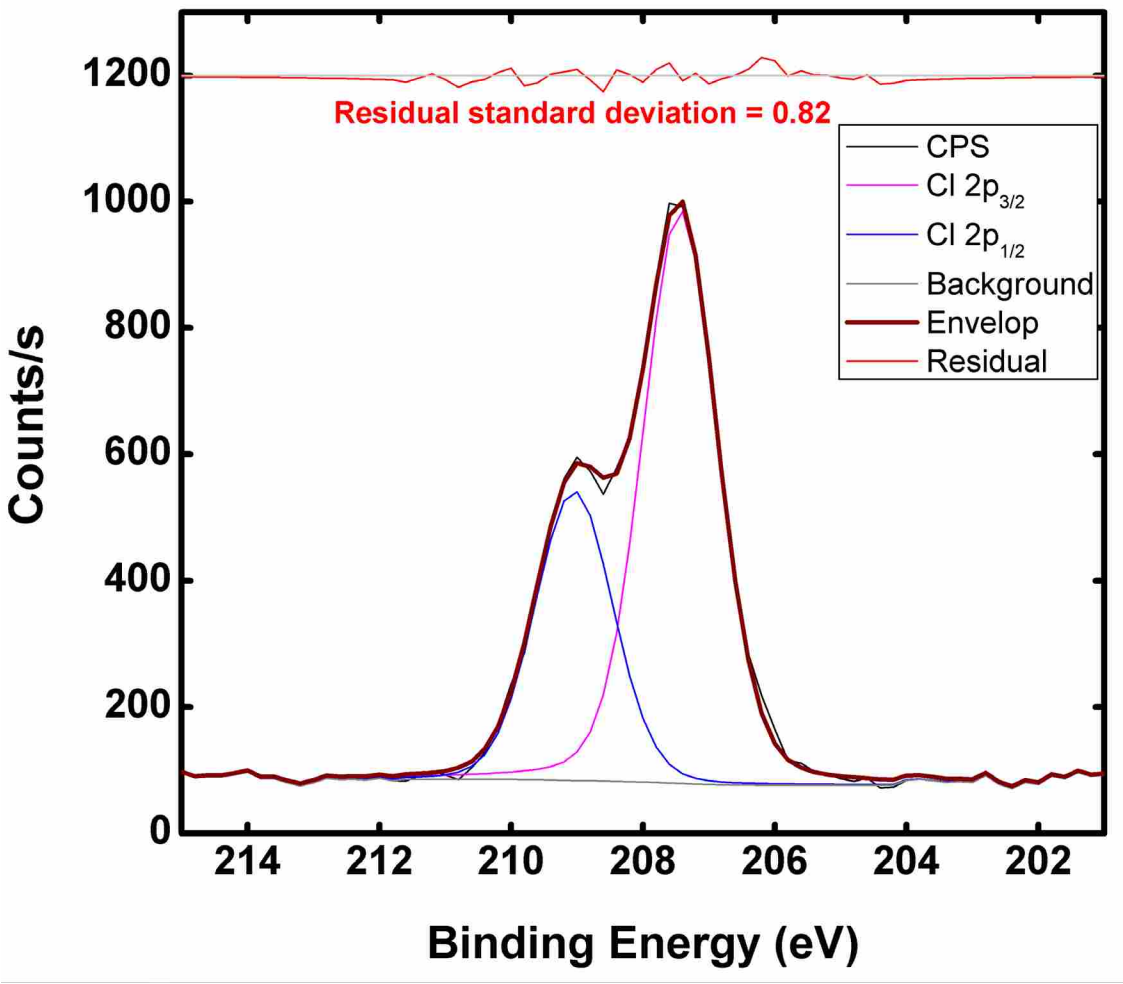

Figure 5.1.5.4. Peak fitting of Cl 2p peak envelope.

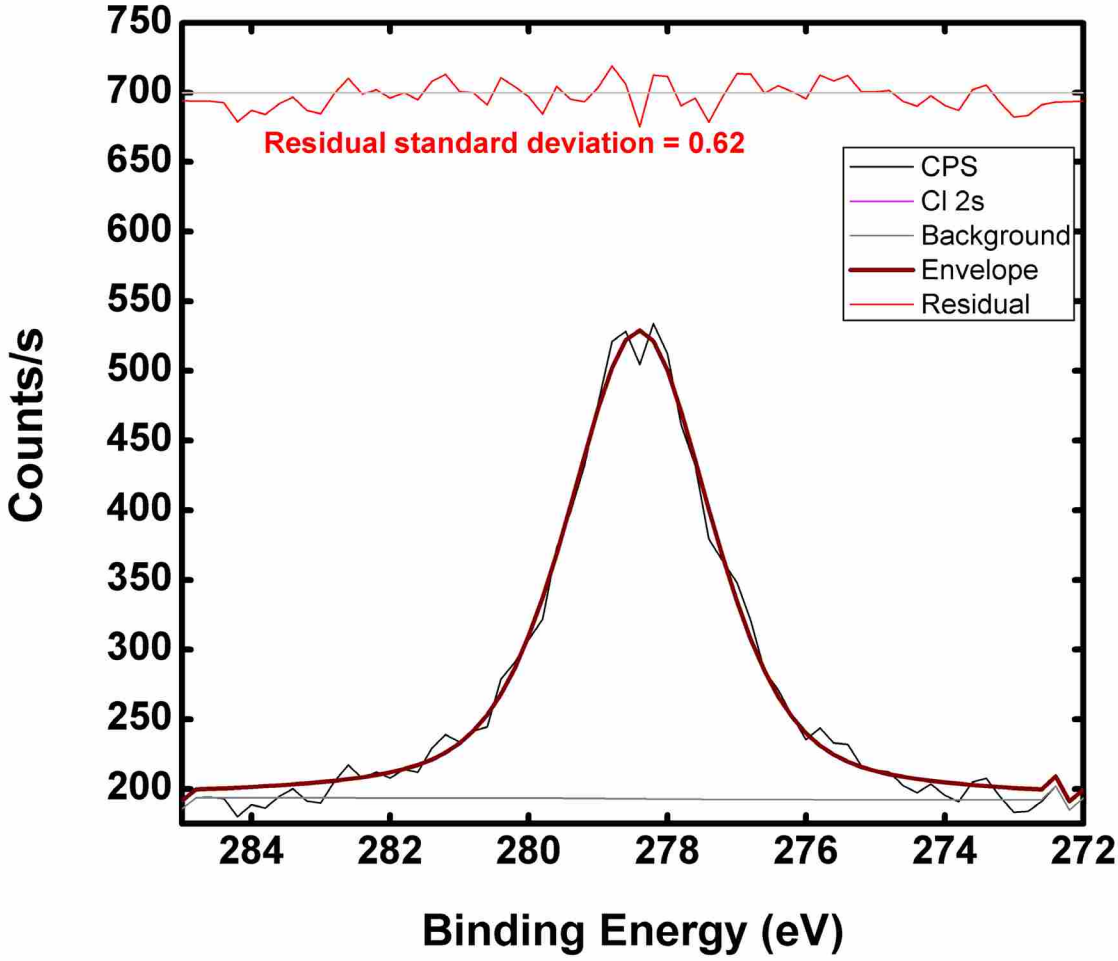

Figure 5.1.5.5. Peak fitting of Cl 2s peak envelope.

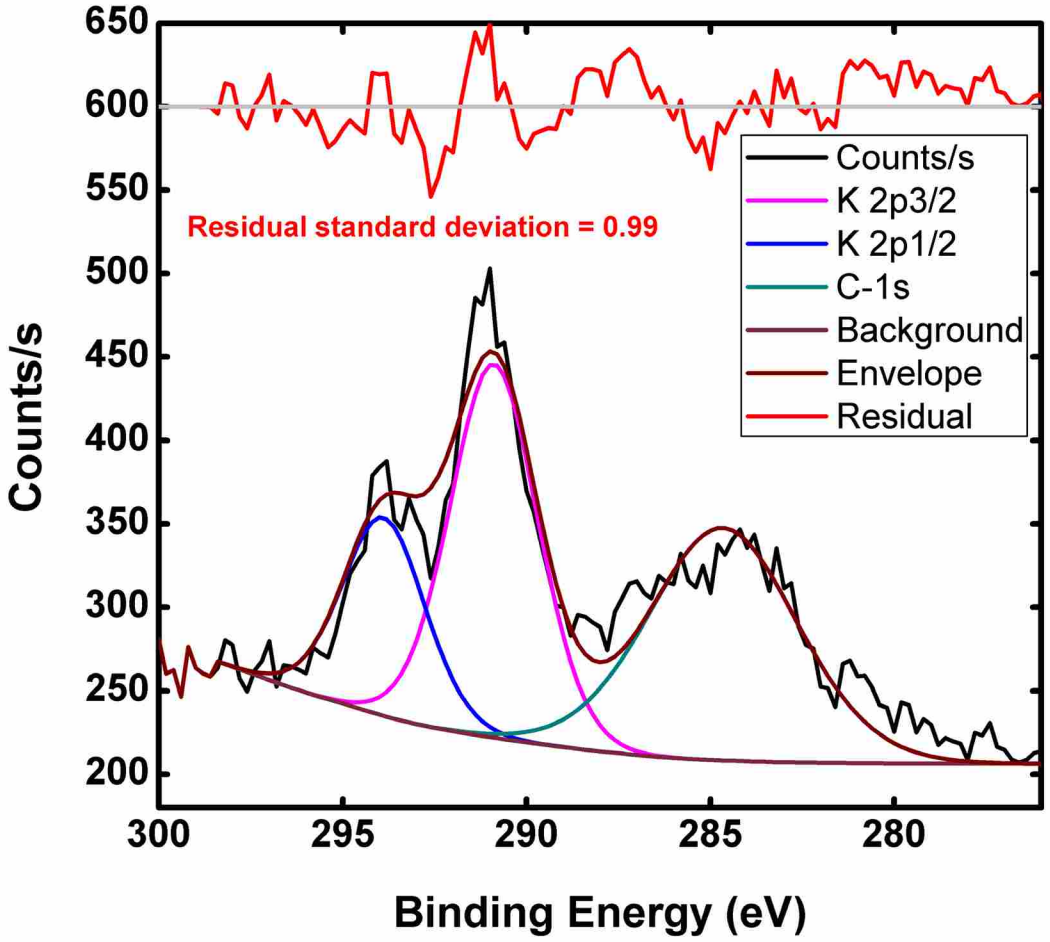

Figure 5.1.5.6. Peak fitting of C 1s and K 2p peak envelopes.

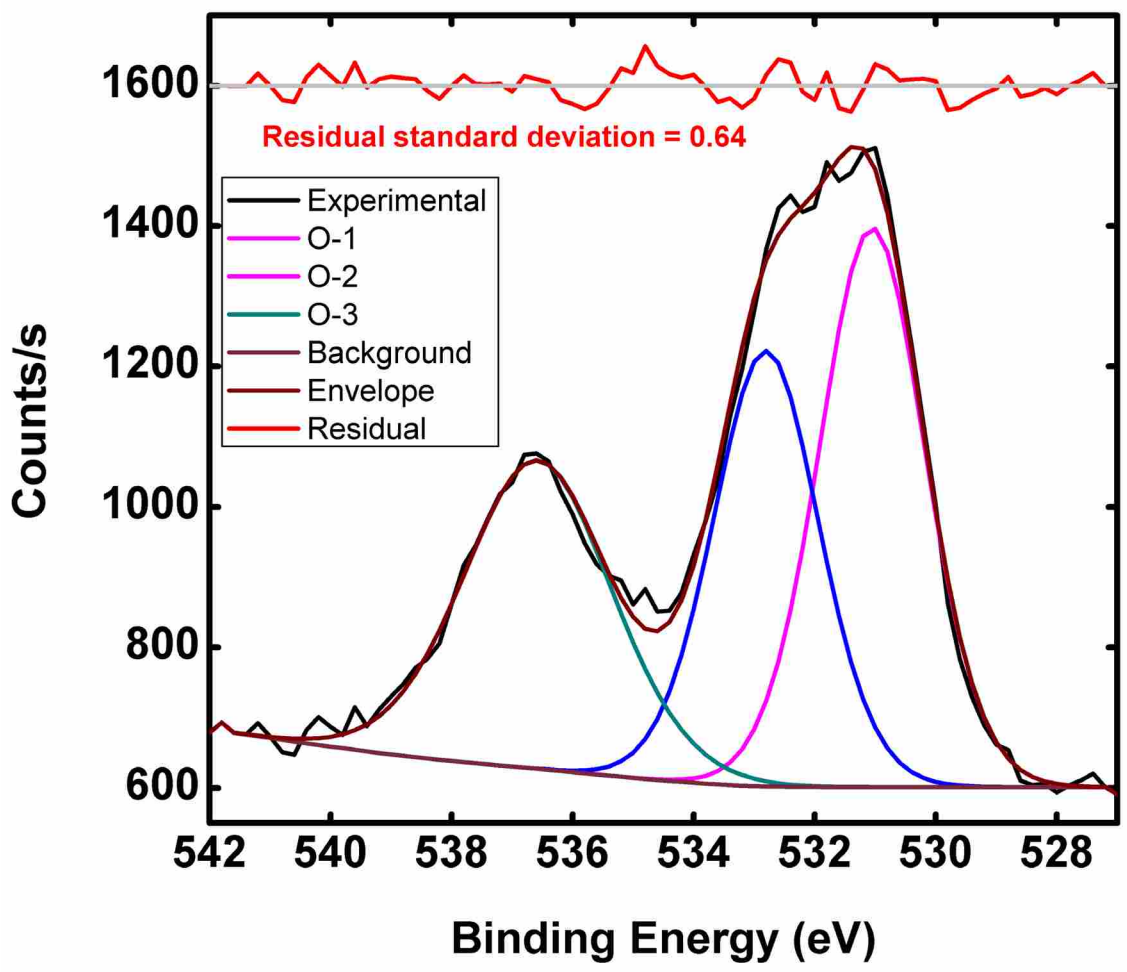

Figure 5.1.5.7. Peak fitting of O 1s peak envelope.

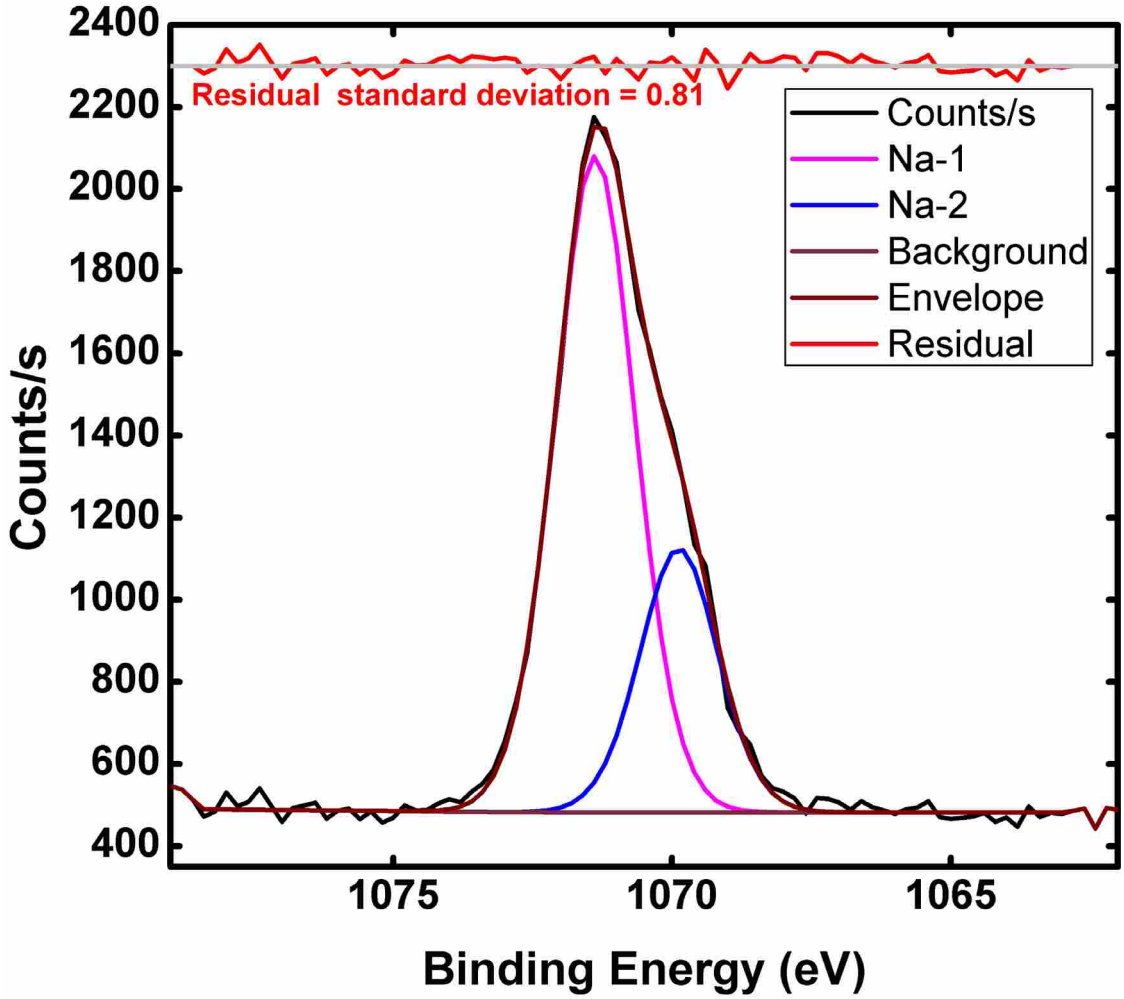

Figure 5.1.5.8. Peak fitting of Na 1s peak envelope.

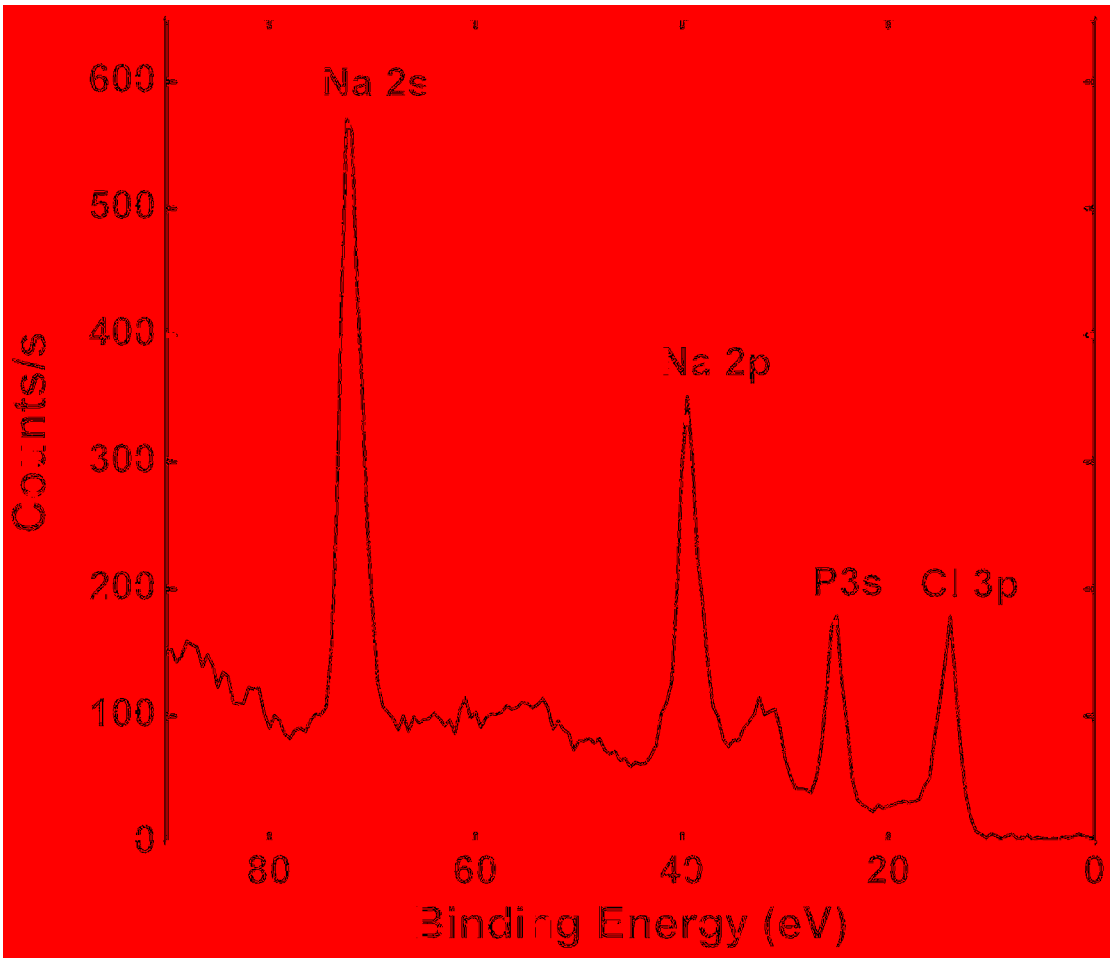

Figure 5.1.5.9. Valance band spectrum of PBS solid.

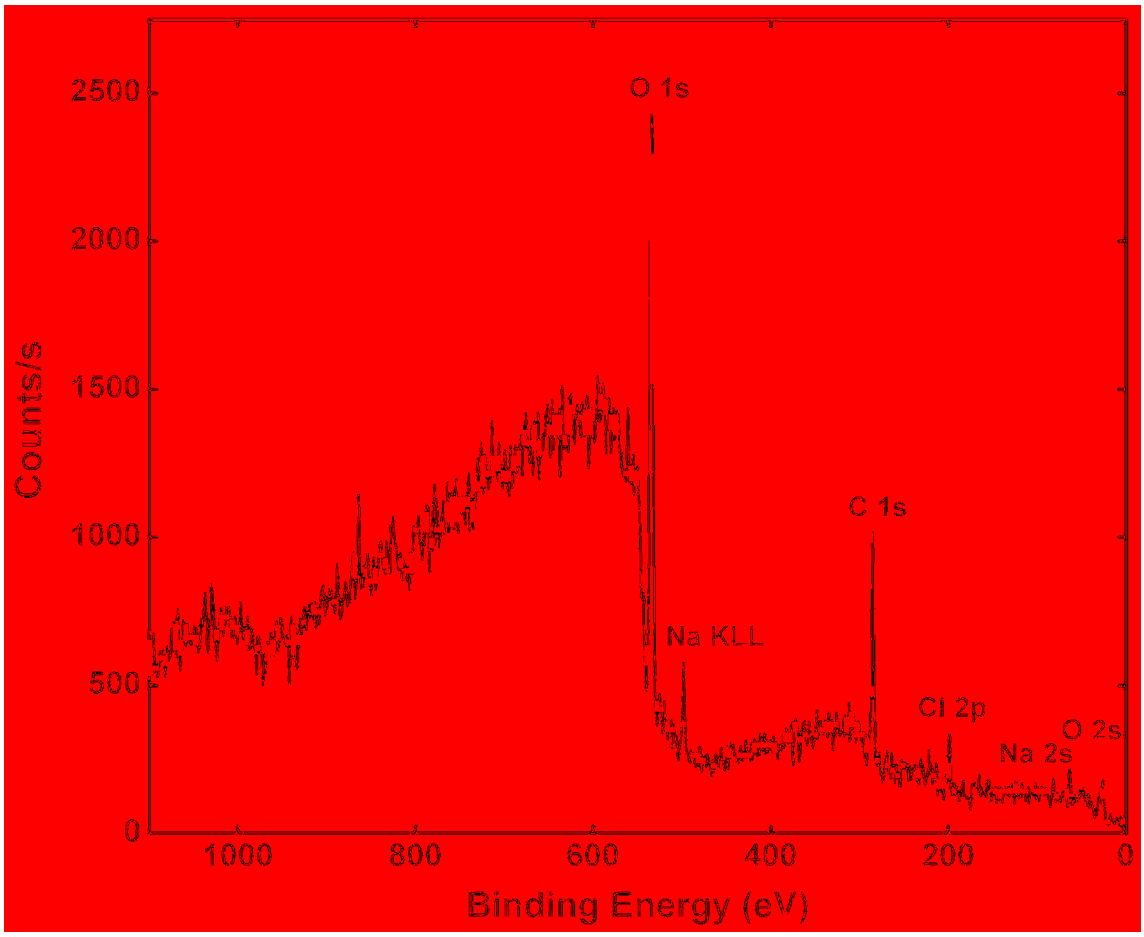

Figure 5.1.5.10. Survey scan of PBS solution.

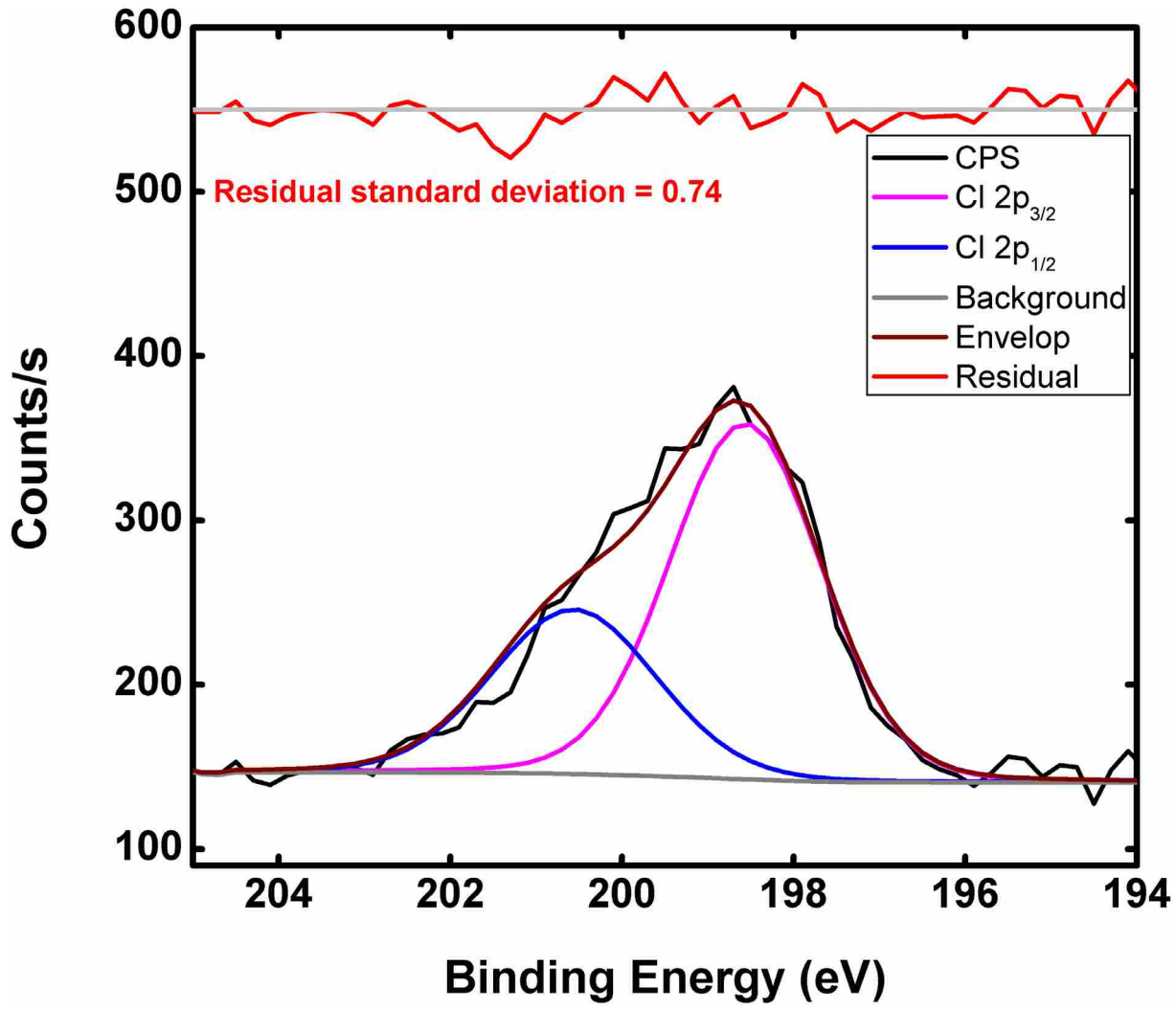

Figure 5.1.5.11. Peak fitting of Cl 2p peak envelope.

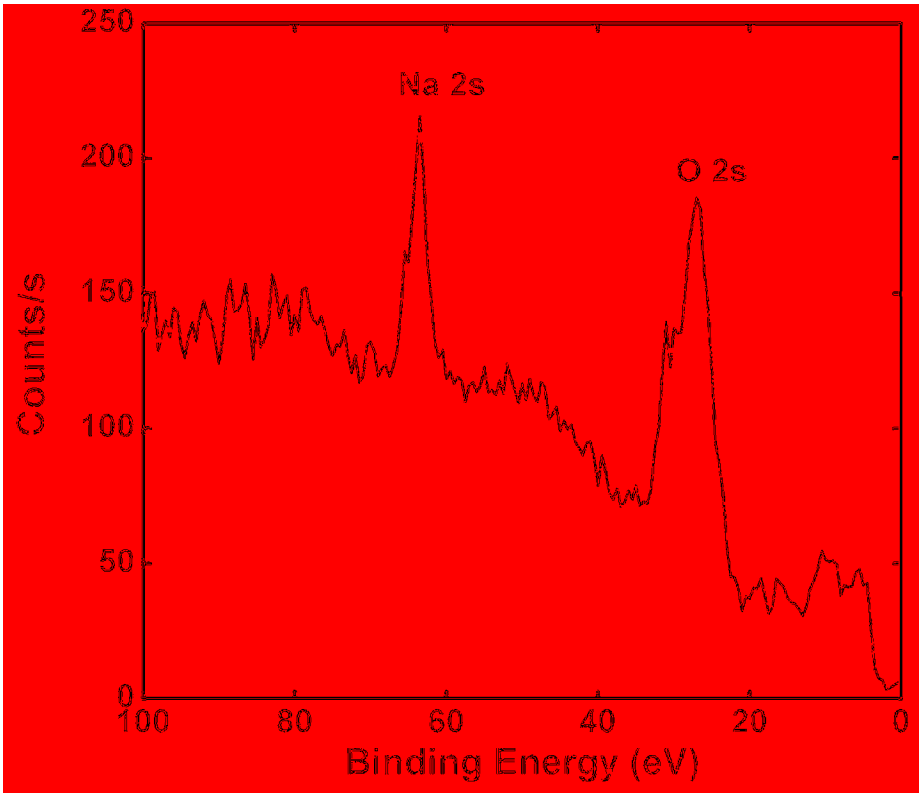

Figure 5.1.5.12. Valance bond spectrum of PBS solution.

5.3 References

1. Dietrich, P. M.; Bahr, S.; Yamamoto, T.; Meyer, M.; Thissen, A., Chemical surface analysis on materials and devices under functional conditions – Environmental photoelectron spectroscopy as non-destructive tool for routine characterization. *Journal of Electron Spectroscopy and Related Phenomena* **2019,** *231*, 118-126.
2. Linford, M. R. R., T.; Shah .; , Near Ambient Pressure XPS (NAP-XPS). A New Paradigm for the Technique. *Vacuum Technology & Coating* August 2018.
3. Salmeron, M.; Schlogl, R., Ambient pressure photoelectron spectroscopy: A new tool for surface science and nanotechnology. *Surf. Sci. Rep.* **2008,** *63*, 169-199.
4. Olivieri, G.; Giorgi, J. B.; Green, R. G.; Brown, M. A., 5 years of ambient pressure photoelectron spectroscopy (APPES) at the Swiss Light Source (SLS). *Journal of Electron Spectroscopy and Related Phenomena* **2017,** *216*, 1-16.
5. Cushman, C. V.; Dahlquist, C. T.; Dietrich, P. M.; Bahr, S.; Thißen, A.; Schaff, O.; Banerjee, J.; Smith, N. J.; Linford, M. R., Trends in Advanced XPS Instrumentation. 5. Near-Ambient Pressure XPS. *Vac. Techno. Coat* **2017,** *August*, 23-31.
6. Patel, D. I.; Roychowdhury, T.; Jain, V.; Shah, D.; Avval, T. G.; Chatterjee, S.; Bahr, S.; Dietrich, P.; Meyer, M.; Thißen, A.; Linford, M. R., Introduction to near-ambient pressure x-ray photoelectron spectroscopy characterization of various materials. *Surface Science Spectra* **2019,** *26* (1), 016801.
7. Rodriguez, C.; Dietrich, P.; Torres-Costa, V.; Cebrián, V.; Gómez-Abad, C.; Díaz, A.; Ahumada, O.; Silván, M. M., Near ambient pressure X-ray photoelectron spectroscopy monitoring of the surface immobilization cascade on a porous silicon-gold nanoparticle FET biosensor. *Applied Surface Science* **2019**.
8. Kjærvik, M.; Hermanns, A.; Dietrich, P.; Thissen, A.; Bahr, S.; Ritter, B.; Kemnitz, E.; Unger, W. E. S., Detection of suspended nanoparticles with near-ambient pressure x-ray photoelectron spectroscopy. *Journal of Physics: Condensed Matter* **2017,** *29* (47), 474002.
9. Kjærvik, M.; Schwibbert, K.; Dietrich, P.; Thissen, A.; Unger, W. E. S., Surface characterisation of Escherichia coli under various conditions by near-ambient pressure XPS. *Surface and Interface Analysis* **2018,** *50* (11), 996-1000.
10. Rieß, J.; Lublow, M.; Anders, S.; Tasbihi, M.; Acharjya, A.; Kailasam, K.; Thomas, A.; Schwarze, M.; Schomäcker, R., XPS studies on dispersed and immobilised carbon nitrides used for dye degradation. *Photochemical & Photobiological Sciences* **2019**.
11. Siegbahn, H., Electron spectroscopy for chemical analysis of liquids and solutions. *The Journal of Physical Chemistry* **1985,** *89* (6), 897-909.
12. Cheng, M. H.; Callahan, K. M.; Margarella, A. M.; Tobias, D. J.; Hemminger, J. C.; Bluhm, H.; Krisch, M. J., Ambient Pressure X-ray Photoelectron Spectroscopy and Molecular Dynamics Simulation Studies of Liquid/Vapor Interfaces of Aqueous NaCl, RbCl, and RbBr Solutions. *The Journal of Physical Chemistry C* **2012,** *116* (7), 4545-4555.
13. Jain, V.; Bahr, S.; Dietrich, P.; Meyer, M.; Thißen, A.; Linford, M. R., Phosphate Buffered Saline (PBS). Aqueous Solution and Corresponding Solid by Near-Ambient Pressure XPS (NAP-XPS). *Surf.Sci.Spectra* **2018,** *Submitted*.
14. Lai, S.; Wang, S.; Luo, J.; Lee, L. J.; Yang, S.-T.; Madou, M. J., Design of a Compact Disk-like Microfluidic Platform for Enzyme-Linked Immunosorbent Assay. *Analytical Chemistry* **2004,** *76* (7), 1832-1837.

15. Kaufmann, H.; Bailey James, E.; Fussenegger, M., Use of antibodies for detection of phosphorylated proteins separated by two-dimensional gel electrophoresis. *PROTEOMICS* **2001,** *1* (2), 194-199.
16. Jiang, X.; Wang, R.; Wang, Y.; Su, X.; Ying, Y.; Wang, J.; Li, Y., Evaluation of different micro/nanobeads used as amplifiers in QCM immunosensor for more sensitive detection of E. coli O157:H7. *Biosensors and Bioelectronics* **2011,** *29* (1), 23-28.
17. Salam, F.; Uludag, Y.; Tothill, I. E., Real-time and sensitive detection of Salmonella Typhimurium using an automated quartz crystal microbalance (QCM) instrument with nanoparticles amplification. *Talanta* **2013,** *115*, 761-767.
18. Okutucu, B.; Dınçer, A.; Habib, Ö.; Zıhnıoglu, F., Comparison of five methods for determination of total plasma protein concentration. *Journal of Biochemical and Biophysical Methods* **2007,** *70* (5), 709-711.
19. Redmile-Gordon, M. A.; Armenise, E.; White, R. P.; Hirsch, P. R.; Goulding, K. W. T., A comparison of two colorimetric assays, based upon Lowry and Bradford techniques, to estimate total protein in soil extracts. *Soil Biology and Biochemistry* **2013,** *67*, 166-173.
20. Gupta, V.; Ganegoda, H.; Engelhard, M. H.; Terry, J.; Linford, M. R., Assigning Oxidation States to Organic Compounds via Predictions from X-ray Photoelectron Spectroscopy: A Discussion of Approaches and Recommended Improvements. *Journal of Chemical Education* **2014,** *91* (2), 232-238.
21. Das, S. K.; Dickinson, C.; Lafir, F.; Brougham, D. F.; Marsili, E., Synthesis, characterization and catalytic activity of gold nanoparticles biosynthesized with Rhizopus oryzae protein extract. *Green Chemistry* **2012,** *14* (5), 1322-1334.
22. Eby, D. M.; Artyushkova, K.; Paravastu, A. K.; Johnson, G. R., Probing the molecular structure of antimicrobial peptide-mediated silica condensation using X-ray photoelectron spectroscopy. *Journal of Materials Chemistry* **2012,** *22* (19), 9875-9883.
23. Ahmed, M. H.; Byrne, J. A.; McLaughlin, J.; Ahmed, W., Study of Human Serum Albumin Adsorption and Conformational Change on DLC and Silicon Doped DLC Using XPS and FTIR Spectroscopy. *Journal of Biomaterials and Nanobiotechnology* **2013,** *4*, 194-203.
24. Vanea, E.; Simon, V., XPS study of protein adsorption onto nanocrystalline aluminosilicate microparticles. *Applied Surface Science* **2011,** *257* (6), 2346-2352.
25. Tougaard, S., Universality Classes of Inelastic Electron Scattering Cross-sections. *Surface and Interface Analysis* **1997,** *25* (3), 137-154.
26. George, G. A., High resolution XPS of organic polymers—the scienta ESCA 300 data base. G. Beamson and D. Briggs. John Wiley & Sons, Ltd, Chichester, 1992. Pp. 295, price £65.00. ISBN 0-471-93592-1. *Polymer International* **1994,** *33* (4), 439-440.
27. Briggs, D.; Beamson, G., Primary and secondary oxygen-induced C1s binding energy shifts in x-ray photoelectron spectroscopy of polymers. *Analytical Chemistry* **1992,** *64* (15), 1729-1736.
28. Kjaervik, M.; Schwibbert, K.; Dietrich, P.; Thissen, A.; Unger, W. E. S., Surface characterisation of Escherichia coli under various conditions by near-ambient pressure XPS. *Surf. Interface Anal.* **2018,** (1-5).
29. Beamson, G.; Briggs, D., *High Resolution XPS of Organic Polymers*. John Wiley & Sons New York, 1992.
30. Singh, B.; Velázquez, D.; Terry, J.; Linford, M. R., Comparison of the equivalent width, the autocorrelation width, and the variance as figures of merit for XPS narrow scans. *Journal of Electron Spectroscopy and Related Phenomena* **2014,** *197*, 112-117.

31. Singh, B.; Velázquez, D.; Terry, J.; Linford, M. R., The equivalent width as a figure of merit for XPS narrow scans. *Journal of Electron Spectroscopy and Related Phenomena* **2014,** *197*, 56-63.
32. Rae, P. J. D., D. M., The properties of Poly(tetrafluoroethylene)(PTFE) in compression. *Polymer* **2004,** *45*, 7615-7625.
33. Shah, D.; Patel, D. I.; Roychowdhury, T.; Rayner, G. B.; O'Toole, N.; Baer, D. R.; Linford, M. R., Tutorial on interpreting x-ray photoelectron spectroscopy survey spectra: Questions and answers on spectra from the atomic layer deposition of Al2O3 on silicon. *Journal of Vacuum Science & Technology B* **2018,** *36* (6), 062902.
34. Tougaard, S., Improved XPS analysis by visual inspection of the survey spectrum. *Surface and Interface Analysis* **2018,** *50* (6), 657-666.
35. Jürgensen, A.; Esser, N.; Hergenröder, R., Near ambient pressure XPS with a conventional X-ray source. *Surface and Interface Analysis* **2012,** *44*, 1100-1103.
36. Jeong, C.; Yun, H.; Lee, H.; Muller, S.; Lee, J.; Mun, B. S., Performance test of new near-ambient-pressure XPS at Korean Basic Science Institute and its application to CO oxidation study on Pt3Ti polycrystalline surface. *Current Applied Physics* **2016,** *16*, 73-78.
37. Erikson, S. K.; Edstrom, K.; Hagfeldt, A.; Hahlin, M.; Rensmo, H.; Siegbahn, H.; Kahk, J. M.; Villar-Garcia, I. J.; Payne, D. J.; Webb, M. J.; Grennberg, H.; Yakimova, R.; Edwards, M. O. M.; Karlsson, P. G.; Backlund, K.; Ahlund, J., A versatile photoelectron spectrometer for pressures up to 30 mbar. *Rev. Sci. Instrum.* **2014,** *46*.
38. Ogletree, D. F.; Bluhm, H.; Hebenstreit, E. D.; Salmeron, M., Photoelectron spectroscopy under ambient pressure and temperature conditions. *Nuclear Instruments and Methods in Physics Research Section A: Accelerators, Spectrometers, Detectors and Associated Equipment* **2009,** *601*, 151-160.
39. Vacogne, C. D.; Brosnan, S. M.; Masic, A.; Schlaad, H., Fibrillar gels via the self-assembly of poly(l-glutamate)-based statistical copolymers. *Polymer Chemistry* **2015,** *6* (28), 5040-5052.
40. Idelson, M., Poly(γ-benzyl-L-glutamate) and other glutamic-acid-containing polymers *Journal of Polymer Science: Polymer Letters Edition* **1985,** *23* (11).
41. Dechant, J., Polymer handbook. 3rd edition. J. BRANDRUP and E. H. IMMERGUT (editors). ISBN 0-471-81244-7. New York/Chichester/Brisbane/Toronto/Singapore: John Wiley & Sons 1989. Cloth bond, ca. 1850 pages, £ 115.00, $175.00. *Acta Polymerica* **1990,** *41* (6), 361-362.
42. McKinnon, A. J.; Tobolsky, A. V., Structure and properties of poly-gamma-benzyl-L-glutamate cast from dimethylformamide. *The Journal of physical chemistry* **1968,** *72* (4), 1157-61.
43. DeLong, L. M.; Russo, P. S., Thermodynamic and dynamic behavior of semiflexible polymers in the isotropic phase. *Macromolecules* **1991,** *24* (23), 6139-6155.
44. Ahmed, M. H.; Byrne, J. A.; McLaughlin, J.; Ahmed, W., Study of Human Serum Albumin Adsorption and Conformational Change on DLC and Silicon Doped DLC Using XPS and FTIR Spectroscopy. *Journal of Biomaterials and Nanobiotechnology* **2013,** *Vol.04No.02*, 10.
45. Foster, R. N.; Harrison, E. T.; Castner, D. G., ToF-SIMS and XPS Characterization of Protein Films Adsorbed onto Bare and Sodium Styrenesulfonate-Grafted Gold Substrates. *Langmuir* **2016,** *32* (13), 3207-3216.
46. Jain, V.; Kjærvik, M.; Bahr, S.; Dietrich, P.; Meyer, M.; Thißen, A.; Linford, M. R., Bovine serum albumin, aqueous solution, by near-ambient pressure XPS. *Surf. Sci. Spectra* **2019,** *accepted*

47. Beamson, G.; Briggs, D., *High Resolution XPS of Organic Polymers* John Wiley & Sons New York, 1992.
48. Briggs, D.; Beamson, G., Primary and Secondary Oxygen-Induced C1s Binding-Energy Shifts in X-Ray Photoelectron-Spectroscopy of Polymers. *Analytical Chemistry* **1992,** *64* (15), 1729-1736.
49. Jain, V.; Biesinger, M. C.; Linford, M. R., The Gaussian-Lorentzian Sum, Product, and Convolution (Voigt) functions in the context of peak fitting X-ray photoelectron spectroscopy (XPS) narrow scans. *Applied Surface Science* **2018,** *447*, 548-553.
50. Frisch, M. J.; Trucks, G. W.; Schlegal, H. B.; Scuseria, G. E.; Robb, M. A.; Cheeseman, J. R.; Scalmani, G.; Barone, V.; Mennucci, B.; Petersson, G. A.; Nakatsuji, H.; Caricato, M.; Li, X.; Hratchian, H. P.; Izmaylov, A. F.; Bloino, J.; Zheng, G.; Sonnenberg, J. L.; Hada, M.; Ehara, M.; Toyota, K.; Fukuda, R.; Hasegawa, J.; Ishida, M.; Nakajima, T.; Honda, Y.; Kitao, O.; Nakai, H.; Vreven, T.; Montgomery, J., J. A.;; Peralta, J. E.; Ogliaro, F.; Bearpark, M.; Heyd, J. J.; Brothers, E.; Kudin, K. N.; Staroverov, V. N.; Kobayashi, R.; Normand, J.; Raghavachari, K.; Rendell, A.; Burant, J. C.; Iyengar, S. S.; Tomasi, J.; Cossi, M.; Rega, N.; Millam, J. M.; Klene, M.; Knox, J. E.; Cross, J. B.; Bakken, V.; Adamo, C.; Jaramillo, J.; Gomperts, R.; Stratmann, R. E.; Yazyev, O.; Austin, A. J.; Cammi, R.; Pomelli, C.; Ochterski, J. W.; Martin, R. L.; Morokuma, K.; Zakrzewski, V. G.; Voth, G. A.; Salvador, P.; Dannenberg, J. J.; Dapprich, S.; Daniels, A. D.; Farkas, Ö.; Foresman, J. B.; Ortiz, J. V.; Cioslowski, J.; Fox, D. J., Gaussian 09, Revision E.01. *Chemical Science* **2015**.
51. Tardio, S.; Cumpson, P. J., Practical estimation of XPS binding energies using widely available quantum chemistry software. *Surface and Interface Analysis* **2018,** *50* (1), 5-12.
52. Zhao, J.; Gao, F.; Pujari, S. P.; Zuilhof, H.; Teplyakov, A. V., Universal Calibration of Computationally Predicted N 1s Binding Energies for Interpretation of XPS Experimental Measurements. *Langmuir* **2017,** *33* (41), 10792-10799.
53. Beard, B. C.; Hare, J., Surface interaction of quaternary amines with hair. *Journal of Surfactants and Detergents* **2002,** *5* (2), 145-150.
54. Beard, B. C.; Johnson, A.; Cambria, F. M.; Trinh, P. N., Electron spectroscopy and microscopy applied to chemical and structural analysis of hair. *J Cosmet Sci* **2005,** *56* (1), 65-77.
55. Beard, B. C.; Johnson, A.; Cambria, F. M.; Trinh, P. N., Electron spectroscopy and microscopy applied to chemical and structural analysis of hair. *Journal of cosmetic science* **2005,** *56* (1), 65-77.
56. Xue, C.-H.; Bai, X.; Jia, S.-T., Robust, Self-Healing Superhydrophobic Fabrics Prepared by One-Step Coating of PDMS and Octadecylamine. *Scientific Reports* **2016,** *6*, 27262.
57. Louette, P.; Bodino, F.; Pireaux, J.-J., Poly(dimethyl siloxane) (PDMS) XPS Reference Core Level and Energy Loss Spectra. *Surface Science Spectra* **2005,** *12* (1), 38-43.
58. Jain, V.; Kjærvik, M.; Bahr, S.; Dietrich, P.; Meyer, M.; Thißen, A.; Linford, M. R., Bovine Serum Albumin (BSA), Aqueous Solution, by Near-Ambient Pressure XPS (NAP-XPS). *Surf. Sci. Spectra* **2018**.
59. Gahmberg, C. G.; Hakomori, S.-i., External Labeling of Cell Surface Galactose and Galactosamine in Glycolipid and Glycoprotein of Human Erythrocytes. *Journal of Biological Chemistry* **1973,** *248* (12), 4311-4317.
60. Martin, N. C.; Pirie, A. A.; Ford, L. V.; Callaghan, C. L.; McTurk, K.; Lucy, D.; Scrimger, D. G., The use of phosphate buffered saline for the recovery of cells and spermatozoa from swabs. *Science & Justice* **2006,** *46* (3), 179-184.

61. O-W, M.; J, D.; P, N.-H.; S, L.; D, K.; J-L, S., New Process for Cell Detachment: Use of Heparin. In *Animal Cell Technology: From Vaccines to Genetic Medicine*, Carrondo, M. J. T.; Griffiths, B.; Moreira, J. L. P., Eds. Springer Netherlands: Dordrecht, 1997; pp 343-348.
62. Lichtenauer, M.; Nickl, S.; Hoetzenecker, K.; Mangold, A.; Moser, B.; Zimmermann, M.; Hacker, S.; Niederpold, T.; Mitterbauer, A.; Ankersmit, H. J., Phosphate Buffered Saline Containing Calcium and Magnesium Elicits Increased Secretion of Interleukin-1 Receptor Antagonist. *Laboratory Medicine* **2009,** *40* (5), 290-293.
63. Wilfinger, W.; Mackey, K.; Chomczynski, P., *Effect of pH and ionic strength on the spectrophotometric assessment of nucleic acid purity*. 1997; Vol. 22, p 474-6, 478.
64. Pérez-Dieste, V.; Aballe, L.; Ferrer, S.; Nicolàs, J.; Escudero, C.; Milán, A.; Pellegrin, E., Near Ambient Pressure XPS at ALBA. *Journal of Physics: Conference Series* **2013,** *425* (7), 072023.
65. Moulder, J. F.; Stickle, W. F.; Sobol, P. E.; Bomben, K. D., *Handbook of X-ray photoelectron spectroscopy*. Physical Electronics, Inc.: USA, 1995.

CHAPTER 6: Conclusions and Future Work

My graduate research was primarily focused on two areas: (i) the preparation, functionalization, and characterization of DCMS and HiPIMS carbon for bioarrays, and (ii) applications of XPS peak fitting in material characterization. In the following section, I will be talking about key findings from each chapter.

6.1 Key Findings from Each Chapter

In chapter 2, we successfully synthesized and performed the functionalization on DCMS and HiPIMS carbon surfaces. The functionalization was done through activation/amidation and halogenation/amination chemsitries. Based on percentage of oxygenated moieties present on each kind of surfaces as determined by XPS, we compared the activity of DCMS and HiPIMS carbon functionalization. Since, HiPIMS carbon is richer in oxygenated species, it has shown higher amount of amidation than DCMS carbon. We observed pretty consistent results with halogentation/amination route, and DCMS surface have shown higher amount of halogenation and subsequent amination than HiPIMS carbon.

To better peak fit and analyze XPS narrow scans, we discuss some of the important line shapes/functions. Chapter 3 talks about these line shapes including GLS, GLP, and Voigt functions that can be used to peak fit XPS narrow scans. Here, the comparison of GLP and GLS line shapes with Voigt functions has been done. This comparison concluded that GLP function is a better approximation of Voigt function. However, these two functions are not interchangeable and have their own place in XPS peak fitting and they both can be useful while peak fitting.

Peak fitting principles were implemented to determine the surface chemical composition of various materials including three amino silanes (APTES, APDIPES, APDEMS) and some unconventional materials that were analyzed by NAP-XPS. Chapter four to nine of this thesis

discuss characterization of these materials. Data were obtained either by conventional XPS or NAP-XPS and peak fitting was done on CasaXPS.

Chapter 4 of this thesis focuses on the deposition of different silanes through chemical vapor deposition and their effect on peptide stability and purity. My contribution in this article includes application of data analysis through XPS peak fitting. Through XPS peak fitting of different narrow scans, deposition of different silanes were confirmed.[243] Here, after the deposition of all three aminosilane, the presence of small nitrogen peak in all three survey scans confirm the deposition.

In chapter 5 we worked on the characterization of Bovine Serum Albumin (BSA) by NAP-XPS and its analysis by peak-fitting C 1s, O 1s and N 1s narrow scans. [ref] Here, peak fitting of C 1s envelope allowed us to determine the kind of environment and different chemical peaks BSA can have. Also, the presence of different kinds of nitrogen and oxygen in their respective peak envelope confirmed the presence of protein.

Chapter 6 of this thesis discusses the analysis of Teflon (polytetrafluoroethylene or PTFE) by NAP-XPS. In this study, we talk about extent of charging at lower pressure that cause a dramatic shift in C 1s and F 1s peak positions. However, acquiring the data at higher pressure, i.e. ca. 1 mbar or more leads to automatic Environmental Charge Compensation by background gas. With increasing pressure, the C 1s and F 1s peaks shift towards their standard binding energy or their natural peak positions. Also, change in equivalent widths with varying pressure and with different illumination times at a constant pressure has been discussed.

Chapter 7 of this thesis includes the analysis of a new polymer poly(γ-Benzyl L-Glutamate) (PBLG), by near-ambient pressure XPS and determination of surface chemistry through peak fitting C 1s, and O 1s narrow scans. In this study, we used three different approaches to peak fit C

1s peak envelope to determine the chemical composition. O 1s peak envelope was also peak fitted to assist the characterization. Also, in this work, we utilized the first principle calculation using the Hartree-Fock method to see the spacing between different 1s orbitals of carbon and oxygen. This provided us a very good theoretical basis for peak fitting, especially for determining the theoretical chemical shifts between different peaks present in the total peak envelope.

Chapter 8 of this thesis includes the analysis of different hair samples by NAP-XPS. This work consists of three different hair samples: (i) blank hair, (ii) colored hair, and (iii) bleached hair. Comparison of silicon, sulfur, and carbon have been done, and results showed that due to dimethicon treatment, colored and bleached samples have shown the presence of silicon which was absent in the case of blank sample. Also, due to an increase in silicon, colored and bleached samples do not show any presence of sulfur, and there is a peak at the lower binding energy in C 1s narrow scan in the case of bleached sample. The presence of C-Si indicates the presence of a linier siloxane polymer that comes from dimethicon.

Chapter 9 of this thesis includes the analysis of an important biological buffer solution called phosphate buffer saline (PBS) and PBS solid. The purpose of this study is to demonstrate the kind of chemical species/peaks possible in the PBS solid and PBS liquid sample.

6.2 Future Work

In my work, I have shown the application of mathematical function/line shapes (GLS and GLP) for peak fitting XPS narrow scans. I have discussed some examples where these functions can be implemented in XPS peak fitting. In our lab we have used various functions to peak fit XPS narrow scans to characterize various materials. Future work should include use of these functions for more complex data sets from XPS and from others techniques as well.

I presented here the functionalization of DCMS and HiPIMS carbon surfaces for their application as interface in bioarrays. I have shown two strategies to chemically attach small biomolecules onto these surfaces. These strategies should be explored more for further bioconjugation with larger biomolecules like DNA and proteins for biosensing.

Moreover, I have functionalized the silicon (100) surface by etching the oxide with HF (this work is not presented in this thesis). Also, I further tried functionalization of this etched surface through Si-C bond formation. Silicon (100) is one of the most widely used substrates in the semiconductor industry. The problem associated with the chemical stability of adsorbates on the silicon surface can be overcome if we can covalently attach the biomolecules onto the surface through Si-C bond formation via liquid phase organic chemistry. Therefore, future work should focus on developing covalent attachment chemistry on silicon.

I worked on material characterization, mostly through XPS peak fitting. I certainly believe there are many opportunities in this area and more to explore. Unfortunately, the literature contains many examples of bad XPS peak fitting that result in poor material characterization. Therefore, there should be more focus on good XPS peak fitting in the literature in order to obtain more accurate characterization of materials.

Appendix A1: Supporting Information for Chapter 2

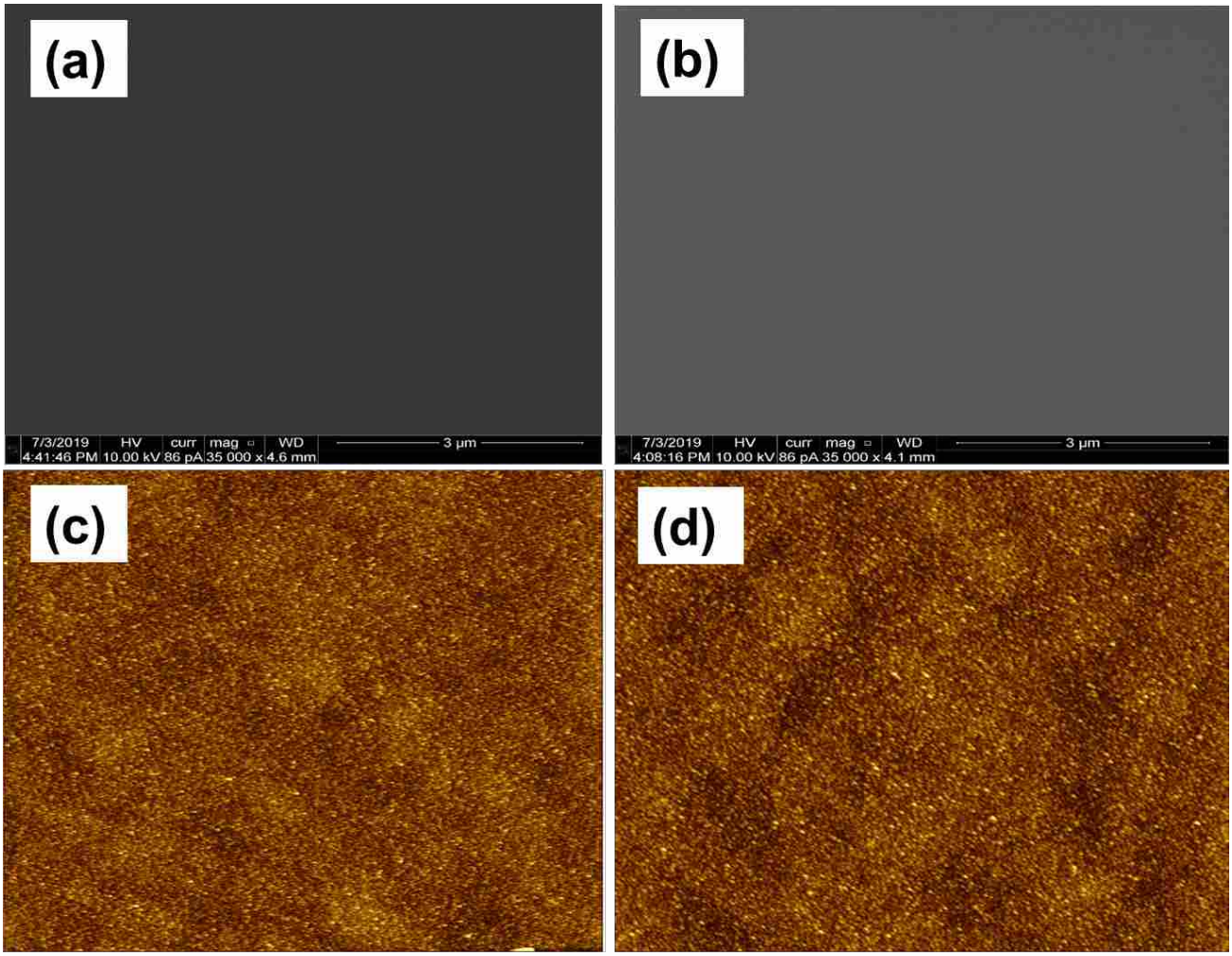

Figure A 1.1. SEM and AFM images of sputtered carbon surfaces. (a) SEM of DCMS carbon at 3 µm scale, (b) SEM of HiPIMS carbon at 3 µm scale, (c) AFM of DCMS carbon, and (d) AFM of HiPIMS carbon. The AFM scale goes from 0 nm (darkest) to 16 nm (lightest).

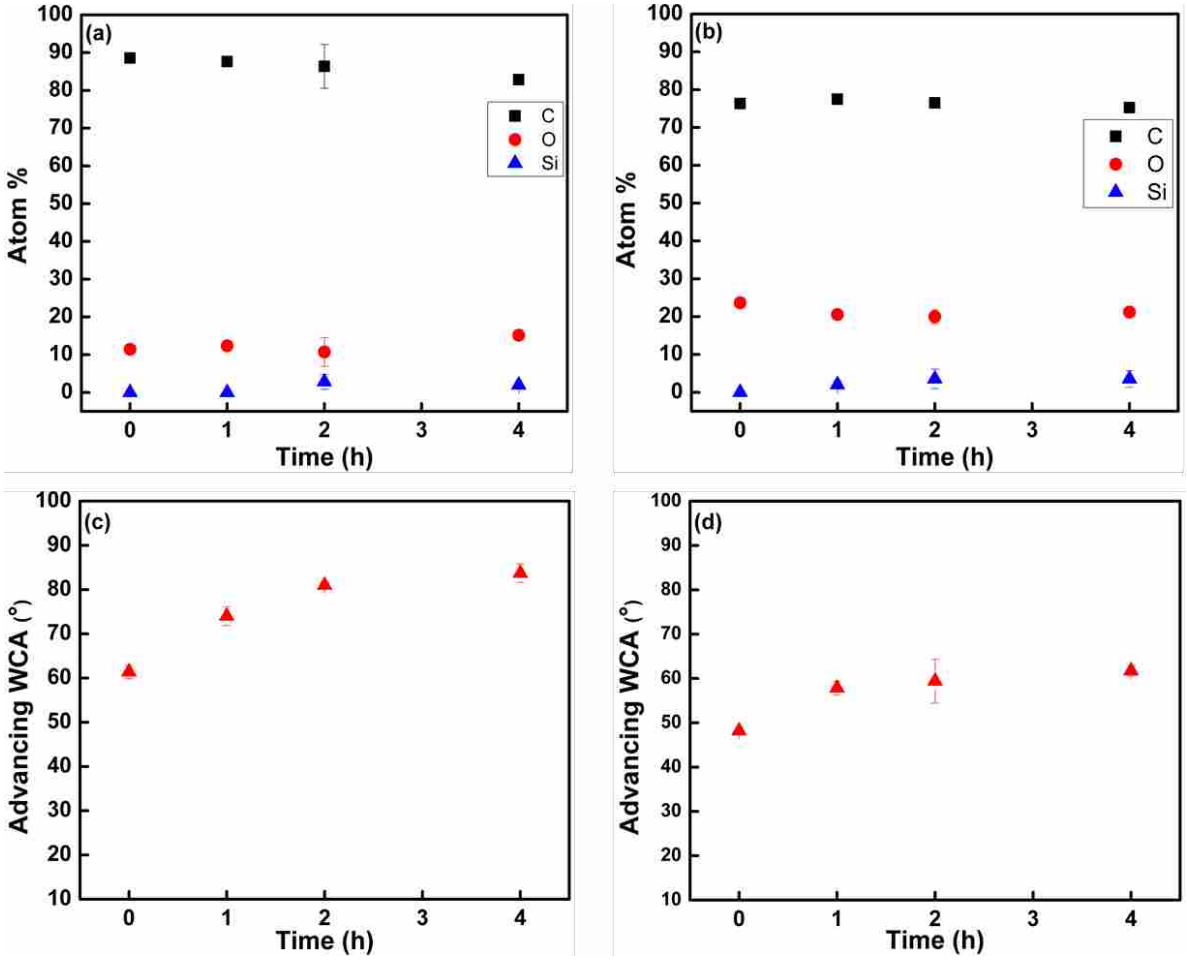

Figure A 1.2. Changes in composition and wetting of sputtered carbon surfaces after heating at 55 °C in water. (a) change in composition of DCMS carbon (b) change in composition of HiPIMS carbon, (c) change in wetting of DCMS carbon, and (d) change in wetting of HiPIMS.

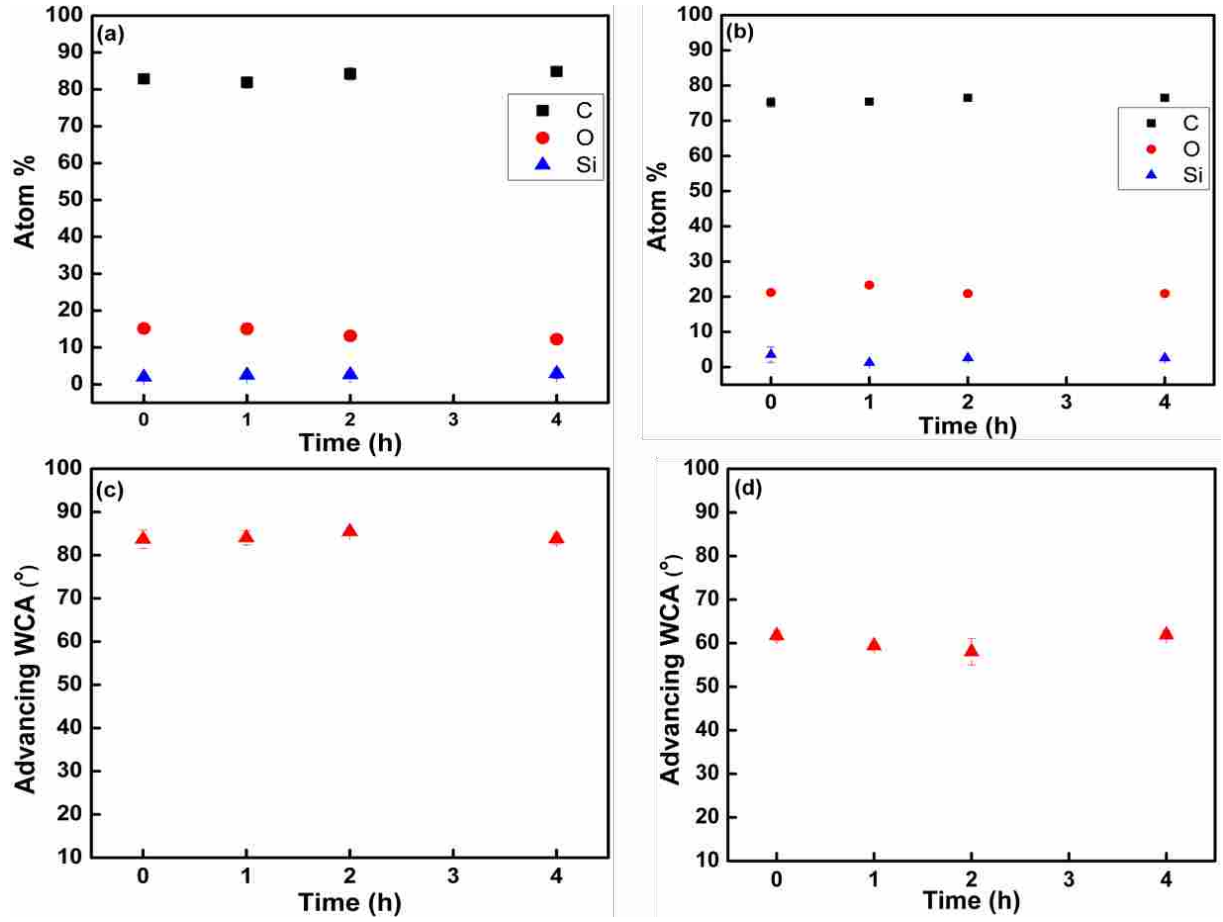

Figure A 1.3. Changes in composition and wetting of sputtered carbon surfaces after heating at 95 °C in water. (a) change in composition of DCMS carbon (b) change in composition of HiPIMS carbon, (c) change in wetting of DCMS carbon, and (d) change in wetting of HiPIMS carbon.

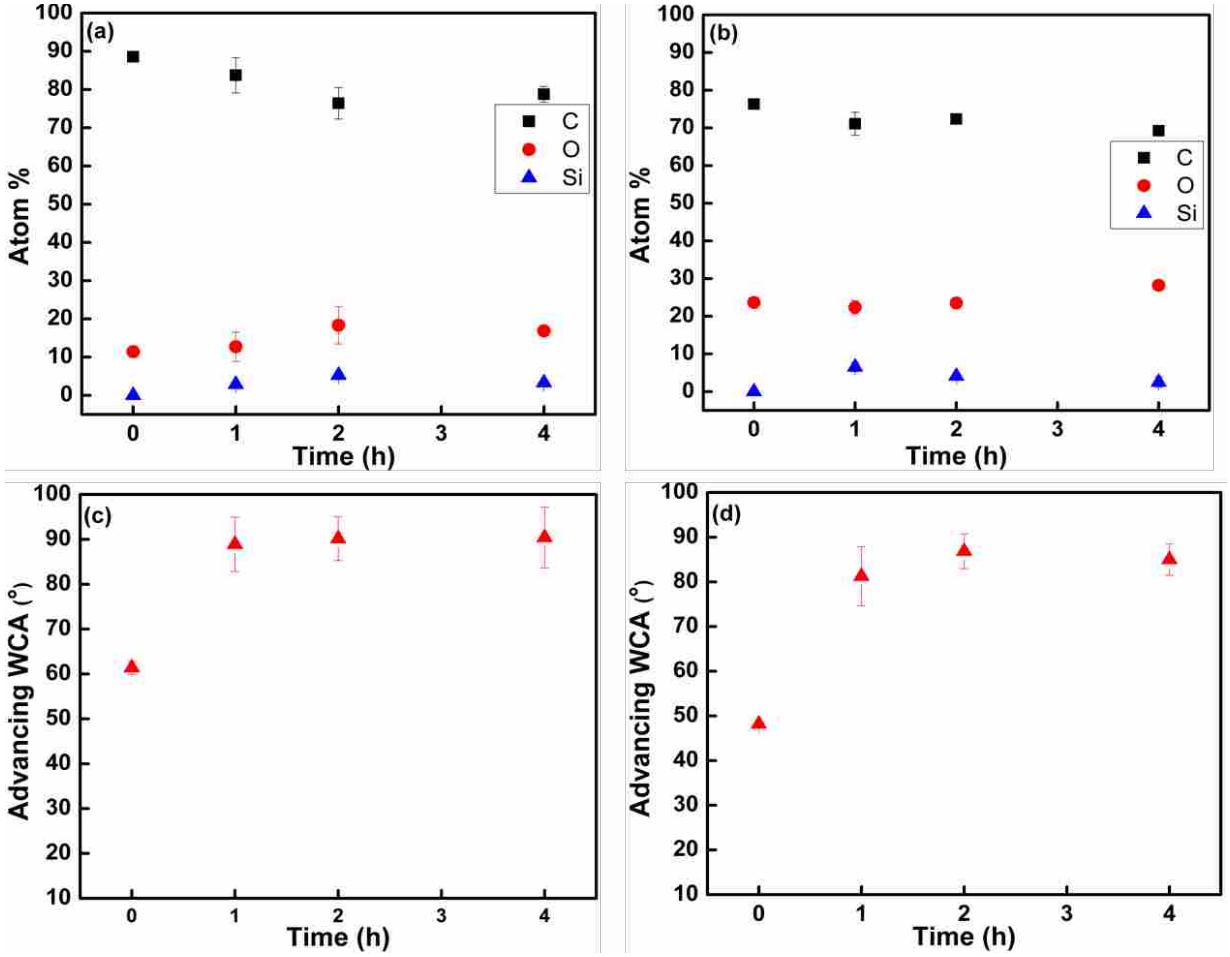

Figure A 1.4. Changes in composition and wetting of sputtered carbon surfaces after heating at 55 °C in Tris buffer. (a) change in composition of DCMS carbon (b) change in composition of HiPIMS carbon, (c) change in wetting of DCMS carbon, and (d) change in wetting of HiPIMS carbon.

Appendix A2: Supporting Information for Chapter 3

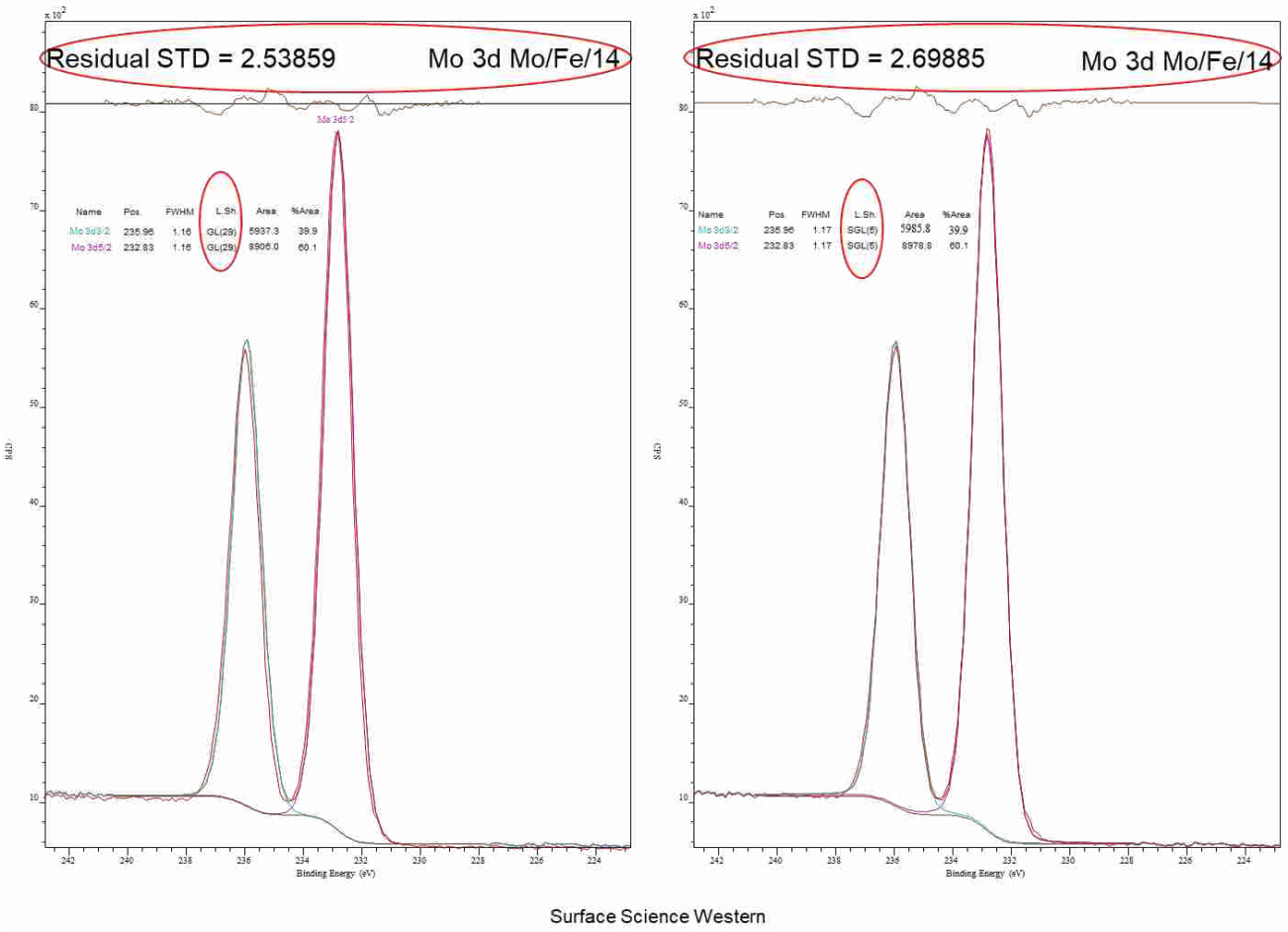

Figure A 2.1. Showing the comparison of GLS and GLP.

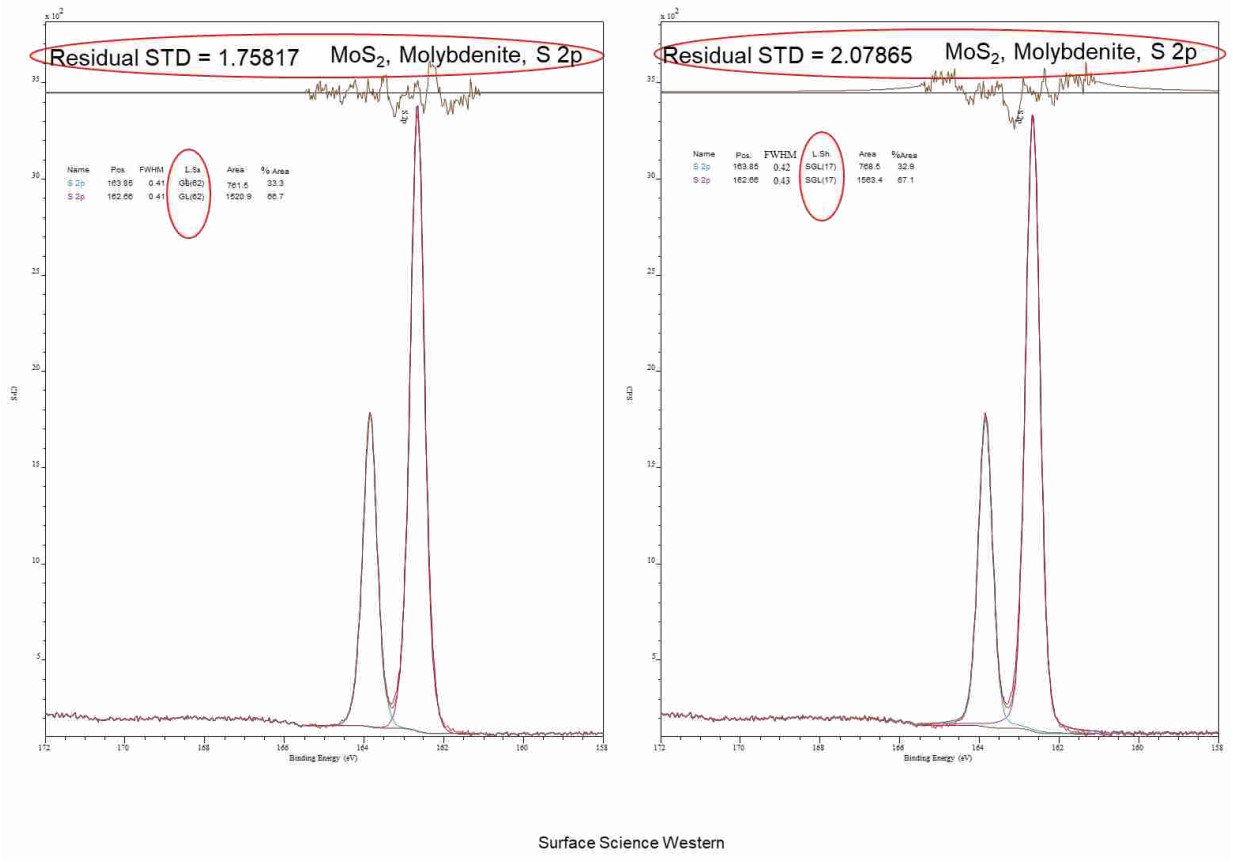

Figure A 2.2. Showing the comparison of GLS and GLP.